Layer detection and snowpack stratigraphy characterisation from digital penetrometer signals

James Floyer, 2008

UNIVERSITY OF CALGARY

Layer detection and snowpack stratigraphy characterisation from digital penetrometer signals

by

James Antony Floyer

A THESIS

SUBMITTED TO THE FACULTY OF GRADUATE STUDIES

IN PARTIAL FULFILLMENT OF THE REQUIREMENTS FOR THE

DEGREE OF DOCTOR OF PHILOSOPHY

DEPARTMENT OF GEOSCIENCE

CALGARY, ALBERTA

APRIL, 2008

© James Antony Floyer 2008

Abstract

Forecasting for slab avalanches benefits from precise measurements of snow stratigraphy. Snow penetrometers offer the possibility of providing detailed information about snowpack structure; however, their use has yet to be adopted by avalanche forecasting operations in Canada. A manually driven, variable rate force-resistance penetrometer is tested for its ability to measure snowpack information suitable for avalanche forecasting and for spatial variability studies on snowpack properties. Subsequent to modifications, weak layers of 5 mm thick are reliably detected from the penetrometer signals. Rate effects are investigated and found to be insignificant for push velocities between 0.5 to 100 cm s^{-1} for dry snow. An analysis of snow deformation below the penetrometer tip is presented using particle image velocimetry and two zones associated with particle deflection are identified. The compacted zone is a region of densified snow that is pushed ahead of the penetrometer tip; the deformation zone is a broader zone surrounding the compacted zone, where deformation is in compression and in shear. Initial formation of the compacted zone is responsible for pronounced force spikes in the penetrometer signal.

A layer tracing algorithm for tracing weak layers, crusts and interfaces across transects or grids of penetrometer profiles is presented. This algorithm uses Wiener spiking deconvolution to detect a portion of the signal manually identified as a layer in one profile across to an adjacent profile. Layer tracing is found to be most effective for tracing crusts and prominent weak layers, although weak layers close to crusts were not well traced. A framework for extending this method for detecting weak layers with no prior knowledge of weak layer existence is also presented. A study relating the fracture character of layers identified in compression tests is presented. A multivariate model is presented that distinguishes between *sudden* and *other* fracture characters 80% of the time.

Transects of penetrometer profiles are presented over several alpine terrain features

commonly associated with spatial variability of snowpack properties. Physical processes relating to the variability of certain snowpack properties revealed in the transects is discussed. The importance of characteristic signatures for training avalanche practitioners to recognise potentially unstable terrain is also discussed.

Acknowledgements

I would like to extend my sincere gratitude to Bruce Jamieson, my supervisor, who has been an inspirational teacher and mentor. This work would not have been possible without his unfailing support.

I thank my fellow graduate students and field technicians for their friendship, energy and tireless assistance with winter fieldwork: Laura Bakermans, Dave Gauthier, Catherine Brown, Thomas Exner, Cam Campbell, Paul Langevin, Ken Matheson, Ali Haeri and Willy Rens.

For fieldwork support and guidance, special thanks are due to Bruce McMahon and Jeff Goodrich as well as the other members of the Avalanche Control Section at Glacier National Park: Eric Dafoe, Johann Schleiss, Jim Phillips, Dean Flick, Mark Harrison, Luc Beaulieu, Zuzana Driedeger and Tom Chalmers. I would like to thank the avalanche forecasting staff at Kicking Horse Mountain Resort: Steve Parsons, Jeremy Cox and Mike Rubenstein. In addition, I extend my gratitude to Mike Wiegele and his staff at Mike Wiegele Heli-Skiing.

I would like to thank Roddy Mackenzie for designing and building the instrument that this research is centred on, as well as Warwick Payten, who provided software related support. Thanks are also due to the staff at the Engineering Machine Shop at the University of Calgary, in particular Rob Scorey and Joe Sabourin.

For reviews of the manuscript, which greatly improved its quality, I am indebted to Bruce Jamieson, Thomas Exner, Mike Smith, Karl Birkeland, Martin Schneebeli, Jerome Johnson, Jo Jacka and Dieter Ayers. I am also indebted to a great number of avalanche professionals in Western Canada and beyond who have shared ideas, experiences and improved my understanding of and respect for the avalanche phenomenon.

Finally, I would like to thank my fiancée, Vérèna Blasy for her understanding, love,

patience and wholehearted support throughout this endeavour. Thank you for sharing your love of life and love of the mountains with me.

Table of Contents

Approval Page . . . ii
Abstract . . . iii
Acknowledgements . . . v
Table of Contents . . . vii
List of Tables . . . x
List of Figures . . . xi
List of Symbols and Abbreviations . . . xiv
1 Introduction . . . 1
1.1 Avalanches in Canada . . . 2
1.2 Types of avalanche . . . 4
1.3 Slab failure . . . 5
1.4 Avalanche forecasting and the role of the snow profile . . . 8
1.5 What is snow hardness? . . . 9
1.6 The SABRE penetrometer . . . 11
1.7 Choice of penetrometer for this study . . . 11
1.8 Winter fieldwork . . . 14
1.8.1 Study areas . . . 14
1.8.2 General operation and safety procedures . . . 15
1.9 In context: How this research may help . . . 16
2 Penetrometer validation . . . 18
2.1 Introduction . . . 18
2.2 Literature review: Snow stratigraphy and penetrometers . . . 19
2.2.1 Early observations and large-scale surveys . . . 19
2.2.2 Manual methods for assessing snow stratigraphy . . . 21
2.2.3 Mechanical instruments for assessing snow stratigraphy . . . 21
2.2.4 Digital snow penetrometers . . . 23
2.2.5 Radar . . . 30
2.2.6 Other methods . . . 31
2.3 General methods . . . 32
2.3.1 Unmodified SABRE penetrometer . . . 33
2.3.2 Modified SABRE penetrometer . . . 34
2.3.3 Manual snow profile measurements . . . 35
2.3.4 Snow stability tests . . . 38
2.3.5 Avalanche observations . . . 40
2.4 Initial testing of the SABRE penetrometer . . . 41
2.4.1 Depth signal . . . 42
2.4.2 Force-resistance signal . . . 51
2.4.3 Temperature signal . . . 54
2.5 Modifications to the SABRE penetrometer . . . 56
2.5.1 Depth measurement platform . . . 58
2.5.2 Data recording system . . . 58

2.5.3 Depth measurement error . . . 59
2.5.4 Modified tip designs . . . 60
2.6 Testing the modified SABRE penetrometer . . . 62
2.6.1 Modified depth signal . . . 62
2.6.2 Correlating force-resistance with hand hardness . . . 65
2.6.3 Repeatability of the force signal . . . 70
2.7 Identifying weak layers . . . 75
2.8 Conclusions . . . 79
3 Rate effects and snow deformation analysis . . . 81
3.1 Introduction . . . 81
3.2 Literature review: Rate effects and snow deformation . . . 82
3.2.1 Rate effects . . . 82
3.2.2 Snow deformation . . . 83
3.3 Methods . . . 85
3.3.1 Rate-effects . . . 85
3.3.2 Snow deformation . . . 86
3.4 Results . . . 89
3.4.1 Rate-effects . . . 89
3.4.2 Snow deformation . . . 91
3.5 Further analysis and discussion . . . 94
3.5.1 Compaction zone build-up . . . 94
3.5.2 Strain analysis of snow deformation . . . 97
3.5.3 Lateral spreading . . . 103
3.5.4 Model applicability . . . 103
3.6 Conclusions . . . 104
4 Layer detection and identification . . . 107
4.1 Introduction . . . 107
4.2 Literature review: layer detection and identification . . . 109
4.2.1 Layer tracing and detection . . . 109
4.2.2 Fracture character . . . 110
4.3 Layer tracing . . . 112
4.3.1 Introduction . . . 112
4.3.2 Method . . . 113
4.3.3 Model testing . . . 119
4.3.4 Results . . . 122
4.4 Weak layer detection . . . 125
4.4.1 Introduction . . . 125
4.4.2 Proposed method . . . 125
4.4.3 Discussion . . . 128
4.5 Predicting fracture character from penetrometer profiles . . . 129
4.6 Introduction . . . 129
4.6.1 Method . . . 130
4.6.2 Univariate analysis . . . 136
4.6.3 Discriminant analysis . . . 144

4.6.4 Discussion . . . 149
4.7 Conclusions . . . 150
5 Case studies of spatial variability . . . 152
5.1 Introduction . . . 152
5.2 Literature review: Spatial variability of snow . . . 154
5.2.1 Scale issues . . . 154
5.2.2 Regional-scale variability . . . 155
5.2.3 Factors important for snowpack variability . . . 156
5.2.4 Slope- and feature-scale variability of snowpack properties . . . 157
5.2.5 Slope- and feature-scale variability of snow stability . . . 160
5.2.6 Summary, spatial variability . . . 162
5.3 Methods . . . 163
5.3.1 Transect surveying . . . 163
5.3.2 Geostatistical methods . . . 165
5.3.3 Scale and climatic issues . . . 167
5.4 Results and analysis . . . 167
5.4.1 Avalanche flank transect . . . 167
5.4.2 Wind affected slopes . . . 175
5.4.3 Rain runnel transect . . . 184
5.4.4 Gully transect . . . 189
5.4.5 Boulder field transect . . . 191
5.4.6 Aspect change . . . 195
5.4.7 Elevation change . . . 198
5.5 Summary and conclusions . . . 199
6 Conclusions . . . 203
6.1 Penetrometer validation . . . 203
6.2 Rate effects and snow deformation analysis . . . 204
6.3 Layer detection and identification . . . 205
6.4 Case studies of spatial variability . . . 206
6.5 Recommendations for further work . . . 207
6.5.1 Penetrometer design . . . 207
6.5.2 Remote penetrometer installation . . . 208
6.5.3 Anisotropic nature of weak layers . . . 208
6.5.4 Snow deformation analysis . . . 210
6.5.5 Weak layer identification from penetrometer signals . . . 211
6.5.6 Spatial variability . . . 212
A SABRE specifications . . . 234
B Datalogger specifications . . . 236
C Correlation between hand hardness and density . . . 237
D Estimate of lateral spreading in the snowbox experiments . . . 239
E Manual snow profiles for the spatial variability case studies . . . 243

List of Tables

1.1 Hand hardness scale. 10

2.1 Commonly used grain types for snow crystals. 37
2.2 Rutschblock scores. 40
2.3 Avalanche size classification. 41
2.4 Cross correlations for each segment of the two pushes shown in Figure 2.11. 50
2.5 Mean force values and force ranges for hand hardness categories. 70
2.6 Pearson correlation coefficient matrix for force values correlated between the four pushes in Figure 2.23. 74
2.7 Matrix of differences in mean force between the four pushes in Figure 2.23. 74

3.1 Snow properties for the layers used for the rate effect experiments. 85
3.2 Snow properties for the layers used for the snow deformation experiments. 88

4.1 Results from the initial layer-tracing testing. 123
4.2 Fracture character classification. From van Herwijnen and Jamieson (2007a). 130
4.3 Variables used in the fracture character comparison analysis. 137
4.4 Discriminant analysis function coefficients for determining sudden/other group membership. 146
4.5 Classification matrix for predicting fracture character from penetrometer signal variables. 149

5.1 Scales applicable to snow processes associated with avalanche formation. 155
5.2 Snow property variations across a fractured slab. n=46 for each case. . . 172

A.1 Specifications of the SABRE penetrometer sensors. 235
A.2 Specifications of the TR1-TruTrac^{TM} rotary encoder wheel. 235

B.1 Specifications of the Campbell Scientific CR1000 datalogger as configured for operation with the SABRE penetrometer and custom depth encoder. 236

C.1 Numerical hardness (strength) values assigned to each hand hardness category 238

D.1 Values used in the lateral spreading effect calculations. 242

List of Figures

1.1 Avalanche fatalities in Canada for the 10 year period from 1998–2007. . . 3
1.2 The two principle types of avalanche. 4
1.3 Slab avalanche with insert showing surface hoar crystals from the weak layer. 5
1.4 The SABRE penetrometer. 12
1.5 Map of the Columbia Mountains showing Rogers Pass and Blue River field stations. 15

2.1 Charles Bradley with his Snow Resistograph c.1970. 23
2.2 The Digital Resistograph. 24
2.3 The Snow Fork. 25
2.4 The Capacitec Probe. 26
2.5 The SnowMicroPen. 27
2.6 The Advanced Snow Sonde. 28
2.7 The SABRE penetrometer during testing. 29
2.8 The modified SABRE penetrometer. 34
2.9 Snowpack stability tests. a) Compression test. b) Rutschblock test. ASARC photos. 40
2.10 Penetrometer depth sensor testing at the Above Schuss Lake field site. . 43
2.11 Force-resistance–depth profiles for two side-by-side pushes. 49
2.12 Measuring the maximum applied force during the force testing experiments. 52
2.13 Plot of peak penetrometer output against applied force for the force testing experiment. 53
2.14 SABRE temperature output from four adjacent pushes compared to a manual temperature profile. 57
2.15 Views of the depth measurement platform. 58
2.16 Different tips tested with the SABRE penetrometer. 61
2.17 Force-resistance–depth profile for 3 different tip shapes. 63
2.18 Depths measured using the encoder wheel on the measuring platform plotted against manually measured push depths. 66
2.19 Manual hand hardness compared to penetrometer force-resistance for three pushes at different locations. 68
2.20 Box and whisker plot of force-resistance values for each hand hardness category. 69
2.21 Plot of snow hardness against density. 71
2.22 Manual snow profile at Fidelity Study Slope site for 11-Mar-2006. 72
2.23 Four neighbouring penetrometer pushes from the Fidelity Study Slope site collected on 11-Mar-2006. 73
2.24 Closeup from the the four pushes shown in Figure 2.23. 76
2.25 Manual snow profile and detail from three penetrometer pushes taken at the Bostock Traverse site on 20-Feb-2007. 78

3.1 Apparatus for performing rate-effect experiments. 86
3.2 Apparatus for analyzing snow deformation patterns around the penetrometer tip. 87
3.3 Typical force and velocity traces for dry, pencil-hardness snow. 89
3.4 Combined force–velocity pairs for all traces for four different snow layers. 90
3.5 "Flow" vectors indicating the velocity of marker particles relative to the penetrometer tip for two different snow layers. 93
3.6 Horizontal and vertical deformation extents for different snow densities using different penetrometer tips. 94
3.7 Combined force–velocity pairs with early-push spike data excluded for four different snow layers. 96
3.8 Deformation rate field for layers 1 and 2. 98
3.9 Normalised strain components for layers 1 and 2. 101

4.1 Typical unfiltered penetrometer profile compared with filtered signal. . . 115
4.2 Tracing a layer from the interpreted signal to an un-interpreted signal. . 120
4.3 Schematic of the steps involved in the proposed weak layer detection model. 126
4.4 Schematic showing compression test geometry and penetrometer push locations for the fracture character comparison study. 132
4.5 Compression test fracture locations interpreted onto four penetrometer pushes. 134
4.6 Univariate plots of the variables shown in Table 4.3 for *sudden* and *other* fracture character groups. 138

5.1 Hypothetical variogram indicating the range, sill and nugget. 166
5.2 Photo of the Bostock-Schuss avalanche flank transect site. 170
5.3 Avalanche flank transect, 17-Feb-2007 from the Bostock-Schuss site. . . . 171
5.4 Plot of average layer hardness for the weak layer, slab and substratum for the Bostock-Schuss avalanche flank transect. 172
5.5 Variograms of force-resistance for the avalanche flank transect. 174
5.6 Photo of the Poetry Slopes site. 176
5.7 Wind affected slope transect, 07-Jan-2007 from the Poetry Slopes site. . . 178
5.8 Variograms for trend-removed snow properties from the Poetry Slopes wind transect. 179
5.9 Normalised plots of layer interface depth and mean force-resistance for the middle layer identified in the Poetry Slopes wind transect. 181
5.10 Photo of the Roundhill site. 182
5.11 Wind affected slope transect, 15-Mar-2007 from the Roundhill site. . . . 183
5.12 Variograms for trend-removed snow properties from the Roundhill wind transect. 185
5.13 Plot of coefficient of variability of layer thickness against mean layer depth for layers identified in the Roundhill wind transect. 186
5.14 Photos of the runnel feature at the Fidelity Study Slope site. 187
5.15 Runnel transect, 13-Mar-2007 from the Fidelity Study Slope site. 188

5.16 Photo of the Above Fidelity Station gully transect site, surveyed on 20-Mar-2006. 190
5.17 Gully transect, 20-Mar-2006 from the Above Fidelity Station Site. 192
5.18 Photo of the Loop-Ross boulder field site, surveyed on 26-Jan-2007. . . . 193
5.19 Boulder field transect, 26-Jan-2007 from the Loop-Ross Site. 194
5.20 Photos of the Gopher Butte aspect transect site. 196
5.21 Aspect transect, 21 to 22-Feb-2007 around Gopher Butte Knoll. 197
5.22 Plots of the cosine of the slope angle and degrees from southwest with interface depth for the Gopher Butte aspect transect. 198
5.23 Elevation transect, 13-Mar-2007 from 1120 to 1850 m elevation on Mount Fidelity. 200

6.1 Ideas for penetrometer design for assessing the shear strength of snow. . . 210

D.1 Plan view of geometry used to assess the effect of lateral spreading on the snow deformation experiments. 240
D.2 Contour plots of lateral spreading for a range of values for the radial extent of the compaction zone and the ratio of compacted to uncompacted snow. 242

E.1 Manual snow profile for the Bostock-Schuss avalanche flank transect. . . 244
E.2 Manual snow profile for the Poetry Slopes wind transect. 245
E.3 Manual snow profile for the Roundhill wind transect. 246
E.4 Manual snow profile for the Fidelity Study Slope runnel transect. 247
E.5 Manual snow profile for the Above Fidelity Station gully transect, east aspect. 248
E.6 Manual snow profile for the Above Fidelity Station gully transect, south aspect. 249
E.7 Manual snow profile for the Loop-Ross boulder field transect. 250
E.8 Manual snow profile for the Gopher Butte aspect transect – northwest-facing slopes. 251
E.9 Manual snow profile for the Gopher Butte aspect transect – southeast-facing slopes. 252
E.10 Manual snow profile for the highest elevation site on the Mount Fidelity elevation transect. 253

List of Symbols and Abbreviations

ASARC	Applied Snow and Avalanche Research, University of Calgary

Penetrometer variables

Δd	difference between manual and calculated depth
Δd_{seg}	depth interval for interpolated penetrometer segment
ϵ_d	depth error
ϵ_i	interpolation error
ϵ_m	manual depth measurement error
ϵ_{se}	standard error
a	acceleration
d_{meas}	total depth of the push, measured on the side of the penetrometer
d_m	manual depth measurement
d_{p_corr}	corrected penetrometer depth
d_{p_int}	total depth of the push, calculated by integrating the acceleration signal
d_p	depth in the penetrometer signal
f	frequency
f_i	interpolation frequency
g	acceleration due to gravity
$g(t)$	depth-time function between interpolation points
l_{ls}	segment length
n_{ss}	number of data points in a segment
r_{max}	maximum correlation
T	time period
t	time
v_p	penetrometer push velocity

Snow deformation

$\dot{\gamma}_{xy}$	shear strain rate component
$\dot{\varepsilon}_x$, $\dot{\varepsilon}_y$	strain rate components, x and y directions respectively
γ_{xy}	shear strain component
ρ	snow density
ε_x, ε_y	strain components, x and y directions respectively
u, v	original (field of view) position field coordinates
x, y	rotated position field coordinates

Signal processing

(ω)	frequency domain
$*$	convolution operator
γ^i	i^{th} post-processing filter
$\mathbf{R}$	autocorrelation matrix
τ	frequency cut-off parameter
ε	error between actual and desired output
a	inverse filter
C	crosscorrelation vector
e	desired output
G	penetrometer force–depth signal
g^i	i^{th} pre-processing filter
H_H	Hann window
H_T	tapered window
W	master wavelet (in unfiltered signal)
w	wavelet (in filtered signal)
w_max, w_min	upper and lower boundaries for the wavelet
y	vertical displacement

Statistics

α	significance level
γ	semivariance
F	F-statistic
n, N	number of data
p	probability associated with a statistic
R^2	coefficient of determination
t	students t-statistic
W	Shapiro-Wilk normality test statistic
Z	randomly distributed variable
z	z-statistic
IQR	interquartile range

Hand hardness

x	incremental integer value for hand hardness category
F	fist
1F	one finger
4F	four finger
P	pencil
K	knife
I	ice

Grain types

DF	decomposing fragments
MF	mixed forms
RG	rounded grains
SH	surface hoar

Stability tests/avalanches

CTE	compression test easy (1 to 10 taps)
CTM	compression test moderate (11 to 20 taps)
CTH	compression test hard (21 to 30 taps)
RB	rutschblock
Sa	skier accidental avalanche
Sr()	skier triggered avalanche, triggered at the distance in m shown in parentheses

Fracture character prediction

SP	sudden planar
SC	sudden collapse
RP	resistant planar
PC	progressive collapse
B	non-planar break
Avg_Grad__A	average hardness gradient above the weak layer
Avg_Grad__B	average hardness gradient below the weak layer
Max_Grad__A	maximum hardness gradient above the weak layer
Max_Grad__B	maximum hardness gradient below the weak layer
Ratio_Slab:WL__A	ratio of slab hardness to weak layer hardness above the weak layer
WL_D	depth to weak layer
WL_H	mean hardness of weak layer
WL_Thick	thickness of weak layer

Chapter 1

Introduction

In Canada, snow avalanches[1] are a significant natural hazard that affect winter recreationalists, transportation corridors, resource industries, energy transmission lines and residential areas (Stethem and others, 2003). Avalanches have been responsible for fatalities in British Columbia, Alberta, Quebec, Newfoundland and Labrador, Yukon, Nova Scotia, Ontario, Northwest Territories and Nunavut (Campbell and others, 2007). In recent years, the majority of avalanche victims have been killed whilst engaging in backcountry winter recreation, typically skiing/snowboarding, snowmobiling and ice climbing.

High resolution, digital penetrometers (Dowd and Brown, 1986; Sihvola and Tiuri, 1986; Louge and others, 1998; Schneebeli and Johnson, 1998; Abe and others, 1999; Mackenzie and Payten, 2002) are being developed for use in avalanche forecasting. These instruments allow rapid assessment of snow stratigraphy that pertains to avalanche formation, such as the depth to a weak layer and the thickness and hardness of an overlying slab. Because of their ability to collect many profiles during the course of a day, digital penetrometers are a favourable tool for the assessment of the spatial distribution of snowpack properties.

There are three principal underlying questions that have directed the work for this thesis. First: is it possible to measure the spatial variability of snow properties using a penetrometer that is practical and affordable for a typical Canadian avalanche forecasting operation? Second: what types of processing or analysis of the penetrometer signal can

[1]Distinctions are commonly made between snow avalanches, ice avalanches (McClung and Schaerer, 1993, p.85 and front cover image), rock/ice avalanches such as the event of 2002 that killed 140 people in the Russian Caucasus mountains (Huggel and others, 2005) and other types of avalanche such as sand pile avalanches (e.g. Bak, 1996). In this thesis, I use *avalanche* synonymously with *snow avalanche* throughout.

be done that might make it a more useful instrument for avalanche forecasters? And third: what can be said about the spatial variability of the snowpack over specific terrain features that have been investigated using a digital penetrometer?

The penetrometer chosen for this study was the SABRE penetrometer (Mackenzie and Payten, 2002), manufactured by Himachal Safety Systems. This thesis is concerned with the design, modification and testing of this instrument. It is concerned with processing the data and visualising them in a way that maximises the usefulness of the information that is obtained. The thesis is also also concerned with using the penetrometer to make objective measurements of snow hardness over specific terrain features that can be associated with avalanches. The ultimate goals are to improve our ability to measure and assess snow stratigraphy, and to improve our knowledge of how this stratigraphy varies over terrain. If these goals can be realised then avalanche professionals will benefit from being able to make better decisions regarding avalanche safety.

1.1 Avalanches in Canada

During the 10 year period between 1998 and 2007, an average of 15 people per year were killed in Canada as a result of avalanches[2]. This represents a rise from the period 1990 to 2000, where the average number of fatalities was 12.5 per year (Stethem and others, 2003) and from the period 1970 to 1996, where the average number of fatalities was 8.5 per year (Jamieson and Geldsetzer, 1996). This rise is attributed to an increase in the popularity of mountain-based winter recreation (Haegeli, 2005). Figure 1.1 shows the breakdown of recent avalanche fatalities in Canada by province and by activity.

Through media coverage, tragedies associated with winter backcountry recreation may define a stereotypical image of what constitutes the avalanche hazard in Canada. However, there are many other aspects to this hazard. These include: exposure to the

[2]Data from the Westwide Avalanche Network, www.avalanche.org.

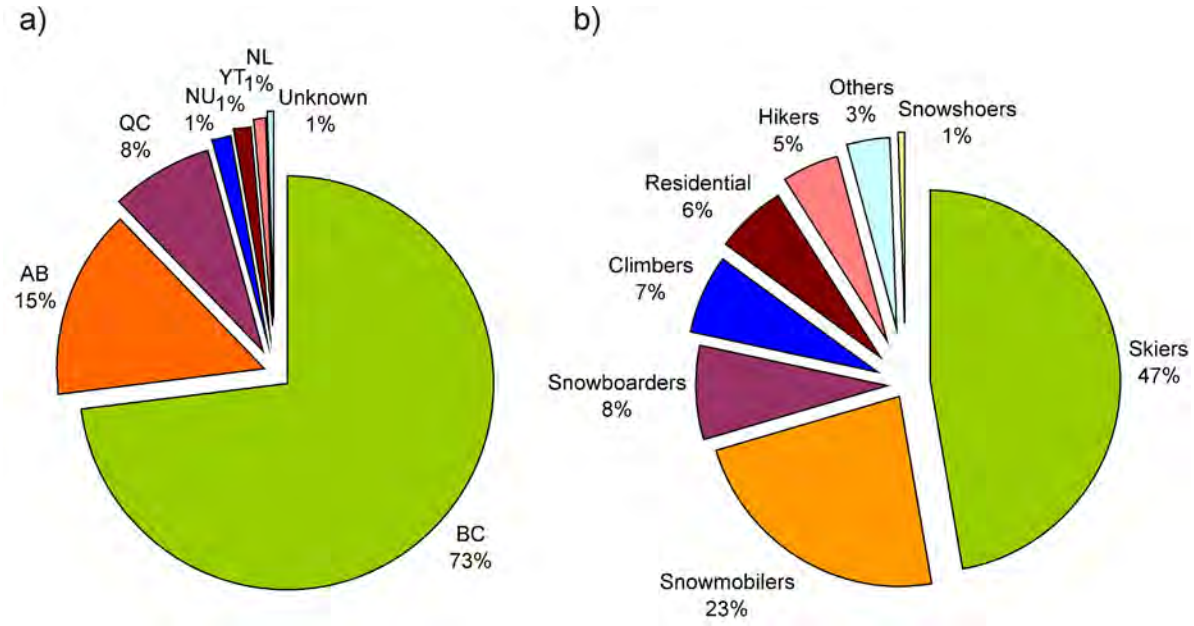

Figure 1.1: Avalanche fatalities in Canada for the 10 year period from 1998–2007 by a) province and b) activity. The Canadian provinces and territories represented are: British Columbia, BC; Alberta, AB; Quebec, QC; Nunavut, NU; Yukon, YT; and Newfoundland and Labrador, NL. Data from the Westwide Avalanche Network, www.avalanche.org.

traveling public on highways that pass through avalanche terrain; exposure to personnel and goods on the railways; exposure to skiers/snowboarders at in-bounds ski resorts; exposure to personnel and the potential destruction of timber in winter forestry harvesting areas; and exposure to mining personnel and equipment around mines and the access roads that service them. In these cases, the typical operator or member of the public does not make their own decisions regarding avalanche safety; instead they rely on professional forecasters who are charged with assessing the avalanche risk and implementing situation-appropriate mitigation procedures that may include closures, passive defences such as snowsheds or reinforced concrete walls, explosive control measures, and non-explosive control measures such as ski-cutting or skier-compaction (e.g. McClung and Schaerer, 2006, p.174). Therefore, avalanches affect a very wide range of people in Canada and work related to improving avalanche safety is important for the well being of Canadians in general.

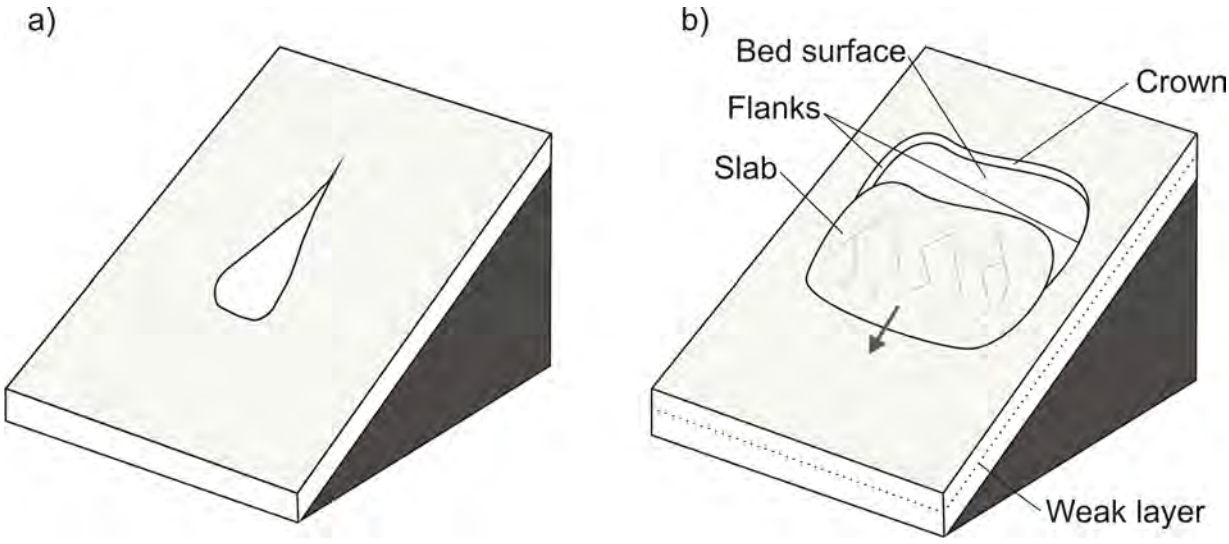

Figure 1.2: The two principle types of avalanche: a) loose snow avalanche and b) slab avalanche. After McClung and Schaerer (2006, p.73).

1.2 Types of avalanche

There are two general types of avalanche: loose-snow avalanches and slab avalanches (e.g. McClung and Schaerer, 2006, p.73). Loose snow avalanches primarily involve snow at or near the surface and initiate at a point, spreading out into a triangular or tear-drop shape as they move down the slope (Figure 1.2a). They involve snow with little or no cohesion, which is readily set in motion if disturbed on a sufficiently steep slope. Slab avalanches initiate by the failure of a thin weak layer that lies beneath a relatively cohesive slab (Figure 1.2b). This results in the release of a block of snow, which then slides down the slope over the bed surface. The wall at the top margin of the slab, exposed by the avalanche release, is known as the crown. The left and right exposed margins are known as the flanks. Figure 1.3 shows an image of a slab avalanche where the crown and bed surface are clearly visible, together with surface hoar crystals from the weak layer that formed the failure plane of this avalanche.

Slab avalanches account for around 95% of avalanche fatalities in Canada (Jamieson and Geldsetzer, 1996, p.16). As just mentioned, slab avalanches require a specific snow-

Figure 1.3: Slab avalanche with the crown and bed surface clearly visible. Insert shows large surface hoar crystals approximately 10 to 20 mm in length, taken from the weak layer that formed the failure plane of this avalanche.

pack stratigraphy in order to form — a cohesive slab overlying a weak layer. A primary piece of information for avalanche practitioners in assessing the likelihood of a slab avalanche occurring on a slope is whether or not this specific type of stratigraphy exists in the snowpack. An experienced forecaster may be able to predict whether the critical layered structure exists from an analysis of the present and past weather conditions. However, a far more accurate assessment is possible if the practitioner looks at the snowpack itself and records and tests the snow stratigraphy directly.

1.3 Slab failure

The classic and widely adopted model of slab avalanche release was developed by McClung (1979), based on a model by Palmer and Rice (1973) describing slope failure in over-consolidated clays, precipitated by strain softening. McClung (1977) had previously shown that snow exhibits strain softening behaviour in a similar way to clay soils, which led him to believe that Palmer and Rice's model could be adapted to describe avalanche release. Strain softening of snow allows shear stress to be concentrated in shear bands in

the weak layer, which underlies the relatively stiffer slab. When the stress over a certain area within the shear bands exceeds a critical value, a shear fracture initiates in the weak layer. The stress concentration model permits avalanche release even when the applied shear stress is less than the shear strength of the weak layer. Once initiated, the fracture propagates rapidly within the weak layer away from the point of initiation. At the top margin of the avalanche, a tensile fracture occurs in the slab, exposing the crown, which is usually at 90° to the bed surface.

McClung and Schaerer (2006) summarised the important condition for slab avalanche instability, which is the balance between the fracture toughness in the weak layer and the stress intensity factor, which is the product of applied shear stress and the square root of a length scale. When the stress intensity exceeds the fracture toughness, crack propagation in the weak layer occurs, often resulting in an avalanche. The stress intensity may exceed fracture toughness from direct loading, either from rapid snowfall, or by applying an external load such as a skier, snowmobile, or explosive charge; or from the indirect process of stress concentration in the weak layer described above. The appropriate length scale is the slab thickness.

Fracture toughness has units kPa $m^{\frac{1}{2}}$ and depends on the shear strength of the weak layer, the stiffness at the bottom of the slab, and the presence of imperfections, or weaknesses that may help initiate the fracture. McClung and Schweizer (2006) argue that the stiffness (which can be assessed by hardness measurements) of approximately the first 20 cm of the slab above the weak layer is critical for determining fracture toughness, and that knowledge of the structure of snow at this point in the snowpack can help predict both the likelihood and the size of the potential avalanche.

There have been variations proposed to the model of McClung (1979). Bažant and others (2003) determined a size effect law to account for different properties of slabs of different thicknesses. Fyffe and Zaiser (2004) used a statistical model of transient local

regions of failed snow, which converged to result in catastrophic failure. Louchet (2001) accounted for creep instabilities by modeling the rate of bond ruptures and subsequent healing (sintering).

More recently, there has been focus on the role of weak layer collapse in propagating fractures within the weak layer. Gauthier (2007) reviewed several sources of experimental evidence and conducted fracture propagation experiments by cutting the weak layer of an isolated snow column using a saw (Gauthier and Jamieson, 2008), and suggested that "recent experimental results are difficult to reconcile with fracture mechanics models". It should be mentioned, however, that McClung (1981) recognised that bending could occur in the slab if the weak layer was thick, resulting in a diagonal shear mode associated with the collapse of the weak layer. Heierli (2005) and Heierli and Zaiser (2006) proposed a fracture model using a propagating bending wave, resulting in weak layer collapse. Heierli and Zaiser (2008) updated this model to apply to the case of inclined slopes and found that for low-angled to moderately steep slopes, weak layer collapse provides most of the energy required for fracture propagation, whereas for very steep slopes, parallel-slip (the mechanism proposed by McClung, 1979) provides most of the required energy for fracture propagation. For slopes in the range of 30 to 45°, which is the critical range of angles for most avalanches, both mechanisms supply energy for fracture propagation, with varying proportions. The amount of energy available from collapse is enhanced with thicker weak layers.

The important aspect of this discussion related to this thesis is the critical nature of snow stratigraphy for avalanche formation. As our understanding of the physical processes occurring in the snowpack improves, there evolves a need for more quantitative measurements of layer properties. High-resolution penetrometers have an important role to play in providing that information.

1.4 Avalanche forecasting and the role of the snow profile

Although the importance of snow stratigraphy is emphasised above as an avenue for improving our assessment of avalanche conditions, assessing the structure of the snowpack has long been one of the cornerstones of operational avalanche forecasting[3]. Bader (1939) was an early worker to describe and record systematic measurements of snow structure. In modern avalanche forecasting, observations of snowpack structure are considered to be *class II* data (McClung and Schaerer, 2006, p.168), or to use the term by LaChapelle (1980), *medium entropy*. Such observations include determining the layered structure of the snowpack and making quantitative measurements on the snow in each layer. *Class I* data are instability factors, and include direct observations about recent avalanches, whumphs (rapid settlements in the snowpack), certain snowpack stability tests (see Section 2.3.4) and the fracture character of any failure interfaces (see Section 4.2.2). *Class III* data are snow and weather factors at the snow surface, and include meteorological variables such as the amount of new snow, wind speed and direction, air temperature and amount of solar radiation.

Class I data usually have the greatest influence on forecasting decisions, followed by class II data. To put it one way: having the right snowpack structure means that avalanches are possible; seeing avalanches proves that they are occurring. Class III data are still very important, but evidence from the first two classes tends to have a more direct bearing. Class III data are often used to determine future forecasting trends: that is, whether snowpack stability is likely to increase or decrease over time.

The standard way to represent snowpack structure is using a snow profile (Fig-

[3]Avalanche forecasting is taken here to mean conventional avalanche forecasting, where observations of avalanches, snowpack structure and meteorological variables are combined in a semi-deterministic and semi-intuitive way by a human forecaster to make a judgement about snow stability (LaChapelle, 1980). Numerical avalanche forecasting, using statistical computer methods, is not considered here, although there is undeniably a place for snow structure (either observed or simulated) in numerical avalanche forecasting.

ure 2.22). At the top of the profile, information about the site, the date and time of recording and some weather parameters are recorded. On the left of the page, hand hardness, (and in some operations, ram-resistance) is graphically recorded for each layer identified in the snow. To the right of this, certain snowpack properties for each layer are recorded. These are: snow moisture content; grain type; grain size; hand hardness; and density of the snow. Details of these measurements are given in Section 2.3.3. Additional comments, such as giving the date of burial of a weak layer, or specifying a stability test result at an interface, are often given.

1.5 What is snow hardness?

McClung and Schaerer (2006, p.75) define snow hardness as: "a measure of the strength of snow in compression." It has units of force per unit area, N m^{-2}, or Pa. At the microstructural level, an applied force must do work overcoming various mechanical processes associated with the ice particle interactions. These processes include: ice contact sintering; sliding and rotation at ice particle contacts; and deformation of ice particles and ice particle contacts in tension, compression, shear, torsion and bending (Johnson and Hopkins, 2005).

Snow hardness is crucial for identifying the snow stratigraphy that favours avalanche formation. It is significantly correlated with density (Mellor, 1964, see also Section 2.6.2). Although density measurements of snow are sometimes taken by avalanche practitioners, they are taken less frequently than hardness measurements, and are usually done to supplement hardness measurements rather than in place of them. The importance of snow hardness is due to the fact that it is directly related to the strength of snow.

In order to measure snow hardness, an object must be pushed into the snow and the force required for the object to be able to penetrate the snow assessed. The most

common measurement of snow hardness is the hand hardness test (Colbeck and others, 1990; Canadian Avalanche Association, 2007). This scale is given in Table 1.1. In the North American version of this test, a force of 10 to 15 N is applied when determining the hand hardness value. + and - qualifiers can by used to indicate slight variations in snow hardness.

Table 1.1: Hand hardness scale with abbreviations and descriptions of each division of the scale. The value assigned is the largest object that can be inserted at the required force.

Name	Abbreviation	Description
Fist	F	Gloved fist can penetrate snow
4-Finger	4F	Four fingers in glove can penetrate snow
1-Finger	1F	One gloved finger can penetrate snow
Pencil	P	Blunt end of pencil can penetrate snow
Knife	K	Knife blade can penetrate snow
Ice	I	Too hard to insert knife

The hand hardness scale is widely used because it is quick, simple, requires very simple tools and provides an intuitive measurement that involves direct interaction between the observer and the snow. It is, however, quite a subjective measurement and results depend on the size of the operator's hand as well as their estimation of how much force they are applying to the snow. It is, of course, possible to measure snow hardness more objectively. There is a variety of instruments that are able to provide repeatable, objective measurements of snow hardness (see Section 2.2) including force-resistance penetrometers. Force resistance penetrometers work by measuring the force that is applied to a tip of a certain size and shape using a load cell. While the force (in N) can readily be converted to a hardness value (in Pa) given the surface area of the penetrometer tip, usually this is not done.

It might seem as though converting the penetrometer force values to hardness values would allow comparisons between different penetrometers to be made. However, one difficulty with snow hardness measurements is the fact that they are dependent on the

size and the shape of the object that is deforming the snow (Mellor, 1964). This is because when snow deforms ahead of a penetrating object, this deformed snow must be removed from ahead of the tip if it is not to accumulate in a zone of compacted snow ahead of the tip. The ease of which the deformed snow is ejected from the penetrometer's path depends on the width of the tip and also its shape, with sharp tips promoting rapid ejection and blunt tips increasing the size of the compacted zone ahead of the tip (see Section 3.3.2). The corollary here is that it is not valid to compare hardness measurements between instruments that have different tips, even if the values are converted to the units of strength. The convention, followed here, has been to leave them as force values with the understanding that they are explicitly linked to hardness values for a specific tip.

1.6 The SABRE penetrometer

The SABRE penetrometer is a multi-sensor, manually-driven snow penetrometer for use in assessing snow stratigraphy. The primary sensor is a piezo-electric load cell which measures the force applied to a 12 mm, rounded tip as it is pushed by hand through the snow. Data are recorded at 500 Hz and stored on a handheld PC. The penetrometer is very field portable, with a total weight of less than 1.5 kg. With additional memory in the handheld PC, a virtually unlimited number of profiles can be stored. A single profile takes about 10 seconds to perform with an additional 30 seconds for data processing and storage. The SABRE penetrometer is shown in Figure 1.4 and further specifications are listed in Appendix A.

1.7 Choice of penetrometer for this study

The choice of the SABRE penetrometer was made based on three factors: availability; cost; and perceived potential for use by Canadian avalanche forecasting operations.

Figure 1.4: The SABRE penetrometer: a) closeup of body and tip (note flanged sides about 7 cm up from the tip); b) handheld PC; c) in use. ASARC photos.

Availability

There are at least seven digital penetrometers that have been developed for use in snow stratigraphy studies. These instruments are described in more detail in Section 2.2.4. Since part of the direction for this work was to assess the potential for penetrometer use by Canadian avalanche forecasting operations, it was decided to limit the choice of penetrometer to those that were either commercially available or had a good potential to become commercially available. With this constraint I was left with four options: the Snow Fork (Sihvola and Tiuri, 1986); the SnowMicroPen (SMP) (Schneebeli and Johnson, 1998); the Capacitec probe (Louge and others, 1998) and the SABRE penetrometer (Mackenzie and Payten, 2002).

The Snow Fork was not considered, due to the requirement to dig a snow pit and manually insert the instrument into the side wall of the pit. Pre-production versions of

the Capacitec probe were being tested by Steve Conger from the Avalanche Research Group University of British Columbia (Conger, 2006, 2007). So as not to duplicate Conger's work, it was also decided not to use this penetrometer. In addition, based on the specifications of the Capacitec probe at the time (Robert Foster, 2004, personal communication), it was felt that the vertical resolution offered by this penetrometer might not be sufficient for detecting weak layers in the snowpack.

Cost

At the time of purchase, the SABRE penetrometer was commercially available from Himachal Safety Systems with a purchase price of US$5,000. This was approximately a quarter of the price of the SMP. The lower cost of the SABRE penetrometer was a significant factor for choosing this instrument.

Perceived potential for Canadian forecasting use

At the time of purchase, it was felt that the SABRE penetrometer had a greater potential for adoption by Canadian avalanche forecasting operations. This was primarily because it was the most lightweight and portable penetrometer and it did not require the use of a motor drive unit or depth measurement platform for use[4]. There were reports of icing and instrument drift problems with the SMP (Kronholm, 2004). There were also reports of problems with the SABRE penetrometer recognising ice layers as hard ground strikes (Howard Conway, 2004, personal communication), however, at the time it was felt that the SABRE penetrometer's problems, which were software-related (Roddy Mackenzie, 2004, personal communication), were likely to be more easily overcome. The marketing of the SABRE penetrometer as a finished product (in contrast to the SMP's development status[5]) was also a factor in the decision to use this penetrometer.

[4]This advantage was substantially reduced with the addition of a depth measurement platform during the penetrometer modifications, described in Section 2.5.

[5]Subsequent research and development of the SMP has been very vigorous and many of the technology issues relating to the icing and drift problems have been resolved (Pielmeier and Schweizer, 2007, also

1.8 Winter fieldwork

Winter fieldwork in avalanche areas presents huge challenges as well as providing moments of great joy from working outside in a stunning mountain environment. This is not the place for a detailed account of ASARC operating procedures, but a description of the winter study areas and a brief note about winter fieldwork safety is appropriate.

1.8.1 Study areas

The Applied Snow and Avalanche Research group at the University of Calgary (ASARC) maintains two field stations: Rogers Pass and Blue River. These are shown in Figure 1.5. Both are in the Columbia Mountains of British Columbia. The Rogers Pass field station is in Glacier National Park and is based at the Parks Canada Glacier Compound at Rogers Pass Summit. This field station is staffed continuously from January to the end of March, mostly by graduate students, who work independently from, but in close communication with, the Avalanche Control Section (ACS) and the Warden Service of Glacier National Park. The ACS is responsible for avalanche forecasting and control along the section of Highway 1 that runs through Glacier National Park.

The field station at Blue River is based at Mike Wiegele Helicopter Skiing. It is typically staffed with two field technicians and graduate students make occasional visits. Staff here work closely with guides and operational staff from Mike Wiegele Helicopter Skiing and frequently use their helicopters to access remote sites.

All penetrometer data used in this study (Chapters 2, 3, 4 and 5) were collected at the Rogers Pass study area. Snowbox data for the rate effect and snow deformation analysis (Chapter 3) were collected at both Rogers Pass and Blue River study areas.

Michael Lehning and Karl Birkeland, 2008, personal communication). With hindsight, this instrument would probably have been a better choice for my project.

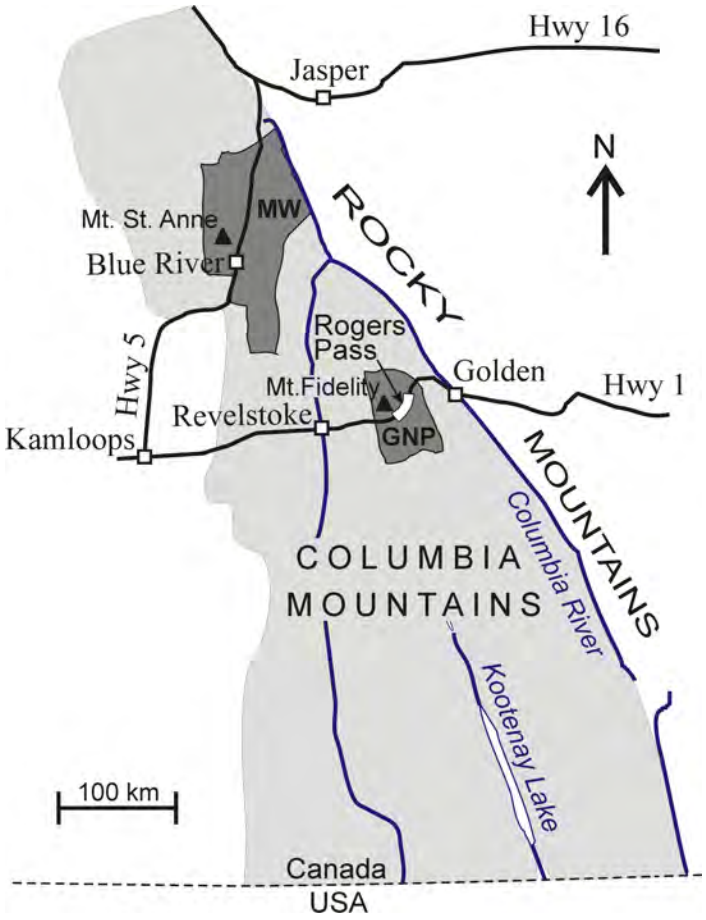

Figure 1.5: Map of the Columbia Mountains showing Rogers Pass and Blue River field stations. Glacier National Park (GNP) and Mike Wiegele Helicopter Skiing tenure (MW) are also shown.

1.8.2 General operation and safety procedures

The ASARC field research program headed by Dr. Bruce Jameison is considered by many to be a leader in promoting good operational practices. Staff members are selected for their ability to make consistent, cautious decisions. At the start of each winter, all staff members undergo two weeks of field training, comprising both mountain skills training and scientific observation consistency training. Occasional mountain skills refresher days are arranged throughout the winter season with experienced local mountain guides. In both fieldwork areas, there is close association between ASARC staff and the local operational staff, with daily meetings to share and discuss observations, forecasts and other

matters relating to mountain safety. Handheld two-way radios are carried in Rogers Pass and at Blue River, and in Rogers Pass a cell-phone provides additional communication capability. Most staff members have wilderness first aid training. Safe winter driving practices are promoted, and staff are encouraged not to drive if conditions (actual or forecasted) deteriorate below a certain point. In the field, staff work as a minimum in a team of two. Team members stay together (or in very close communication) at all times and all team members must agree before committing to a travel plan through avalanche terrain. If any team member becomes uncomfortable with the avalanche terrain travel plan for any reason, a "no questions asked" turnaround policy is in place.

1.9 In context: How this research may help

There are approximately 500 avalanche professionals working in Canada (Clair Israelson, 2005, personal communication). Within this group there is interest in penetrometer technology that may assist with daily forecasting or increasing our understanding of issues associated with the spatial variability of snow. However, despite the fact that digital penetrometers have been in development since the 1980's, they have not yet been adopted for operational use by forecasters in Canada. This thesis presents new research which addresses some of the knowledge gaps which are barriers to adopting penetrometer technology.

Chapter 2 is concerned with the validation of a specific instrument, a SABRE penetrometer, that has aspects of design appropriate to the needs of Canadian forecasting operations. The initial field validation, which is presented in Section 2.4, indicated that modifications would be necessary in order to meet research objectives using this penetrometer. These modifications were implemented (Section 2.5) and the modified penetrometer subsequently field tested (Section 2.6). Recommendations for further pen-

etrometer modifications are outlined in Section 6.5.1.

The SABRE penetrometer is manually driven through the snow, which means that push rates during the course of a push and between successive pushes will vary. Chapter 3 examines whether data collected using a variable-rate, manually driven penetrometer are valid considering the potential problems with rate effects. This is important, since being able to dispense with a motor-drive decreases the weight and increases the portability of the penetrometer; these attributes are highly prized by avalanche field practitioners. The first study to specifically test for rate effects using a manually driven penetrometer is described in Section 3.3.1. Also presented in Section 3.3.2 is a characterisation of snow deformation processes that act at the penetrometer tip, including a calculation of relative strain rates in the snow surrounding the penetrometer tip.

Chapter 4 deals with data processing tasks that aim to improve the useability of penetrometer data. At present, the significant amount of data that can be collected by the SABRE penetrometer requires lengthy data processing procedures to render it useful for snowpack analysis. A layer tracing algorithm is presented in Section 4.3, based on Wiener spiking deconvolution that traces identified components of the penetrometer signal, such as a weak layer, across other profiles in a transect or a grid of profiles. A framework for extending this technique to the problem of weak layer detection is presented in Section 4.4, where a penetrometer profile can be scanned for possible weak layers.

Chapter 5 reports on the results from spatial measurements of snowpack properties made using the modified SABRE penetrometer. Transects of penetrometer profiles across a number of alpine terrain features that can affect snow stability are presented. The spatial structure of some of the transects is analyzed within the range of the measurement scale. The notion of characteristic signatures over different terrain features is advanced as a tool for helping avalanche forecasters and general backcountry users assess possible trigger areas within the snowpack.

Chapter 2

Penetrometer validation

2.1 Introduction

The SABRE penetrometer is as a multi-sensor, manually-driven snow penetrometer for use in assessing snow stratigraphy. It was provided with the following sensors: a piezo-electric sensor coupled to a 12 mm diameter, rounded tip to measure force-resistance; a thermocouple calibrated with a thermopile to measure snow temperature; and an accelerometer for calculating penetration depth.

This chapter is concerned with testing and validating this instrument, which was done prior to undertaking the snow variability studies. It is important to know the abilities and limitations of an instrument before using it to make any kind of qualitative assessments of snow structure or variability. I present here details of comprehensive field testing of this instrument that was performed independently from the instrument manufacturers. Such testing was required due to the newness of the design and the fact that no testing independent from the manufacturers had been reported.

For a reasonable assessment of snow stratigraphy, and to allow comparisons of different profiles to be made, it was considered that the following specifications were required: depth to be accurate to ± 1 cm and precision better than ± 1 mm. Force resistance to be consistent between pushes and able to resolve subtle variations in snow hardness.

One aspect of penetrometer validation, which is very important both for the use of this instrument and for the viability of manually-pushed penetrometer in general is the rate effect. This is the effect that changes in the penetration velocity during the push caused by manually inserting the penetrometer into the snow has on the force-resistance

output. Although this is an integral part of validating this instrument, it is dealt with in its own chapter, Chapter 3, due to its importance as a subject.

2.2 Literature review: Snow stratigraphy and penetrometers

2.2.1 Early observations and large-scale surveys

Early observations of the alpine snowpack and its relationship with avalanches date back to the early 1700's (Pielmeier and Schneebeli, 2003a). Pielmeier and Schneebeli report on several studies, predominantly by Swiss authors, done prior to the 1930's, and describe how the relationship between the stratigraphy of snow and avalanche formation became to be recognised. They suggest that around 1930, more formalised methods for observing and recording snow stratigraphy and other observations important for avalanche formation became adopted.

Bader (1939) describes a repeatable method for recording snow surveys on horizontal terrain for use in time profiles. Density measurements were made on major stratigraphical units identified within the snowpack, as well as interim measurements within these layers. Snow was classified based on grain size, hardness and moisture content. The grain size classification was a three-point scale: fine grain; medium grain; and coarse grain. Hardness was a four-point scale: loose or soft; medium hard; hard; and very hard. Moisture content was a two-point scale: wet or dry.

de Quervain (1950) developed a five-point hand hardness scale which he correlated to ram-resistance results from the Swiss Ramsonde. His scale was: gloved fist; gloved flat hand; one extended finger(!); sharp pencil; and knife blade. These corresponded to ram-resistances of 0 to 3 kg, 3 to 15 kg, 15 to 50 kg, 50 to 150 kg and over 150 kg force respectively.

Klein (1950) reports on a national Canadian survey of the physical characteristics of the snow cover in ten locations across Canada that was done from January to May 1947. Weekly, full-depth snow profiles were observed and measurements of the depths to layer boundaries, snow temperatures, hardness, average grain size, average grain shape and specific gravity were recorded for each layer identified in the snowpack. This survey was repeated in subsequent years (Pearce and Gold, 1951). Two instruments were used for measuring the hardness of snow: the conical ram, known as the Kegelsonde, which appears to be identical to the Swiss ramsonde described below; and the Canadian hardness gauge. The Canadian hardness gauge was a force gauge to which discs of different diameters could be attached for use in different snow types.

The Snow, Ice and Permafrost Research Establishment in the USA (SIPRE, 1954) provided instructions for making and recording snow observations, with the stated aim of "the preparation of maps showing the distribution and changes in features and properties of the snow cover which may affect military operations". The authors specified that the thickness, dominant crystal type, density, temperature, hardness and wetness of each well defined layers should be recorded. The hardness measurements were to be made using mechanical push-gauges, either the Canadian hardness gauge described above, or a slight variant, the SIPRE hardness gauge.

The United Nations Educational, Scientific and Cultural Organization (UNESCO, 1970) issued guidelines on snow observations. Their motivation, however, was the hydrological "inventory of the world's annual ice and snow masses", rather than immediate forecasting for avalanches. This reflected on their recommendation for only a monthly assessment of the stratification of snow and hardness profile.

2.2.2 Manual methods for assessing snow stratigraphy

In Canada today, standard snowpack observations are carried out according to Canadian Avalanche Association (CAA) guidelines (Canadian Avalanche Association, 2007). These guidelines are based on those issued by the Avalanche Research Centre of the National Research Council of Canada (NRCC, 1981), which in turn are based on an internal Parks Canada staff training manual by V.G. Schleiss and W.E. Schleiss. A typical manual snow profile begins with identification of layers using a combination of visual inspection and changes in penetration resistance with depth determined by inserting a crystal screen or other suitable object into the snow. Once identified, the following properties for each layer are recorded: hand hardness; grain type; grain size; liquid water content; and density. More details on these measurements are given in Section 2.3.3. The hand hardness scale, which is the most relevant measurement here, is described by Colbeck and others (1990) is a six-point scale, shown in Table 1.1. In Canadian practice (Canadian Avalanche Association, 2007, p.19), the maximum force required to push the described object into the snow is 10 to 15 N as opposed to 50 N specified by Colbeck and others. Additionally, + and - qualifiers can by used to indicate slight variations in snow hardness. For example, a value of 1F+ is slightly less hard than P-. The qualifiers enhance this scale to an 18-point scale.

2.2.3 Mechanical instruments for assessing snow stratigraphy

Mechanical devices have long been used to measure snow stratigraphy. Seligram (1936) describes the technique of "sounding" for assessing the stratigraphy of the upper snowpack by inserting a pointed stick or a ski stick with the basket removed. He also describes an instrument designed by K. Eugster to measure the "penetrability" of individual layers of snow, essentially a pressure gauge to which different piston heads could be attached. This was the instrument that inspired the design of the Canadian Hardness gauge (Klein,

1946, 1950) described above. According to Pielmeier and Schneebeli (2003a), Eugster also developed the first shear frame for measuring the shear strength at the interface between layers.

Haefeli (1939) developed the Swiss ramsonde from penetrometers used in soil mechanics. The device, which is still used in some avalanche forecasting operations, consisted of a 40 mm, 60° conical metal tip at the end of a shaft onto which a weight can be repeatedly dropped. The tip is placed on the snow surface and driven into the snow by repeatedly dropping the weight. The ram resistance, or hardness, is derived from an energy equation by noting the drop height of the weight and the depth of penetration into the snow. LaChapelle and Perla (1967) noted that the device worked well for hard slabs but was highly inaccurate for soft snow due to the initial displacement when placing the instrument on the snow. They modified Heafeli's penetrometer such that a weighted cone dropped as one unit from a set height above the snow surface; they called this the drop cone penetrometer. Gubler (1975) improved the Ramsonde hardness equation to account for energy losses from the weight guide and shaft couplings.

One of the limitations of the Swiss Ramsonde is that the resolution is too poor to identify weak layers in the snowpack. To address this, Bradley (1966) developed the Snow Resistograph (Figure 2.1). This instrument comprised of a blade tip mounted on the end of a shaft which was mechanically connected to a scribe and paper spool mechanism. According to Karl Birkeland (2008, personal communication), two upwards facing cones, one on each side of the shaft, were mounted on the blade. The instrument was first pushed to the bottom of the snowpack and then rotated by 90°. It was then withdrawn manually at an approximately constant rate. The resistance to upwards movement encountered by the blade/cones, of total top surface area of 6.7 cm^2, was balanced by a spring in the shaft. This caused the scribe to be deflected and the deflections were recorded onto the paper spool, which advanced at a rate consistent with the rate of withdrawal. It it unclear why

Figure 2.1: Charles Bradley with his Snow Resistograph c.1970. John Montagne photo.

Bradley's instrument has not enjoyed greater prominence in snow profile observations. Pielmeier and Schneebeli (2003a) suggest that the weight and cost of the instrument were prohibitive for its use to become widespread, while Schneebeli and Johnson (1998) suggest that the force range of the instrument was too limited. It may also have been difficult to turn the blade at the bottom of the snowpack in snow types other than depth hoar.

2.2.4 Digital snow penetrometers

Dowd and Brown (1986) developed a digital version of Bradley's Resistograph, called the Digital-Thermo Resistograph. This instrument was fitted with a 60° conical shaped tip of 23.5 mm diameter and used a semi-conductor strain gauge and an optical rotary encoder to measure force-resistance and depth respectively. Pielmeier and Schneebeli (2003a) state that the resolution of this instrument was 5 mm and precision for the depth measurements was given by Bradley as ±1 mm. There were plans to use the same instrument to record snow temperature profiles, hence the *Thermo* element in the instrument's name. It appears, however, as though this functionality was never realised. Brown and Birkeland (1990) produced an improved version of this instrument with no

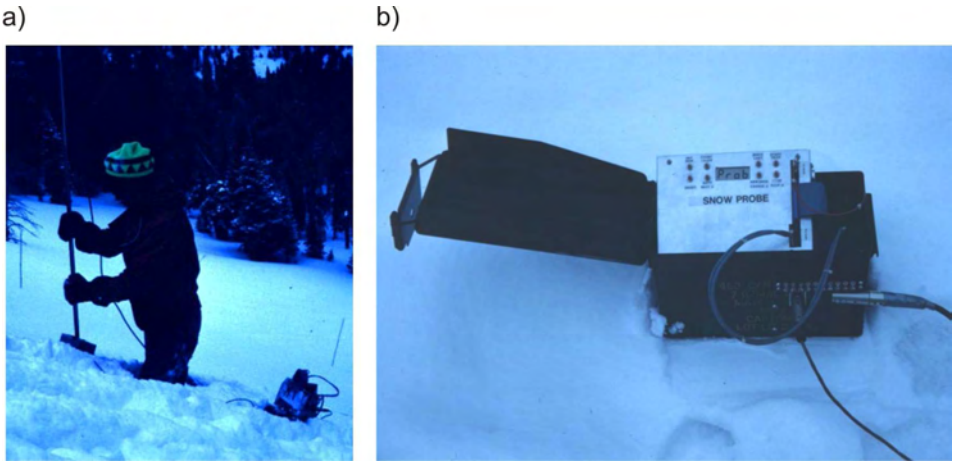

Figure 2.2: The Digital Resistograph. a) In use during a spatial variability study; b) Closeup of the microprocessor. Note the protective case made from an ammunition can. Karl Birkeland photos.

temperature sensor called the Digital Resistograph (Figure 2.2). Birkeland and others were able to use this instrument to assess the spatial variability of snow slab hardness in the Bridger Range, Montana (Birkeland and others, 1995). See Section 5.2 for more details on studies pertaining to the spatial variability of snow. Birkeland and others reported that weak layers thinner that 2 cm could not be discerned using the Digital Resistograph.

Independently from Dowd and Brown, Schaap and Föhn (1987) developed a similar penetrometer with a conical tip of diameter 11.3 mm. The instrument was pushed manually into the snow; Schaap and Föhn recommended a push velocity of 2 cm s^{-1}. This velocity was chosen to be consistent with the standard cone penetrometer velocity used in soil penetration tests. Output was recorded onto a battery-operated chart recorder. Schaap and Föhn report good general correlation between the penetrometer results and ram resistance determined using a Swiss Ramsonde, with the penetrometer discerning more layers. They note that layers of 1 to 2 tip diameters thick were not readily identified unless the hardness contrast between adjacent layers was particularly pronounced.

Sihvola and Tiuri (1986) developed a snow permittivity penetrometer called the Snow

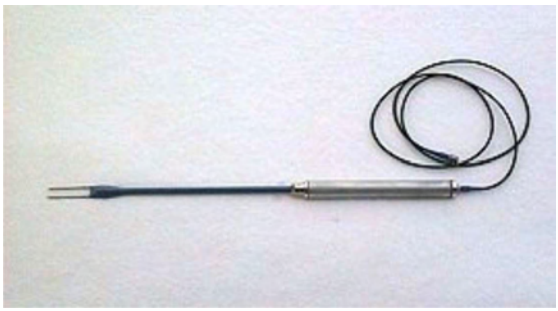

Figure 2.3: The Snow Fork. Pirjo Toikka photo.

Fork (Figure 2.3). The instrument comprised of a two-pronged wire resonator that was inserted into the snow. An alternating current was applied to the resonator and both the real and imaginary components of the dielectric permittivity of the snow were measured. The real component was measured directly from the ratio of the resonant frequency in air to that in snow; the imaginary part was calculated by measuring the broadening of the resonance curve when the penetrometer was in the snow compared to when it was in the air. Sihvola and Tiuri relate the imaginary part of the signal to snow wetness and the real part to a relationship between density and wetness. The instrument was designed to be pushed horizontally into the snow, which means that a snow pit was required to use this instrument. The depth was controlled manually by inserting the fork at different points within the snowpack. This instrument is commercially available.

Louge and others (1998) developed a different penetrometer to measure the dielectric permittivity of snow called the Capacitance Probe (Figure 2.4), based on snow-capacitance theory published by Louge and others (1997). Louge and others's penetrometer used a much smaller (2.5 mm vertical dimension and 8 mm horizontal dimension), shielded capacitance sensor mounted on the tip of a snow probe. A profile of the effective dielectric permittivity (the ratio of output voltage in air to output voltage in snow) with depth was generated from a 16 kHz oscillating current supplied to the capacitance sensor. They determined snow densities by matching the measured dielectric permitivity to

Figure 2.4: The Capacitec Probe. Steve Conger photo.

an empirically determined relationship between dielectric permittivity and density. This empirical relationship was determined using an instrument called a Snow Press, which allowed capacitance measurements to be made on a snow sample while it was being densified in a controlled way. The depth was measured using a rotary potentiometer mounted on a platform.

As with Sihvola and Tiuri's instrument, both a real (in-phase) and complex (out-of-phase) component of the effective dielectric permittivity could be resolved. Measurement of the complex component differed slightly in that it was the phase lag that was measured between the oscillator and the guard surrounding the sensor. Louge and others do not give physical interpretations as to how the real and imaginary parts of the dielectric permittivity relate to snow micro-structure. Foster and others (2002) reported that the real part of the signal provided an accurate index of density when verified against a manually dug snow pit and that vertical resolution was in the order of 2.5 mm. Conger (2007) also found good correlation between densities determined using the Capacitance Probe and densities measured using traditional snow density cutters. Depth was measured using a rotary encoder wheel,

Schneebeli and Johnson (1998); Johnson and Schneebeli (1998) developed a constant-speed penetrometer know as the SnowMicroPen (SMP) (Figure 2.5). This device used an

Figure 2.5: The SnowMicroPen in use by Eric Lutz during a spatial variability study in the Bridger Range, Montanna, USA. Karl Birkeland photo.

electric motor to drive a 5 mm diameter, 60° conical-shaped tip into the snow. The sensor measured force-resistance at a frequency of 5 kHz, which, given a constant drive velocity of 20 mm s^{-1}, resulted in a force measurement being taken every 4 μs. Schneebeli and others (1999) used the high resolution of the SMP to correlate the coefficient of variation of the force-resistance signal to a textural index defined as the ratio of mean grain size in μm to the density of snow in kg m^{-3}. Johnson and Schneebeli (1999) derived several microstructural snow parameters from a theory of cone penetration into snow (published in full in Johnson, 2003), and used the SMP to measure these parameters for four different snow types. Several authors (e.g. Pielmeier and Schneebeli, 2000; Birkeland and others, 2004; Kronholm and others, 2004) have used the SMP to assess the spatial variability of snow (see Chapter 5 for more details).

Abe (1999); Abe and others (1999) developed a multi-sensor penetrometer, called the Advanced Snow Sonde (also called the New Generation Rammsonde, Figure 2.6), with three snow property sensors and a depth sensor. The snow property sensors on this instrument were a load-cell for measuring force-resistance, a photometer for measuring the reflectivity of an active light source, and an electrical conductivity sensor. The

Figure 2.6: The Advanced Snow Sonde in use by Osamu Abe. Tsutomu Nakamura photo.

tip for measuring force-resistance was a 60° conical tip of 30 mm in diameter. The depth was measured using a magnetostrictive linear positioning sensor that employed the Wiedemann effect, and had a reported precision of 0.1 mm. This system required the penetrometer to be pushed through a ring magnet placed on the snow surface (the blue "box" in Figure 2.6). Abe and others considered that their most sensitive sensor and therefore the one best suited for detecting thin weak layers was the photometer. They assert that the penetrating force cone was not suitable for detecting thin layers since the cone height was greater than the extent of the thin layer.

Mackenzie and Payten (2002) developed a force-resistance and temperature penetrometer known as the SABRE penetrometer. This penetrometer was developed to be particularly lightweight and portable, with the supplied unit weighing 1.5 kg including data acquisition equipment. Recording frequency was 500 Hz and the penetrometer was manually driven into the snow at a variable rate. The unique features of the SABRE penetrometer were it's rounded tip shape, the use of an accelerometer to measure the depth, and the use of a thermopile to measure temperature. The rounded tip shape was chosen to concentrate the snow deformation near the front of the tip (Roddy Mackenzie, personal communication). However, studies on soil penetrometers (Fritton, 1990; Smith and

Figure 2.7: The SABRE penetrometer during field testing. It is over 4 m long! ASARC photo.

Mullins, 2001, p.379) indicates that a blunt tip shape enhances the development of a zone of compacted material that moves ahead of the tip as it is pushed through the material, and this is likely to generate irregular deformation patterns thereby reducing the vertical resolution (see Chapter 3). The accelerometer alleviated the need for a depth measuring platform, as found on most of the other snow penetrometers listed above. Although this aim was a good one, and one that, if perfected, could substantially enhance the useability of penetrometers, the accuracy of the accelerometer was questioned in this study (see Section 2.4.1) and found to be insufficiently precise for assessing snow variability. A thermopile was used as the primary temperature sensor in an attempt to improve the response time when measuring temperature from a rapidly moving penetrometer with a relatively large thermal mass.

2.2.5 Radar

Frequency modulated, continuous wave (FMCW) radar systems have been used to remotely assess snow depth, water equivalence and snow stratigraphy without disturbing the snow cover. Ellerbruch and Boyne (1980) were early researchers in this field and report on the use of such a system to determine these parameters using an X-band (8.2 to 12.4 GHz) FMCW radar system. They suggested that the depth to the top of depth hoar, identified in their manual snow profile, could be monitored using their system. Gubler and Hiller (1984) installed two upwards-pointing FMCW systems (also X-band) in avalanche slide paths. They were able to measure the seasonal build-up of snow cover in the paths and also measure a time sequence of the increase in snow depth from an artificially triggered avalanche in one of the paths. Fujino and Wakahama (1985) noticed a distinct increase in attenuation of the radar signal in measurements of wet snow, which decreased the reflection from underlying interfaces.

Holmgren and others (1998) used a sled-mounted FMCW radar system operating in the X-band to reliably measure snow depths of up to 3 m in the arctic. However, they noted that the stratigraphy of snow could not be measured well at this frequency and discussed the trade-off between radar penetration into snow, which is better at lower frequencies, and reflector resolution, which is enhanced at higher frequencies. Koh and others (1996) were able to make slightly more detailed measurements of snow stratigraphy at the Ka-band (26.5 to 40 GHz) in a shallow snowpack (48 cm). Their radar was able to pick up two major transitions within the snowpack. However, they present a manual snow profile which contains significantly more detail than the radar reflections were able to provide.

Marshall and others (2004) compared C-band (2 to 6 GHz), X-band and Ku-band (14 to 18 GHz) and concluded that in mid-sized, dry snowpacks of approximately 130 cm in depth, the Ku-band system was the best choice for assessing both snow depth and

stratigraphy. For deep or wet snowpacks they recommended using the C-band system. Marshall and others (2007) compared measurements between an extended Ku-band (8 to 18 GHz) FMCW radar system and the SMP penetrometer described in Section 2.2.4. Crusts and ice layers in the snowpack were readily identified using the FMCW radar and these correlated well with the SMP profiles. The authors noted, however, that weak layers could not be readily identified using this kind of radar system. They also pointed out that an amplitude-based interpretation of the reflections was problematic when dealing with thin ice layers less than 5 mm thick, due to very pronounced changes in reflectivity for small changes in the ice layer thickness. To overcome this problem, they used a method for identifying layers based on the spatial continuity of the radar signal.

Based on the literature, it appears as though FMCW radar systems are well suited to assessing variations in snowpack depth but less suited for determining snow stratigraphy. An exception for this is crusts and thick ice layers, which can be traced with confidence across profiles. Weak layers and subtle variations in layer properties appear to be less readily detected. The variable frequency means that resolution is a function of depth, which could be a detriment to layer identification. Signal attenuation in moist or wet snow may limit radar-measured stratigraphy to dry snowpacks. Although expertise in using FMCW radar systems was available at the University of Calgary, because of the drawbacks listed above, as well as time constraints, I decided against undertaking a comparison study between FMCW radar and the SABRE penetrometer.

2.2.6 Other methods

Many methods for assessing snow stratigraphy have been employed by a variety of researchers over the years. These include: dye tracing; smoke staining using a bonfire; thin-thick- and serial-section photography; translucent profiles; optical computer tomography; near-infrared photography; and seismology, (Pielmeier and Schneebeli, 2003a) in addi-

tion to the manual, penetrometer and radar techniques already described. Please refer to Pielmeier and Schneebeli's excellent review for further details on these methods.

Yosida (1956) performed laboratory experiments using a thin blade snow penetrating apparatus. He used this apparatus primarily to investigate rate effects of deforming snow samples. Gleason (2005) also performed laboratory penetration tests by deforming snow using a wide plate mounted to a piston. See Section 3.2 for more details on Yosida and Gleason's experiments.

Jamieson (1987) reviewed a variety of different methods for measuring snow hardness, including several of the methods described above. Additionally, he describes: the Kinosita Hardness Gauge, similar to the Swiss Ramsonde but utilising a disk-shaped probe tip; the Ski Edge Hardness Gauge, which is a Kinosita Hardness Gauge fitted with a narrow rectangular probe tip; the Conic Hardness Tester, comprising of a cone-shaped dart that is launched into the snow; the Proctor Needle, useful for measuring the bearing capacity of snow roads; the Vicksburg Cone, similar to the Proctor Needle; the Drop Cone test, where a cone penetrometer is dropped from from a known height into the snow; and the California Bearing Ratio test, also designed for road testing, in which a truck-mounted piston is forced into the snow and compared to the response when forced into crushed rock.

2.3 General methods

I describe here the general procedures for operating the SABRE penetrometer and for performing standard manual snow profiles. These methods are common to many of the individual tests that were performed during the penetrometer validation. Methods that are specific to individual tests are explained within the relevant sections.

2.3.1 Unmodified SABRE penetrometer

The unmodified SABRE penetrometer required two operators: one to push the penetrometer into the snow and one to operate the recording software on the hand held PC (see Figure 2.7 and Figure 1.4c). The operating procedure was as follows.

1. The penetrometer was assembled and connected to the hand held PC.
2. The penetrometer was held steady above undisturbed snow by one operator. The second operator initiated the recording sequence on the hand held PC.
3. The penetrometer was held steady above the snow for a further two seconds to allow baseline force and acceleration sensor values to be calculated.
4. The penetrometer was pushed vertically into the snow as smoothly as possible, at a rate of approximately 50 cm s^{-1}. In order to protect the tip from hard ground strikes, it was desirable to stop the push 20 cm or more above the ground. To help this, the depth of the snowpack in the local area was assessed with a regular avalanche probe prior to using the penetrometer.
5. Approximately two seconds after the end of the push, the second operator ended the recording sequence on the hand held PC.
6. The depth attained by the penetrometer was read off the scale on the side of the shaft with the aid of a ruler (since the scale was indicated every 100 mm) and recorded.

If the penetrometer stopped in the middle of a push for some reason, such as hitting a thick crust, then the profile was discarded. Error messages were also generated if the push duration was too short, if the penetrometer was not held in a vertical plane or if the penetrometer struck the ground or other buried object such as a branch of a tree. In such cases, the profile was also discarded.

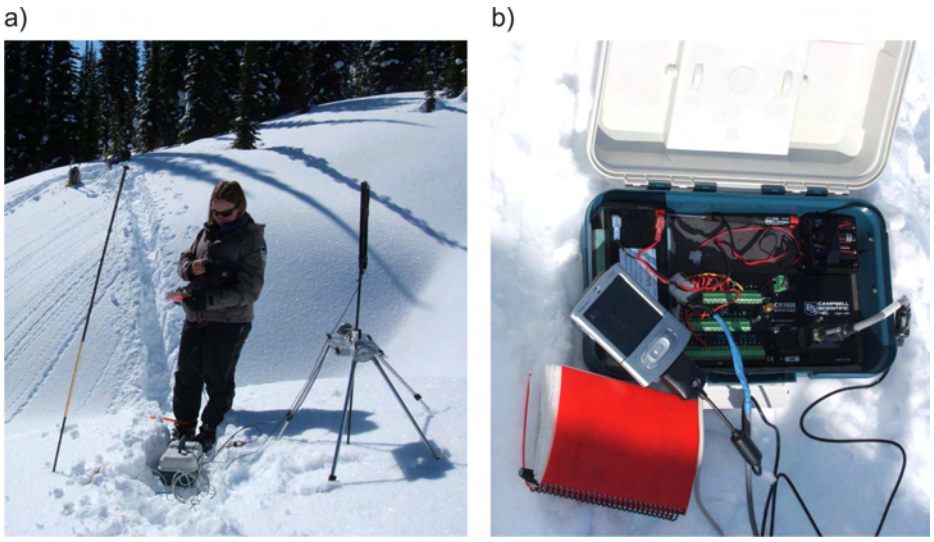

Figure 2.8: The modified SABRE penetrometer. a) In use during a survey. Depth measurement platform visible. b) Datalogger. ASARC photos.

2.3.2 Modified SABRE penetrometer

The modified SABRE penetrometer included a depth measuring platform (Figure 2.8a; see also Section 2.5), which required assembly before use and was placed gently on the snow at the location where the push was to be conducted, trying not to disturb any snow under the platform. A Campbell Scientific CR1000 datalogger (Figure 2.8b) was used in place of the hand held PC and was operated using a keypad (Figure 2.8b shows the setup prior to the installation of the keypad), which proved to be robust, and its screen was readable in bright light conditions. The penetrometer was pushed through a hole in the depth measuring platform, where a rotary encoder wheel resting on the penetrometer shaft turned as the penetrometer was pushed into the snow. Once again, the penetrometer velocity was kept as constant as possible and care was taken not to stop during the push. The two second pause was required at the beginning of the push but not at the end. The total depth of the push was manually recorded using the scale on the side of the penetrometer shaft.

2.3.3 Manual snow profile measurements

Site, weather and snowpack parameters were recorded at each site investigated. Snow profile observations were generally done to Canadian Avalanche Association guidelines (Canadian Avalanche Association, 2007). Notable differences were that thin layers of less than 1 cm were recorded and that all depths were measured from the snow surface, even for full-depth profiles.

During a manual snow profile, a snow pit was first dug to the depth required by the study being undertaken. A clean, vertical front wall was was prepared using a shovel, perpendicular to the fall line of the slope, and a similar side wall prepared on the shaded side of the pit parallel to the slope. The following parameters were measured:

Site and weather parameters

Site parameters that were recorded were: location, in UTM coordinates, using a GPS; Elevation, in m, using a barometric altimeter and/or GPS; and a site description, including general terrain shape, proximity to trees or other features of interest, and any other pertinent details about the site being investigated.

Weather parameters that were recorded were: cloud cover; wind speed and direction; and air temperature. See Canadian Avalanche Association (2007) for more details on these measurements.

Snowpack measurements

Temperature

Temperature measurements were made shortly after the snow pit was dug so as to minimise temperature changes due to the exposure of the snow to the air. Temperatures were measured on the shaded side wall every 10 cm using an Oakton thermistor thermometer and recorded to the nearest 0.1°C. The temperature probe of the Oakton thermometer was pushed approximately 10 cm into the snow, parallel to the snow layers. The Oakton

thermometer has a stated accuracy of ±0.2°C and resolution of ±0.1°C. If the temperature variation was low (around 0.2°C per 10 cm, or less) then temperatures were recorded only every 20 cm below a depth of 1 m.

In addition to the snow temperatures, the snow surface temperature was taken by laying the thermometer temperature probe on the snow surface and shading it using a shovel blade.

Layers

Layers were identified on the shaded side wall of the snow pit and traced around onto to the front wall. Layers were identified by assessing changes in snow hardness using either a crystal screen, a finger or a section of a solid ruler pushed into the snow and moved up and down in the snow to detect hardness changes. Once all the layers had been identified, the depth to each layer interface was measured using a solid folding ruler that was fixed in the corner of the snow pit. Depths were recorded to the nearest 0.5 cm, except for very thin layers, which were recorded to the nearest mm.

Hand hardness

The hand hardness scale used by Canadian avalanche forecasters has previously been described in Section 1.5 and is summarised in Table 1.1. This scale was used for assessing hand hardness in all manual snow profiles used in this study.

As previously discussed, this scale suffers from problems with subjectivity and variations between operators due to different hand sizes and different applied force. In order to reduce the variation in hand hardness measurements between operators, at the beginning of each winter season, all ASARC staff members engage in *consistency training*, where each staff member compares their assessment of hand hardness with that of others. Staff members whose values are frequently harder or softer than that of others were encouraged to modify their assessments in line with others.

Grain form and grain size

Snow crystal grain form was recorded for each layer identified in the snowpack as well as for the surface snow. Grain form was identified by gently scraping crystals onto a crystal screen and viewing the crystals through a hand lens with 8× magnification.

Crystal form was identified according to the International Commission on Snow and Ice (ICSI) international classification for seasonal snow on the ground (Colbeck and others, 1990). The principal classes of snow crystal identified in snow profiles from the Columbia Mountains are shown in Table 2.1.

Crystal size was assessed with the aid of 1 mm, 2 mm and 3 mm grids etched onto the crystal screen. When measuring grain size, the very smallest and the very largest grains were ignored and the minimum and maximum extent of the remaining grains recorded to the nearest 0.5 mm or the nearest 0.2 mm for very small grains.

Table 2.1: Commonly used grain types for snow crystals.

ICSI Class*	Name	Abbreviation used in this study	Symbol
1	Precipitation particles	pp	
1d	Stellars, Dendrites		
1f	Graupel		
2	Decomposing fragments	DF	
3	Rounded grains	RG	
4	Faceted crystals		
4c	Mixed forms	MF	
5	Depth hoar		
6b	Rounded polycrystals		
7a	Surface hoar	SH	
8	Ice masses		
9	Crust		
9e	Melt freeze crust		

*International Commission on Snow and Ice (ICSI) international classification for seasonal snow on the ground numerical class with alphanumerical sub-class designations. See Colbeck and others (1990) for the full classification.

Liquid water content

Snow for each layer was classified as dry if the measured snow temperature was below -0.1°C; moist if the temperature was reading -0.1°C to 0°C and snow formed clumps if lightly squeezed with the hand; and wet if the temperature was reading -0.1°C to 0°C and free water was visible in the snow using a hand lens.

Density

Due to time constraints, density measurements were only made in about 50% of the manual snow profiles. For measuring density, a 100 cm^3 tube-shaped density cutter was used to extract a small core of snow, which was weighed on an electronic scale with an accuracy and precision of 1 g. Densities were measured in each layer with a thickness equal to or greater than 4 cm. During measurements, the scale was sheltered from wind and snowfall to reduce measurement errors. Conger (2007) performed a detailed error analysis of measuring snow density and found density measurement errors to be -5% to +4% for this density cutter. He argues that the slight bias towards low readings represents a tendency for undersampling caused by snow falling out of the tubes during measurement.

2.3.4 Snow stability tests

Frequently, the identification of thin weak layers in manual snow profiles was aided using snow stability tests such as the compression test or Rutschblock test (Canadian Avalanche Association, 2007, p.32 and p.28 respectively). Brief descriptions of these tests are given below.

To perform a compression test (Figure 2.9a), a snow column of 30 cm × 30 cm × ∼120 cm snow is isolated using a snow saw. A shovel blade is placed on top of the column and is repeatedly impacted by tapping it with a gloved hand. First, 10 taps are done with the fingertips, moving the hand from the wrist. Next, 10 taps are done with the fingertips

or knuckles, moving the hand from the elbow. Finally, 10 taps are done with an open hand or fist, moving the hand from the shoulder. At any point if a fracture appears in the snow column, the number of taps taken to initiate this fracture is recorded, along with the depth of the fracture, the fracture character (van Herwijnen and Jamieson, 2007a) and the grain type and size at the fracture interface. Fracture character is rapidly gaining acceptance as a good method for discriminating between weak layers prone to releasing slab avalanches and other weak layers. Section 4.5 deals with the subject of predicting fracture character from penetrometer signals and the different fracture character classes are described there.

To perform a Rutschblock test (Figure 2.9b), a 2.0 m $\times$ 1.5 m $\times$ $\sim$1.2 m block of snow is isolated by first digging a 2 m wide front wall and then cutting the sides and the back wall using a rutschblock cord or a long saw. The sides can also be dug out using a shovel and the back wall can be cut in some cases using straight-backed skis. The column is then incrementally loaded by a person on skis or a snowboard. This person gently approaches from the top and steps onto the top third of the isolated block. The person then loads the block by rapidly bending their knees and dropping to a crouched position. This is repeated a second time. The next loading step involves jumping onto the same spot. This is followed by the operator stepping down to a position half way down the isolated block and performing two drops from the knees and a jump. The Rutschblock score is assessed as a number between 1 and 7 according to Table 2.2. In addition to the Rutschblock score, the Rutschblock release type is recorded (Canadian Avalanche Association, 2007, p.33) as *edge of block* for fractures that release 0 to 30% of the block; *most of block* for fractures that release 40 to 80% of the block; and *whole block* for fractures that release 90 to 100% of the block. Grain type and grain size at the fracture interface are also recorded.

Table 2.2: Rutschblock scores.

Rutschblock score	Description
1	Failure during cutting or approach to the block.
2	Block fails as the person steps onto it from above.
3	Block fails during the initial drop to the knees.
4	Block fails during the second drop to the knees.
5	Block fails during the jump on the top third of the block.
6	Failure at any point during stepping onto the lower half of the block, bending twice from the knees at this point and jumping once.
7	No failure after the sequence above has been carried out.

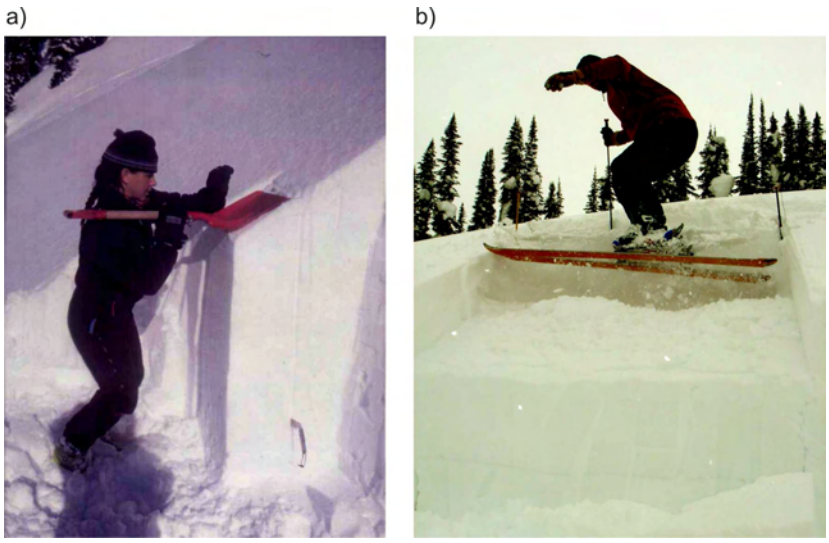

Figure 2.9: Snowpack stability tests. a) Compression test. b) Rutschblock test. ASARC photos.

2.3.5 Avalanche observations

Avalanche observations were made according to Canadian Avalanche Association guidelines (Canadian Avalanche Association, 2002, p.35). The occurrence date was noted, as well as the avalanche type (slab or loose snow), aspect, elevation, slope angle, approximate dimensions (width, length and crown height), size, trigger, and the suspected weak layer. The size classification used was the standard classification used by Canadian avalanche forecasting operations (Canadian Avalanche Association, 2002, p.36). This is an absolute scale (i.e. avalanche sizes may be compared between different paths) and is

shown in Table 2.3. Note that half sizes were used for avalanches that were between two size classes.

Table 2.3: Avalanche size classification.

Size	Avalanche destructive potential	Typical mass	Typical path length
1	Relatively harmless to people.	<10 t	10 m
2	Could bury, injure, or kill a person.	10^2 t	100 m
3	Could bury and destroy a car, damage a truck, destroy a wood frame house, or break a few trees.	10^3 t	1000 m
4	Could destroy a railway car, large truck, several buildings, or a forest area up to 4 hectares.	10^4 t	2000 m
5	Largest snow avalanche known. Could destroy a village or a forest of 40 hectares.	10^5 t	3000 m

There are two basic types of avalanche trigger: natural and artificial. Within each of these two types, there are many sub-types; a full list is given in Canadian Avalanche Association (2002, p.39). The avalanches discussed in this thesis were artificially triggered: either skier controlled (Sc), which were released deliberately by ski cutting; or remotely skier-triggered (Sr), in which case they were triggered accidently from some distance away (the distance is given in m in parentheses after the *Sr* designation, e.g. Sr(30) represents an avalanche triggered remotely from a distance of 30 m).

2.4 Initial testing of the SABRE penetrometer

Initial testing of the SABRE penetrometer was done in the winter of 2004–2005. Tests were performed to assess the accuracy and repeatability of the depth signal, the force signal and the temperature signal. Tests were performed at a variety of locations within Glacier National Park.

2.4.1 Depth signal

Method

Data used to assess the accuracy of the depth signal were collected over three days and at three different sites within Glacier National Park. The three sites were:

1. 20-Feb-2005: Fidelity Study Plot. Elevation 1860 m (treeline). East-facing site with a slope angle of 27°. This site was a sheltered, gladed area surrounded by medium sized and medium density trees.

2. 21-Feb-2005: Below Roundhill Station. Elevation 2075 m (alpine). Southeast-facing slope with a slope angle of 8°. Although Roundhill itself is a wind-blown ridge and is the location for a remote wind sensor, the site used in this study was a little way down the ridge in a more sheltered location.

3. 03-Mar-2005: Above Schuss Lake. Elevation 1900 m (treeline). Northeast-facing slope with a slope angle of 23°. This site was a little way above Schuss Lake itself on a slope with occasional stands of sparse trees. This site was in a moderately sheltered location (see Figure 2.10).

A total of 42 penetrometer pushes was collected at the three different sites. To test the accuracy of the depth signal, features in the manual snow profiles that would be obviously and uniquely identifiable in the penetrometer signal were sought, such as crusts, pronounced density changes and weak layers. These were measured manually in the snowpack to the nearest 0.5 cm using a 2 m folding ruler at the exact location of the penetrometer. This was done by carefully exposing a snow wall along the hole down which the penetrometer had just been pushed. The best marker layers were found to be crusts and pronounced density changes. Either one or two marker layers per push were used.

Figure 2.10: Penetrometer depth sensor testing at the Above Schuss Lake field site. Note the variable and thick rain crust traced in the snow approximately 50 cm below the snow surface. This illustrates the importance of digging out the penetrometer to measure the depth of the layer at the exact location of the penetrometer. ASARC photo.

The location of the marker layers in the penetrometer signals was found by visual inspection and layer depths were only recorded if the layer in question could be identified with confidence. More than half of the marker layers that were recorded manually could not be confidently identified in the penetrometer profiles and were therefore discarded from the analysis. In total, 32 depths to marker layers in the penetrometer signals were recorded, which had corresponding manually recorded depths.

Errors associated with the manual depth measurements include parallax measurement errors, slope effect[1], and misalignment of the ruler. Combined with the fact that the depths were recorded to the nearest 0.5 cm, the estimated accuracy for the manual

[1]The penetrometer was pushed vertically and its shaft is 2.0 cm in diameter at its widest point. A 30° slope therefore results in a 1.2 cm difference between the depth indicated on the lower side of the penetrometer compared to that indicated on the higher side (±0.6 cm). Standard procedure was to record the value at the halfway point between the lower and upper values. It is likely that some inconsistencies occurred.

measurements is ±1.5 cm.

Two methods for processing the raw penetrometer data were used: the original SABRE software supplied with the penetrometer; and alternative processing software that I wrote using Microsoft's Visual Basic software. With the original SABRE software, the start of the push was automatically determined when the acceleration signal indicated an increase in downwards velocity. The acceleration signal $a(t)$ was integrated twice over the duration of the push, T to provide the depth signal, given by:

$$d_p(t) = \iint_T a(t)\ dt\ dt\ . \tag{2.1}$$

As a result of signal noise and processing errors (Himachal Safety Systems, 2004), and presumably also inaccuracies from the accelerometer itself (this was not tested directly), the total depth calculated for a push through integration was often different from that measured directly against the side of the penetrometer. In order to correct for this, the software applied a linear scaling constant to the processed depth signal. The corrected depth is given by:

$$d_{p_corr}(t) = \frac{d_{meas}}{d_{p_int}} d_p(t)\ , \tag{2.2}$$

where d_{meas} is the total depth of the push measured directly against the side of the penetrometer and d_{p_int} is the total depth of the push calculated by integrating the acceleration signal.

Environmental changes, mostly temperature, affect the baseline values of the force transducer and the accelerometer (i.e. values associated with zero load and zero acceleration). These baseline values must be removed from each signal to ensure consistency between pushes performed during different test conditions. As previously described, the penetrometer was held at rest for two seconds right at the snow surface just before the beginning of the push. The software calculated the mean force and acceleration values during this period.

In the alternative processing software, which I wrote in an attempt to improve the penetrometer depth signal processing (and also gain control over the processing sequence), the start and end of the push were manually assessed from raw plots of force vs. time and acceleration vs. time. In other ways the processing was very similar to that described above. Baseline acceleration and force values were removed by removing the trend of their respective signals during the at-rest period at the start of the push.

In addition to the layer depths, the total depth of the push was also assessed. Depths measured on the side of the penetrometer were compared to processed depths from the accelerometer. For this comparison, only the alternative processing software was used, since with the SABRE software, the depth correction, which automatically assigns the manually recorded value as the push depth, could not be overridden.

Results and discussion

Differences between the manually measured depths and depths interpreted from the penetrometer signal were calculated as:

$$\Delta d = d_m - d_{p_corr} \ , \tag{2.3}$$

where d_m is the manually measured layer depth from the snow profile.

The standard deviation for differences between the manually measured depths and depths interpreted from the penetrometer signal was 14.6 cm, with a mean value of 3.1 cm (n=32) using the SABRE software. When processed using the alternative software, the standard deviation was 10.8 cm and the mean difference 8.5 cm. Because we know the true values with some confidence (i.e. the manually measured depths), these values are good estimates for the standard error for the penetrometer depth signal (e.g. Davis, 1973, p.308). The penetrometer profiles processed using the alternative software show a greater degree of consistency, although their absolute values are further away from the manually measured values compared with those processed using the SABRE software.

The difference between the means of the manually measured and interpreted layer depths were tested for significance using a one-tailed paired t test (e.g. McClave and Sincich, 2006, p.457). If this difference is significant, there may be a constant offset in the depth measurements. An assumption of the paired t test is that the differences between the two pairs of sampled depths are normally distributed. This was tested for using the Shapiro-Wilk normality test (Shapiro and Wilk, 1965), which yielded results of W=0.98 with p=0.75 for differences between the manually measured depths and the SABRE-processed profiles and W=0.97 with p=0.65 for differences between the manually measured depths and the alternative software-processed profiles. In both cases, there is insufficient evidence to reject the null hypothesis that the differences between the paired samples come from a normally distributed population and so we may proceed with the paired t test.

For the SABRE software-processed depths compared with the manually measured depths, t=1.21 with p=0.12. This result is insignificant at the α=0.05 level and therefore the means are not significantly different. For the alternative software-processed depths compared with the manually measured depths, t=4.35 with p<0.001. This result is significant at α=0.05 and we accept that the alternative software-processed depths are significantly shallower than the manually measured depths.

One reason to explain the significant difference for the alternative software processing is that it is hard to assess the start of the push by visual inspection of the raw force–time and acceleration–time plots. This job is made harder because the penetrometer does not register force values for snow with hand hardness values of *fist*. The reason that the penetrometer cannot detect fist hardness snow became readily apparent during one field day when I simply dropped the penetrometer tip (removed from the rest of the penetrometer assembly) into some new snow and it fell easily through the entire layer of fist hardness snow due to its weight alone. At normal penetrometer velocities, there can

therefore be no impact from the tip on the load cell when snow hardness is insufficient to support the weight of the penetrometer tip.

Although the difference between processed and measured depths was not significant for the SABRE software processing, from a visual inspection of the pushes, it appears as though the SABRE software also has difficulty in determining the start of the penetrometer push in some cases. Sometimes it appears as though additional signal has been added to the start of the push. This might have been due to not holding the penetrometer absolutely stationary at the beginning of the push—holding the penetrometer in this way was often somewhat ergonomically difficult. Sometimes the software appears not to have recognised the start of the push; in this case the push may have been started too gently.

The results of the total depth analysis were even more striking. Push depths calculated using the alternative processing software with the depth correction turned off varied from 50% to 200% of the manually recorded depths. Using a data set of 20 pushes, the standard error for the uncorrected depths was 84.5 cm. Clearly this is a very large error. It is also one that has been recognised by the manufacturers, which is why they correct for the depths using the manual measurements. The manufacturers claim, however, that this is a consistent error caused by electronic interference. I demonstrate below that this error is not consistent and instead fluctuates considerably over the course of a push.

Neighbouring pushes

The example I use to illustrate the nature of these fluctuations concerns two pushes that were performed just 20 cm apart, in an area where there was not much apparent variability in the snowpack. These two pushes were collected at the Above Schuss Lake site on 03-Mar-2005 (see above for site description). Although only one push-pair is considered here, this example is representative of other push-pairs that were performed

at this location and at others.

These two pushes are shown in Figure 2.11. Many similarities in shape between the two traces can be seen, but the depths are not consistent; instead they show a kind of *concertina* shape, with some sections appearing more expanded and some sections appearing more compressed. The measured depths to three layers traced between the penetrometer profile locations varied by only 1-2 cm, so I am confident that the variability seen between the two pushes cannot be explained by snow variability alone. The penetrometer profiles were processed using the alternative processing software, which was selected for its higher depth consistency.

The two pushes were cross-correlated with each other using Pearson's correlation coefficient (e.g. McClave and Sincich, 2006, p.625). The pushes were interpolated to a regular depth interval of 0.05 mm and the pushes were truncated to the same length (only 0.5 cm of truncation was required). In order to account for possible differences in the offset of the start of the push, a lag of up to 10% of the push depth was allowed in the cross-correlation. The best correlation, r_{max}, was found to be 0.71 at zero lag.

The results of the cross-correlation of the whole push were compared to cross-correlation results for the individual segments of the push, defined in Figure 2.11. Since the each segment length was not identical for each push, the shorter segment was first interpolated to a regular depth interval of 0.05 mm. Then the longer segment was interpolated to a regular depth interval given by:

$$\Delta d_{seg} = \frac{l_{ls}}{n_{ss}}, \tag{2.4}$$

where l_{ls} is the length of the long segment and n_{ss} is the number of interpolated data points in the short segment. Again, some lag was allowed to account for inaccuracies in assessing the start point of each segment. The results of the cross-correlation by segment are shown in Table 2.4. Correlations for segments 1, 3, 4, 5 and 7 are all higher than the correlation when taking the pushes as a whole. Segments 2 and 6 have lower

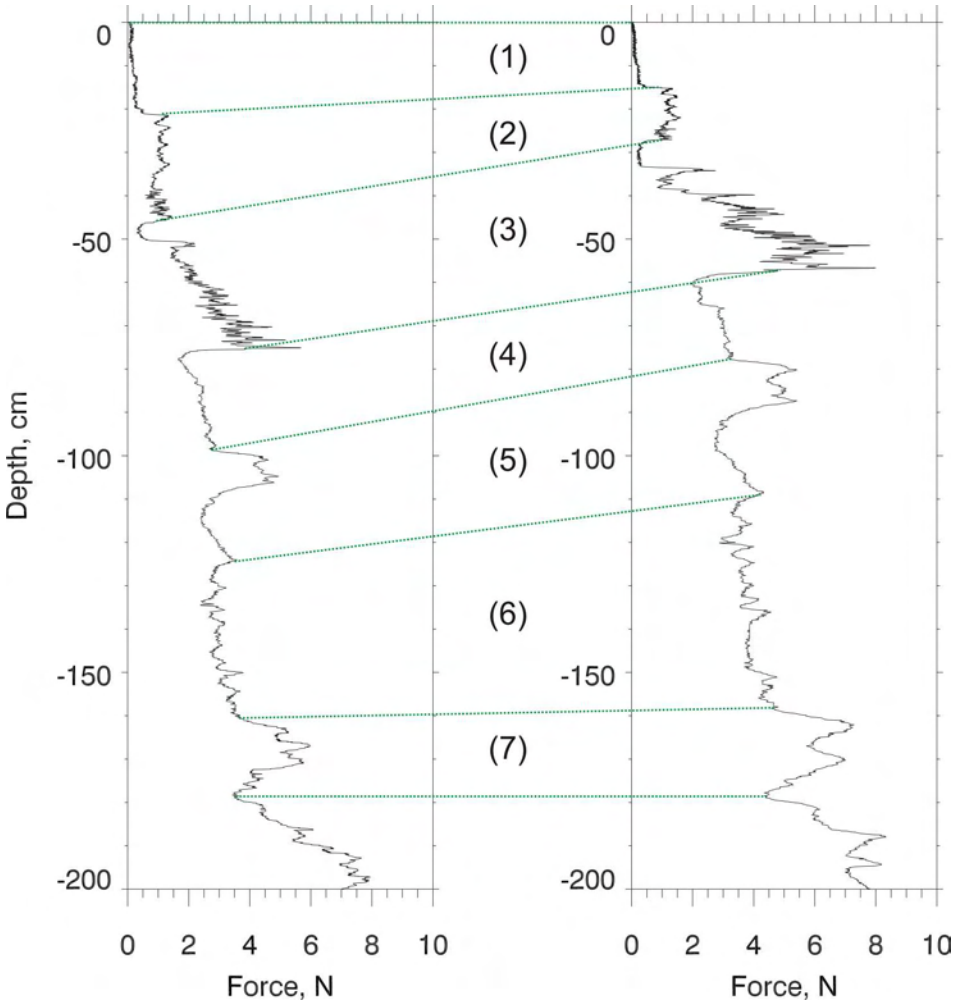

Figure 2.11: Force-resistance–depth profiles for two side-by-side pushes with selected snowpack interfaces traced from one profile to the other. Segment numbers shown in parentheses.

correlations; these likely represent segments where irregular fluctuations in the depth signal were particularly pronounced. The mean value for the cross-correlation when performed by segment is 0.76, which is higher than the value for the pushes taken as a whole, although still significantly less than 1, which would be the case if the two signals were identical.

The evidence is strong that much of the observed variability between these two pushes is due to variation in the depth signal rather than spatial variability in the snowpack. The overall improvement in correlation when done by segment, however, was not as

big as expected. Segments 2 and 6 in particular still have correlations that are less than the original overall correlation. These segments bring down the average of the correlations done by segment. Further subdividing these segments may improve the correlation further, although some of the low correlation may be due to spatial variability in the snow.

Table 2.4: Cross correlations for each segment of the two pushes shown in Figure 2.11.

Segment	Pearson's correlation coefficient	Lag (mm)
1	0.82	0
2	0.47	32
3	0.89	1.5
4	0.80	3.5
5	0.97	0
6	0.63	-6.5
7	0.76	0.5

Summary

Overall, depth accuracy averaged about 20% of the depth (using the alternative processing software standard error of 10.8 cm and an average layer depth of 62 cm). Frequently, depths to obvious layers/interfaces were in error by 30% or more and with no depth correction, total depth errors from the accelerometer were found to be as much as 200%.

For an assessment of spatial variability in an avalanche setting, where forecasters consider a weak layer depth change from, say, 50 to 60 cm to be important, this degree of depth variability in the penetrometer signal was considered to be too great for the requirements of this study. This was the basis for the decision to build a depth measuring platform (Section 2.5.1) to improve the accuracy of the depth signal.

2.4.2 Force-resistance signal

Method

The force signal was tested by comparing the output from the SABRE penetrometer's load cell with the force applied to the penetrometer while it was being pushed through the snow. The experiment was conducted at the Fidelity Study Slope site on 29-Mar-2005, on an east-facing slope at 1890 m elevation with a slope angle of 25°. The force was applied by hand, via a mechanical force gauge that was able to record the maximum applied force (Figure 2.12). Thirty-seven pushes of approximately 50 cm in length were performed into snow of different hardness. Since the maximum applied force was recorded, there was no requirement for the push to be in uniform snow. In order to reduce problems with a unwieldy, long, swaying probe, several sections of the penetrometer shaft were strapped together to reduce its length. This also provided a convenient point to attach the hook of the force gauge. The maximum reading on the force gauge was recorded in kg to the nearest 0.025 kg. The mass of the penetrometer (0.74 kg) was added to this and then the reading was converted to N by multiplying by g (taken as 9.81 m s^{-2}).

As the penetrometer was being pushed into the snow, the output from the load cell was recorded onto the handheld PC. This output was processed using the alternative processing software described in the previous section (Section 2.4.1). From this, the peak penetrometer output in mV was obtained for each push.

Results and discussion

A plot of peak penetrometer output against maximum applied force is shown in Figure 2.13. Peak penetrometer output shows a linear response to increasing applied force, except for very low applied force values. The regression analysis, which was significant at α=0.05 with p<0.001, indicates that no force registers on the penetrometer output until 13.7 N of force is applied to the penetrometer (including its weight). This is far more

Figure 2.12: Measuring the maximum applied force during the force testing experiments. The peak penetrometer output was recorded on a handheld PC. ASARC photo.

than the just the weight of the penetrometer tip, which by itself exerts only 0.2 N force on the snow.

The extra force required to initiate output on the penetrometer signal could be accounted for in four ways. First, there may be additional friction in the linkage to the load cell that must be overcome to initiate a force-response in the load cell. Second, there is an indentation just behind the penetrometer tip which is designed to allow the tip to move in and out in order to exert a force on the load cell. If not cleared from a previous push, this snow, which may have become hardened, must be compressed before the force can be transmitted to the load cell. Third, there is friction on the side of the penetrometer shaft that is reducing the force transmission to the tip, although this contribution is probably very small due to the low coefficient of friction between snow and steel (approximately 0.03). Fourth, the shape of the penetrometer shaft is causing it to be supported in places other than just at the tip. This is likely the biggest cause of the discrepancy for this experiment. It should be noted that the first and second points above will lead to a reduction in the resolution of the penetrometer, whereas the third and fourth are only a problem when comparing applied force to the measured response

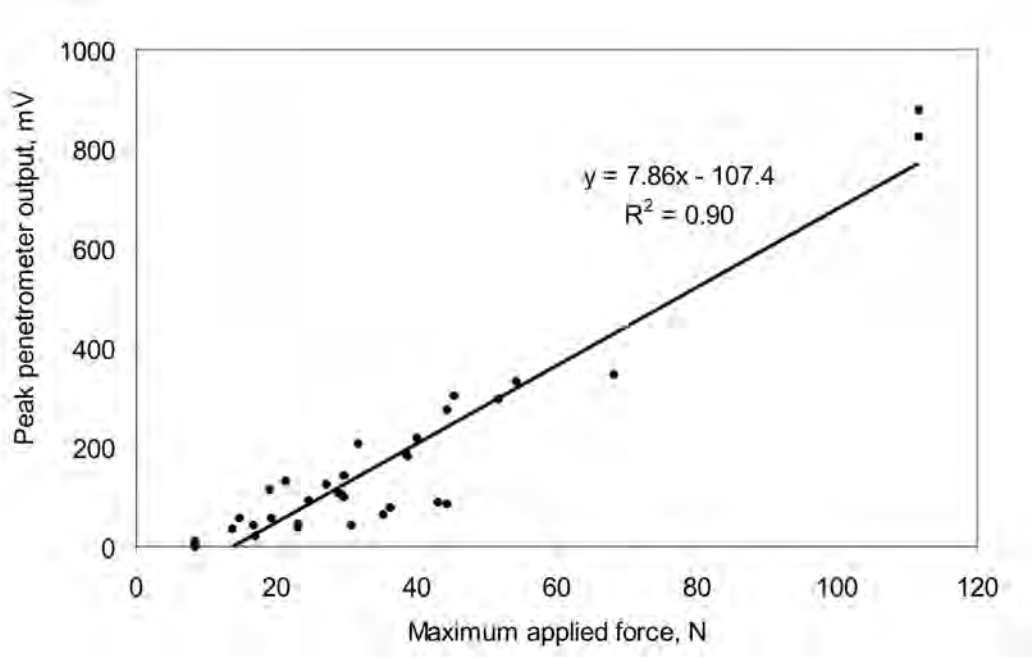

Figure 2.13: Plot of peak penetrometer output against applied force for the force testing experiment. Linear regression line and equation are shown.

on the penetrometer tip.

The slope of the regression indicates that once the initial friction or support has been overcome, the load cell gives an output of 7.86 mV N^{-1}. This is far lower that the manufacturer's calibration of 16.67 mV N^{-1}. Additionally, the gradient of the line is influenced by the two extreme points at high force-resistance values; without these data, the gradient would be slightly lower still. However, once again the effect of the support of the penetrometer shape must be considered, which will spread the applied force over both the tip itself and the flanged sides of the penetrometer shaft (see Figure 1.4). For this reason, I retained the original calibration coefficient for the purposes of calculating the force values from the penetrometer output.

The good regression fit (R^2=0.90) indicates that force sensor values can be reasonably reliably predicted from the manual force measurements, and that the relationship is linear. However, the standard deviation of the residuals was 62.2 mV, which is quite

considerable. It is likely that there are significant errors in measuring the manual force values in the method described. It is also possible that there are errors in the force sensor itself, or that the deformation patterns caused by the penetrometer tip give rise to these variations. Deformation patterns are addressed in Chapter 3, where I conclude that a rounded tip shape is not optimal for penetrometer use. This prompted testing of different tip shapes, which is discussed in Section 2.5.4. To separate sensor errors from the force measurement errors, a better approach might be to simply compare the consistency of the force measurements between neighbouring pushes. This was done to some level in the previous section, where I argued that despite inaccuracies in the depth signal, the force values were reasonably consistent and that similar shapes of features could be readily identified between the pushes. The correlation analysis, however, was hampered by the inaccuracy of the depth signal.

At this point in the analysis, suffice it to say that I was reasonably confident that the force sensor was working adequately. This issue will be addressed again using data from the modified penetrometer (Section 2.6.3) after modifications to the penetrometer's depth signal have been discussed.

2.4.3 Temperature signal

Method

In order to test the temperature signal from the SABRE penetrometer, four penetrometer pushes were performed within a 2 m radius, between 1 and 3 m from a snowpit in which a manual temperature profile had been taken. Tests were performed on 03-Mar-2005 at the Above Schuss Lake site (see Section 2.4.1 for site description). Manual temperatures were recorded at 10 cm intervals on the shaded side of the snowpit soon after the pit wall had been exposed. Temperatures were recorded using the Oakton thermistor thermometer previously described (Section 2.3.3).

Results and discussion

The temperature output from the four penetrometer pushes together with the manual temperature profile is shown in Figure 2.14. All the profiles (both penetrometer and manual) can be characterised in a broad sense as starting off relatively warm, reaching a minimum at some depth and then getting warmer towards the base of the snowpack. However, the minimum temperature in the penetrometer temperature profiles ranged from -12 to -7°C, which was approximately 2 to 3°C lower than the lowest temperature in the manual profile. Additionally, the location of the minimum varies considerably between the profiles, from 35 to 100 cm below the snow surface for the penetrometer profiles compared to 20 cm for the manual profile.

The penetrometer depths were measured using the accelerometer, so it is highly likely that some of this variation is due to inaccuracies in the depth signal. However, the observed spread in the location of the minimum temperature points was far greater than the variation expected from the inaccuracies in the depth signal alone.

There is a lag between the the temperature change in the snowpack and when the penetrometer senses that temperature change, and therefore it appears as though the response time of the thermopile is not sufficient for the penetration speeds attained during penetrometer pushes. There is a fundamental opposition in needs between the force sensor, which for a manually pushed penetrometer must travel relatively fast so as to deform snow in the brittle deformation range (see Chapter 3) and the temperature sensor, which require a slow push so as to be in thermal equilibrium with the snow.

There are also significant fluctuations in the penetrometer signals that do not appear on the manual temperature profile. One might advance the hypothesis that these fluctuations represent real changes in temperature in the snowpack, since the sample spacing of the penetrometer temperature profiles is far greater than the sampling of the manual profiles. However, none of the fluctuations between the penetrometer profiles

are in agreement with each other, despite the fact that they were all collected within a 2 m radius. For this reason, it is unlikely that the small-scale fluctuations represent true temperature variations; instead it is possible that some component in the penetrometer is causing electrical interference with the thermopile, or that the thermopile is not suitable for measuring snow moving across it's window because of the effects of pressure melting as the penetrometer is driven through the snow.

At some point during the penetrometer modifications (see Section 2.5) the thermopile stopped working entirely. Since early temperature results did not correlate well to manual temperature profiles, it was decided not to repair the faulty thermopile, in order to reduce the risk of damaging other components in the penetrometer. As such, the temperature measuring capacity of the SABRE penetrometer was not investigated further. In my opinion, layer detection from the penetrometer profiles was not compromised by the absence of the temperature profiles.

2.5 Modifications to the SABRE penetrometer

The modifications to the SABRE penetrometer comprised of adding a depth measurement platform, and changing the data recording system. The latter had the effect of increasing the recording frequency of the force signal to 1000 Hz. A range of different penetromter tips were tested, although in the end, the original tip was retained.

While testing the different penetrometer tips, it became apparent that the force transducer was not sensitive enough for use with the new, smaller tips. At that time, the penetrometer tip was partially dismantled to investigate the possibility of replacing the piezo-electric load cell. It was concluded that this would require a complete re-build of the entire penetrometer, and this option was discarded. During the course of this investigation, however, the thermopile temperature sensor was rendered inoperable, either

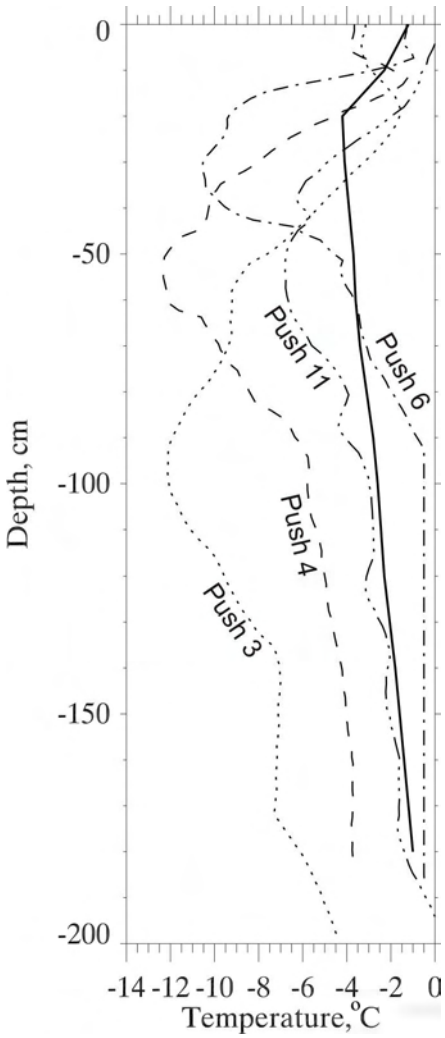

Figure 2.14: SABRE temperature output from four adjacent pushes (dashed, labeled) compared to a manual temperature profile done close to the penetrometer profiles (solid line).

through physical damage to the sensor or to a component of the electronic circuitry. As previously mentioned, this was not repaired, since early analysis of the temperature profiles indicated that these were unlikely to yield high-resolution information about snow stratigraphy, and it was felt that there was too great a risk of damaging other components of the system if a repair was attempted.

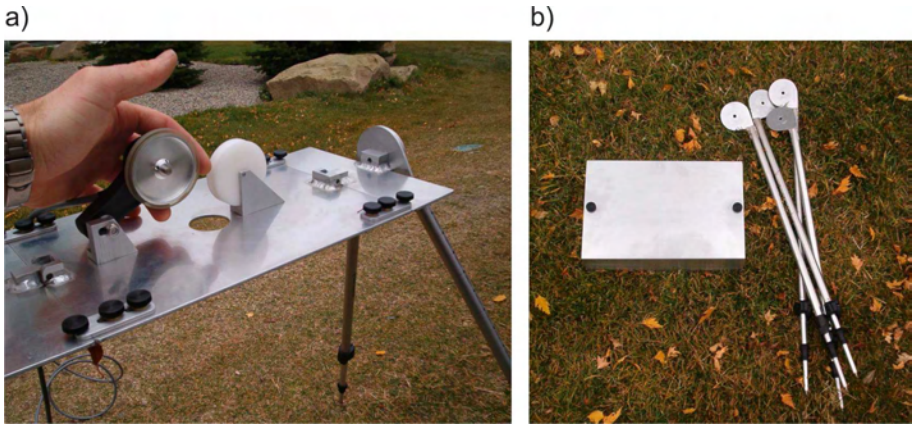

Figure 2.15: Depth measurement platform: a) in operational mode; b) folded up with protective lid in place, ready for transit. ASARC photos.

2.5.1 Depth measurement platform

I designed the depth measurement platform in the fall of 2005 and it was built by the Civil Engineering Machine Shop at the University of Calgary. The depth measurement platform is shown in Figure 2.15. It comprised of a 3 mm aluminium base plate with adjustable ski-pole legs with an Encoder Products Company TR1-TruTrac^{TM} optical encoder wheel mounted in the centre (see Appendix A for specifications). The legs were removable and the sides of the base plate folded up. A lid secured the platform and protected it for transport. Although the small nuts used the secure the base plate sides were found to be a little fiddly when setting the device up with gloves on, overall it performed well in a variety of terrain and snow conditions, and was reliable. Another benefit of this measurement system was that it allowed horizontal displacements to be measured for the rate experiments in Chapter 3.

2.5.2 Data recording system

A new data recording system was required primarily to be able to synchronise the force signal with the depth measurements from the new depth encoder wheel. A Campbell Scientific CR1000 datalogger was used (see Appendix B for specifications). Although

the CR1000 was able to record a single ended voltage, such as the output from the force sensor, at 1000 Hz, the pulse counter, that measured the output from the encoder wheel could only be recorded at 100 Hz. Therefore interpolation of the depth signal was necessary. For most of the analysis, a simple linear interpolation was used, although for the rate effect experiments in Chapter 3, a cubic convolution interpolation method (Park and Schowengerdt, 1983) was used.

2.5.3 Depth measurement error

Since the recording frequency is constant but the push velocity varies, the depth resolution is less at higher velocities. For a constant velocity, this resolution is equivalent to the spacing of the interpolated data points. The error at constant velocity is given by:

$$\epsilon_c = \frac{v_p}{f_i}, \tag{2.5}$$

where v_p is the push velocity and f_i is the interpolation frequency. For v_p=50 cm s^{-1}, interpolating to 1000 Hz, the best resolution that can be possibly be achieved is therefore 0.5 mm.

The velocity is not constant throughout the push, however. Hummel (1947) (simplified from original error estimates published in Hummel, 1946) gives an approximate maximum interpolation error for non-zero accelerations of:

$$\mid \epsilon_i \mid \leq \frac{(t_1 - t_0)^2}{8}_{\,max} \mid g''(t) \mid, \qquad t_0 < t < t_1, \tag{2.6}$$

where $g(t)$ is the actual function describing how the depth varies with time between the interpolation points and $_{max} \mid g''(t) \mid$ is the maximum value of its second derivative. It is impossible to measure $g(t)$, since by definition, its frequency is higher than the native recording frequency. However, a useful estimate can be obtained from the maximum observed acceleration. An analysis of acceleration magnitudes across three representative pushes (which included crusts, where velocity changes are likely to be most pronounced),

found the acceleration magnitudes to be less than 5 m s^{-2} (approximately 0.5 g) for over 98% of the pushes.

Using a value of 5 m s^{-2} for $g''(t)$ in Equation 2.6 yields an maximum estimated interpolation error of 0.00625 s. For a velocity of 50 cm s^{-1}, this is equivalent 3.1 mm, which is quite a large error. For the interpolation error to be in the region of 1 mm, at this velocity the acceleration must be kept to about 1.6 cm s^{-2}.

The use of the cubic convolution interpolation method should reduce the interpolation errors in most cases and has the additional benefit of smooth second order derivatives (i.e. acceleration). Reprocessing the entire data set with this interpolation method would have taken considerable time, however, so with the exception of the rate effect analysis in Chapter 3, this was not done.

2.5.4 Modified tip designs

A variety of different tip shapes and sizes were manufactured and tested with the SABRE penetrometer. Diagrams of the modified tips are shown in Figure 2.16. They comprised of a 6 mm rounded tip, a 6 mm, 60° conical tip and blade-shaped tips of three widths: 30 mm, 40 mm and 60 mm.

Figure 2.17 shows the results of three nearby pushes with different tip shapes. The 40 mm blade hardly registered on the force scale. This is due to a lack of sensitivity in the piezo-electric load cell (or the initial amplification of its signal). The 6 mm rounded and conical tips, as well as the 30 mm blade tip gave profiles that were even less pronounced than that of the 40 mm blade tip. These tips were therefore not considered to be viable alternatives to the original tip.

The 60 mm blade tip gave a profile of similar amplitude to the original 12 mm rounded tip (Figure 2.17). The blade design offers the ability to break a relatively large number of bonds in the snow, thereby providing a sufficient reaction for the load cell to measure but

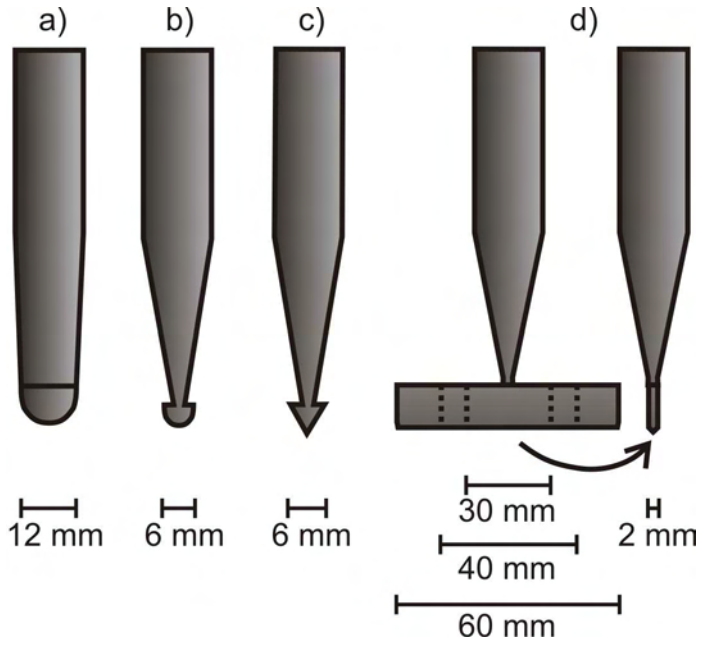

Figure 2.16: Different tips tested with the SABRE penetrometer. a) original 12 mm rounded tip; b) 6 mm rounded tip; c) 6 mm, 60° conical tip; and d) front and side views of the blade-shaped tip, which was tested at three different widths.

with the advantage that the bonds are broken over a smaller vertical range in the snow. The vertical range for the blade is approximately 1 mm compared with 6 mm for the original tip. I hoped that this would increase the vertical resolution of the penetrometer and the ability to detect thin weak layers. In some parts of the signal, the resolution of the 60 mm blade tip is similar or even slightly better than the original tip. However, in other parts of the signal, the response is flat and details that are picked up by the original tip are not seen with the 60 mm blade tip. The reason for this is probably because the blade had a tendency to tilt and twist as the it was being pushed into the snow. When that occurred, extra friction occurred at the point where the tip exited the shaft and decreased its sensitivity. As as result of this inconsistency, the 60 mm blade tip was not used and I reverted to using the original tip. It is possible that a penetrometer that was designed from the outset for a blade shaped tip could realise the advantages predicted for the blade tip design. This would be a good avenue for further work.

In hindsight, a 12 mm conical shaped tip should have been tested for use as an alternative tip design. Results from the deformation experiments (Floyer and Jamieson, 2006) indicate that the deformation zone ahead of a conical shaped tip is slightly smaller than that for a rounded tip, and therefore a small improvement in vertical resolution might have been realised.

Overall, I consider that the vertical resolution of the penetrometer could be improved by using a smaller tip. However, it became clear that in order to change this, several aspects of the penetrometer would need to be redesigned, including the load cell, the front of the penetrometer shaft and the instrument recording rate. This was beyond the scope of this project and was not pursued further.

2.6 Testing the modified SABRE penetrometer

2.6.1 Modified depth signal

Methods

The marker layer experiment described in Section 2.4.1 was repeated using the modified penetrometer setup with the depth measuring platform. 20 profiles were collected over two days in March 2006 at the Above Fidelity Station site, which is on an east aspect at 1910 m with a slope angle of approximately 7°. The site is characterised as slightly convoluted terrain with small-scale rolls and valleys. A total of 28 layers were confidently identified in the penetrometer signals and matched with corresponding manual measurements.

Additionally, total push depths measured using the depth measuring platform were compared with total push depths measured manually on the side of the penetrometer shaft. This was done for all profiles collected in 2006, which amounted to a total of 559 profiles.

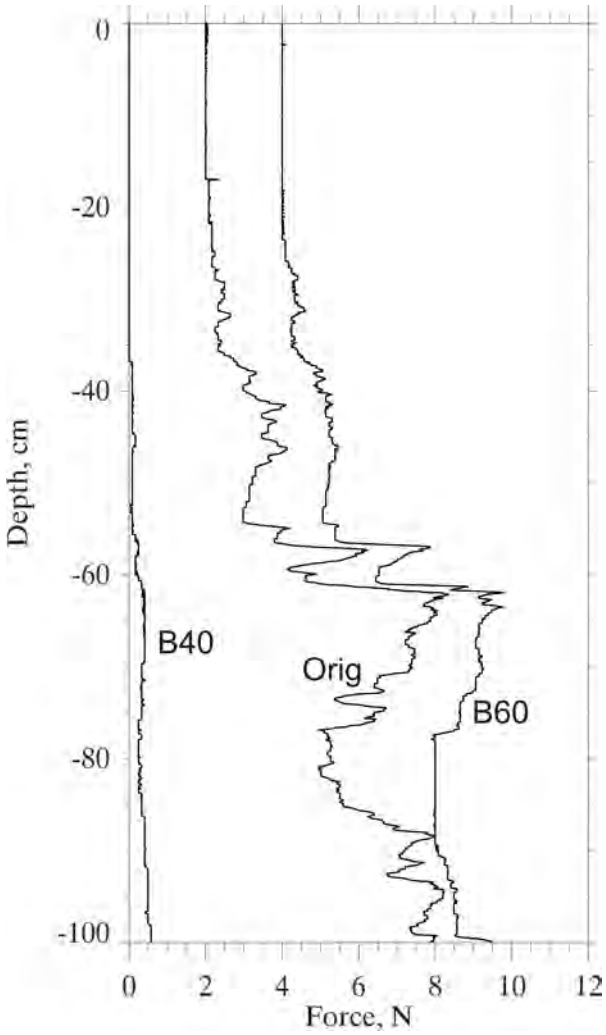

Figure 2.17: Force-resistance–depth profile for 3 different tip shapes: 40 mm blade (B40); original 12 mm rounded tip (Orig); and 60 mm blade (B60). Force values are offset by 2 N for Orig and by 4 N for B60.

Results and discussion

In the same way as the pre-modification testing, differences between the manually measured layer depths and those interpreted from the penetrometer signal were calculated from Equation 2.3. The standard deviation for differences between the manually measured depths and depths interpreted from the modified penetrometer signal was 1.8 cm, with a mean value of 0.75 cm (n=28). Again, the standard deviation for the paired differences may be used to estimate the standard error in the depth signal.

The standard error of 1.8 cm includes the error associated with measuring the manual layers, which was estimated as ±1.5 cm. Since errors in measuring the manual layer depths and those associated with the interpreted depths should be independent, we cannot simply subtract the manual error from the standard error to get the error from the penetrometer signal. Instead the depth error was calculated as follows (e.g. Taylor, 1982):

$$\epsilon_d = \sqrt{\epsilon_{se}^2 - \epsilon_m^2} \,, \tag{2.7}$$

where ϵ_{se} is the standard error and ϵ_m is the error associated with measuring the manual layers. Using the values above, the error associated with measuring layer depths using the modified penetrometer depth, ϵ_d, is therefore estimated as ±1.0 cm.

The results from the comparison between total push depths measured by the depth measuring platform and those measured manually on the side of the penetrometer shaft are shown in Figure 2.18. Most of the data show very good agreement between the measuring platform and penetrometer shaft measurements, although there are some outliers that show significant deviation. The mean difference between the measurement platform values and the penetrometer shaft values is 1.0 cm, which is similar to the value of 0.75 cm calculated from the layer depths above. The direction of this offset is such that the values measured on the side of the penetrometer shaft are slightly longer than those measured using the depth measurement platform. This could be due to the fact that the tip of the penetrometer was often pressed slightly into the soft surface snow at the start of the push before recording commenced.

The outliers almost certainly represent pushes where there was a significant perturbation of the encoder wheel, either adding extra revolutions, for values significantly above the trend line, or missing revolutions, for values significantly below the trend line. Extra revolutions could possibly be added if the penetrometer loses contact with the wheel allowing it to spin, while the penetrometer simultaneously slows down. It is also possible

that in some cases, the recording sequence was initiated too early, when the penetrometer was still being moved into position, and therefore still some distance above the surface of the snow. Missed revolutions are possible if the penetrometer slipped off the encoder wheel during a push and the wheel stopped turning while the penetrometer continued to be inserted into the snow. Also, when air temperatures were relatively warm, moist snow had a tendency to stick to the penetrometer shaft, which fouled the encoder wheel and caused the wheel to slip on the penetrometer shaft.

When any kind of *slip* or *spin* error was noticed during field work, it was standard practice to discard the push in question. It is extremely likely, however, that not all such pushes were filtered out in the field. If we assume, as there is reason to, that the pushes with large depth errors are due to encoder wheel–penetrometer contact problems, it is easy to discard these at the processing stage simply by setting a threshold disparity between the depth measured by the encoder wheel and the depth measured on the side of the penetrometer. For the spatial variability studies in Chapter 5, I set this disparity to 3 cm. If the encoder wheel measured push depth differed from that read from the side of the penetrometer shaft by more than 3 cm then the push was not used in the analysis.

Assuming that the wheel does not slip on the penetrometer shaft during the push, the precision of the depth signal (i.e. the resolution, as opposed to the absolute accuracy) should be equivalent to that discussed in Section 2.5.3, which is about ± 1 mm for velocities less than 50 cm s^{-1} and moderate accelerations.

2.6.2 Correlating force-resistance with hand hardness

Method

Ten force-resistance profiles were used to calibrate the force-resistance measurements from the SABRE penetrometer with manual hand hardness measurements. Each profile was taken at a different site on a different day. Manual snow profiles were performed 0.5

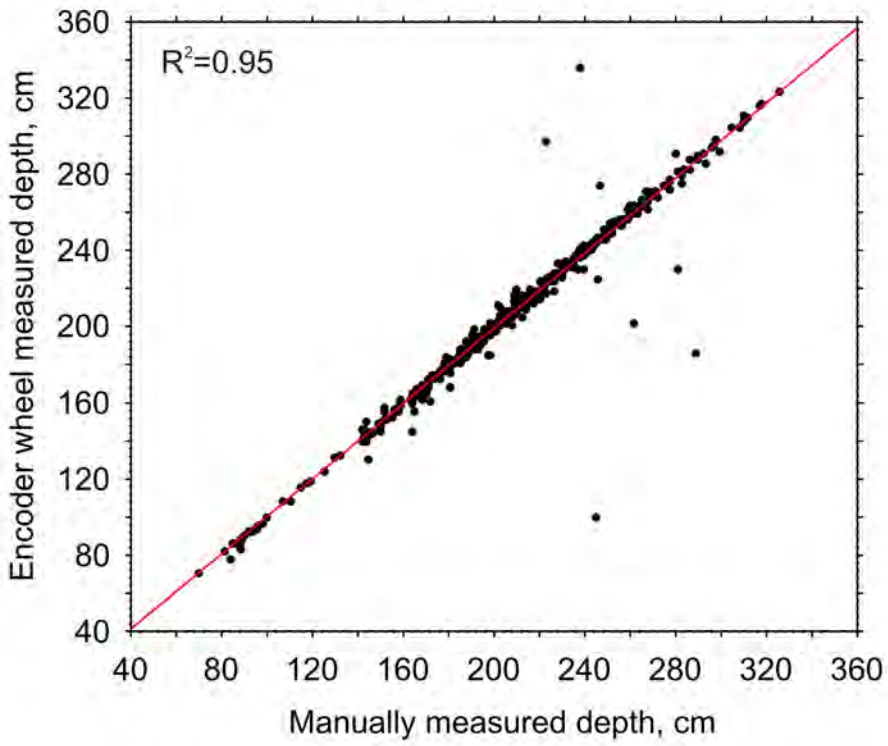

Figure 2.18: Depths measured using the encoder wheel on the measuring platform plotted against manually measured push depths.

to 1.5 m from the penetrometer profiles.

The penetrometer push signals were divided into sections using the layer depths from the manual snow profiles. For each penetrometer push *layer*, the mean force-resistance value was calculated. Since the penetrometer pushes were not performed at exactly the same location as the manual snow profiles (a considerable source of error), layers that were less than 5 cm thick were verified against the manual profiles and if necessary, shifted slightly to better align the manual and penetrometer profiles. The mean force value was found for each layer from the penetrometer force signal. A total of 133 layers were assigned mean force values in this way.

Results and discussion

Profiles from three of the pushes used to correlate the hand hardness with force-resistance are shown in Figure 2.19; the general patterns observed in these profiles are consistent with those of the profiles not shown. General agreement between the manual hand hardness and the penetrometer force-resistance signal is quite good, although in many parts, the force-resistance signal shows far greater detail. A noticeable transition that the penetrometer did not pick up is the transition from P to P+ at approximately 100 cm depth in the first profile (Above Fidelity Station site). The penetrometer profile is actually quite flat at this point; it is more usual to see fine-scale variations in the penetrometer signal. It is possible that snow became jammed in the depression between the penetrometer tip and the penetrometer shaft during this push. Since this is speculation, however, and was not noted at the time of the push, these layers were not excluded from the analysis.

Figure 2.20 shows the range of mean force-resistance values from the different layers for each category of hand hardness. The mean force-resistance measured using the penetrometer shows an exponential trend with increasing hand hardness. In general, the range increases with increasing hardness. The mean value for the 4F+ category is noticeably higher than the trend and its range is greater. This category contained only five values, which makes it particularly susceptible to measurement errors. The number of layers in the K hardness category was also five, and there were only two F- layers. The other categories contained 7 to 18 layers.

The exponential fit in Figure 2.20 had a regression equation of $6.25 \times 10^{-3} e^{6.00x}$, where x is the incremental integer value for the hand hardness category, starting at 1 for F-, 2 for F, etc.. Mean values for each category were calculated from this equation, as well as ranges; these are shown in Table 2.5.

It is cautioned that the values in Table 2.5 apply only to the specific tip shape of the SABRE penetrometer. Also, for conversion between mV and N, the manufacturer's

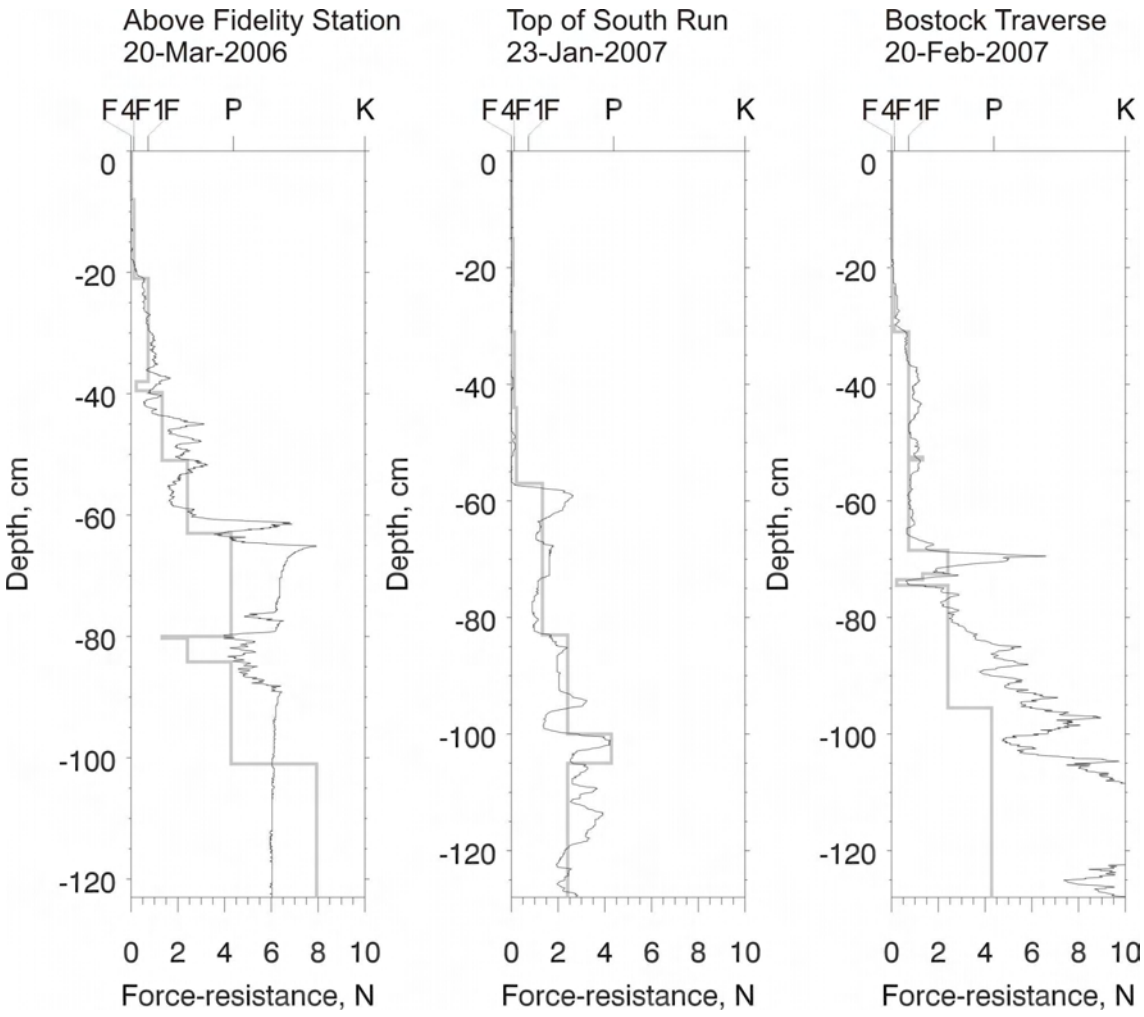

Figure 2.19: Manual hand hardness (thick, grey line) compared to penetrometer force-resistance (thin black line) for three pushes at different locations.

calibration value of 16.67mV N^{-1} was used; if this value is in error then there will be corresponding errors in the tabulated force values. However, since the primary use of this information is to allow comparison between penetrometer signal and hand hardness to be made (such as in Figure 2.19, the absolute force values are of less relevance than their relative divisions.

One of the problems with this analysis is that it is hard to separate the variability in the penetrometer signal from the subjectivity of the hand hardness scale. Measurements for in-between categories is especially subjective, since the operator must interpolate

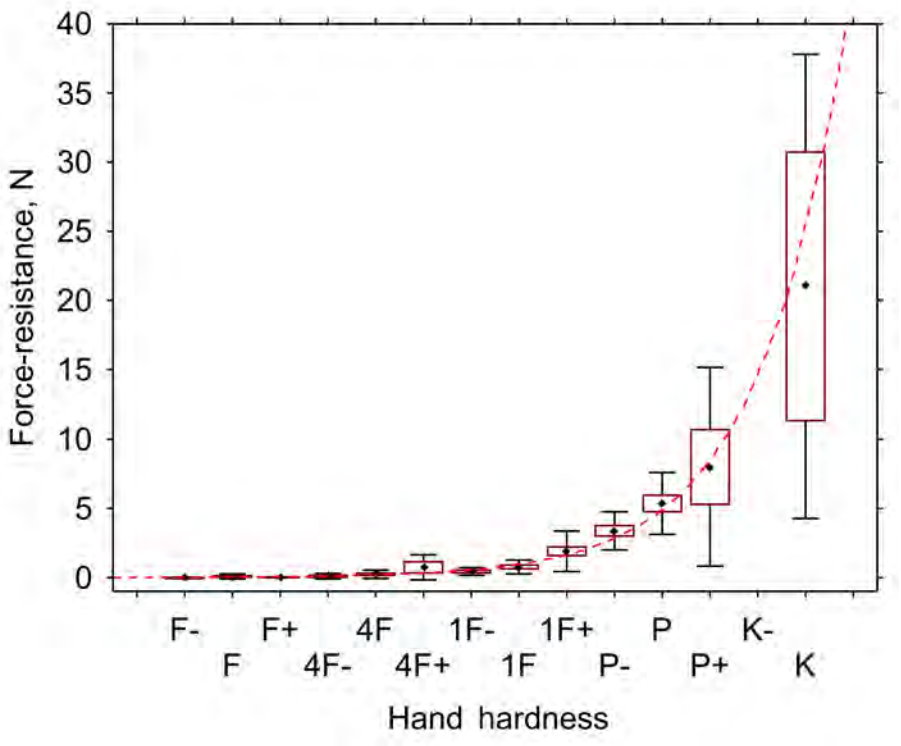

Figure 2.20: Box and whisker plot of force-resistance values for each hand hardness category. Central point (small diamond) represents the mean; boxed inner range represents the standard error; and the outer whiskers represent the standard deviation. Exponential trend line is shown (dashed line).

between two points on the scale that are more readily measured (e.g. to assess a layer as 4F+ the operator must interpolate one third of the way between 4F and 1F, the points which can be measured using the operator's gloved hand). However, it should be noted that these qualifiers were only intended to offer the ability to distinguish small relative hardness differences between adjacent layers by a single operator.

The subjectivity of the hand hardness scale can be demonstrated by considering a plot of hand hardness with density (Figure 2.21 – see Appendix C for details of how this graph was created). Although there is a clear trend of increasing hardness with density, different snow densities have a high range of associated hardness values. Of course, here too there are two possible explanations for the variability shown in the graph. Either there is a wide range of subjectivity when assessing the hand hardness or else there

Table 2.5: Mean force values and force ranges for hand hardness categories.

Category	Mean force (N)	Force range (N)
F	0.00	N/A
F+	0.04	0.0 to 0.05
4F-	0.06	0.05 to 0.1
4F	0.12	0.1 to 0.2
4F+	0.22	0.2 to 0.3
1F-	0.40	0.3 to 0.5
1F	0.73	0.5 to 1.0
1F+	1.33	1.0 to 1.8
P-	2.41	1.8 to 3.3
P	4.38	3.3 to 5.9
P+	7.94	5.9 to 10.7
K-	14.4	10.7 to 19.4
K	26.1	19.4 and above

is a poor correlation between hand hardness and density. Since hardness depends on bonding, grain type, grain size and temperature, as well as density, some variability is expected. Mellor (1964), however, presents graphs of unconfined compressive strength (i.e. hardness, but measured objectively) with density for different snow samples which appear to have very good correlation, far better than the correlation in Figure 2.21. This combined with field experience of measuring hand hardness, and the frequency at which field practitioners have differences of opinion when assessing it, gives weight to the argument that much of the variability is due to the subjectivity of the hand hardness scale.

2.6.3 Repeatability of the force signal

Method

Four penetrometer pushes were collected from the Fidelity Study Slope site on 11-Mar-2006. This site was an east-facing slope at 1890 m elevation with a slope angle of 25°. The site was as an open, uniform slope that was surrounded by trees giving protection from strong winds. The trees were not too close so as to give problems with tree-bombs,

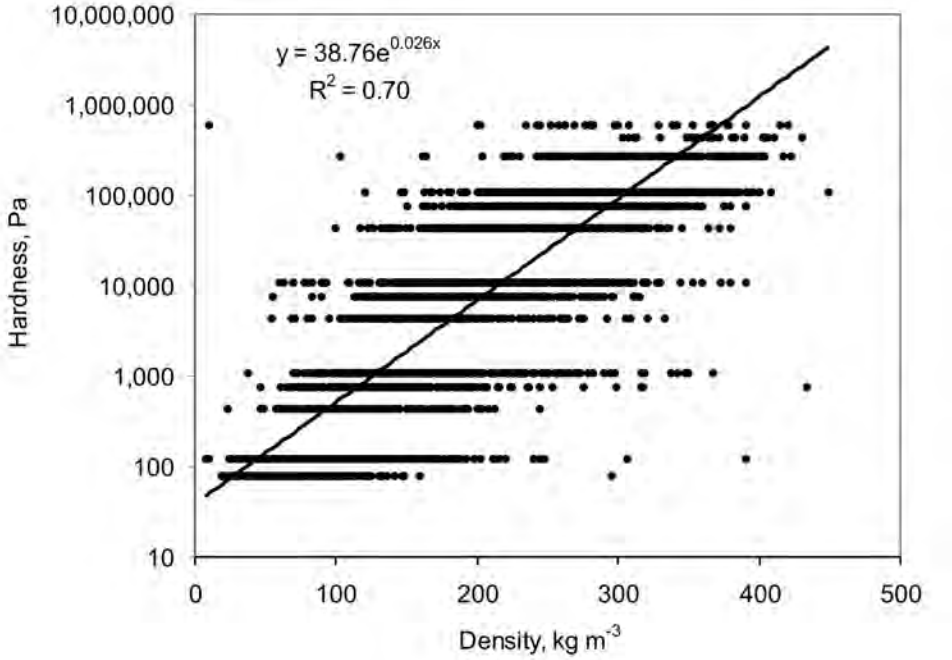

Figure 2.21: Plot of snow hardness against density for 5371 individual layer samples.

which are masses of snow that fall from trees during periods of wind or warming. The penetrometer pushes were collected 50 cm apart in a line perpendicular to the fall line of the slope. The first push was collected approximately 1 m from a manual snow profile, the profile from which is shown in Figure 2.22.

To test for consistency of shape between pushes, the penetrometer pushes were correlated with each other using Pearson's correlation coefficient. Prior to correlation, the pushes were interpolated to a regular depth spacing of 0.05 mm. A small amount of lag was allowed (up to 20 mm) to ensure there were no offset problems caused by misalignment of the penetrometer tip at the snow surface. To test for consistency of the magnitude of force values between pushes, the mean difference of paired force values between each pair of pushes was calculated at the optimum lag. This difference was tested for significance using a two-tailed, paired z-test at α=0.05.

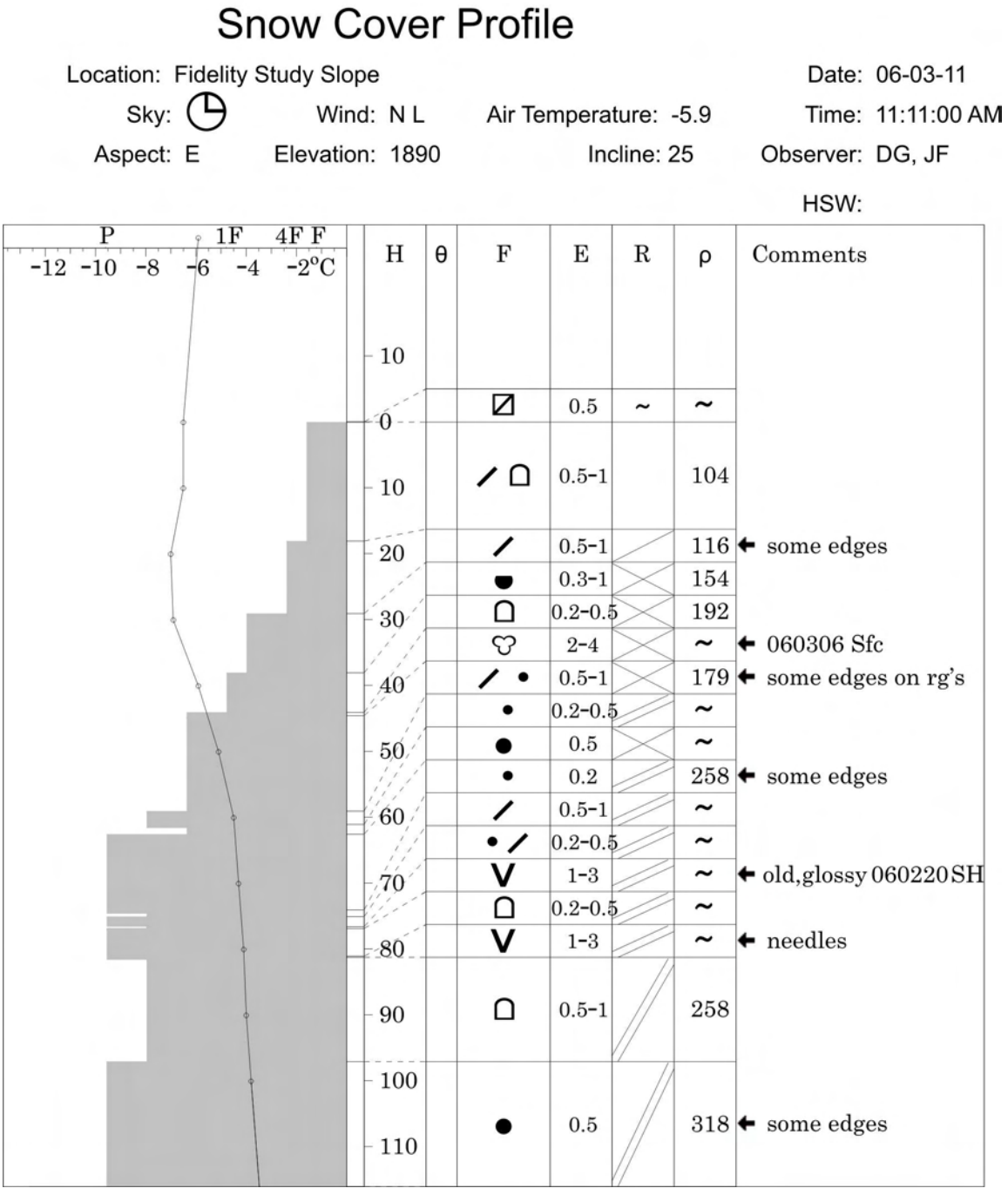

Figure 2.22: Manual snow profile at Fidelity Study Slope site for 11-Mar-2006.

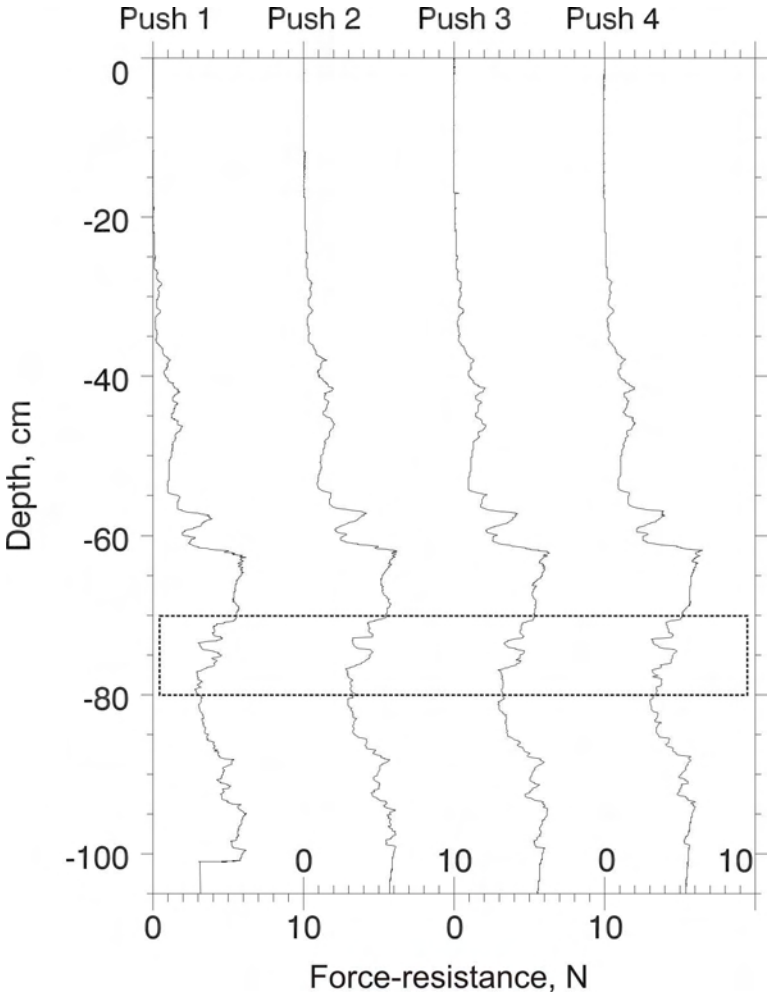

Figure 2.23: Four neighbouring penetrometer pushes from the Fidelity Study Slope site collected on 11-Mar-2006. Boxed region is shown expanded in Figure 2.24

Results and discussion

Figure 2.23 shows the four pushes. Visual inspection reveals that the pushes are very similar to each other both in magnitude and shape. Results of the correlation are shown in Table 2.6. The correlation coefficient values range from 0.93 to 0.95 indicating that there are very good correlations between all of the pushes. Offsets (magnitude of the lags) varied from 2.5 to 3.05 mm, which is well within the accuracy of ± 1 cm stated in Section 2.6.1.

Two inferences can be draw from these results. First the shape of the force signal of

Table 2.6: Pearson correlation coefficient matrix for force values correlated between the four pushes in Figure 2.23. Values in parentheses represent the lag used for optimum correlation. N varied from 2000 to 2100 and in all cases, $p<0.001$.

	Push 1	Push 2	Push 3	Push 4
Push 1	1	0.93 (-2.95 mm)	0.94 (-2.8 mm)	0.94 (-3.05 mm)
Push 2		1	0.94 (+2.5 mm)	0.94 (-2.6 mm)
Push 3			1	0.95 (-2.7 mm)
Push 4				1

the penetrometer appears to be very consistent under, what were, optimum conditions. Second, there was very little spatial variability in the snow cover at this site on the day the snow was measured.

Table 2.7 shows the correlation coefficients of the differences between the mean force values. The differences range from 0.13 to 0.28 N. All, except for the differences between pushes 3 and 4, are significant at α=0.05. For low resistance layers, differences of this magnitude may have a significant influence. For 1F snow, they represent about 30% of the expected force values in this range. For P snow, they represent about 5% of the expected force values. Some of the difference is doubtless accounted for by real variations in the snow. However, these results still indicate that caution should be used when assessing force-resistance changes between pushes, especially for low-resistance layers.

Table 2.7: Matrix of differences in mean force between the four pushes in Figure 2.23. z and p statistics also shown for each push pair. N varied from 2000 to 2100.

	Push 1	Push 2	Push 3	Push 4
Push 1	0	0.26 N (z=-3.84; $p<0.001$)	0.28 N (z=-4.10; $p<0.001$)	0.25 N (z=-3.64; $p<0.001$)
Push 2		0	0.19 N (z=2.80; p=0.005)	0.16 N (z=-2.23; $p<0.02$)
Push 3			0	0.13 N (z=-1.86; $p<0.06$)
Push 4				0

2.7 Identifying weak layers

One of the most pertinent questions when assessing a penetrometer for use in an avalanche forecasting setting is whether or not it is able to identify weak layers. I present two examples that illustrate the limit of detection of weak layers using the SABRE penetrometer.

Fidelity Study Slope example

The first example is from the 06-Mar-2006 Fidelity Study Slope array described in the previous section (Section 2.6.3) and shown in Figure 2.22. Figure 2.24 shows a closeup of the four pushes for depths between 70 and 84 cm. From the manual snow profile (Figure 2.22) the sequence of layers around this depth is as follows:

1. 62.5 to 74 cm: P hardness, rounded grain (RG) layer, measured density of 258 kg m^{-3}
2. 74 to 75 cm: P- hardness, decomposing fragment (DF) layer
3. 75 to 76.5 cm: P hardness, RG and DF layer
4. 76.5 to 76.8 cm: P- hardness, SH layer, buried on 21-Feb-2006
5. 76.8 to 81 cm: P hardness, mixed form (MF) layer
6. 81 to 81.2 cm: P- hardness, surface hoar (SH) layer, buried on 20-Feb-2006
7. 81.2 to 97 cm: P- hardness, MF layer

This is a convenient system of layers, due to the number of identifiable, thin layers. In the closeup of the pushes (Figure 2.24), the upper DF layer (layer 2) is easily identifiable in all four pushes. The upper SH layer (layer 4) can be very faintly seen in push 1 and push 3 but not in push 2 or 4. It is doubtful that without the detailed manual profile whether this layer would be identified at all, since it is a very subtle *blip*. This layer is right on the limit of the identification capabilities of the SABRE penetrometer.

The lower interface, identified in Figure 2.24 with unlabeled arrows, is where I assume the transition from P to P- hardness to be. This transition is difficult to make out, since

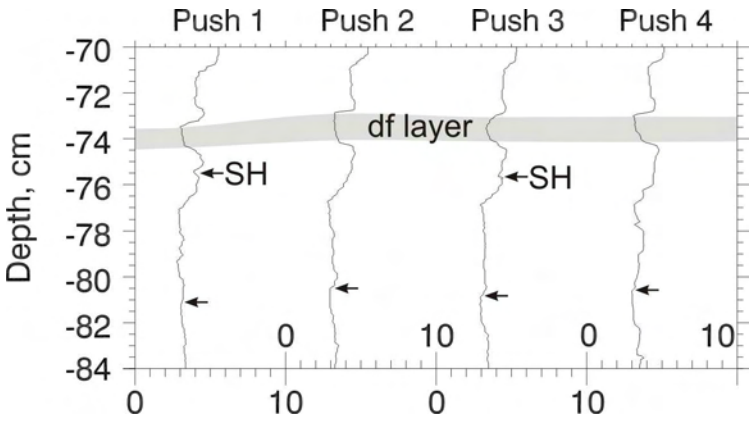

Figure 2.24: Closeup from the the four pushes shown in Figure 2.23. Decomposing fragment layer (grey region), 20-Feb-2006 surface hoar (arrow labeled SH), and lower interface discussed in text (arrow only) shown.

the magnitude of the force signal does not vary much at this point. At the top of this interface is a very thin (2 mm) SH layer, which is not distinguishable at all from the layer below. This is not that surprising, since the hand hardness value is identical to the layer below. However, it does indicate that this type of very thin weak layer can not be identified using the SABRE penetrometer.

Bostock Traverse example

The second example is from three pushes collected at the Bostock Traverse site on 20-Feb-2007. This site was on a north east-facing slope of 15° at an elevation of 1300 m. The site was surrounded by dense, mature forest. This site was investigated about two weeks after the burial of a very pronounced surface hoar layer, buried on 04-Feb-2007 in this location. The three penetrometer pushes were collected within 1 m of each other.

The manual snow profile for this area as well as detail of the penetrometer pushes for depths from 67 to 82 cm is shown in Figure 2.25. The sequence of layers around this

depth is as follows:

1. 54.5 to 70 cm: 1F hardness, decomposing fragment (DF) layer, measured density of 169 kg m^{-3}
2. 70 to 74 cm: P- hardness, rounded grain (RG) layer
3. 74 to 77 cm: 1F+ hardness, DF and RG layer
4. 77 to 78 cm: 4F+ hardness, surface hoar (SH) layer, buried on 04-Feb-2007
5. 78 to 97 cm: P- hardness, RG layer, measured density of 280 kg m^{-3}

The upper RG layer, which is harder than the surrounding snow, shows up prominently on the profiles as a peak. In the manual profile, the next two layers transition to lower hardness values, 1F+ and 4F+ respectively. In the penetrometer profiles, however, an extra small peak is visible, just above the SH layer, at a depth of 75 cm in push 1. This small feature is not visible in the manual profile. Below this is the 04-Feb-2007 SH layer, which is quite prominent in all three of the pushes. It appears as though a surface hoar layer that is 1 cm thick with a good hardness contrast, is readily identifiable using the SABRE penetrometer.

The presence of the thin, slightly stiffer layer above the weak layer could have had an impact on snow stability in this area. Many authors (e.g. McClung, 1981; McClung and Schaerer, 2006; Schweizer and Jamieson, 2007) have argued that a pronounced hardness contrast between the weak layer and the overlying slab increases the likelihood of avalanches. There were two notable avalanches that released on this interface very close to the location of the Bostock Traverse site. One of these avalanches occurred three days before these profiles were collected and was a size 2.5, remotely-triggered avalanche, triggered by a person on skis, 100 m from where the avalanche actually occurred. The second occurred two days before, was also remotely-triggered (from 150 m away), and was a size 3 avalanche. It is possible that the presence of this slightly stiffer layer, combined with the good preservation of large surface hoar crystals, decreased the stability of the snow

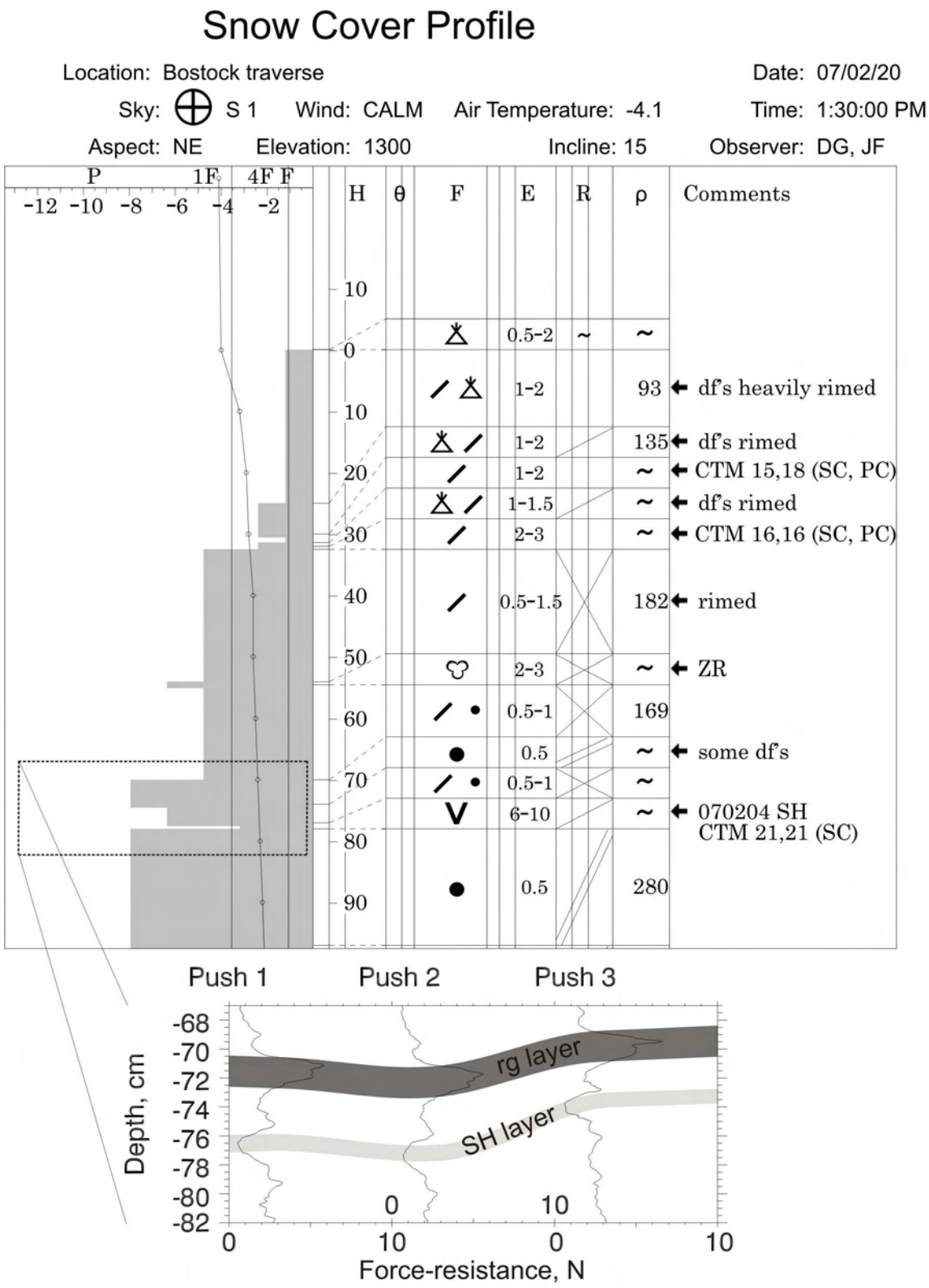

Figure 2.25: Manual snow profile and detail from three penetrometer pushes taken at the Bostock Traverse site on 20-Feb-2007. Harder, rounded grain layer (dark shaded region) and 04-Feb-2007 surface hoar (light shaded region) shown.

in this area. The information about the extra stiffness just above the weak layer was not readily gleaned from the manual profile alone, although the field workers assessing the snow to prepare the manual profile may well have been able to sense this transition in the field.

2.8 Conclusions

The unmodified SABRE penetrometer was found to have a force sensor that gave consistent readings between pushes in similar snow. The depth sensor was found to have errors of 20 to 30%, which was considered to be too great for assessing snow variability. The temperature sensor produced output that bore broad resemblance to the shape of the manual temperature profiles, but absolute values could not be accurately determined. The temperature sensor subsequently stopped working and was not repaired.

The SABRE penetrometer was unable to reliably distinguish differences in snow with a hardness less than 4 finger.

Modifications to the shape and size of the tip were unsuccessful and none of the different tip shapes tried improved the quality of the force signal. The 60 mm blade shaped tip showed the most promise in this respect, although the penetrometer would need further, substantial modifications to eliminate twisting and torsional problems caused by this shape of blade.

A depth measuring platform was added to the penetrometer system and this improved the depth accuracy to ± 1 cm. Precision was calculated to be about 1 mm for usual push velocities and acceleration magnitudes, providing there is no slip between the encoder wheel and the penetrometer shaft and accelerations are less than 1 g. If the velocity and acceleration magnitude are both high, precision can drop to 3 mm or worse. It is therefore of vital importance that a smooth push be maintained; the velocity should also

not exceed about 50 cm s^{-1}.

Mean force values and force ranges were calculated for different hand hardness values (see Table 2.5). These values are specific to this instrument. For each hand hardness category, the measured range of penetrometer force values in that hardness category extends quite far into neighbouring categories. The subjective nature of the hand hardness scale is at least part of this problem and makes precise conversion between hand hardness and penetration force-resistance impossible.

Force values may vary by as much as 0.3 N between pushes into snow of the same hardness. This may be significant when interpreting low-resistance layers and care should be used interpreting absolute force values using the SABRE probe.

Based on the examples presented, as well as from experience interpreting approximately 20 other thin layers in several hundred profiles, weak layers of 5 mm or more can be reliably identified using the SABRE penetrometer, providing there is a reasonable hardness contrast between the weak layer and the surrounding layers (approximately 0.5 to 1 N). In some cases, thinner layers can be identified in individual profiles, down to as thin as 2 mm, although they can not be traced reliably between neighbouring pushes.

Chapter 3

Rate effects and snow deformation analysis

3.1 Introduction

It is well known that the mechanical behaviour of snow depends on the rate of loading (e.g. Yosida, 1956; Mellor and Smith, 1966; McClung, 1979; de Montmollin, 1982; Fukue and Yong, 1987; Fukuzawa and Narita, 1993; Schweizer, 1998). At low rates, deformation is generally in the ductile regime and considerable strain can be accommodated without failure. At high rates, snow fails in a brittle manner once the applied stress exceeds the elastic limit of snow. Since the SABRE penetrometer is a variable-rate device, and no instructions were provided to correct for rate effects, there is an implicit assumption that there is no rate dependence within the normal operating velocity range of the device. This assumption is tested here.

In this study, results are presented from field-experiments designed to measure how the force-response on the SABRE penetrometer varies with velocity for in-situ snow samples of low to medium density (approximately 100 to 350 $\mathrm{kg\,m^{-3}}$). Studies on in-situ field samples are under-represented in the literature, despite the fact that this is the prevalent range of densities for avalanche slabs (McClung and Schaerer, 2006, p.92). The velocity range attained in this study was greater than in previous studies and results are compared for layers of different snow properties. An analysis of how snow deforms around the SABRE penetrometer tip is also presented, from deformation experiments performed in a clear plastic box. Despite some reservations about the method used for this experiment, this analysis is presented, since it aids the interpretation of the rate effect experiment results.

This study has implications for further development of variable rate penetrometers that could find application for avalanche forecasting or hydrology. The primary advantage to variable rate penetrometers is the elimination of a motor drive unit, which saves weight and reduces complexity. In a field environment where portability and ease of use is critical, this advantage could be considerable.

3.2 Literature review: Rate effects and snow deformation

3.2.1 Rate effects

Various authors have tried to assess the impact of rate effects on different types of snow deformation. Gubler (1975) performed experiments with a Rammsonde penetrometer using sieved snow of an unspecified density. He reported a strong rate effect with mean hardness values decreasing by approximately one order of magnitude as penetration velocities increased from 6.8×10^{-3} to 65 cm s^{-1}. Fukue (1979) deformed uniform snow samples at different rates in a cold-laboratory using a thin blade. He determined a transition between ductile and brittle deformation in age-hardened (sintered) snow of $0.25\,\mathrm{mm\,s^{-1}}$ for a blade 0.6 mm thick and 12 mm wide. Federolf (2005) deformed snow samples in a decelerating regime using an instrument called the "Fast Snowdeformer". The force on a free-falling piston and its displacement were recorded during impact for a variety of initial impact velocities on dense, well-sintered snow ranging from 420 to 525 kg m^{-3}. His results showed a flat response between piston velocity and the impact force per metre. de Montmollin (1982) performed rate effect experiments using a 100 cm^2 shear frame in snow with densities ranging from 170 to 430 kg m^{-3}. He determined that the ductile to brittle transition was within the range 1 to 5 mm min^{-1}. Using a larger shear frame of 250 cm^2, Jamieson (1995) determined that rate effects when pulling shear frames in weak layers in undisturbed snow were negligible, as long as the loading time

was less than 1 s. Fukuzawa and Narita (1993) deformed laboratory-grown depth hoar samples using a mechanical apparatus and reported a ductile–brittle transition at strain rates of between 8×10^{-5} and $2\times10^{-4}\,\mathrm{s}^{-1}$. Narita and others (1992) performed similar experiments with rounded grains with a density of 300 kg m^{-3} and found the ductile–brittle transition to be 6.5×10^{-4} s^{-1}. Schweizer (1998) reports values for the ductile–brittle transition of 1×10^{-3} s^{-1} for small rounded grains (<0.5 mm) and 1×10^{-4} s^{-1} for larger rounded grains (≈1.0 mm).

3.2.2 Snow deformation

Yosida (1956) deformed a number of snow samples of different properties in the laboratory using a plate. The snow samples were marked using soot that was sieved into the snow at intervals, and deformation by the plate was done next to a window, through which deformation patterns could be observed. In all cases, a plug of snow was pushed ahead of the plate. For newly deposited and compact snow, the zone of compacted snow lay almost immediately underneath the deforming plate; for wet and granular snow, this zone spread out further laterally away from the sides of the plate. When an ice crust was deformed, irregular fractures at the plate margins were seen.

Fukue and Yong (1987) identified two zones associated with these plate deformation experiments: compression shear, directly under the plate, where primary deformation was in compression; and direct shear, under the margins of the plate, where the primary deformation was in shear. They argued that strain hardening occurred as snow grains were pressed together, increasing adhesion between grains. They noticed that granular snow exhibited a saw-tooth stress–deformation curve at a strain rate of 8×10^{-3}, which they attributed to shear failure and strain hardening repeatedly and alternatively taking place. More recently, Gleason (2005) used particle image velocimetry (PIV) to determine displacement vectors and strain in a layered snowpack subjected to deformation by a flat

plate. He concluded that snowpacks with hard layers distributed the load horizontally compared with relatively uniform snowpacks that distributed the load mostly in the vertical direction.

Johnson (2003) developed a micromechanical theory of cone penetration in granular materials, such as snow, from observations and theory associated with the development of the SnowMicroPen (Schneebeli and Johnson, 1998; Johnson and Schneebeli, 1999). In his work, the penetration resistance was related to the penetrometer effective surface (PES), defined as the area of the perimeter of a zone of compacted snow (compaction zone) that forms under the penetrometer tip. The PES depends on the diameter of the tip, microstructural snow properties and also, importantly, the cone angle. As the cone angle exceeded 120°, penetration resistance was found to increase dramatically. Kronholm (2004) applied this model to determine the compressive strength and the elastic modulus for different snow layers from a penetrometer signal. He found that the model performed well for values of compressive strength but that values of the elastic modulus were approximately two orders of magnitude lower than accepted values.

For deformation involving rounded, or blunt-nosed penetrometer tips, it is necessary to turn to literature from soil mechanics. Gill (1968) observed that soil bodies were liable to form on blunt penetrometer tips, including spherical tips. Mulqueen and others (1977) deformed clay and sandy soils with 10 mm, 30° conical and 10 mm rounded penetrometer tips, and found that for relatively low density soils, penetration resistance for the rounded tip was significantly higher than for the sharp tip. As soil densities increased, the differences between the tips became less. High soil moisture content also decreased the difference between the tips. (Smith and Mullins, 2001, p.379) states that soil builds up on probe tips when the tip angle exceeds 90°.

White and Bolton (2004) determined displacement and strain fields for soil deformation beneath flat-ended, square based piles driven into sand using PIV. They concluded

that strain paths are initially vertical in compression, followed by horizontal movement associated with shear as the soil elements flow around the pile shoulder.

3.3 Methods

3.3.1 Rate-effects

A manually driven SABRE penetrometer (Mackenzie and Payten, 2002), designed and built by Himachal Safety Systems, inc. was used to measure the force-response of snow in this study (Figure 3.1). The SABRE penetrometer was driven horizontally at a range of velocities into four different thick, uniform snow layers. The number of pushes into each layer ranged from 18 to 30 and velocities up to 120 cm s^{-1} were attained. The properties of the tested layers are given in Table 3.1.

The details of the SABRE penetrometer have been described in Sections 1.6 and 2.3.2. The custom-built displacement measuring platform (see Section 2.5.1) was turned through 90° and was used to measure the horizontal displacement of the penetrometer into the side wall of a snow pit (Figure 3.1). The displacement measuring platform also served as a guide to keep the penetrometer within the layer of interest. The supplied data collection device from the SABRE penetrometer was not used; instead the amplified output from the piezo-electric sensor was recorded at 1000 Hz with a Campbell Scientific CR1000 datalogger, as previously described. The same datalogger was used to record the

Table 3.1: Snow properties for the layers used for the rate effect experiments.

Layer	Hand hardness	Moisture	Density ($kg\,m^{-3}$)	Grain size (mm)	Grain type	Thickness (cm)
1	pencil	dry	376	0.5 - 1.0	MF*	36
2	pencil	moist	280	1.0	RG*	30
3	1-finger	dry	199	0.5 - 1.5	DF*	21
4	4-finger	dry	115	1.0 - 2.0	DF*	4

*MF–mixed forms; RG–rounded grains; DF–decomposing fragments.

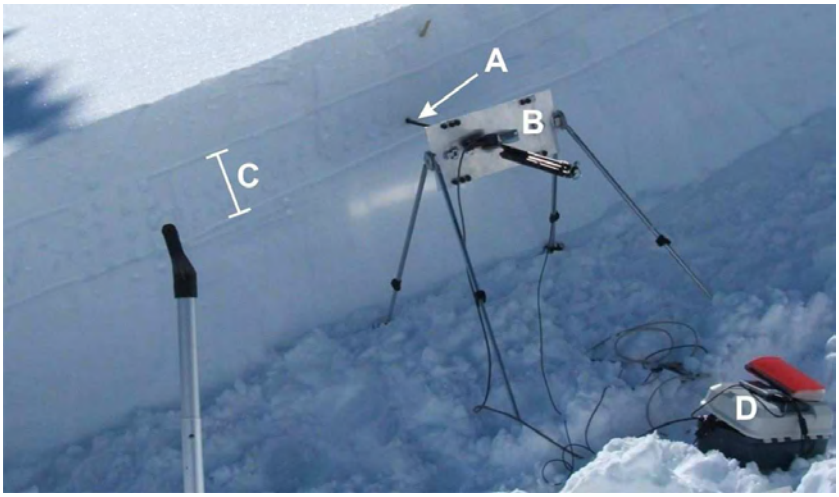

Figure 3.1: Apparatus for performing rate-effect experiments. The SABRE penetrometer (A), guided by the displacement platform (B) was pushed horizontally into a thick, uniform snow layer (C). Data was recorded on a datalogger (D). ASARC photo.

horizontal displacement, although due to equipment limitations, this was at a lower rate of 100 Hz. The displacement signal was interpolated to 1000 Hz using a cubic convolution interpolation method (Park and Schowengerdt, 1983) within the Interactive Data Language (IDL). Mean velocities (and corresponding mean force values) were averaged over distances of 1 cm or a minimum of 20 force measurements. This latter criterion ensured that for higher velocities, at least two measured displacement points were used for velocity calculations, preventing oversampling of the interpolated displacement signal. The cubic convolution interpolation method was chosen over linear interpolation to reduce interpolation errors for pushes with rapid acceleration or deceleration (see Section 2.5.3).

3.3.2 Snow deformation

Additional apparatus was used to analyze snow deformation at the penetrometer tip (Floyer and Jamieson, 2006). As previously mentioned, Gleason (2005) has used a similar concept to measure snow deformation around a wide plate, and White and others (2001, 2003) and White and Bolton (2004) have used this technique to investigate soil

deformation beneath piles. A clear, stiff plastic "snowbox" of dimensions $30 \times 20 \times 5$ cm with removable sides (windows) was filled with snow from a uniform layer of at least 7 cm thick and then "seeded" with chilli flakes. In order to fill the box with minimal snow compaction, two of its sides were removed before being pushed horizontally into the snow layer and cut out using a metal spatula. A brass rod with a tip of the same size and shape as that of the SABRE penetrometer was pushed vertically through the snow against the window with the chilli flake markers. The process was recorded using a video camera at a frame rate of 30 fps.

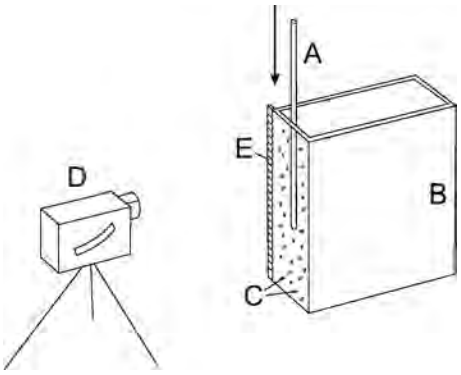

Figure 3.2: Diagram of apparatus for analyzing snow deformation patterns around the penetrometer tip. A shaped brass rod (A) was pushed manually into a snowbox with removable sides (B) that was filled with uniform snow and seeded with chilli flakes (C). The pushes were recorded with a video camera (D). A ruler fixed to the side (E) was used to convert deformation vectors from pixels to mm.

Pushes into a number of different layers were filmed in this way, using three different shaped penetrometer tips; a rounded, 12 mm diameter tip of the same size and shape as the SABRE penetrometer tip; a 90°, 12 mm diameter conical tip; and a blade tip with the thin end of the blade (2 mm, sharpened) pressed against the snowbox window. Results from these layers were used to assess the dependence of deformation patterns with snow density and for the different tip shapes for dry snow. Two further layers, a high density dry snow layer and a low density moist snow layer, were selected for more detailed PIV analysis. The properties of these layers are shown in Table 3.2.

Table 3.2: Snow properties for the layers used for the snow deformation experiments.

Layer	Hand hardness	Moisture	Density ($kg\,m^{-3}$)	Grain size (mm)	Grain type	Temperature (°C)
1	pencil	dry	330	0.5 - 1.2	rg*	-2.4
2	fist	moist	80	2.0 - 3.0	pp*	0.0

*rg–rounded grains; pp–precipitation particles.

Particle image velocimetry (PIV) (Crocker and Grier, 1996) was used to analyze the deformation patterns from the snow box videos. The IDL routines used in the PIV analysis were modified versions of those used by Crocker and Grier; in this analysis, the chilli-flake markers in the snow were tracked from frame to frame to generate displacement vectors. The routines identified marker particles based on their size, elipticity and brightness, so chilli-flakes, which had a range of sizes, shapes and colours, were well suited to this task. During tracking between frames, a maximum particle movements distance was specified, which reduced tracking errors associated with the misidentification of particles. In practice, however, despite careful processing of the raw video images, approximately 5% of displacement vectors were influenced by false tracking.

The snowbox method used in this study has been criticised (Jerome Johnson; Jo Jacka, 2008, personal communication), since the full rod was used in the deformation experiments. They suggested that a better approach would be to use split-axis rods to create a true axisymmetric deformation environment. The use of the full rod meant that only a small part of the rod (the tangent along the length of the shaft) was in contact with the window of the snow box. At the tip, this would have resulted in snow being pushed into the window and then sideways along the inside of the window. The amount of lateral spreading is estimated for certain snow densities in Section 3.5.3, although it is likely that this estimation does not account for all of the complicated deformation patterns that this geometry introduces. There was insufficient time to repeat the field experiments for this study. Therefore, on Jerome Johnson's recommendation, the deformation pattern results

are interpreted qualitatively, and used to assess differences in snow deformation patterns between two different types of snow. With care not to overstate the interpretation, these experiments nonetheless provide some insight into the nature of snow deformation beneath a rounded penetrometer tip.

3.4 Results

3.4.1 Rate-effects

For the rate effect experiments, a typical force-displacement trace (Figure 3.3) shows a spike near the start of the push before settling asymptotically to a constant level, despite variations in the velocity during the course of the push. The force varied considerably between pushes into different types of snow, as expected. There were also smaller variations between adjacent pushes into the same snow layer. To account for these within-layer variations, the difference between the constant level portion of the individual trace and the mean constant level portion of the layer was subtracted from each trace.

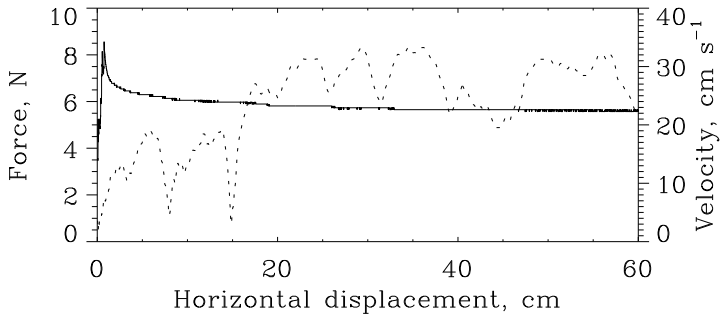

Figure 3.3: Typical force (solid line) and velocity (dashed line) trace for dry, pencil-hardness snow.

Each normalised force-displacement trace was sampled many times; each sample comprised of mean force and velocity values averaged over 20 to 100 data points. This acted to smooth local variations in the force signal and allowed the differentiation of a sufficient number of displacement values to give a reliable local velocity value. The sampled

force-velocity pairs from all traces into each layer are shown in Figure 3.4, including pairs taken from the spike at the start of each trace. Force values increase as the hardness and density of snow increases, as expected. Note that the jump in the force-response from 1-finger snow to pencil snow (0.64 to 5.2 N) was found to be far greater than the jump from 4-finger snow to 1-finger snow (0.38 to 0.64 N), despite there being one hardness step in each case. This result is consistent with the exponential relationship between penetration resistance and hand hardness found in Section 2.6.2.

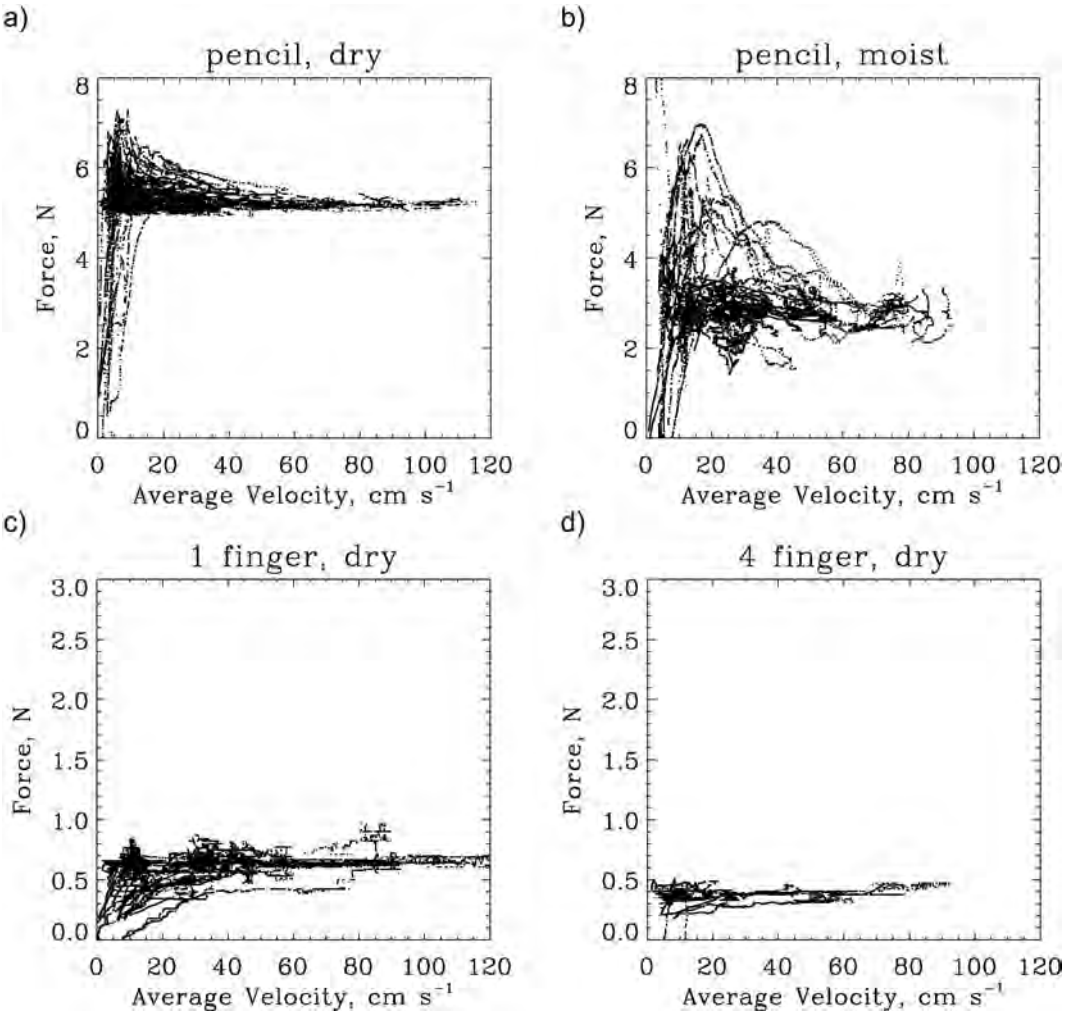

Figure 3.4: Combined force–velocity pairs (all data used) for all traces for a) dry pencil snow; b) moist pencil snow; c) dry 1-finger snow; d) dry 4-finger snow.

For both pencil hardness snow layers (Figures 3.4a and 3.4b) there are considerable

spikes in the force-response at lower velocities: 5-15 $\mathrm{cm\,s^{-1}}$ for the dry pencil layer; and 15-30 $\mathrm{cm\,s^{-1}}$ for the moist pencil layer. There are smaller, far less pronounced spikes at around 10 $\mathrm{cm\,s^{-1}}$ for the 1-finger and 4-finger layers (Figures 3.4c and 3.4d). The moist pencil layer (Figure 3.4b) shows considerable variation in force values, even for higher velocities, which is in sharp contrast to the dry snow layers that level off to a smooth level at higher velocities. This is likely due to successive bonding and release of snow at the head of the deformation zone caused by the high moisture content, a phenomenon known as ratcheting (e.g. Hassan and Kyriakides, 1992).

3.4.2 Snow deformation

By using a moving body coordinate system relative to the penetrometer tip, vectors can be generated that appear to "flow" around a stationary penetrometer tip. These flow vectors for the two different layers are shown in Figure 3.5a. It may be helpful to imagine the coordinate shift as keeping the penetrometer stationary and bringing the snow up to meet the penetrometer.

Interestingly, the particles are deflected before they reach the penetrometer tip itself. The low relative deformation rates immediately below the penetrometer tip can be interpreted as indicating a plug or "compacted zone" of snow that is forced ahead of the penetrometer tip. This zone undergoes only a slow turnover of snow material. In Figure 3.5a, the compacted zone for high density dry snow is relatively small, extending about three quarters of a tip diameter below the penetrometer tip. It also appears to be moving off to one side slightly; this is possibly due to heterogeneities in the snow or possibly due to a sideways motion that may have been applied as the rod was being pushed into the snow.

By comparison, the compaction zone for low density moist snow (Figure 3.5b) extends much further in front of the tip, approximately two tip diameters. There are marker

particles (labled CP in Figure 3.5b) with relative movement that is focused around a point; these are interpreted as particles that remained contained within the compacted zone as the rod was pushed into the snow. The differences between the high density dry snow and the low density moist snow in Figure 3.5 are striking, largely because inter-grain adhesion plays a particularly strong role in binding the snow together for moist snow.

The implications of the presence of the compacted zone is that snow deformation initiates at the outer margins of this zone, rather than at the penetrometer tip itself. Hence, the force response at the penetrometer originates from snow-on-snow deformation, transmitted through the densified snow of the compacted zone to the penetrometer tip. The zone where the resistive force components aggregate against the passage of the penetrometer tip is therefore the deformation zone; the outer margin of this zone is referred to as the stress bulb (stresses will extend slightly beyond the outer margin of the deformation zone, although, since the yield strength of snow is extremely low, they will extend very little). The larger the compacted zone, the more "spread out" the stress bulb will be; this will tend to smooth stratigraphic transitions in the snowpack.

From the images in Figure 3.5, and from others not shown, the extent of the deformation zone, or stress bulb, was measured for a range of different snow densities for three different tip shapes: 12 mm diameter rounded, 12 mm diameter 90° conical and 60 mm wide $\times$ 2 mm thick, sharpened blade, with the narrow end pressed against the snowbox window. The results are presented in Figure 3.6.

The horizontal extent of the deformation zone for different tips and different snow densities is shown in Figure 3.6a. The trend for all tip shapes is a gradual increase in the amount of horizontal deformation with increasing density. The blade tip shape shows substantially lower horizontal deformation than the rounded and conical tip shapes; horizontal deformation extents for these latter two cannot be readily distinguished.

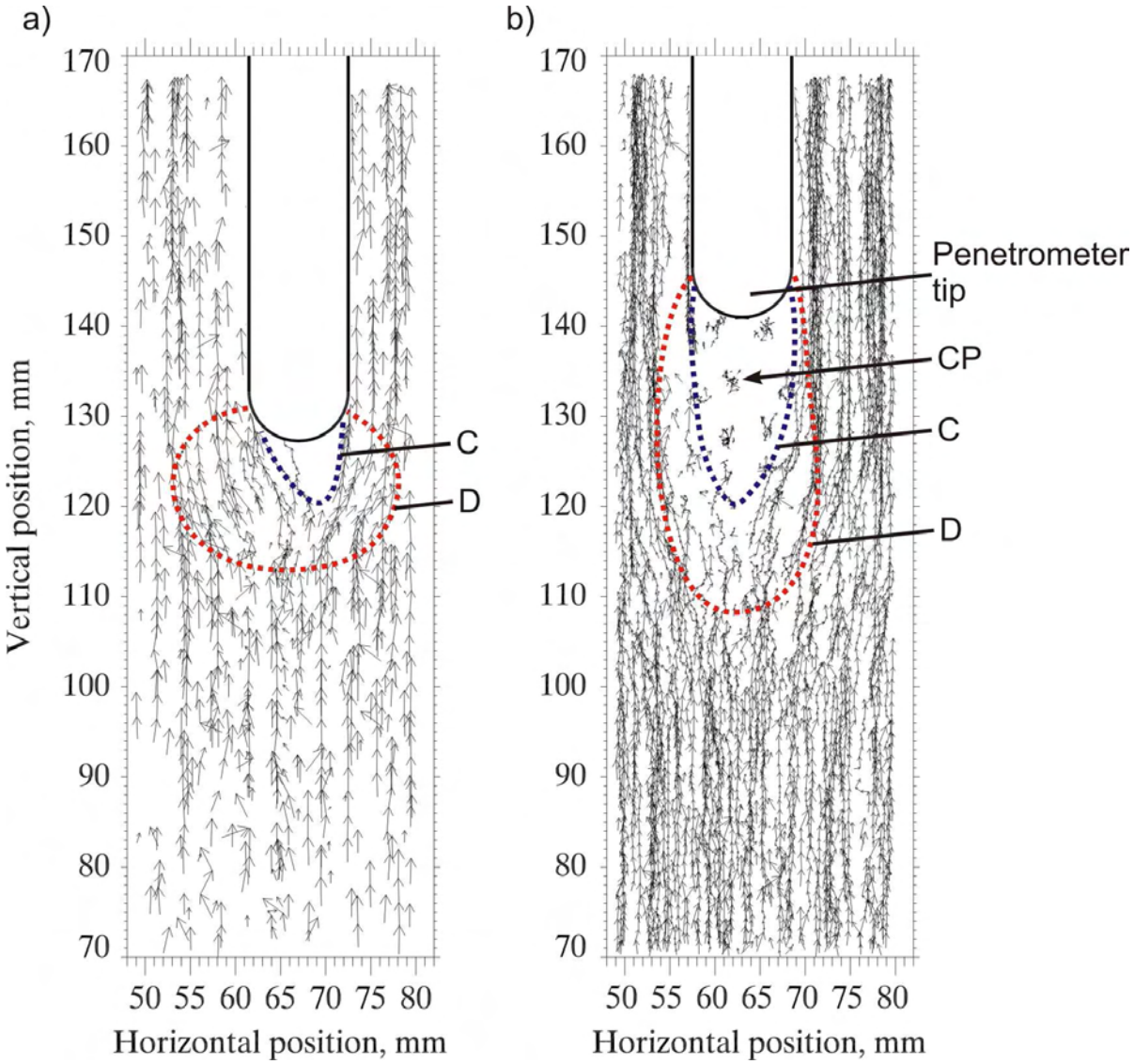

Figure 3.5: "Flow" vectors indicating the velocity of marker particles relative to the penetrometer tip for a) layer 1, high density, dry snow; and b) layer 2, low density moist snow. Interpreted boundaries of the compacted zone (C) and deformation zone (D) shown for each layer. Compacted zone particle (CP) represents a marker particle that remained contained within the compacted zone, showing little relative movement. There are more vectors for layer 2 because the density of the chilli flake seed particles was greater for this layer.

The vertical extent of the deformation zone is shown in Figure 3.6b. In this graph there is no clear trend for increasing deformation zone extent with density. As for horizontal deformation, the blade design shows the least vertical deformation zone extent. In most cases, the deformation extent for the conical tip was less than that for the rounded tip shape.

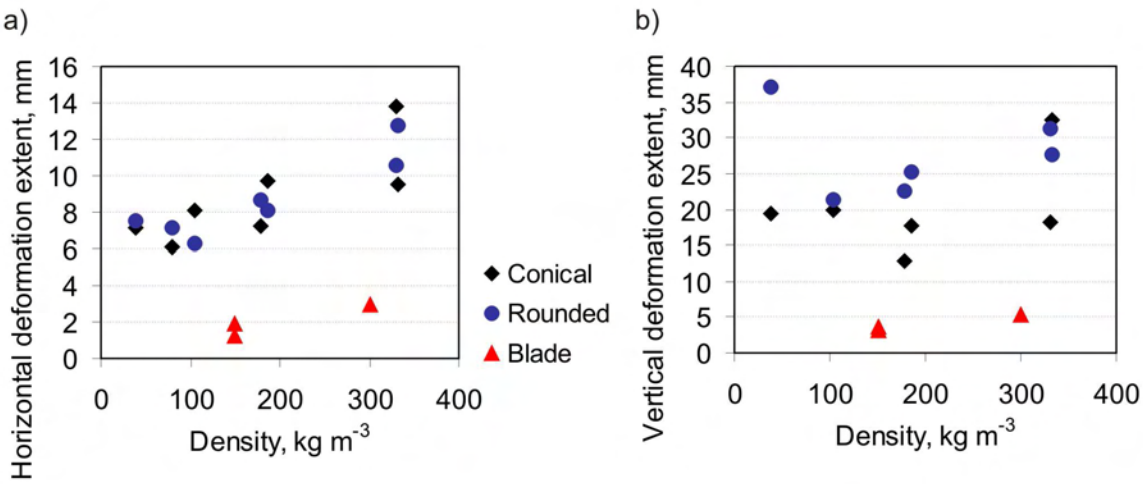

Figure 3.6: a) Horizontal; and b) vertical deformation extents for different snow densities using different penetrometer tips.

3.5 Further analysis and discussion

3.5.1 Compaction zone build-up

During the early part of a penetrometer push, the compacted zone must build up in front of the tip before a steady deformation state is reached. Gill (1968) describes a mechanism for soils in which soil initially compacts under a blunt penetrometer until shear forces through the compacted zone exceed the strength of the compacted soil. At this point, a shear surface develops leaving a soil plug in front of the penetrometer that moves into the soil. It is hypothesised that the formation of the compacted zone in snow may follow this model give rise to the spikes in the force–velocity traces in Figure 3.4. If this is the

case, it is expected that the force spikes are only found in the early part of the push. In order to test this, up to 6 cm (less if there was no spike) of data from the start of the signal were removed for each individual push. Since a wide range of push velocities was used during the experiments, many of the low velocity data points still remained in the data sets for each layer, with the exception of the moist pencil layer, for which no data less than $5\,\mathrm{cm\,s^{-1}}$ remained.

The force-velocity response for the truncated data sets is shown in Figure 3.7. Both pencil hardness layers show a considerable reduction in the magnitude of the low velocity spike, with the removal of early-push data. For the moist pencil layer, considerable variations in force with velocity still remain, likely due to the ratcheting effect previously described. Changes in the 1-finger and 4-finger layers are mostly seen in the removal of values below the mean where the force is ramping up to its velocity independent value.

The pronounced reduction in magnitude of the low velocity spike for the pencil hardness layers indicates that the early push spike is likely due to the development of the compacted zone for harder snow layers. For less hard layers, the force-response during the development of the compacted zone may actually be lower than during the steady deformation state (compare Figure 3.4c to Figure 3.7c).

For all the dry layers, there is a greater range of force values at lower velocities compared to higher velocities. This indicates that simple rate effects may play a small role, mainly in influencing the variability of the force-response, although the scale of this effect is far less than that of the compacted zone effect. There should be some caution with this assertion, however, since there are fewer data points at higher velocities.

Linear regression lines were fitted to each layer and are shown on each graph in Figure 3.7. The gradient of these lines ranges from -4.6×10^{-4} to $3.0 \times 10^{-4}\,\mathrm{N\,s\,cm^{-1}}$, an almost flat response for each layer. In general, once a steady deformation state is reached, force values vary very little with velocity for the range of velocities in the experiments

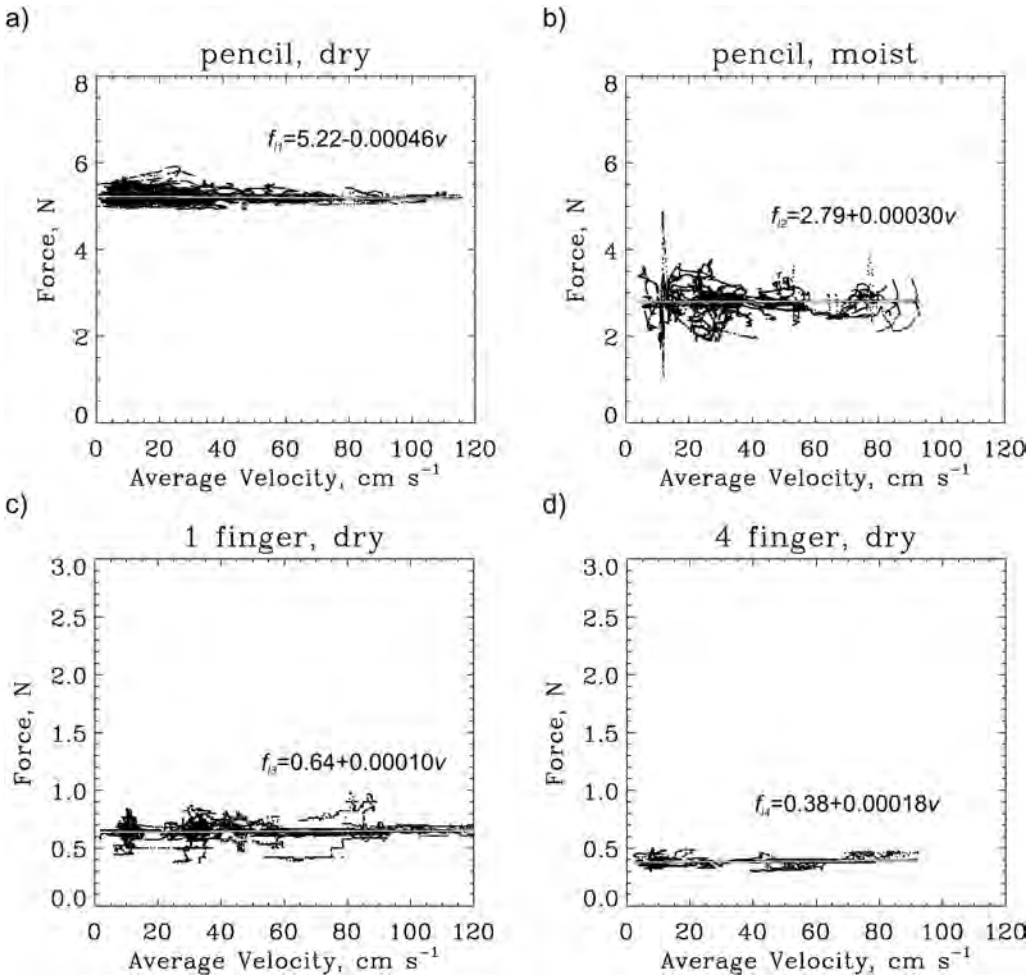

Figure 3.7: Combined force–velocity pairs with early-push spike data excluded for: a) dry pencil snow; b) moist pencil snow; c) dry 1-finger snow; d) dry 4-finger snow. Regression lines and coefficients are shown on each graph. $R^2 = 0.99$ for a), c) and d); $R^2 = 0.96$ for b).

(approximately 0.5 to 100 cm s^{-1} for the dry snow layers and 5 to 90 cm s^{-1} for the moist snow layer). In moist snow, far more variability in the force value is likely to be encountered, but there is still no relationship between the force and velocity within the given velocity range.

3.5.2 Strain analysis of snow deformation

In order to test for the presence of shear bands at the compacted zone boundary that might help support the argument that the build-up of the compacted zone is responsible for the early-push spikes, strain analysis was performed on the two snowbox pushes from the deformation experiments. Although data from more than two pushes were available, due to time constraints and uncertainties with the snowbox method, it was decided to limit the analysis to two highly contrasting snow types (high density dry snow and low density moist snow).

First, deformation rate fields were generated for the two snowbox pushes by combining 5 frames of data from the moving body PIV described above and then subtracting the real-space displacement of the penetrometer over those five frames. This generates a displacement rate field that is relative to the penetrometer tip but with vectors that represent actual particle movement. The deformation rates fields are shown for each layer in Figure 3.8. To visualise what these refer to, it may be helpful to imagine the camera moving downwards at the same rate as the penetrometer tip, with vectors generated by summing the displacement over five successive frames.

Direct comparison of the magnitude of the displacement rate vectors between the two pushes is problematic, since the push velocities were different for each push. During the time interval of 1/6 s, particles moved a maximum of 6.0 mm for layer 1 with a push velocity of 92.5 mm s^{-1} (Figure 3.8a) and 4.5 mm for layer 2 with a push velocity of 41.7 mm s^{-1} (Figure 3.8b).

The extent, shape and character of the displacement rate fields offer better comparison between the two layers, since these parameters are less affected by differences in push velocity. The deformation zone, where snow is actively being deformed under the penetrometer tip, is much larger for the low density moist snow push (layer 2) than for the higher density dry snow push (layer 1). The vectors indicate a strong vertical down-

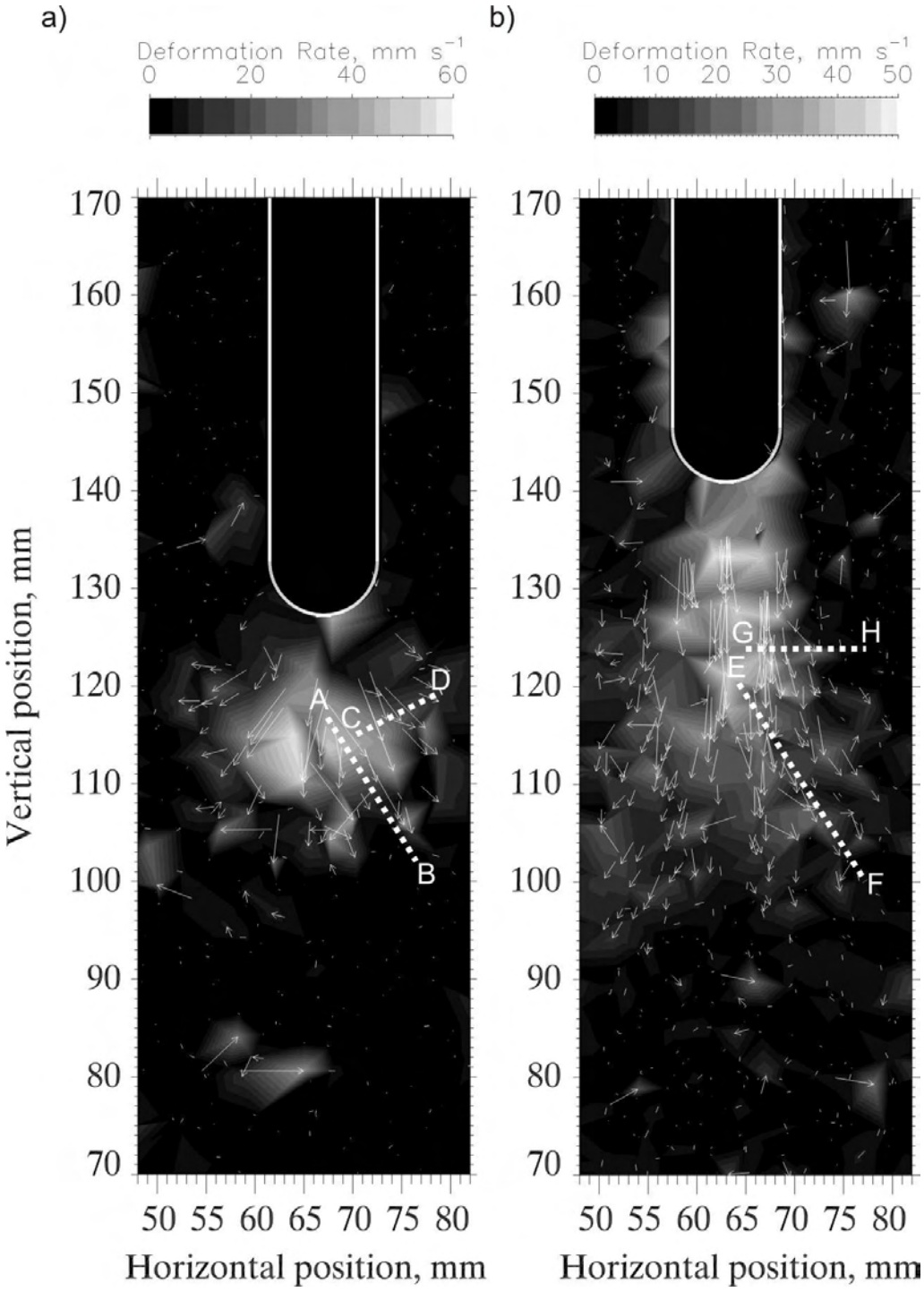

Figure 3.8: Deformation rate field for a) layer 1 (high density, dry snow); and b) layer 2 (low density, moist snow). Shading represents interpolated deformation rates; arrows represent actual particle movement over five frames. Normalised strain components were calculated over two transects for each layer (dashed white lines).

wards component extending some distance below the penetrometer tip, indicating that a large compacted zone is being pushed ahead of the penetrometer tip. Its large size is likely enhanced by the moisture content of the snow, which promotes capillary adhesion between snow grains. Most of the horizontal deformation occurs lower down, about 20 to 40 mm below the penetrometer tip. In contrast, for higher density dry snow, vertical and horizontal components are more balanced and there are not as many large vectors pointing vertically downwards. The style of deformation is more abrupt but occurs over a smaller volume of snow.

Yan and others (2004) provide a framework for interpolating strain rates for large deformations; in the case of their work, for morphing objects in animated computer graphics. When a small region of snow is deformed, there are three components to the deformation: a change in shape of the region, which, for a compressible material such as snow, can include a change in volume; a translation; and a rotation. In this analysis we calculate strains in two dimensions, making the assumption that deformation patterns are radially symmetrical around the penetrometer tip. The limitations of this assumption have been stated previously and errors associated with this are discussed further in Section 3.5.3.

In two dimensions, there are three independent strain components: ε_x, ε_y and γ_{xy}. For an infinitesimal region of snow R undergoing deformation, ε_x and ε_y are the local scaling components in the x and y directions respectively, also known as the tensile strain components. A positive value for ε_x indicates that the region is in tension along the x direction and a negative value represents compression; similarly for ε_y along the y direction. γ_{xy} is the shear strain component, which is positive if the relative angle between lines initially in the x and y directions becomes smaller after deformation and negative if the angle so defined becomes larger.

The strain components depend on the orientation of the axes. In order to evaluate the

maximum strain rate values around the penetrometer tip, the axes are rotated relative to the camera's field of view. This rotation is given by:

$$\begin{bmatrix} x \\ y \end{bmatrix} = \begin{bmatrix} u\cos\theta + v\sin\theta \\ v\cos\theta - u\sin\theta \end{bmatrix} , \tag{3.1}$$

where x and y are the rotated axes; u and v are the original horizontal and vertical axes (the camera's frame of view) and θ is the angle between the original and rotated axes.

The strain components are related to the deformation field by:

$$\begin{bmatrix} \varepsilon_x \\ \varepsilon_y \\ \gamma_{xy} \end{bmatrix} = \begin{bmatrix} \frac{1}{2}\left[(\frac{dx'}{dx})^2 + (\frac{dy'}{dx})^2 - 1\right] \\ \frac{1}{2}\left[(\frac{dx'}{dy})^2 + (\frac{dy'}{dy})^2 - 1\right] \\ \frac{dx'}{dx}\frac{dx'}{dy} + \frac{dy'}{dx}\frac{dy'}{dy} \end{bmatrix} , \tag{3.2}$$

where x and y are the position field components in the principal and secondary directions respectively before deformation; and x' and y' are position field components after deformation. The strain rate components are given by:

$$\begin{bmatrix} \dot{\varepsilon}_x \\ \dot{\varepsilon}_y \\ \dot{\gamma}_{xy} \end{bmatrix} = \frac{1}{T}\begin{bmatrix} \varepsilon_x \\ \varepsilon_y \\ \gamma_{xy} \end{bmatrix} , \tag{3.3}$$

where T is the time period over which the deformation occurs.

Since the errors introduced by using a full rod pressed up against a flat window are considerable, and since the push velocities were different for the different layers, the strain rate fields are normalised to the maximum total linear strain rate for each layer, given by:

$$\dot{\varepsilon}_{max} = \ _{max}\sqrt{\dot{\varepsilon}_x^2 + \dot{\varepsilon}_x^2} \, . \tag{3.4}$$

Using normalised strain rate components allows comparison of the relative contribution of the compressive and shear components to be assessed for each push. The individual

strain field components were analyzed over transects, which were chosen by visual inspection over regions that represented the maximum compressive and shear regions within the deformation field. This approach was necessary, since spurious vectors, caused by misidentification of some marker particles in the PIV analysis gave many false peaks in $\dot{\varepsilon}_x$ and $\dot{\gamma}_{xy}$ when fields of the strain components were generated. The transects are shown as dotted white lines in Figure 3.8. For each transect, the axes were rotated so that the x axis was parallel to the given line and the y axis was perpendicular to the given line.

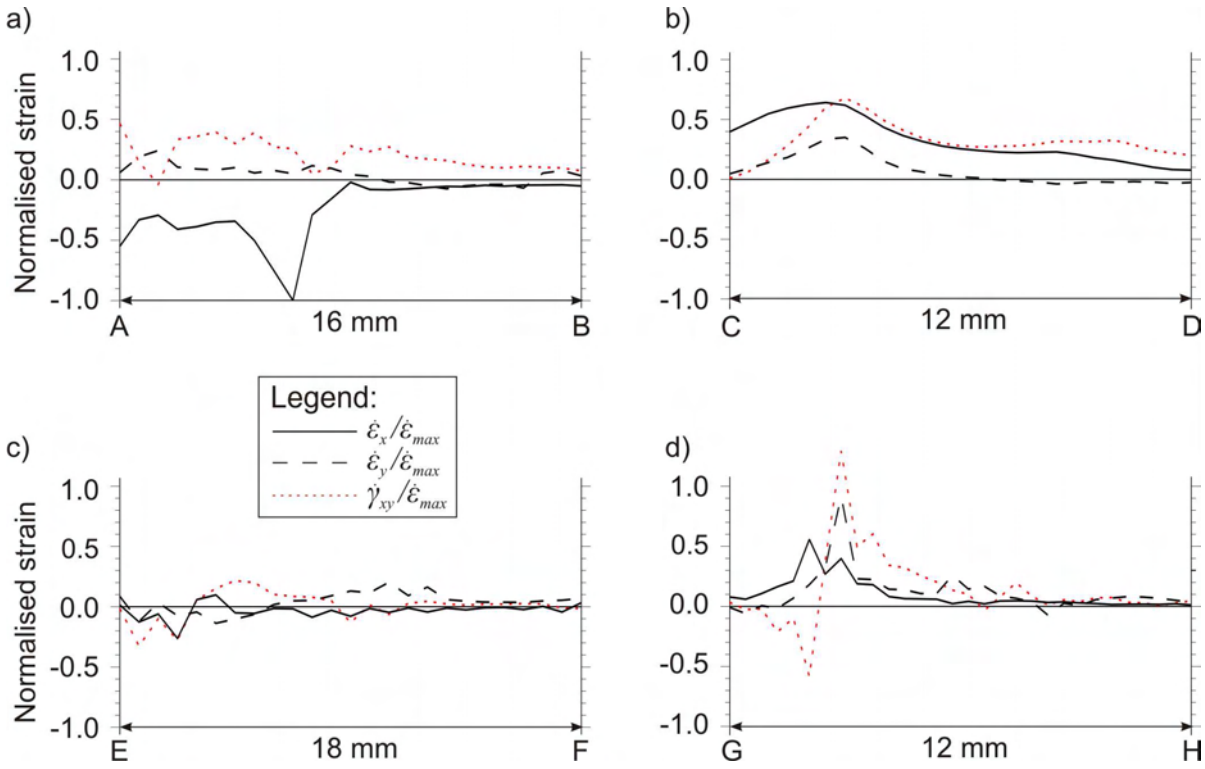

Figure 3.9: Normalised strain components for a) Layer 1, transect A—B; b) layer 1, transect C—D; c) layer 2, transect E—F; d) layer 2, transect G—H. Solid black line represents normalised strain rate parallel to transect; dashed black line represents normalised strain rate perpendicular to transect; dotted red line represents normalised shear strain rate.

For transect A—B (Figure 3.9a), $\dot{\varepsilon}_x$ is negative, indicating compression parallel to A—B, which is most intense about one third of the distance between A and B. There is an abrupt terminus to this zone of compression, which corresponds in Figure 3.8a to

the lower margin of particle deformation. $\dot{\varepsilon}_y$ is of relatively low magnitude compared with $\dot{\varepsilon}_x$, although it is positive in the first half of the transect, indicating there is slight tension perpendicular to the transect in this region. There is some shear ($\dot{\gamma}_{xy}$) although the amount of shear is approximately half as much compared with transect C—D (Figure 3.9b). The peak in $\dot{\varepsilon}_x$ in transect C—D occurs almost directly under the margin of the penetrometer, indicating the presence of a shear band at this point.

For transect E—F (Figure 3.9c), the relative magnitude of all three strain components is relatively low. $\dot{\varepsilon}_x$ is generally negative, indicating this region is in compression. By contrast, transect G—H (Figure 3.9d) shows a high magnitude peak in strain rates, corresponding to the region directly below the edge of the penetrometer (Figure 3.8b). The peak in $\dot{\gamma}_{xy}$ is particularly high, indicating that this is an intense shear band, which is consistent with observations from the displacement field (Figure 3.8b).

For both layers, there is evidence that there are regions where shear strain is high; these regions lie directly under the margin of the penetrometer tip. This is further evidence for the existence of a compacted zone, since for this zone to be maintained, regions of shear must exist at the margins of the compacted zone, or plug of snow being pushed ahead of the penetrometer tip.

Although confidence in the absolute values of strain rates from this analysis is low, values for $\dot{\varepsilon}_x$ and $\dot{\gamma}_{xy}$ in the order of 0.1 to 1 s^{-1} were obtained. These values are towards the higher end of strain rate values reported from a range of general geo-engineering applications (Hentz and others, 2004). Such high strain rates are plausible; however, considering the extremely porous and deformable nature of snow. These values are also three to four times higher than the ductile–brittle transition for snow, which is around $1 \times 10^{-4}\ s^{-1}$. It appears likely therefore that the spikes in the rate effect graphs are not a result of transitioning between the ductile and brittle deformation regimes.

3.5.3 Lateral spreading

As previously noted, a major limitation of the experimental procedure for the snow deformation experiments concerns the use of a full rod next to the snowbox window. This likely influenced both the rate and pattern of snow deformation snow. Lateral spreading is expected to be at a maximum just above the tip itself, where horizontal deformation is high, as snow flows around the penetrometer tip. Lateral spreading at this point was estimated to be approximately 1 mm for layer 1 and 2 mm for layer 2, for a 12 mm diameter rounded tip. The calculations used to estimate lateral spreading are shown in Appendix D. This effect could be better constrained by comparing the experiments described with experiments using a split-axis penetrometer, as suggested previously. For now, however, these values represent the best estimate of the errors introduced by the experimental setup.

3.5.4 Model applicability

As mentioned in the literature review, penetrometer theory is fairly well developed for conical tips. The Johnson (2003) model of force response on a cone penetrometer takes the following general form:

$$F = \bar{f}_p \bar{N}_c \zeta \tag{3.5}$$

where $\bar{f}_p$ is the average force contribution of microstructural elements in contact with the penetrometer effective surface (PES), $\bar{N}_c$ is the average number of microstructural elements in contact with the PES and ζ is a statistical term accounting for the variability in snow structure.

Determining the PES for cases where the size of the deformation zone is large compared to the size of the compacted zone, as is the case for the rounded penetrometer tip investigated here, is problematic, since the PES is not a well defined surface, as it is for sharp cones, but instead a broad zone. However, the shape of this zone is still critical

to the problem and the methods presented here may help to determine this. At a qualitative level, it is suggested that the leading edge of the compaction zone forms a slope with an angle of repose that is determined by the strength of the bonds and the friction between snow grains. The outer extent of the deformation zone extends in a bulb-shape below and sideways out from the compaction zone. The zone associated with the PES lies between these two boundaries. For a quantitative assessment, further experiments using improved methods and a range of penetrometer tip sizes are required.

3.6 Conclusions

There was no substantial dependence of the force-response on velocity over the velocity range tested, provided that (up to) the first 6 cm of penetration was excluded from the analysis. Therefore, within this velocity range, a manually driven penetrometer does not suffer from rate effects caused by variations in velocity during its push. Very low velocities were not tested, and these results may not be applicable below 0.5 cm s^{-1} for dry snow and 5 cm s^{-1} for moist snow.

During the first 6 cm of displacement (for a rounded 12 mm diameter tip), pronounced spikes in the force-response were noted for higher hardness layers. This was attributed to the development of a densified zone of snow that built up ahead of the tip from initial compaction of snow material. At some point, shear forces exceeded the strength of the snow in this zone and a plug of densified snow was pushed ahead of the rounded penetrometer tip. This plug, or compacted zone, was observed in snowbox experiments using PIV.

One implication of this is that penetrometer pushes should not stop during a push. If the penetrometer stops, snow in the compacted zone has a chance to re-bond with the surrounding snow. When motion resumes, these bonds, as well as static friction between

the grains must be overcome, resulting in a spike that may not be related to an increase in snow hardness at that point.

A further implication of this is that a penetrometer profile could show a spurious spike in its signal, if either its initial layer is hard or it transitions from a low-resistance to a high-resistance layer due to the development of a compacted zone. The effect of this transition is likely to be greater in the first instance than the second, although this remains untested. This effect may affect both manually driven and motor-driven penetrometers.

For 12 mm diameter penetrometer, a good working velocity range, would be approximately 30 to 100 cm s^{-1}, applicable for both moist and dry snow. Below 30 cm s^{-1}, there was higher variability for some of the layers tested. Having a reasonably high lower bound also guards against the possibility of accidently stopping during a push, especially if a transition into a stiff layer or a crust is encountered. In a practical situation, having sufficient momentum to force the probe through such features is important, since it is hard for a human operator to instantaneously increase the applied force to the penetrometer if a rapid hardness gradient is encountered.

Compacted zones developed in all snow types tested; however, it appears as though their development has a greater influence on the force-response for high resistance snow layers. Compacted zones in low density moist snow may be particularly large due to the combination of the enhanced capillary cohesion due to the presence of free water and the low strength of the surrounding snow.

Tensile strain was found to be at a maximum, and in compression, immediately below the compacted zone. Peak shear strain occurred under the side of the penetrometer shaft. For the layer of low density moist snow, the shear bands were particularly pronounced.

Lateral spreading affected the snowbox experiments and prevented reliable calculations of absolute strain rates. Despite the uncertainty associated with the calculations,

the values obtained were three to four orders of magnitude greater than those reported for the ductile–brittle transition for snow. It is therefore likely that deformation is predominately in the brittle regime.

The amount of lateral spreading was estimated to be 1 to 2 mm for the layers tested. An improved experimental setup would employ split-axis penetrometer tips to overcome this effect and create a true axisymmetric deformation environment.

The results presented here are specific to one penetrometer tip shape and size, namely a rounded, 12 mm diameter tip. By comparison with other studies done on conical penetrometer tips, the relatively large compacted zone effect seen in these experiments indicates that the rounded tip shape may not be the best choice for a snow penetrometer. Making the tip sharper and reducing the tip diameter (coupled with a more sensitive load-cell) would likely enhance the SABRE penetrometer's ability to detect thin weak layers in the snowpack.

Chapter 4

Layer detection and identification

4.1 Introduction

Using a digital penetrometer, such as the SABRE penetrometer, a large number of stratigraphic profiles can be collected over the course of a field investigation. During winter field studies, up to 80 profiles per day could be collected and surveyed using the modified SABRE probe. Other groups have reported higher numbers using other instruments (e.g. Birkeland and others, 2004). As equipment becomes more portable and easier to use, the number of profiles that can be collected is likely to increase.

A consequence of the large amount of information that can be gathered using digital penetrometers is that a large amount of data must be quickly processed if they are to be used in a timely manner for the purposes of avalanche forecasting. In this chapter, three data processing methods are presented for analyzing digital penetrometer signals. All three are novel approaches and have not been previously reported by others. The first two are involved with tracing and detecting weak layers and other layers of interest in the snow. The third attempts to predict the fracture character of failure interfaces identified from compression tests. The methods are:

1. **Layer tracing** — this method automatically traces a layer of interest (e.g. a weak layer) that has been manually identified in one profile, across other profiles in a transect or a grid, even though the depth of the layer may change and the exact signal shape associated with this layer may vary. This method features Wiener spiking deconvolution where the user specifies the layer or interface to search for as a 'wavelet'. This method was to trace layers in some of the spatial variability

studies in Chapter 5.

2. **Weak layer detection** — A framework is presented for extending the layer tracing algorithm in point 1 to detect the presence of a potential weak layer in a penetrometer signal. The proposed method is to scan the penetrometer signal using a database containing a range of known weak layer profile segments. If a good match is found, the portion of the signal being analyzed is flagged as a possible weak layer. This method is presented as a framework only and has not yet been developed into an operational model, due in part to the small number of weak layer examples available, and in part because of the significant amount of work required to properly develop and test this method.

3. **Predicting fracture character from penetrometer profiles** — this method attempts to predict the fracture character from a layer identified in a penetrometer profile using a multivariate statistical model. The model is built using information from portions of penetrometer signals associated with different types of fracture identified in compression tests. Suitable variables are selected for the analysis using a univariate analysis and the classification done using linear discriminant analysis.

Note that methods 1 and 2 have been reviewed and accepted for presentation at the 4th Canadian Conference on Geohazards, Quebec City, May 20-24, 2008. Much of the text in these sections (Section 4.3 and 4.4) is slightly modified from a version submitted for inclusion in the conference proceedings of this conference. Publication in this thesis is with permission of the conference organisers.

4.2 Literature review: layer detection and identification

4.2.1 Layer tracing and detection

Wiener spiking deconvolution was developed during WWII by Norbert Wiener to separate radar signals from noise (Leinbach, 1995). This technique is commonly used for processing seismic reflection data but has general applications for separating a desired component of a signal of constant sampling interval from unwanted components within that signal. Examples of applications relevant to natural hazards include processing seismic signals from earthquakes, and monitoring volcanism from infrared remote sensing images. Floyer (2003) suggested that this technique might be useful for forecasting avalanches from hourly remote meteorological data.

It is generally accepted that dry slab avalanches initiate in a thin weak layer which lies beneath a thicker, cohesive slab (e.g. McClung and Schaerer, 2006). Recognising the presence of weak layers in manual snow profiles as well as the overlying slab properties is therefore fundamental to slab avalanche forecasting. In the absence of direct observations of avalanche occurrences, it is the next most pertinent type of information for assessing the stability of the snowpack (LaChapelle, 1980; Schweizer and others, 2003). McClung (1995) devised a rule-based model to help forecasters assess the stability of a snow profile. Contributions from each of a variety of snow profile attributes including, among others, layer hardness, layer thickness, crystal size and crystal form, were combined using rules devised through a series of interviews with expert forecasters. Schweizer and Jamieson (2003), following work by McCammon and Schweizer (2002), found that differences between the hardness as well as grain size of the weak layer and adjacent layers were significantly larger for unstable profiles compared with stable profiles. Schweizer and Jamieson (2007) included these variables along with the absolute values for hand hardness and grain size (see Colbeck and others, 1990) as well as the Rutschblock score

(see McClung and Schaerer, 2006) in a model for predicting whether a given snow profile should be considered stable or unstable. They reported prediction levels of 65-77% if the depth to a potential failure plane was known. If the principal weakness was unknown, prediction levels were lower at 53-62%.

Pielmeier and Schweizer (2007) classified potential failure layers in penetrometer signals collected with a SnowMicroPen (SMP) (Schneebeli and Johnson, 1998). They found significant differences between certain micromechanical characteristics of the penetrometer signal, the most significant of which was the structural element length of grains in the failure layer (Johnson and Schneebeli 1999). Potential failure layers were pre-identified using human interpretation and there was no report on the performance of the classification if the potential failure layers were not pre-identified. Birkeland et al. (2004) suggested that a change in the maximum penetration resistance within a weak layer may indicate an increase in bond strength within that layer.

4.2.2 Fracture character

The first classification scheme for fracture character was presented by Birkeland and Johnson (1999) and was originally reported in association with the stuffblock test, in which an isolated column of snow of the same dimensions as a compression test was loaded dynamically by dropping a stuff sack filled with snow at 10 cm increments. Their classification was known as shear quality, and comprised of three qualitative ratings: Q1, failures characterised by a clean and smooth shear plane, with possible weak layer collapse; Q2, failures characterised by a mostly smooth shear with more resistant sliding of the slab on the shear plane; and Q3, failures characterised by an irregular or rough shear plane. Birkeland and Johnson noted that shear quality was applicable to other snowpack stability tests, such as the rutschblock and compression tests. Johnson and Birkeland (2002) argued that using this system improved slope stability assessment, particularly for

tests which had high snowpack test scores (indicating stability) but whose shear quality was classified as Q1. The shear quality system has been adopted for use in the USA (Birkeland, 2004; Greene and others, 2004).

In Canada, Jamieson (1999) described a system for recording the character of failures, which could be applied to compression and other snowpack tests. His system was a four-point scale comprising of: progressive compression, describing fractures that were relatively indistinct and in which failure advanced over subsequent taps; thin planar, in which sudden fracture of a weak layer of less than 1 cm occurred; sudden collapse, in which thicker weak layers experienced sudden, noticeable downwards displacement; and non-planar break, in which failures were not confined to a plane.

This system was modified by van Herwijnen and Jamieson (2005, 2007a), who split Jamieson's thin planar category into two, which were: sudden planar, describing sudden planar fractures that crossed the column in one loading step and in which the block slid easily on the weak layer; and resistant planar, describing planar or mostly planar fractures that required more than one loading step to cross the column and/or the block did not slide easily on the column. van Herwijnen and Jamieson (2007a) were also able to show, by comparing compression test and fracture character results from skier-triggered and non–skier-triggered slopes, that fracture character was a better indicator of slope stability than the compression test scores. Furthermore, they showed that combining compression test scores with fracture character gave the best predictions for slope stability from the point of view of skier triggering. This five-point classification (see Table 4.2 for full descriptions) is currently in use in Canada (Canadian Avalanche Association, 2007, p.40).

Schweizer and Wiesinger (2001) presented a three-point scheme for rating the quality of rutschblock fractures as: clean, partly clean, or rough. Schweizer (2002) modified these categories to: smooth, rough, or irregular. Schweizer also presented release type classification for rutschblock tests; this classification described the proportion of the block

that slid during a test in: whole block, part of the block, or only an edge categories. A similar classification to this is now in use by Canadian avalanche operations (Canadian Avalanche Association, 2007, p.33).

There have been suggestions that fracture character is more spatially continuous over alpine terrain than snowpack test scores, although so far this has been hard to prove. Johnson and Birkeland (2002) discusses spatial homogeneity, listing it as a possible reason for why shear quality may be more reliable for assessing slope stability than test scores. Birkeland (2004), however, points out that the probability of having a more uniform spatial distribution is far higher when there are only three categories (compared to 30 for compression test scores and 7 for rutschblock scores). Campbell (2004) analyzed spatial arrays of rutschblock tests and determined that 22 out of 29 arrays (comprising of 6 to 64 tests per array) had consistent sudden planar fracture character. Since 83% of all his tests were recorded as sudden planar, it is unknown whether other categories show similar consistency.

4.3 Layer tracing

4.3.1 Introduction

For developing the layer tracing algorithm, penetrometer profiles were collected from a variety of sites in Glacier National Park using the modified SABRE penetrometer. For use in this analysis, all penetrometer profiles were interpolated to a regular depth spacing of 0.05 cm. Also in this analysis, the term *layer* is referred to as being a small section of a penetrometer profile that contains a visually distinct signal that is of interest. This section of the signal may correspond to an actual snowpack layer, such as a weak layer or a crust, or it may correspond to an interface between two adjacent snowpack layers.

4.3.2 Method

The basic steps in the layer tracing method comprise of:

1. Expert identification of the layer (or interface) of interest in the original penetrometer signal.
2. Pre-processing of the penetrometer signals.
3. Wiener spiking deconvolution.
4. Post-processing of the deconvolved output to determine most likely location of the layer of interest in the profile being analyzed.

Expert identification of layer of interest

A short, contiguous section of the original penetrometer profile (Figure 4.1a) is defined as the region of interest and this forms the master wavelet, defined as:

$$W = G_0(y); \quad y = (y_{w_max} : y_{w_min}) \ , \tag{4.1}$$

where $G_0(y)$ is the original force-depth signal and y_{w_max} and y_{w_min} define the upper and lower boundaries respectively of the layer of interest identified by an expert.

Pre-processing

Pre-processing is done on both the original penetrometer signal, $G_0(y)$ and the penetrometer signal being analyzed $G_a(y)$. The notation $g^i_{0,a}$ is adopted here to describe processing steps that are applied to both the original signal and the signal being analyzed (subscripts $0, a$). The superscript i denotes, in roman numerals, the order in which these steps are performed. The association with the depth (y) as the independent variable is assumed from here on and dropped from the notation.

A condition of Wiener deconvolution is that there is an identifiable component contained within a signal that is otherwise comprised of random noise. Random noise is characterised by a Gaussian distribution with a mean of zero. In order to approximate

this condition, the broad trend is first removed and then a high pass filter applied, which retains the information pertinent for thin-layer or layer-interface identification.

The broad trend is removed by fitting a least-squares, fourth order polynomial to both signals and retaining the residuals.

$$g^I_{0,a} = G_{0,a} - f_{0,a} \ , \tag{4.2}$$

where $f_{0,a} = a_0 + a_1 y + ... + a_4 y^4$ and the coefficients a_0 to a_4 were found by minimising the sum of squares between $G_{0,a}$ and $f_{0,a}$.

A high pass filter is subsequently applied to the trend-removed data. This is applied in the frequency domain using fast Fourier transform (FFT) and inverse FFT methods (e.g. Ifeachor and Jervis, 1993, p.53) to convert to the data into frequency domain and back to the spatial domain respectively.

$$g^{II}_{0,a}(\omega) = (1 - H_H) \times g^I_{0,a}(\omega) \ , \tag{4.3}$$

where (ω) denotes that the filter is applied in the frequency domain and H_H is a Hann window (e.g. Taylor, 1994, p.436) defined as:

$$H_H = \begin{cases} \frac{1}{2}(1 + \cos(\pi \frac{y}{\tau})) & |y| < \tau \\ 0 & otherwise \end{cases} \ . \tag{4.4}$$

τ is the frequency cut-off parameter used to control which wavelengths are accepted by the filter. τ was set relative to the total depth of the penetrometer signal, d_{p_int}. In practice, for a 200 cm push sampled at an interval of 0.05 cm, setting $\tau = d_{p_int}/2.5$ gave a cut-off wavelength of approximately 8 cm, which worked well. Figure 4.1 shows how a typical processed signal compared to the unfiltered signal.

Wiener spiking deconvolution

The method of Wiener spiking deconvolution reduces a signal component contained within a signal G to a desired output e by applying an inverse filter a. a is found

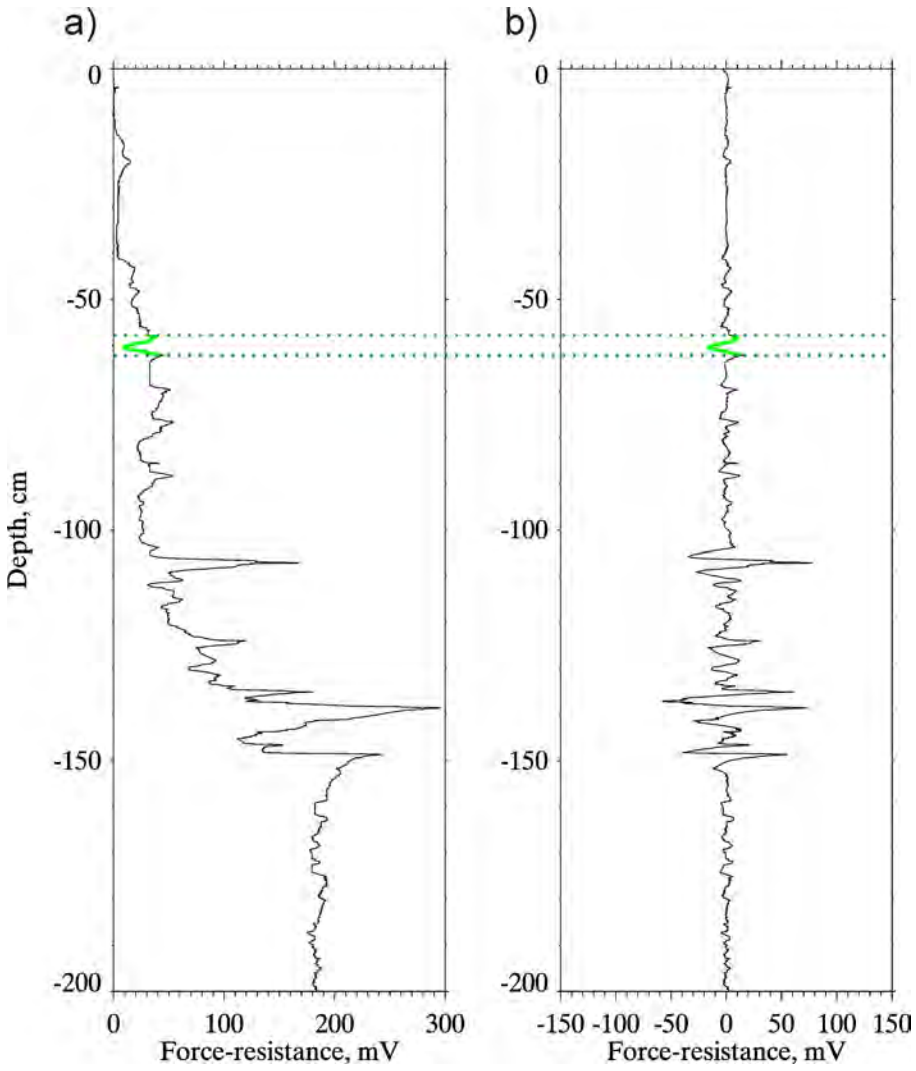

Figure 4.1: a) Typical unfiltered penetrometer profile. A weak layer is interpreted from this signal at a depth of 60 cm and this is assigned to be the master wavelet. b) Filtered signal from a) with trend removed and a high pass filter applied.

by defining a wavelet w as the portion of the signal that is being sought, which is a small portion of the master signal G_0. The desired output e must also be specified, which is set as a spike marking the upper boundary of the layer of interest.

Once the inverse filter a has been calculated, it can be used to make a search through another signal G_a. If another section of G_a is encountered that is similar to the wavelet w, then the signal at this point will be transformed to a spike that represents the location of this similar layer. If the condition that the rest of the signal comprises of random noise is met (which is not the case, and is discussed in Section 4.3.2), then the rest of the signal, which bears no resemblance to w is reduced to 0.

The inverse filter a is defined such that:

$$\hat{e} = a * \omega \ , \tag{4.5}$$

where $*$ represents the convolution operator (e.g. Ifeachor and Jervis, 1993, p.6). $\hat{e}$ is the estimation of the desired output e, which is an n-length vector comprising of a unit spike at e_0 with values at all other points being zero:

$$e = (1, 0, \ldots, 0) \ . \tag{4.6}$$

The wavelet w is defined over the same interval as the master wavelet in Equation 4.1 but is taken from the pre-filtered signal g_0^{II}.

$$w = g_0^{II}(y); \quad y = (y_{w_max} : y_{w_min}) \ . \tag{4.7}$$

From Robinson and Treitel (1980), the general form of the matrix equation for an optimum filter a is:

$$\mathbf{R}a = C \ , \tag{4.8}$$

where $\mathbf{R}$ is the autocorrelation matrix of the wavelet w and C is the crosscorrelation

vector between w and e. In expanded form, this can be written as:

$$\underbrace{\begin{bmatrix} r_0 & r_1 & \cdots & r_{n-1} \\ r_1 & r_2 & \cdots & r_{n-2} \\ \vdots & \vdots & \ddots & \vdots \\ r_{n-1} & r_{n-2} & \dots & r_0 \end{bmatrix}}_{\mathbf{R}} \underbrace{\begin{bmatrix} a_0 \\ a_1 \\ \vdots \\ a_{n-1} \end{bmatrix}}_{a} = \underbrace{\begin{bmatrix} c_0 \\ c_1 \\ \vdots \\ c_{n-1} \end{bmatrix}}_{C} . \tag{4.9}$$

The inverse filter a is optimal in the sense that it least-squares minimises the error between the actual and desired outputs. This error is given by the scalar ε, summed over the n elements in e:

$$\varepsilon = \sum_{i=0}^{n-1} (e_i - \hat{e}_i)^2 \ . \tag{4.10}$$

For good detection, the energy build-up characteristics of e must be matched to the energy build-up characteristics of w. The wavelet w is said to be minimum-delay if all its energy is concentrated towards the front of the wavelet. In this case, $e = (1, 0, \ldots, 0)$, with the spike at the beginning as in Equation 4.6. w is said to be a maximum-delay wavelet if all its energy is concentrated towards its end and in this case the desired output is modified to be $e = (0, 0, \ldots, 1)$, with the spike at the end of the vector. In the more general case of a mixed delay wavelet, the error from Equation 4.10 is iteratively calculated for a range of different positions for the spike in e from 0 to $n-1$. The position m that minimises ε is then used to calculate the optimum inverse filter a. If e is varied from its original form in this way, then the final deconvolved output must be offset by m if the spikes are to match up with the start of the layer of interest.

The final step is to use the inverse filter a to deconvolve the signal being analyzed. The final deconvolved output is calculated by:

$$\Gamma = a * g_a^{II} \ . \tag{4.11}$$

Post-processing

If the penetrometer profiles being analyzed change in hardness smoothly over the whole range of depths except at the layer of interest, then the pre-processing algorithms in Section 4.3.2 would indeed reduce the signal to the layer of interest + random noise approximation. However, the penetrometer profiles that were collected in the Columbia Mountains of British Columbia frequently contained layers of a similar wavelength to that of the layer of interest, but that did not represent the layer being identified. Additionally, it was common for the magnitude of the variations to increase with depth. Using the method above, if a layer of the same shape as the master wavelet is encountered but is twice the amplitude, then the resulting spike at this location will be twice as high as the spike generated when the wavelet is deconvolved with itself (termed the wavelet spike from here on). In order to get around this problem, the deconvolved data were further filtered as described below.

In a similar manner to the pre-processing filters, the post-processing steps $\gamma^i_{0,a}$ must again be performed in the order described by the roman numeral i. To reduce the effect of high magnitude, short wavelength layers such as crusts that tend to generate spurious detection spikes, the difference between the deconvolved output and the wavelet spike was taken and normalised to unit wavelet spike.

$$\gamma^I_a = \frac{\hat{e} - \sqrt{(\hat{e} - \Gamma_a)^2}}{\hat{e}} \ . \tag{4.12}$$

Note: if the signal + random noise condition is not closely approximated then better results will be obtained by replacing $\hat{e}$ in Equation 4.12 with $\Gamma_0(y = y_{w_min})$.

Since there is expected to be some correlation between the depth of the layer of interest in the original profile and the profile being analyzed, the results are filtered based on depth. The filter comprises of a somewhat arbitrary, user-defined window, which can be varied according to the expected variability of layered depths in the local

area. For this analysis, a tapered window was used, with a central portion of 1's over a range 10 cm above and 10 cm below the location of the wavelet in the original profile, with a further 5 cm at each end of taper, where the filter tapered linearly from 1 to 0. This window is applied in the spatial domain and:

$$\gamma_a^{II} = H_T \; \gamma_a^I \; , \tag{4.13}$$

where H_T is the tapered window described above.

The final step is to rank the spikes in the filtered, deconvolved output γ_a^{II}. A fully automated implementation of this scheme might simply select the highest ranked spike as the layer of interest, whereas an expert system could present the user with a selection of a small number of likely locations for the layer of interest. The original interpreted layer and the traced layer for two different examples are shown in Figure 4.2, with the top 10 ranked spikes shown for each example.

For implementation of the layer tracing algorithm, the Interactive Data Language (IDL) v6.2 was used. Routines for finding the autocorrelation matrix, and the crosscorrelation matrix and for generating the filter windows were coded from scratch. IDL's built in CONVOL routine was used for performing the convolution operations and the FFT routine was used for performing the fast Fourier transforms. The length of the wavelet has the greatest influence on performance time. On a 1.7 GHz computer running Microsoft Windows XP, processing time for running the layer detection routine on a single profile was approximately 0.25 s for a 3 cm wavelet containing 60 data points and 5 s for an 8 cm wavelet containing 160 data points. Wavelets greater than the wavelength cut-off (8 cm in our case) should not be used.

4.3.3 Model testing

The layer tracing algorithm was tested by tracing several layers of interest across three different transects of penetrometer profiles that were collected using the modified SABRE

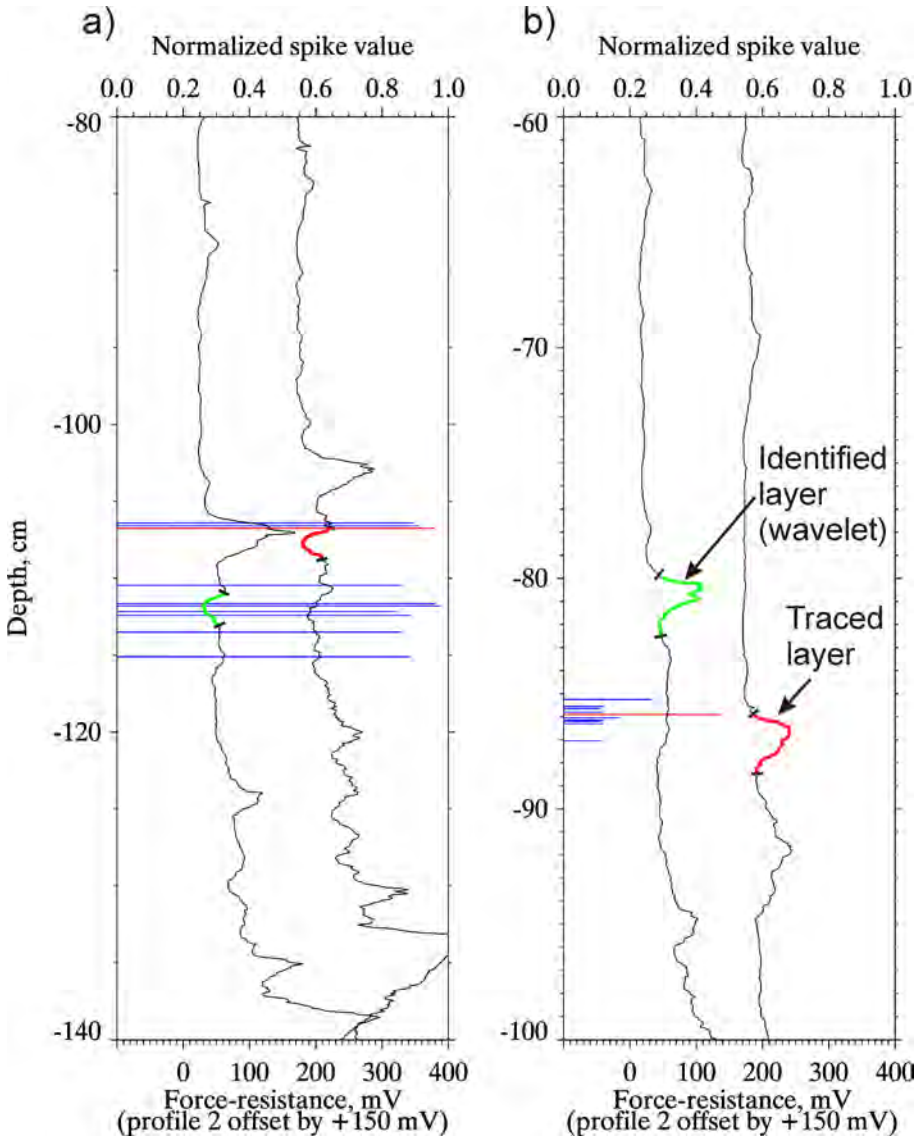

Figure 4.2: Tracing a layer from the interpreted signal (left signal in each frame) to an un-interpreted signal (right signal in each frame) for: a) a weak layer and; b) a peak representing a relatively hard layer. The spikes represent the 10 most likely positions for the location of the traced layer. Note that in a) there are several possible positions for the traced layer and the one chosen actually has the third highest spike value. In b) there in only one viable position and the spike value at this point is much greater than the other spikes.

penetrometer. The transects were collected in the winter of 2007 from the Columbia Mountains in British Columbia; transects 1 and 2 comprised of 11 individual profiles, and transect 3 comprised of 17 individual profiles. Transect 1 was collected on 21-Feb-2007 on a slope that varied gradually in aspect from NW to NE. Profile spacing for this transect was approximately 2 m. Transect 2 was collected on 15-Mar 2007 on a wind-affected slope with significant variability in snow cover depth. Profile spacing for this transect was approximately 0.5 m. Transect 3 was collected on 17-Feb-2007 on the flank of a size 2 remote triggered avalanche (triggered by a skier from a distance of 100 m). It was suspected that the weak layer (04-Feb-2007 SH) had been fractured at this point, since lateral fractures were visible in the slab that extended into the region of snow beyond the avalanche flank. Profile spacing for this transect was 15 cm.

The layers of interest were grouped into four categories: Crusts (or thin, high resistance layers); weak layers; interfaces (rapid increases in force-resistance); and other layer types that did not fit into the other three categories. The testing method comprised of identifying a layer of interest in the first profile and then tracing it across subsequent profiles in the transect using the developed algorithm. Each time a layer of interest was traced to a new profile, the layer that had just been identified became the new reference layer and was assigned as the new master wavelet. In this way, identification of a layer in a new profile was performed using layer information from the closest profile, rather than from the first profile in the transect.

If the layer was judged to have been correctly identified (based on a manual expert comparison between the two signals) by one of the top 10 ranked deconvolution spikes, then this was recorded along with the rank of the spike that best represented the position of the identified layer. If the correct position of the layer was not represented by any of the top 10 ranked deconvolution spikes, then the layer was considered not to have been identified.

4.3.4 Results

The number of profiles correctly identified for each layer that was traced across the transect is shown in Table 4.1. Most of the layers were identified quite well, although not always by the most prominent spike. Four out of 25 of the layers were not well identified. How well each layer was traced can be compared by looking at the mean rank of the deconvolution spike for the identified layers. It is clear that crusts, or spikes representing thin high-resistance layers perform best using this layer-tracing algorithm. The crust layers tested had mean rank values between 1.1 and 2.0. Interfaces between layers of different resistances performed the next best, with those showing a sharp increase in force-resistance performing better than those showing a more gradual increase.

The identification of the weak layers was more variable. The low density shallow layer, which was in the relatively quiet, upper part of the signal, performed particularly well, with a mean rank value of 1.2. The weak layer buried 04-Feb 2007 (a surface hoar layer that was recorded with a thickness of 10 mm in a manual profile close to, and on the same day as transect 1) had a mean rank value of 2.7 when traced across transect 1. This layer was identified with less confidence in transect 2 but the layer that was identified was traced across this transect in all but one profile, with a mean rank value of 3.1. This weak layer was also traced in transect 3, where it was suspected that it had been fractured. In this case the mean rank value was 5.1, and was not traced at all in two of the profiles. It is likely that the fractured nature of this layer, and its proximity to a relatively hard layer associated with a pronounced spike in the signal were detrimental to the ability to trace this layer. Overall, layers in the "other" category, which represented fairly nondescript layers, performed the least well compared to the other layer types.

Layers that were not identified well are of interest as they provide insight to the limitations of the method. The thick low density zone was quite a prominent low-resistance layer, although it was characterised by fairly gradual hardness transitions. Since the

Table 4.1: Results from the initial layer-tracing testing.

Layer description	Transect	Number of profiles in which layer identified	Number of profiles in which layer **not** identified	Mean rank of spike identification
Crusts				
High density peak 60 cm	1	10	0	1.1
Lower crust at approx. 130 cm	1	9	1	1.2
Thin near-surface sun crust	2	10	0	1.2
Double-peaked near-surface crust	2	10	0	1.9
Lower crust $\sim$ 110 cm	2	9	1	2.0
Slab above 04-Feb-2007 SH	3	18	0	1.3
Spike at 70 cm	3	18	0	2.0
Pronounced res. change at 85 cm	3	18	0	1.7
Crust, 125 cm	3	18	0	1.6
Weak layers				
Weak layer (04-Feb-2007)	1	10	0	2.7
Thick (8 cm) low density zone	1	1	9	5.0
Low resistance shallower layer	2	10	0	1.6
Weak Layer (04-Feb-2007)	2	9	1	3.1
Fractured weak layer (04-Feb-2007)	3	16	2	5.1
Interfaces				
Sharp, high magnitude change	1	10	0	1.2
Sharp, low magnitude change	1	10	0	2.1
Uneven resistance change	2	10	0	3.4
Sharp, high magnitude change	3	18	0	3.3
Hard–soft resistance change	3	18	0	3.4
Other				
Flat portion within layer	1	9	1	3.4
Small depression near crust	2	0	10	N/A
Broad low res. layer near crust	2	8	2	4.5
Subtle peak	3	9	9	5.0
Double peak	3	15	3	2.5
8 cm broad depression	3	1	17	9.0

thickness of this layer was the same as the cut-off wavelength of the high-pass filter (8 cm), it is likely that there was very little residual signal remaining after filtering to allow for unique identification. The other layer that performed poorly was the broad, low density layer near a crust. Again, its broad nature probably meant that some of its unique characteristics were filtered out and the proximity to the crust was likely responsible for "drowning" the signal at this point with many spurious spikes associated with rapid signal transitions near the crust.

Signals from a higher resolution penetrometer with a smaller, sharper tip, such as the SMP, would show some definite advantages, although have a higher computational cost. As the number of points in the wavelet increases, the processing time required for the algorithm becomes dominated by computing the FFT and inverse FFT. A simple strategy exists for limiting this problem: choose wavelets with a number of data points equal to an integral power of two (e.g. Ifeachor and Jervis, 1993, p.64). The main advantages of the SMP would be due to the smaller, sharper tip. This would give be a signal that was more spatially consistent, allowing for more reliable tracking from one profile to another. The likelihood of spurious spikes in the signal, which have an adverse effect on layer detection, would be reduced, as the plug of compacted snow ahead of the tip would be substantially reduced. Higher resolution signals, up to a point, may help fully and more reliably define the layer shape, which would help detection. At the point where additional signal information is at the microstructural level, which is expected to give random spikes associated with breaking individual grain bonds (Johnson and Schneebeli, 1999), no extra detection ability would be achieved.

4.4 Weak layer detection

4.4.1 Introduction

Computer-assisted weak layer detection promises to greatly enhance the ability to interpret penetrometer signals in terms of slope stability. If such interpretations become easy and reliable, penetrometer use, which at the moment is confined largely to research-based institutions, is likely to become widely adopted for avalanche forecasting. The method proposed below builds on the weak layer tracing method described above. While the proposed detection method has not yet been implemented and tested, the results of the layer tracing method indicate that there is potential for its use in layer detection. At the very least, this method warrants further consideration.

4.4.2 Proposed method

In the layer-tracing method described above, it was assumed that a given layer was present in the signal being analyzed and the optimum location for that layer was sought based on values from the deconvolved output. In the layer-detection method, the assumption that a given layer is present is removed, and we use the deconvolved output values to indicate the likelihood of finding a particular layer within this signal. This can be repeated many times using different potential layers that are assigned as the master wavelet to test for the presence of a range of weak layer types.

The steps required for implementing this model are shown schematically in Figure 4.3. Focus is placed on the detection of weak layers, since these layers are of particular interest to avalanche forecasters. However, this technique could just as well be used to look for crusts or other features within the penetrometer signal. The first step is to build a database of weak layers from expert interpretation of penetrometer signals combined with knowledge of the prevailing snow stability. Each weak layer wavelet includes the

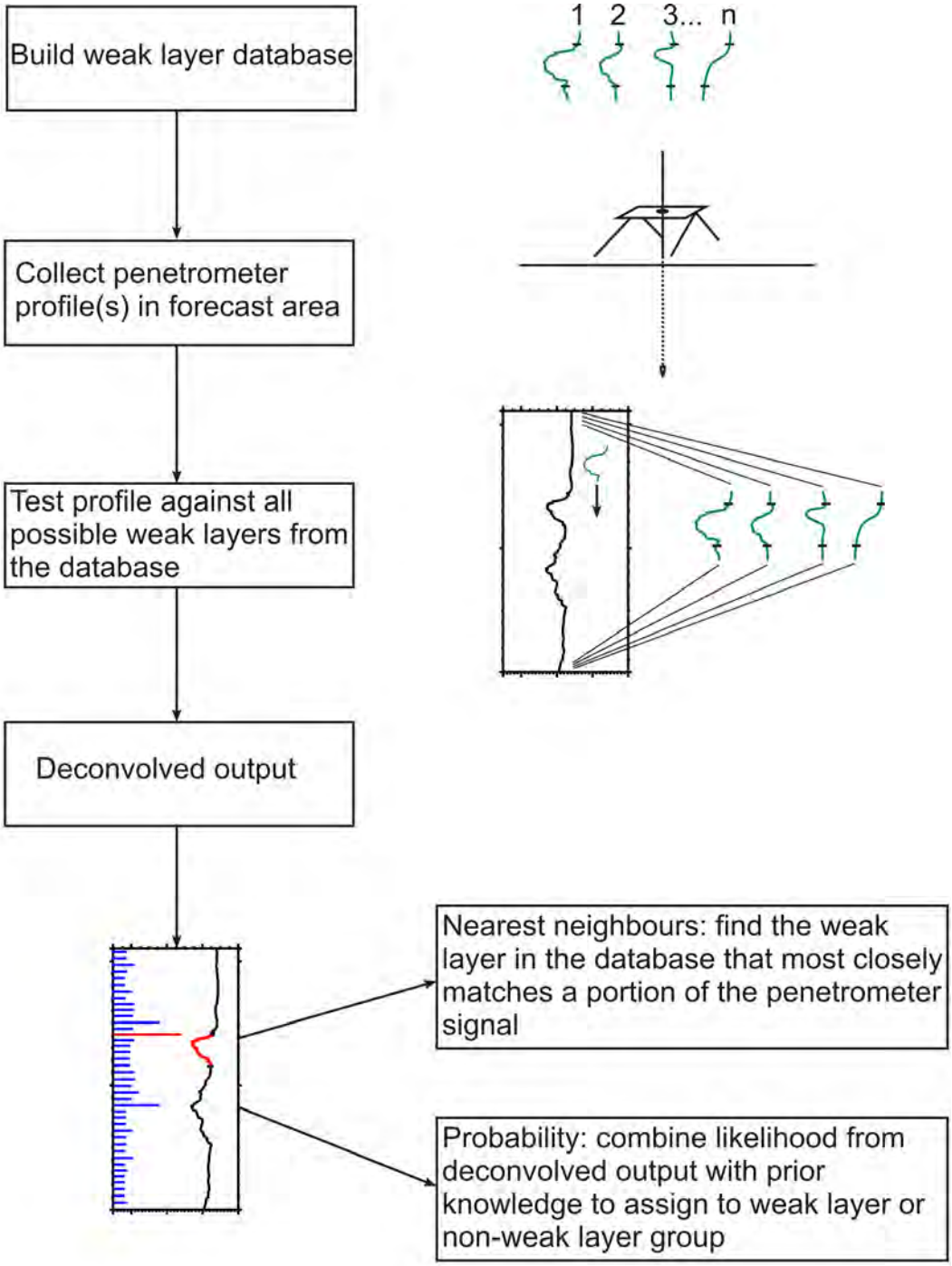

Figure 4.3: Schematic of the steps involved in the proposed weak layer detection model.

transition from the slab, through the weak layer itself and into the underlying snow. Information about local avalanche conditions, stability test results and other information helpful to avalanche forecasters should be retrievable against the weak layer wavelets. Next, the deconvolution technique outlined in Section 4.3 is performed a number of times on the penetrometer signal being analyzed, using, as the master wavelet, a different weak layers from the database for each run. In the most general case, we can set the depth filter to be unity for all depth values, thereby making no assumptions about the likely depth of the weak layer. In practice, however, it is likely that better results will be achieved if detection is focussed within a specified range of depths, say ± 15 cm compared to the input weak layer depth. This is acceptable, since the shape of a weak layer that causes avalanches at, say, a depth of 40 cm is likely to be different from one that causes avalanches at 100 cm.

Preliminary testing suggests that detection of similar looking layers from one profile to another profile collected at a different time and place but with similar snowpack characteristics is quite good. The length of the wavelet, however, appears to have a significant impact on the magnitude of the deconvolved output. It will likely be necessary to fix the number of data points for each wavelet to a uniform value and this must be investigated further before a working model can be implemented.

In an operational model, the deconvolved output could be used in two possible ways. First, it could be used in a nearest neighbours approach to establish the closest match between the penetrometer signal and the database of potential weak layers. The information about avalanche conditions associated with the highest ranked match could be used by the forecaster to help make a judgment regarding current conditions. Second, the deconvolved output could be assigned as a metric to indicate the likelihood of that point representing a weak layer. The probability density function describing the probability of a given output value representing a weak layer could be generated from a testing

set of known weak layers. This framework shares many similarities with an avalanche forecasting scheme presented by McClung and Tweedy (1994), although our initial focus is on forecasting the presence of weak layers rather than direct forecasting of avalanche occurrences. As with McClung and Tweedy's model, the posterior probability for group membership (in this case into weak layer/non-weak layer categories) could be modified using prior expert knowledge. Such knowledge could take the form of an expert opinion of how likely a weak layer was to be found in a given snowpack, a likely depth of burial or likely hardness characteristics of the weak layer and slab.

4.4.3 Discussion

Many researchers (Schneebeli and others, 1999; Pielmeier and Schneebeli, 2003b; Kronholm, 2004) have argued that a vertical resolution in the order of a few micrometres is necessary for reliable weak layer detection from force-resistance penetrometer signals. This is not disputed here at all, although it is argued that additional useful information can also be gleaned from the *shape* of the weak layer signal. Analyzing the shape of a penetrometer signal in this way may not require such high resolution measurements as those required for determining weak layers from micromechanical models.

Although very high resolution signals may not be required for this analysis, there is no reason why these methods could not be applied to higher resolution penetrometer data, such as that from the SMP, although code optimisation may be required to get the algorithm to run in a reasonable time. Also, the micromechanical information available could be combined with the shape analysis available from this method to further enhance weak layer detection. This might be achieved by altering the posterior probability of a layer being a weak layer based on a probability density function linking the micromechanical information to the probability of being a weak layer. Such an approach may also benefit the layer tracing method; in this case by weighting the position which most

closely matches the micromechanical characteristics of the layer being traced.

4.5 Predicting fracture character from penetrometer profiles

4.6 Introduction

Assessing the character of fractures identified in compression tests[1] has gained rapid acceptance among avalanche forecasting operations in Canada over the last five to ten years. van Herwijnen and Jamieson (2007a) showed that the interpretation of compression test results could be improved when information about the fracture character was included in the assessment. Jamieson and others (2007) found a correlation between the number of sudden fractures in a snow profile and the local avalanche danger. Fracture character refers to the style or quality[2] of the fracture, and the classification used in this study is by van Herwijnen and Jamieson (2007a), which has been adopted by the Canadian avalanche profession. This classification scheme is shown in Table 4.2.

Since different fracture characters are associated with different types of snow stratigraphy (van Herwijnen and Jamieson, 2007a), and the SABRE penetrometer is able to measure the force-resistance of the stratigraphy with high resolution, it is reasonable to expect that the fracture character of failure layers might be identified from penetrometer signals. To test this hypothesis, a fracture character comparison study study was undertaken, to compare penetrometer signals with the fracture character results from nearby compression tests. In this study, a univariate analysis is first used to assess a large number of potential predictor variables from the penetrometer signals. The most significant variables are then selected for use in a linear discriminant analysis, which is

[1] Although the fracture character classification was designed for, and built using, data from compression test results, it has been applied to (but not validated for) other types of small-column fracture tests, such as the hand shear test (Jamieson and others, 2008) and rutschblock test (Campbell, 2004).

[2] The American system for classifying compression test fractures is known as the shear quality classification (Birkeland and Johnson, 1999).

Table 4.2: Fracture character classification. From van Herwijnen and Jamieson (2007a).

Class	Abb.	Sudden/other	Description
Sudden planar	SP	Sudden	A thin planar* fracture suddenly crosses the column in one loading step *and* the block slides easily** on the weak layer.
Sudden collapse	SC	Sudden	Fracture crosses the column with a single loading step and is associated with a noticeable collapse of the weak layer.
Progressive compression	PC	Other	A fracture of noticeable thickness compression which usually crosses the column with a single loading step followed by a step by-step compression of the layer with subsequent loading steps.
Resistant planar	RP	Other	Planar* or mostly planar fracture that requires more than one loading step to cross the column and/or the block does not slide easily** on the weak layer.
Non-planar break	B***	Other	Non-planar, irregular fracture.

*Planar determined by straight, continuous, fracture lines on front and side walls of column.
**Block slides off column on steep slopes. On low-angle slopes, hold sides of the block and note resistance to sliding.
***B used as an abbreviation in this study. Note BRK is the official designation for Canadian operations (Canadian Avalanche Association, 2007, p.40).

used to classify portions of the penetrometer signals based on fracture character.

4.6.1 Method

Compression tests and penetrometer profiles were collected in close proximity to each other at a number of different sites during the winter of 2007-2008. Following the selection of a suitable test site, a manual snow profile was recorded (see Section 2.3.3) and two compression tests performed on the front wall of the snow pit. The basic method for undertaking a compression test has been described previously in Section 2.3.4. Depths to fracture interfaces were measured to the nearest 1 cm. To help assess the fracture character of a failure, two people were usually employed while performing a compression

test: an operator to tap the shovel and load the snow column, and an observer to assess the character of the fracture and record the results. It was found that the observer was often able to get into a better position for viewing fractures on the side of the snow column, allowing better judgement of the fracture character. In addition, having two people to witness fractures decreased the subjectivity of classifying the fractures.

The relative locations of the compression tests and penetrometer pushes used for the fracture character comparison study is shown in Figure 4.4. Three penetrometer pushes were performed approximately 30 cm upslope from the top of the compression test columns and were spaced approximately 30 cm apart; this distance was the minimum distance required to allow positioning of the depth measuring platform and also provided a small margin to guard from disturbances caused by cutting out the compression test column. The penetrometer pushes were performed immediately after the compression tests had been conducted to prevent temperature changes, caused by exposing the front wall of the snow pit to the air, from influencing snow hardness.

A total of 78 profiles was recorded, from 28 different site-days and 16 unique sites. For sites that were visited more than once on different days, care was taken to select a previously undisturbed site for the new set of measurements. Some profiles were discarded due to discrepancies in the depth signal (see Section 2.6.1). In order to prevent the same fracture being included in the analysis more than once, only one penetrometer push was interpreted from each site-day investigated. There were between one and seven fractures identified in each compression test. Sometimes, fractures only appeared in one compression test and not the other. When this occurred, fractures that were present in either test column were deemed to be interpretable in the penetrometer profile.

Identification of weak layers in the penetrometer signals was done manually, by looking closely at the shape of the penetrometer signal near the depth recorded for the fracture in the compression test. The depth to the top and the bottom of the weak layer for

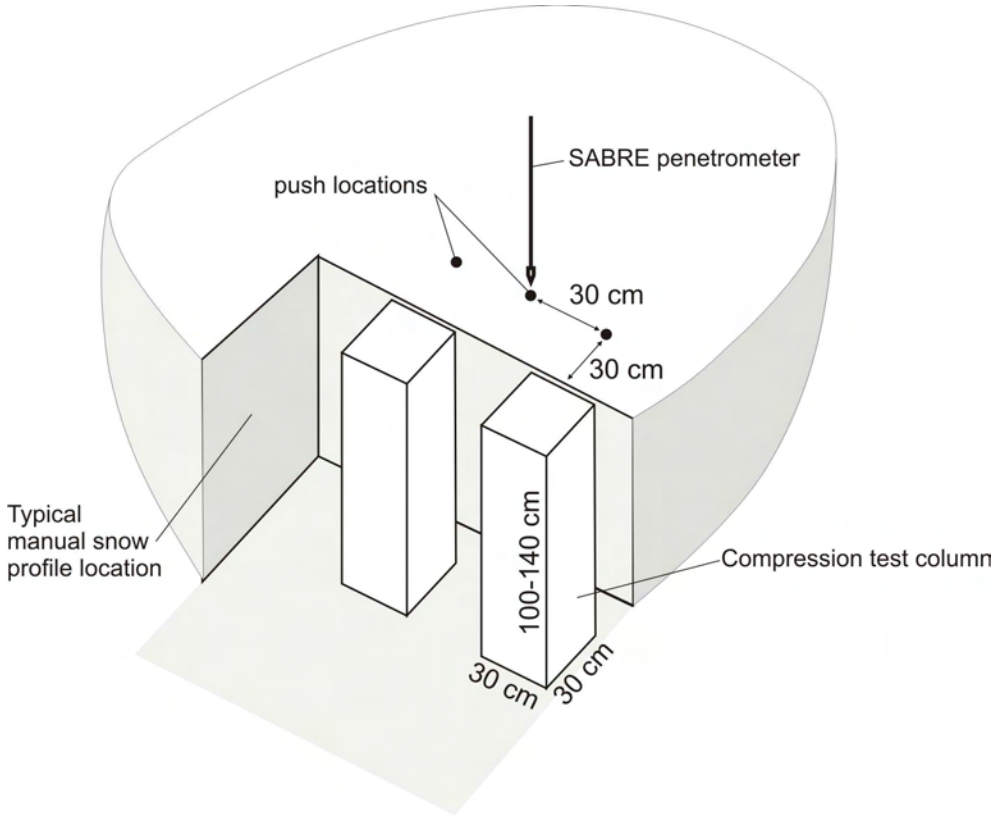

Figure 4.4: Schematic showing compression test geometry and penetrometer push locations for the fracture character comparison study. Depth measuring platform not shown.

each fracture was recorded. Interpretation was aided using the manual snow profiles. In many cases there was an obvious weak layer, with lower resistance compared to the surrounding snow. In others, this structure was not apparent; in these cases the fracture was considered to be at an interface, and the depths to the top and bottom were recorded as the same value (weak layer with zero thickness). For the remainder of this analysis, the term *weak layer* applies to both weak layers (with a thickness) and interfaces (without thickness).

Since the penetrometer depth accuracy was ±1 cm and the accuracy in assessing the fracture depths was ±1 cm, in the interpretation of the penetrometer signals, weak layer locations were permitted to vary 2 cm above and below the depth that was recorded in the compression test. This constraint was necessary to reduce the potential bias of

preferentially choosing certain feature shapes for certain fracture character classes.

Fractures in low resistance snow could not be interpreted due to the inability of the SABRE penetrometer to reliably distinguish hardness differences in snow of this type (see Section 2.6.2). Fractures that occurred in fist hardness and in some cases, 4-finger hardness snow were impossible to identify in the penetrometer signals and were excluded from the analysis.

In total, 83 weak layers/interfaces were identified in the penetrometer signals. Of these, 41 were resistant planar fractures, 20 were sudden collapse, 14 were non-planar breaks, seven were sudden planar, and 1 was a progressive compression. Due to the low numbers of sudden planar and progressive compression fractures, it was decided to combine the classes into *sudden* fractures (sudden collapse and sudden planar) and *others* (resistant planar, non-planar breaks and progressive compression); this grouping reflects the higher incidence of skier-triggered avalanches associated with sudden fractures (van Herwijnen and Jamieson, 2007a).

Four examples of interpreted penetrometer pushes are shown in Figure 4.5, with the corresponding compression test results indicated at each fracture location. Weak layers (with thickness) are shown with a horizontal grey bar, with the top of the bar representing the top of the weak layer and the bottom of the bar representing the bottom of the weak layer. Interfaces (with no thickness) are shown with a dotted grey line.

The 04-Feb-2008 surface hoar layer features in the first three of these profiles (Figure 4.5a, b and c). Although these profiles were taken at different sites, it is interesting to note that as the depth of burial increased, the stiffness of the slab immediately above this weak layer increased. This weak layer was also associated with avalanches that occurred near to the sites investigated either on or close to the date the profile was gathered. The avalanche associated with the Bostock Traverse site was a remote triggered size 3 avalanche, triggered from 150 m away. The size and nature of this avalanche was due to

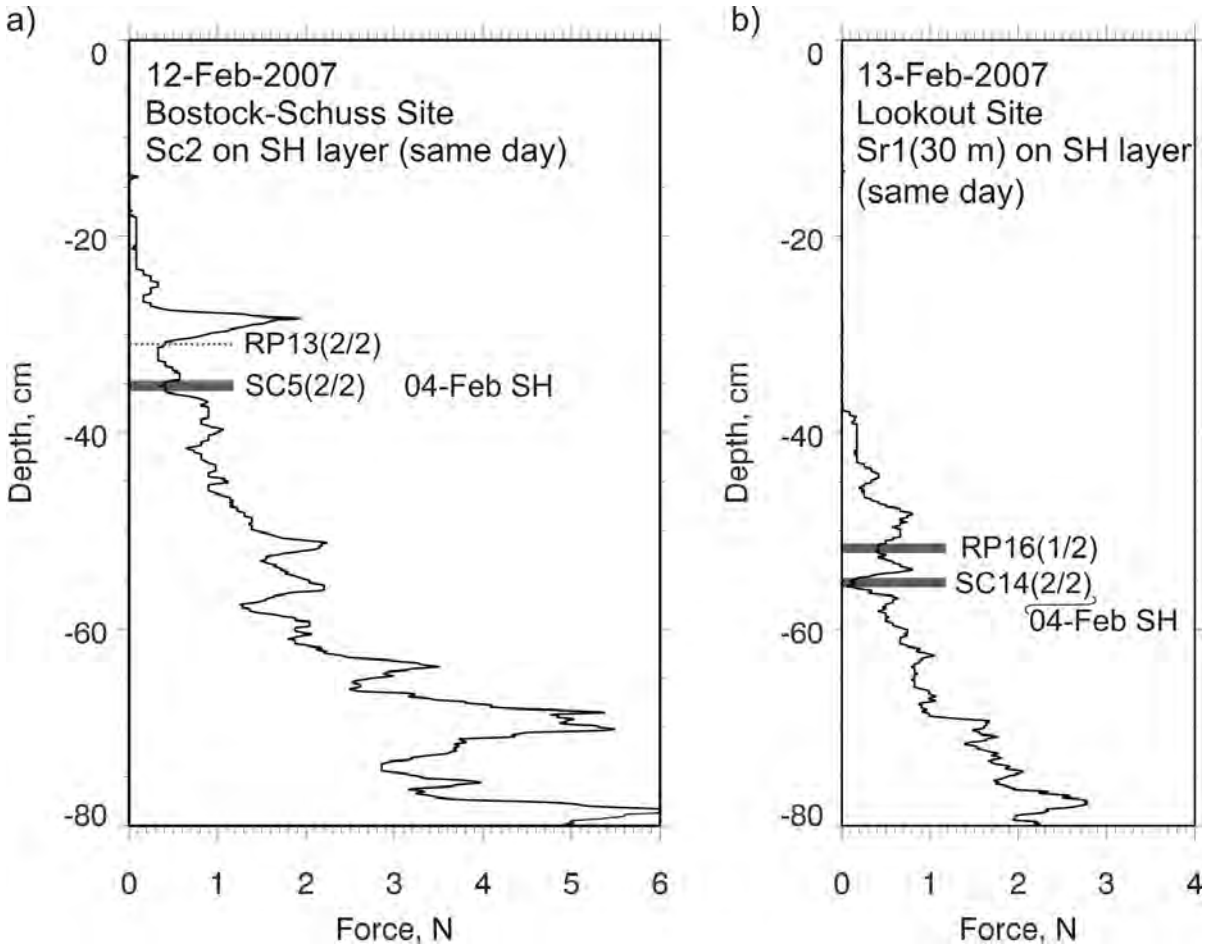

Figure 4.5: Compression test fracture locations interpreted onto four penetrometer pushes. Weak layers (with thickness) shown with a grey bar; interfaces (with no thickness) shown with a grey dotted line. Local avalanche observations noted: a) Bostock--Schuss site—skier controlled size 2 (Sc2); b) Lookout site—skier remote size 1 from 30 m (Sr(30)); c) Bostock Traverse site—recent skier remote size 3 from 150 m (Sr(150)); and d) Gopher Butte site—no recent local avalanche observations.

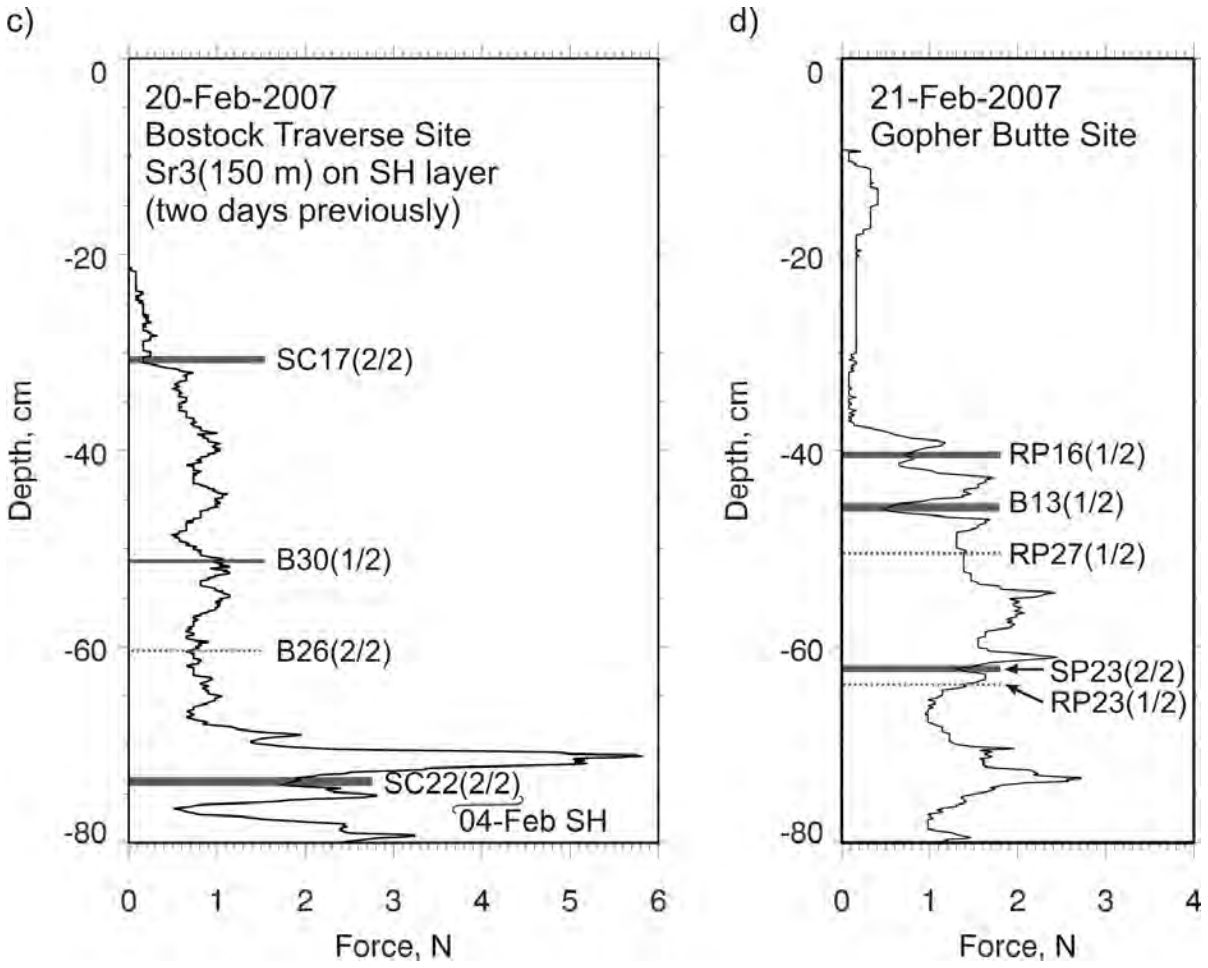

Figure 4.5 continued.

the well preserved surface hoar crystals that made up the weak layer, but it was likely aided by the relatively stiff lower slab just above the weak layer that is evident in the penetrometer profile. The 04-Feb-2008 surface hoar layer is not visible in this profile from the Gopher Butte site (Figure 4.5d). Of note is the break at about 46 cm, which appears to be associated with a prominent weak layer. When interpreting this profile, this layer may well appear to resemble the shape that might be expected from a sudden collapse fracture. It is possible that small scale variability meant that had the compression test been performed at this exact site, a sudden collapse fracture would have resulted. It is also possible that the penetrometer signal alone is insufficient for uniquely identifying all types of fracture.

4.6.2 Univariate analysis

A number of variables describing the fracture weak layer or interface were extracted from the penetrometer signals. These variables are listed in Table 4.3. In the variable names given, an "A" in the name means that the parameter was assessed above the top of the weak layer, over a distance in mm given by the proceeding number. A "B" in the name means that the parameter was assessed below the bottom of the weak layer, again over the given distance in mm.

Box plots of the interquartile range (IQR) for each of the variables are shown in Figure 4.6, separated into fracture character groups (sudden or other). Outliers, defined as values lying between distances of 1.5(IQR) and 3(IQR) from the hinges of the box plot, and extreme values, defined as values greater than a distance of 3(IQR) from the hinges, are shown in the plots. Non-outlier maximum and minimum values are also shown. t and p statistics for the separation of group means are shown in Table 4.3. A positive t value indicates that the other group mean is higher than that of the sudden; a negative t value indicates that the sudden group mean is higher.

The univariate plots were analyzed to try to determine which variables contribute to discriminating between the sudden and other fracture character groups. The following variables are described:

Weak layer depth (WL_D)

Weak layer depths varied from 8 to 114 cm. The plot of WL_D against fracture character in Figure 4.6 shows the median depth for sudden fractures to be 60 cm compared to 40 cm for other fractures. The upper hinge of the IQR is the same for both groups, although the lower hinge of the IQR extends to a greater depth for sudden fractures. Since many fractures that occurred in the upper portion of the snowpack were removed from the analysis, only the lower hinge can be reliably interpreted. It suggests that sudden

Table 4.3: Variables used in the fracture character comparison analysis. t and p statistics shown for the separation of *sudden* and *other* group means (n=83 for each variable).

Variable name	Units	t	p	Description
WL_D	cm	2.70	0.009	Weak layer depth
WL_Thick	mm	-4.84	<0.001	Weak layer thickness
WL_H	N	-1.36	0.177	Mean weak layer hardness
Ratio_Slab_WL_10A		-1.69	0.095	Ratio of mean slab hardness to mean weak layer hardness. Mean slab hardness calculated over 10, 20, 50, 100 and 200mm above the top of the weak layer.
Ratio_Slab_WL_20A		0.74	0.464	
Ratio_Slab_WL_50A		1.16	0.248	
Ratio_Slab_WL_100A		1.19	0.238	
Ratio_Slab_WL_200A		1.11	0.271	
Avg_Grad_1A		1.52	0.132	Average hardness gradient over a distance of 1, 5, 10, 20 and 50 mm above the top of the weak layer.
Avg_Grad_5A		2.47	0.016	
Avg_Grad_10A	N mm^{-1}	3.03	0.003	
Avg_Grad_20A		3.14	0.002	
Avg_Grad_50A		3.18	0.002	
Avg_Grad_1B		-1.94	0.056	Average hardness gradient over a distance of 1, 5, 10, 20 and 50 mm below the bottom of the weak layer.
Avg_Grad_5B		-2.09	0.039	
Avg_Grad_10B	N mm^{-1}	-1.99	0.050	
Avg_Grad_20B		-2.44	0.017	
Avg_Grad_50B		-2.31	0.024	
Max_Grad_1A		-2.14	0.035	Maximum hardness gradient over a distance of 1, 5, 10, 20 and 50 mm above the top of the weak layer.
Max_Grad_5A		-2.30	0.024	
Max_Grad_10A	N mm^{-1}	-2.23	0.028	
Max_Grad_20A		-2.76	0.007	
Max_Grad_50A		-2.11	0.038	
Max_Grad_1B		-3.53	0.001	Maximum hardness gradient over a distance of 1, 5, 10, 20 and 50 mm above the top of the weak layer respectively.
Max_Grad_5B		-3.79	<0.000	
Max_Grad_10B	N mm^{-1}	-2.87	0.005	
Max_Grad_20B		-3.22	0.002	
Max_Grad_50B		-3.38	0.001	

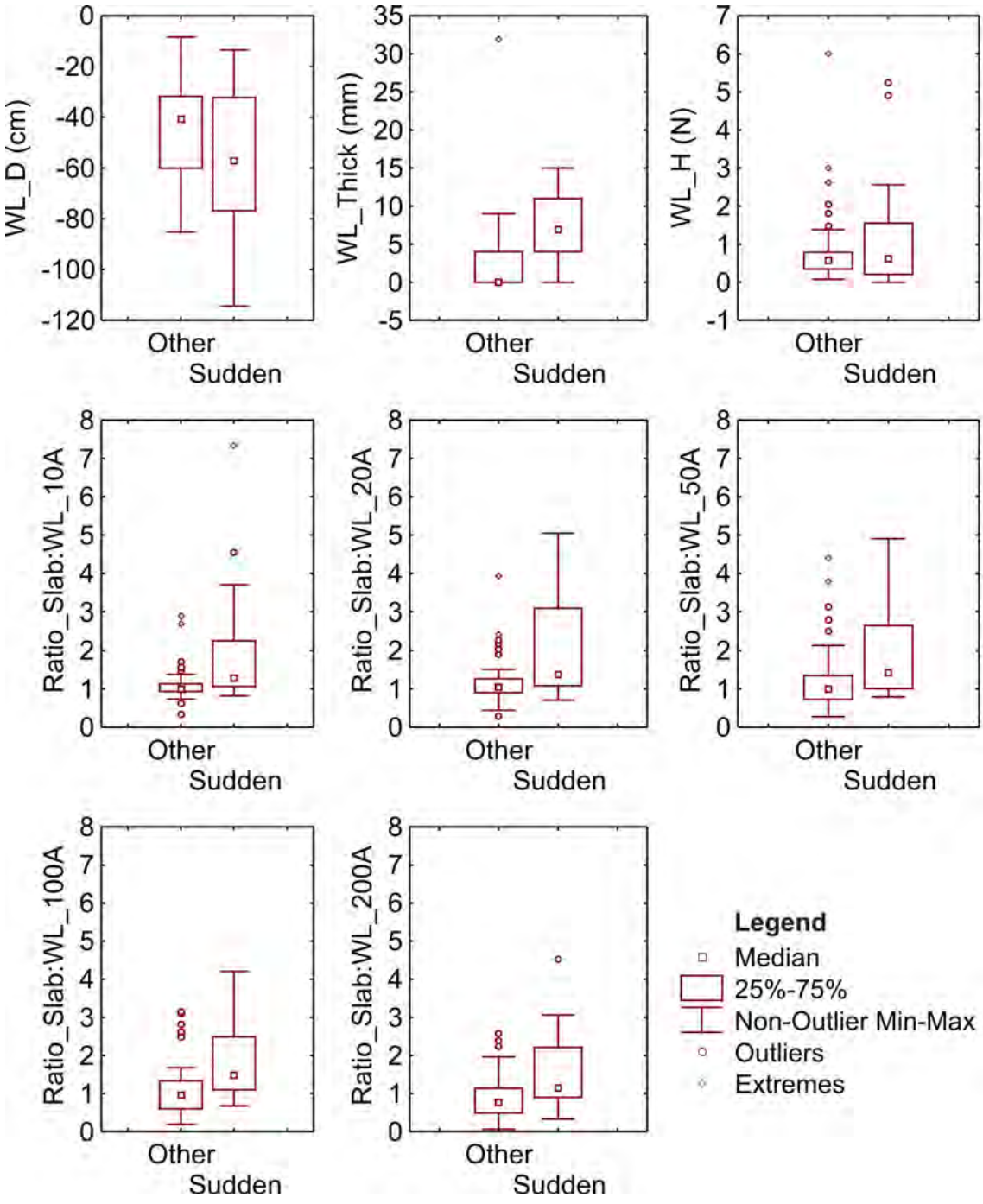

Figure 4.6: Univariate plots of the variables shown in Table 4.3 for *sudden* and *other* fracture character groups.

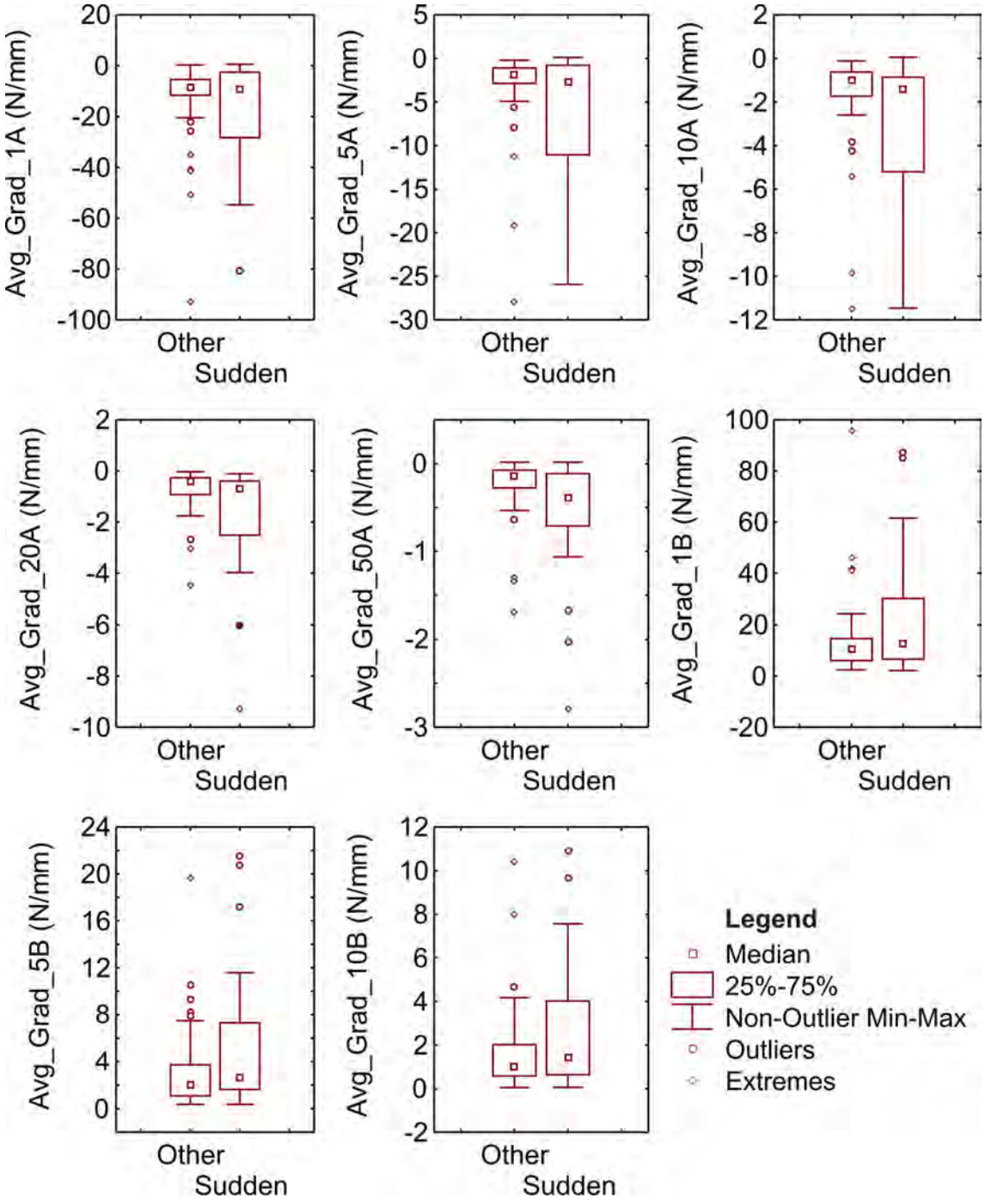

Figure 4.6 continued.

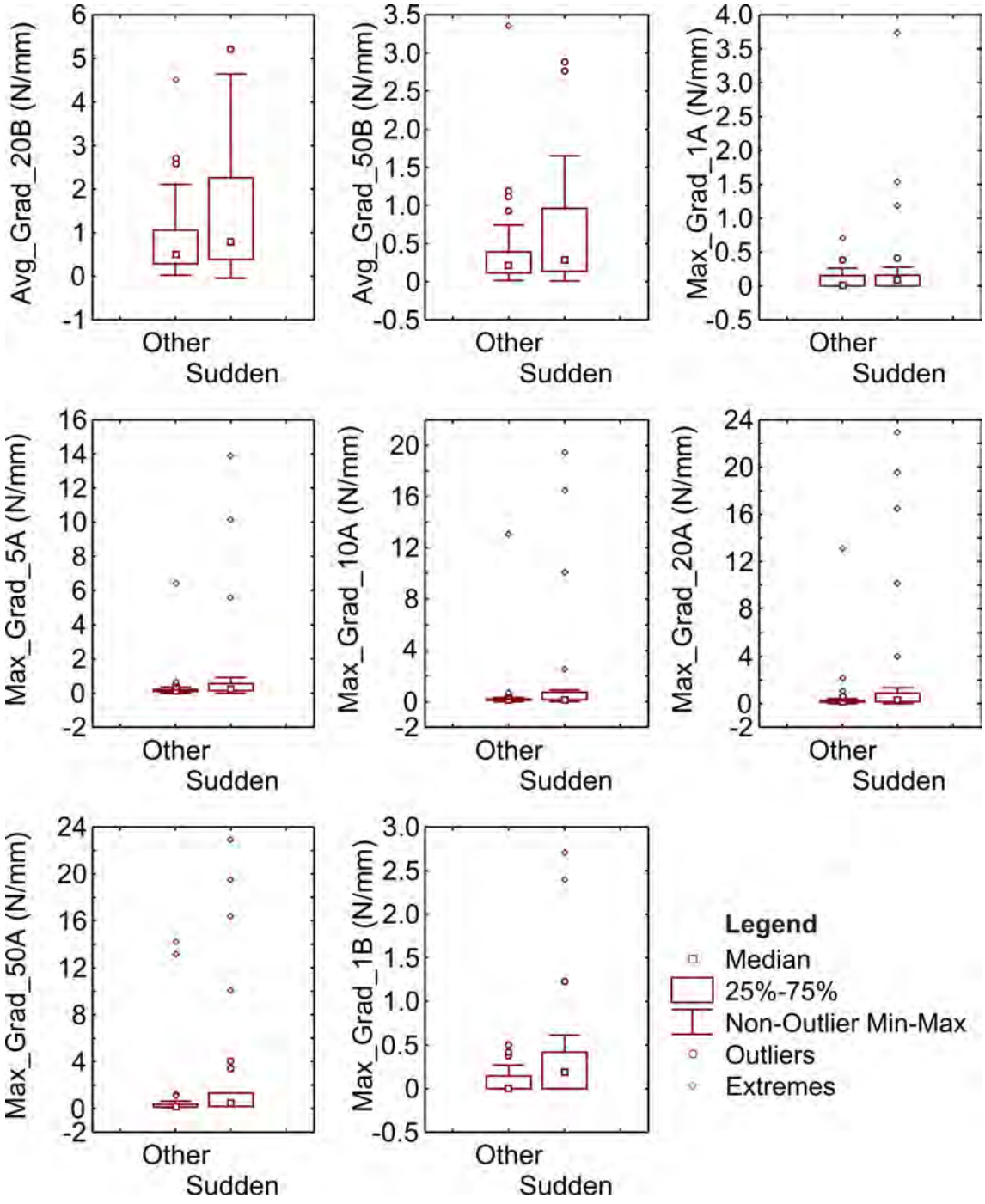

Figure 4.6 continued.

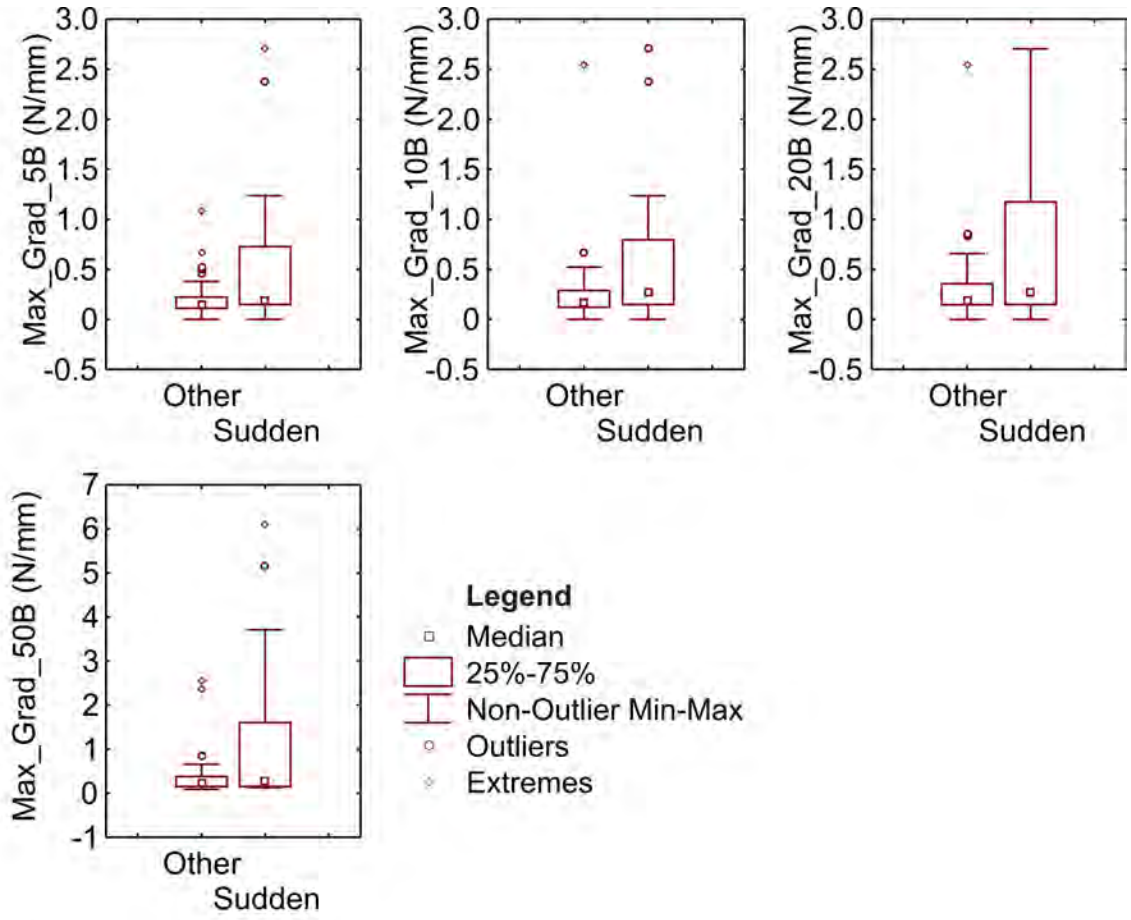

Figure 4.6 continued.

fractures are more likely to persist to greater depths compared with other fractures. From Table 4.3, group means for this variable were significantly different at α=0.05.

Weak layer thickness (WL_Thick)

The box plot of WL_Thick in Figure 4.6 shows the median weak layer thickness for sudden fractures to be 7 mm with an IQR from 4 to 11 mm. For other fractures, median weak layer thickness is 0 mm with an IQR from 0 to 4 mm. This variable offers good discrimination into the two fracture character classes, and t=-4.84 (p<0.001) indicates group separation is highly significant at α=0.05. These values are apparently different from those reported by van Herwijnen and Jamieson (2007a), who found the median weak layer thickness to be 6 mm for SC fractures, 11 mm for RP fractures and 8 mm for B

fractures. However, van Herwijnen and Jamieson used the total thickness of the layer in which the fracture occurred, even if the actual fracture was very thin and only accounted for a small fraction of the thickness of that layer. In contrast, this study uses the extent of the weak layer or interface, although there was some subjectivity in interpreting weak layer thickness from the penetrometer profiles.

It is likely that the greater thickness found for sudden fractures was caused in part by the larger number of SC fractures in the sudden group compared to SP fractures. In addition, the SC fractures were dominated by one particular weak layer, the 04-Feb-2007 surface hoar layer, which was a particularly thick and widespread weak layer; surface hoar crystals of up to and in some cases exceeding 30 mm were found in this layer at some sites.

Mean weak layer hardness (WL_H)

The box plot of WL_H in Figure 4.6 shows median WL_H for both sudden and other fractures to be 0.7 N, which indicates that there is no overall tendency for sudden fractures to occur in less resistant snow. This is confirmed by the insignificant t test result (t=-1.36, p=0.177). The IQR is greater for sudden fractures, indicating that sudden fractures occur over a greater range of snow hardness compared with other fractures.

Ratio of slab:weak layer hardness (Ratio_Slab:WL_A)

Comparing the 5 box plots of Ratio_Slab:WL_A in Figure 4.6, for all slab thicknesses, the ratio of slab hardness to weak layer hardness is higher for sudden fractures compared to other fractures. For slab thicknesses of 10, 20, 50 and 100 mm, the median ratio lies between 1.3 and 1.5 for sudden fractures and 1.0 for other fractures. For a slab thickness of 200 mm, ratios are lower for both groups, with sudden fractures having a ratio of 1.1 and other fractures having a ratio of 0.7.

This suggests that the layer above weak layers associated with sudden fractures are

harder than those associated with other fractures. However, none of the group separations for these variables were significant at α=0.05 (Table 4.3). This slightly surprising result indicates that the ratio of slab hardness to weak layer hardness may not offer discrimination between sudden and other group membership.

Average hardness gradient above/below (Avg_Grad_A/B)

From the 10 box plots of Avg_Grad_A/B in Figure 4.6, average hardness gradients above the weak layer are generally negative (i.e. decreasing hardness with increasing depth) while average hardness gradients below the weak layer are generally positive (i.e. increasing hardness with increasing depth). This is expected by virtue of the weak layers being weak (i.e. having lower resistance compared with the surrounding snow).

As the distance away from the weak layer increases, both above and below the weak layer, average hardness gradient magnitudes decrease. This is expected, since for most of the signals analyzed, the penetrometer signal flattened off at some distance away from the weak layer. Differences between group means for average hardness gradients above the weak layer were significant for 5, 10, 20 and 50 mm (Table 4.3).

The main trend common to all the average hardness gradients above the weak layer (1, 5, 10, 20 and 50 mm) is that the range of gradients associated with sudden fractures is greater than for other fractures. Median values have a greater magnitude for sudden fractures. There are a considerable number of outliers, especially for the other group; in many cases, these overlap with the non-outlier min-max for the sudden group. This indicates that the discriminatory power of these variables may not be that high.

The trend for the average hardness gradients below the weak layer follows the same pattern as the gradients above the weak layer, except for the fact that the absolute values of the gradients are positive rather than negative. Differences between group means for average hardness gradients below the weak layer were significant for 5, 20 and 50 mm

(Table 4.3).

Maximum hardness gradient above/below (Max_Grad_A/B)

From the box plots of Max_Grad_A/B in Figure 4.6, the IQR for maximum hardness gradients above the weak layer shows values of greater range and magnitude for sudden fractures compared to other fractures, except when the gradients are assessed over a distance of 1 mm. A similar trend is observed for gradients below the weak layer. This trend could be explained by the fact that sudden fractures may be more likely to be associated with weak layers that show a pronounced hardness change in the penetrometer signal. Sudden/other group separation was significant for all maximum hardness variables above and below the weak layer (Table 4.3).

The maximum hardness gradient plots show a considerable number of outliers and extreme values. These are especially prominent for maximum hardness gradients above the weak layer for larger distances away from the weak layer. In some cases, these values may be due to irregular fluctuations in the penetrometer signal, or, for larger distances away from the weak layer, they may be due to features in the snowpack that are not necessarily related to the fracture weak layer or interface.

Variables selected for the discriminant model

The following variables were selected for the discriminant model, based on having significant t test scores and showing good discriminatory power in the box plots: WL_Thick, Avg_Grad_20A, Avg_Grad_20B, Max_Grad_20A and Max_Grad_5B. In order to reduce collinearity, only one variable from each group of variables was selected.

4.6.3 Discriminant analysis

A linear discriminant analysis (e.g. Manly, 1994, p.107) was performed using the variables selected from the univariate analysis in the previous analysis. Discriminant analysis seeks

to find a linear combination of the predictor variables, $Z = A_1X_1 + A_2X_2 + \ldots + A_mX_m$, that exhibits the largest difference between group means relative to the within-group variance.

For discriminant analysis, it is advantageous to use group sizes that are approximately equal. This ensures that the a-priori probability of predicting sudden group membership is the same as predicting other group membership, and should result in parity between classification rates for the two groups. Equal group size was achieved by eliminating records from the other category using a random number generator. Out of an original 110 data points, only 54 were selected: 27 for each group. Due to the small group sizes, a leave-one-out cross-validation approach was used for independent validation of the model.

A condition for discriminant analysis is that the within-group covariance should be the same for both groups. This was tested using Box's M test, which tests the null hypothesis that the covariances do not differ. Values of Box's M=460 with $p<0.001$ were obtained, which suggests that the covariance is not the same for both groups. However, Manly (1994, p.112), points out that excellent discrimination may be still possible despite violations of this condition, although statistical significance of group separation may not be valid. StatSoft (2007) points out that Box's M test is particularly sensitive to deviations from multivariate normality, and should not be taken too "seriously". Tabachnick and Fidell (2007, p.252), citing Hakstian and others (1979), agree with this assessment and further add that if sample sizes are equal, which in this case they are, then robustness of the significance tests is expected, even if Box's M is significant at p=0.001. It is likely, therefore, that the analysis is not compromised by this deviation from the homogeneity of the covariance matrix, and the analysis may proceed.

Group separation is indicated using Wilks' Lambda (e.g. Wilkinson, 1990, p.270), which is the ratio of within-groups sums of squares to the total sums of squares. It takes a value between 0 and 1 with a value near 0 indicating that the (multivariate) group

means are different and a value near 1 indicating that group means are the same. For this analysis, Wilks' Lambda=0.43, which is encouraging, as it indicates reasonable group separation between sudden and other fractures. The associated F statistic is 5.4, with p=0.007, which indicates (despite warnings from Manly) that group separation is likely to be significant at α=0.05.

The standardised discriminant function weights and the factor structure coefficients (loadings) are shown in Table 4.4. The discriminant function weights denote the unique (partial) contribution of each variable to the discriminant functions, while the structure coefficients denote the simple correlations between the variables and the functions; therefore, the structure coefficients are more appropriate for substantive interpretations of the functions (StatSoft, 2007). In both cases, a positive value indicates positive correlation with sudden fractures, whereas a negative values indicates positive correlation with other fractures.

Table 4.4: Discriminant analysis function coefficients for determining sudden/other group membership.

Factor	Standardised discriminant function weights	Factor structure coefficients
WL_Thick	0.80	0.59
Max_Grad_5B	0.61	0.51
Avg_Grad_20A	-0.17	-0.42
Avg_Grad_20B	0.35	0.36
Max_Grad_20A	0.02	0.32

From the factor structure coefficients in Table 4.4, it is clear that weak layer thickness contributes the most to group separation, with thick layers selecting for sudden fractures. This has an intuitive explanation that thick weak layers are associated with sudden collapse fractures, which account for the bulk of the sudden fractures. It is possible that some sudden planar fractures may also be associated with relatively thick weak layers, although not sufficiently thick to be classified as sudden collapse. In view of this, it

would be interesting to repeat this analysis with a data set containing a larger number of sudden planar fractures.

The variable that contributes the next most in terms of group discrimination, maybe surprisingly, is the maximum hardness gradient up to 5 mm below the weak layer. For this variable, the absolute value for the maximum was used, so the positive value means that a greater maximum hardness gradient selects for sudden fractures. The average hardness gradient 20 mm below the weak layer also contributes to discrimination, although to a lesser extent. These two variables combined indicate that a stiffer substratum may favour sudden fractures.

The effects of substratum properties have not been as extensively investigated as slab properties. Recently, Habermann and others (in press) have shown, using simulations of static skier loading, that skier induced stress at the weak layer is greater when hard layers or crusts are found below the weak layer than when they are found above it. This result agrees with previous results from Jamieson and others (2001), who found that deep, persistent weak layers (the fracture character was not recorded, but it might be reasonable to assume that it was sudden) persisted for longer when the substratum was stiff; also with field studies by Savage (2007), who noted that all large, deep avalanches in the study area were associated with very stiff substratums. However, this result was not detected in an earlier study by Schweizer and Jamieson (2003), who found that a pronounced hardness difference was important for distinguishing stable profiles from unstable profiles, but that the sign of the hardness change did not matter.

It should be noted, however, that Habermann and others simulations involved calculating the applied stress at the weak layer; therefore it is likely that these results pertain mainly to fracture initiation. Fracture character, on the other hand, is regarded to be more associated with fracture propagation. Schweizer and Camponovo (2001) suggested that fracture propagation depends on the difference in stiffness between the weak layer

and both adjacent layers. van Herwijnen and Jamieson (2007b) argue that an increase in the hand hardness difference between the weak layer and adjacent layers indicates a decrease in the relative modulus of the weak layer, which increases the fracture energy at the weak layer interface. Their data showed a significant correlation between high fracture propagation propensity and the hardness difference between the weak layer and the layer above; however, the correlation with the hardness difference between the weak layer and the layer below was insignificant. Therefore, current models of fracture propagation assume that the hardness of the substratum is important, although so far, data to back that claim up are lacking. The results of this study lend weight to there being a link between the substratum hardness and propensity for sudden fractures in compression tests.

Both the average gradient and the maximum gradient 20 mm above the weak layer also contribute to group separation, with factor loadings of -0.42 and 0.32 respectively (Table 4.4). The negative value for the average gradient is associated with the negative average gradient values above the weak layer (generally a decrease in hardness with an increase in depth); so a higher negative value still indicates that higher values are associated with sudden fractures. These variables relate to the generally accepted view that a stiffer layer of snow above the weak layer is important for fracture propagation (van Herwijnen and Jamieson, 2007a).

The discriminant function was used to classify the weak layer/interfaces identified in the penetrometer signals into sudden or other fracture character groups. During the leave-one-out cross-validation method used in this analysis, the discriminant analysis function was built N times, where N is the number of weak layer records from the equalised data set (N=54). On each occasion, one record was withheld and classified using the function built without using that record. As a result, the exact coefficients for the discriminant functions built during the test would have varied slightly from those shown in Table 4.4.

Table 4.5 shows the results of the classification. 77.8% of sudden fractures were correctly classified and 81.5% of other fractures were correctly classified. The overall prediction rate was 79.6%. Classification parity was good between the two groups.

Table 4.5: Classification matrix for predicting fracture character from principle components of the penetrometer signal variables. Results in parentheses show actual numbers.

Class	Sudden	Other
Sudden	(21) 77.8%	(6) 22.2%
Other	(5) 18.5%	(22) 81.5%
Overall classification rate: 79.6%		

4.6.4 Discussion

This is a promising result, although some limitations and cautions must be stated. The model was built and tested using pre-identified weak layers. It has not been tested for the general case of being able to identify a potential fracture with no prior information about the depth to a potential failure interface. In order to build this kind of model, an additional category of *no fracture* would need to be created, which could be populated with random sections of the penetrometer signal not associated with compression test fractures in the training set of profiles.

The sample size was fairly small and the sudden fractures were predominantly associated with one weak layer, the 04-Feb-2008 surface hoar layer. As such, the model is likely to be detecting largely for sudden collapse fractures. More penetrometer pushes in snowpacks with sudden planar fractures are needed to reliably test the model's ability to predict this kind of fracture.

There was a strong possibility for bias when interpreting the fractures in the penetrometer profiles. Since the fracture character of the layer that was being interpreted in the penetrometer pushes was known, there was a tendency to select certain features in the penetrometer signal that were perceived to be associated with that type of frac-

ture. In this way, the model is more likely to predict features that were actively selected during the interpretation. Since it is expected that certain types of fracture, (especially sudden collapse fractures), have a characteristic penetrometer signal, this bias is hard to overcome. It was limited to some extent by the constraint on varying the depth. Further improvements in the depth accuracy of the penetrometer or in assessing the depth of the fractures in compression tests would allow a tighter constraint on the depth location and further reduce this bias. Another possible way to reduce this bias would be to interpret the penetrometer signals without knowing the fracture character of the compression test failures.

4.7 Conclusions

A method for tracing layers across a transect of penetrometer signals has been presented. This method was successful in tracing layers across the transect in 13 out of 15 cases tested. The layer tracing algorithm performed well for crusts, as well as for weak layers and other interfaces that were not positioned near to a crust. For weak layers and other interfaces near to a crust, it may be more appropriate to trace the crust and infer the layer/interface of interest from the position of the crust.

Although the layer-tracing results presented here are initial results, additional experience using the layer tracing algorithm for tracing layers across penetrometer profiles used in spatial variability studies (Chapter 5) was in broad agreement with the results presented here. Further work optimising the pre- and post-processing filtering may further enhance the layer tracing ability.

A framework for extending this method to the problem of generic detection of weak layers in penetrometer signals has been presented. The next step will be to build and test the weak layer detection model. This will require populating a database with several

known weak layers identified in a range of different penetrometer profiles. The influence of wavelet length on the deconvolved signal output needs to be investigated further before this model can be implemented.

Although the layer tracing and layer detection methods were designed for use with data from a force-resistance penetrometer, there is no reason why they could not also be applied to high-resolution penetrometer signals from other snow properties, such as capacitance and optical reflectivity.

A method for predicting the broad fracture character groups (sudden or other) from penetrometer signals has been presented, based on a multivariate statistical analysis of penetrometer signals interpreted against fracture character results from nearby compression tests. Using a leave-one-out cross-validation method, overall classification rates of approximately 80% were achieved. Weak layer thickness, maximum hardness gradient 5 mm below the weak layer and the average hardness gradient 20 mm above the weak layer contributed the most to discriminating between the two groups.

The layers were pre-identified as being associated with compression test fractures; this model is expected to perform far less well in the general case when layers have not been matched to compression test results. In order to formulate the model for application in this general case, a third, *no fracture* category would be required.

Results for the sudden category were almost certainly biased towards sudden collapse fractures, which dominated the data set used in this study. More observations are necessary to be able to distinguish between sudden collapse and sudden planar fractures in the sudden category, as well as between the resistant planar, progressive compression and non-planar break fractures within the other category.

Chapter 5

Case studies of spatial variability

5.1 Introduction

The physical properties of the alpine snowpack are highly variable in both time and space. Snow strength depends on various physical properties (e.g. Mellor, 1965), and the formation of slab avalanches depends on the failure, in a mechanical sense, of the snow in the weak layer, for a given applied stress. Therefore, it is reasonable to assume that variations in snowpack properties translate into variations of snow stability. Since the variability of snowpack properties generally exceeds the ability to measure and detect these variations, snowpack variability, and by extension, snow stability variability, is often considered to be an inherent property, which must be dealt with using a probabilistic approach (Sommerfield, 1980).

This probabilistic approach to stability evaluation over terrain is especially important for backcountry travelers, for whom even obtaining a limited number of snowpack property observations may be detrimental to other valid objectives, such as enjoying an unbroken ski run, or covering a certain amount of distance to find shelter to prevent being stranded outside after nightfall. It is suggested that over time, practitioners develop mental images (Reisberg and Chambers, 1991) of how the snowpack varies over different terrain features, and this assists with assessing snow stability over terrain features. These mental images are built from: field evidence, such as seeing rocks uncovered in thin snow cover areas; prior field testing, such as previous probing of snow depths in a similar area, or digging snow pits or trenches in areas associated with variability; training, either formally or informally, learning about snowpack variability from others;

and occasionally from direct experience, witnessing or being caught in an avalanche and then assessing the nature of the snowpack variability from the shape, depth and hardness variations along the crown and flanks of the avalanche. For the training component, case studies showing how snowpack properties vary over terrain might be very important for improving a forecaster's ability to integrate spatial variability into stability assessments.

Several transects of penetrometer profiles are presented in this study over different terrain features at different scales. The novel approach here is the systematic surveying of terrain features where variability is expected; most previous studies have focussed on slopes with relatively uniform snowpack properties. Although these transects were taken in specific areas with specific snowpack characteristics, it is argued that the variability in layer depths and hardness is indicative of more general patterns of variability that can be expected for similar features in other areas, or for the same feature at a different time (as long as snow conditions are not too different). When transects are done over representative features, they can be thought of as identifying characteristic signatures of variability over terrain. In order to properly characterise these signatures, more transects or grids of profiles will be necessary over a range of features in different snow climates. The set of transects presented here represents a good start to this characterisation using digital penetrometer technology, and is the first study to present transects of penetrometer profiles over a wide range of alpine terrain features.

The transects are presented in a similar manner to seismic profiles; when adjacent profiles are aligned, the spatial structure of the layers becomes apparent from the signal traces. The spatial structure is analyzed for some transects using geostatistical methods, and in some cases, the observed trends are related to causal processes.

5.2 Literature review: Spatial variability of snow

5.2.1 Scale issues

Blöschl and Sivapalan (1995); Blöschl (1999) introduced the notion that a scale triplet was applicable for measuring the spatial (and temporal) distribution of hydrological processes, comprising of: extent, spacing and support. Extent (in the spatial domain) refers to the total area or volume assessed by the survey. Spacing refers to the distance between measurement points. Support refers to the area or volume associated with an individual data measurement. Haegeli and McClung (2003) recognised the importance of this concept when matching the input data scale with the output data scale for numerical forecasting models, and suggested that the quality of the model output could be significantly reduced if these scales were not in agreement.

The concept of spacing has a direct analogy with the idea of sampling in signal analysis. It is commonly known that the highest measurable frequency is half the sampling frequency (e.g. Ifeachor and Jervis, 1993, p.18). In the time domain, this is known as the Nyquist frequency (Grenander and Cramér, 1959, p.316); in the spatial domain, the equivalent is the Nyquist wavenumber (equal to half the sampling wavenumber). Both Nyquist frequency and Nyquist wavenumber can be restated in terms of the sample spacing; they are equivalent to the reciprocal of twice the sample spacing.

McClung and Schaerer (2006), based on LaChapelle (1980), described three spatial operating scales for avalanche forecasting: synoptic (at the scale of a mountain range: $>10^4$ km^2); meso-scale (a highway or ski-area scale: $>10^2$ km^2); and micro-scale (avalanche path or terrain feature scale: <10 km^2). Kronholm (2004) refined this scheme, adding several further classes. Kronholm's revised process scale is shown in Table 5.1.

In this study, the term *feature-scale* is adopted to refer specifically to terrain features, such as a gully or wind ridge, that form a component of the potential avalanche slope. As

such, the length range for this scale is at the lower end of that of the slope-scale length range defined by Kronholm.

Table 5.1: Scales applicable to snow processes associated with avalanche formation. After Kronholm (2004).

Scale	Description	Length
Grain-scale	Microstructural elements in the snow, e.g. grains and grain clusters.	10^{-4}–10^{-2} m
Layer-scale	Typical snow layer thickness.	10^{-2}–10^{-1} m
Snowpack-scale	Typical depth of the snowpack.	10^{-1}–5 m
Slope-scale	Typical avalanche slope. Wind redistribution possible at this scale.	5–10^{2} m
Basin-scale	Basin or mountain containing slopes of different aspects, inclinations and elevations.	10^{2}–10^{3} m
Mountain range	Synoptic scale influences on snow cover.	10^{4}–10^{5} m

5.2.2 Regional-scale variability

Researchers have recognised that synoptic-scale weather patterns give rise to regional variations in snow cover, which results in corresponding regional patterns of avalanche activity. Roch (1949) classified the Western United States into three snow climate zones: Coastal Alpine, adjacent to the Pacific Coast; Middle Alpine, or transitional to the east of the Coast Range; and High Alpine, or Rocky Mountain climate associated with the Rocky Mountains that lie further in the interior. LaChapelle (1966) described the most prevalent meteorological conditions for each climate zone: relatively mild and wet for the Pacific Coast; generally colder for the transitional, or intermountain zone, but still with high amounts of precipitation; and cold and dry for the Rocky Mountains. He also described a fourth climate zone, the coastal transition zone, with mild temperatures but slightly lower than those of the Pacific coast, and with with slightly less precipitation.

Armstrong and Armstrong (1987) quantified ranges for the amount of precipitation, snow cover depths and temperatures associated with Roch's classification, adopting the terms "maritime", "intermountain" and "continental" to refer to the respective climate

zones. Mock and Birkeland (2000) reviewed these classifications using an extensive 25 year record of meteorological and avalanche data and concluded that, whereas generalisations of regional snow cover distributions are usually fairly applicable, occasional winters produced unusual snow cover distributions that would normally be associated with a different snow climate zone. Other studies (LaChapelle and Armstrong, 1976; Mock and Kay, 1992; Mock, 1995) present more detailed descriptions of variations in snow within certain regions of the USA.

In Canada, McClung and Tweedy (1993); McClung and Schaerer (2006) adopted the same snow climate zones as Armstrong and Armstrong, but used the term "transitional" to describe the intermountain zone. Haegeli and McClung (2003) conducted a regional study of the transitional zone and found that in Canada, this zone has a strong maritime component. They also found that about 45% of avalanches associated with persistent weak layers ran on facet–crust combinations and about 50% ran on surface hoar. They noted that a lack of high-elevation historical meteorological data in Canada is a limitation for determining regional snow climate trends.

5.2.3 Factors important for snowpack variability

Several authors have suggested that wind is a very important source of spatial variability. Seligram (1936) devoted several chapters to describing the effects of wind erosion, transport, and deposition, including wind-packing resulting in the formation of slabs conducive for avalanche formation. Atwater (1954) lists wind as the eighth (out of ten) factors for avalanche formation but states, "The eighth factor is wind action, and it is the most important and versatile of all." Conway and Abrahamson (1984) suggested that wind might be a key factor in explaining significant variations in snow strength.

Male and Gray (1981) describe the significant variations of solar radiation that occur for varying slope angles, aspect and time of year. The impact of aspect variations on

near surface warming was investigated by Bakermans (2006), who found that there was a significant increase in daytime warming for more southerly aspects in the top 30 cm of the snowpack. This increase was less pronounced when there was considerable cloud cover.

McClung and Schaerer (2006, p.114) indicate that ground roughness increases the strength of a slope by anchoring the snowpack until the snow is deep enough to cover the features with a smooth surface. At that point, high temperature gradients associated with the relatively low snow depths over these features can promote facet or depth hoar growth, leading to instabilities. Logan (1993) found that temperature gradients over rocks could frequently exceed the threshold required for facet development, which resulted in changes in snowpack structure over these features.

Colbeck (1991) described several of the interactions between snowpack processes and the layered structure of snow that create variability within the snowpack. Among other aspects, he describes: the importance of wind for the formation of snowpack layers with variable physical properties; the requirement of layers for the formation of facets and depth hoar; the effect of layers on heat and moisture flow within the snowpack; and routing patterns caused by within-layer channeling of meltwater. He concluded that placing more emphasis on layers when modeling snowpack processes would lead to a better understanding of the physical interactions within the snowpack. Schweizer and others (2003) listed terrain, new snow, wind and temperature as the primary factors contributing to snowpack variability.

5.2.4 Slope- and feature-scale variability of snowpack properties

Sommerfield (1980) recognised the intrinsic nature of the variability of snow strength, and suggested that a statistical approach (in his case, a Weibull extreme statistical model of snow strength) was necessary to account for such variability when considering the failure,

leading to fracture of the snow slab.

Conway and Abrahamson (1984) made field measurements of the shear and tensile strength of snow, for slopes with recent avalanches and for unfractured slopes. They found pronounced variability in both shear strength and tensile strength for both the "stable" and the "unstable" slopes, although the unstable slopes showed the greatest degree of variability. Measurements of shear strength on unstable slopes ranged from 10 to 1320 N m^{-2}. Schweizer and others (2007) calculated the overall coefficient of variability of Conway and Abrahamson's experiments as 65% for stable slopes and 82% for unstable slopes. Conway and Abrahamson attributed the variations in snow strength to the presence of deficit zones[1], which had been implicitly proposed by McClung (1979, 1981) in his model of avalanche release precipitated by strain softening. Schweizer and others (2003, 2007) have argued that rather than detecting deficit zones, it is more likely that they simply measured the spatial variability of snow strength.

Conway and Abrahamson (1988) used spatial statistics to assess the extent of the supposed deficit zones and found that the wavelength of the low strength regions was less than 3 m. They suggested that in order to capture similar variability, strength measurements should span at least 3 m and be done at a spacing of 0.5 m. Föhn (1988) reported less strength variations in the weak layer compared to Conway and Abrahamson, with a coefficient of variability of 38% on stable slopes.

Kronholm (2004); Schweizer and others (2007) described a study by Chernouss (1995, unseen), in which the author analyzed the spatial autocorrelation of four snow properties: snow depth, density, new snow thickness, and new snow strength. He concluded that snow thickness was the most spatially variable property. Aside from Conway and Abrahamson (1988), this is likely one of the first studies to employ spatial statistics for assessing the

[1]These zones within the weak layer are also known as super-weak zones (Bader and Salm, 1990), and are thought to be instrumental for concentrating stresses in the weak layer just prior to avalanche release (see Section 1.3).

variability of snow properties.

Birkeland and others (1995) investigated the variability of penetration resistance of snow over two sites using a digital resistograph (see Section 2.2.4), a wind affected slope and a sheltered site with a rough substrate. Snow depth was found to be positively correlated with penetration resistance at the first site but not at the second. At the second site, penetration resistance was found to be lower in areas overlying rocks. Birkeland and others noted that patterns of variability were complex and that several compounding factors were in operation. They also recommended that individual layers should be identified and analyzed, rather than using the complete resistograph profiles. Kronholm and others (2004) investigated the spatial trends of penetration resistance of individual layers measured using a SnowMicroPen (SMP, see Section 2.2.4). All layers were found to be spatially continuous and he did not detect the sill in the variogram analysis, indicating that the spatial trends extended beyond the measurement range (extent).

Jamieson (1995); Jamieson and Johnston (2001) used shear frames to measure the variability of weak layer shear strength in level study plots and avalanche start zones. The mean coefficient of variability was 14% for the level study plots and 18% for avalanche start zones. They also noted that the overall range of shear strength measurements spanned a factor of 20, from 0.1 to 2 N m^{-2}.

Birkeland and others (2004) measured the thickness and penetration resistance of the same surface hoar layer from SMP measurements at two adjacent sites, with the surveys done six days apart. The results were compared to a shear strength index calculated from quantified loaded column tests (Landry and others, 2001). The shear strength index was found to increase over the measurement interval which indicated an increase in the stability of the slope. The maximum penetration resistance as well as the variability of the penetration resistance also increased over this period. This finding was in contrast to other studies that have associated an increase in variability with reduced slope stability.

Lutz and others (2007) further analyzed these data and found that hardening of the weak layer–substratum interface correlated with the increase in the shear strength index. They were also able to detect a reduction in weak layer thickness over the measurement interval and used this as evidence to suggest that the weak layer gained strength in part by surface hoar penetration into the substratum, as proposed by Jamieson and Schweizer (2000).

5.2.5 Slope- and feature-scale variability of snow stability

Several studies have investigated the variability of point stability measurements in avalanche start zones. Jamieson and Johnston (1993) and Jamieson (1995) investigated the variability of rutschblock test results on potential avalanche slopes and found there was a 67% probability of a single rutschblock test giving the median score of an array of tests done on the same slope, and 97% probability of giving a score within one step of the median. They suggested that for repeatable results, uniform slopes with low variability should be selected when performing rutschblock tests.

Stewart (2002) and Stewart and Jamieson (2002) investigated the variability of drop hammer tests in avalanche start zones. They found that visually, clusters of above average and below average stability were found, but correlating these clusters to physical changes in the snowpack was difficult. Slab thickness showed the strongest correlation with reduced stability, indicating that thinner spots in the snowpack were more unstable.

Landry (2002) presented results suggesting that point stability assessments measured using a quantified loaded column stability test were only representative of overall slope stability 52% of time. Landry and others (2004) increased that assessment to 75% of the time, when statistically unrepresentative sets were withdrawn from the sample set, dramatically increasing the assessment of the usefulness of stability test results when done in small numbers.

Kronholm and others (2003) and Kronholm and Schweizer (2003) investigated the spatial variability of stuffblock and rammrutsch test results in potential avalanche slopes. They found some autocorrelation between the test results (this contradicted a previous study by Kronholm and others (2002), where no autocorrelation had been found), indicating clustering; however a characteristic size for the clusters could not be determined.

Campbell (2004) investigated the spatial variability of rutschblock scores using large arrays of rutschblock tests and found that in some instances, very low scores could be found adjacent to very high scores. Some degree of clustering was noted, and in one array, clustering corresponded to a small depression, where the surface hoar was observed to be particularly well developed. Overall, Campbell concluded that the spatial variability of rutschblock test results (and by extension, slope stability) was a result of many compounding factors, and that in most cases, there was no simple correlation with just one factor. Campbell and Jamieson (2005, 2007b) reanalyzed these data using a multivariate approach, and found that overall, slope angle and weak layer depth were important factors for determining rutschblock score. They also noted that deeper weak layers, which usually gave higher rutschblock scores (indicating greater stability) were more variable than shallower weak layers. Campbell and Jamieson (2007a) investigated the clusters of lower stability test results and found that the clusters ranged in extent from 1.7 to 3.2 m. They argued that these values probably represented minima, due to the limits of the array sizes.

Fyffe and Zaiser (2004), based on a model by Zaiser (2004), simulated avalanche release using a numerical cellular automata model that implicitly included the spatial variability of weak layer shear strength. They found that simulated avalanches were more likely to occur for high shear strength variability and proposed a calculation to allow adjustments of slope stability assessments made on the basis of shear frame measurements by making a correction to the stability index based on the relative variability

of the shear frame measurements. Using a slightly modified version of Fyffe and Zaiser's model, Kronholm and Birkeland (2005) introduced a characteristic length scale of 4 m for the variations in weak layer shear strength; this value was based on a variogram analysis of shear strength measurements in weak layers. They found that highly auto-correlated slopes with a low nugget to sill ratio were more likely to produce simulated avalanches that propagated over large areas compared with slopes that exhibited less spatial autocorrelation.

5.2.6 Summary, spatial variability

The coefficient of variability varied dramatically between different studies for both snow properties and stability test results. Interpretations as to whether spatial variability promotes or hinders stability also vary. Schweizer and others (2007) pointed out that part of the confusion has arisen due to the wide variety of different measurement tests and techniques. Additionally, they noted that surveys at different scales and using tests with different measurement supports have been compared, when not always appropriate to do so.

In order to further advance our understanding of the role of spatial variability in affecting slope stability, it may be helpful to follow the lead of Kronholm and Schweizer (2003); Schweizer and others (2003); McCammon and Sharaf (2005); Gauthier (2007); as well as other authors, in separating the components of avalanche release into fracture propagation and fracture initiation, and assess the effect of spatial variability with respect to each. This may help explain why in some instances, an increase in variability promotes instability, whereas in others, it promotes stability. The bulk of studies indicate that fracture initiation is more likely to occur when spatial variability of snow properties is high. Fracture propagation, however, appears to be favoured by spatially continuous snowpack structures, which may be characterised by lower degrees of spatial variability,

especially at slope scales. Since avalanches require both fracture initiation and fracture propagation, spatial variability associated with avalanches will likely be balanced between these often opposing requirements.

5.3 Methods

5.3.1 Transect surveying

The spatial variability of snow stratigraphy was investigated across slopes and terrain features for which variability was expected. The terrain features and slopes that were tested were: wind affected slopes, a gully, a slope with rain runnels, a boulder field, elevation and aspect changes, and the unreleased snow adjacent to the flank of an avalanche. In all cases either a straight line, or a contoured transect of penetrometer profiles at approximately uniform spacing was performed across the feature or slope in a direction chosen to encompass the maximum degree of variability.

The transects were done at different scales, with profile spacing chosen with respect to the wavelength of the features being investigated. The runnel transect was the smallest scale survey, with a transect length of 1.3 m and profile spacing of just 5 cm. (Much care was needed to prevent snow disturbance and to keep the penetrometer pushes absolutely vertical for this transect.) Several slope-scale features were assessed with transect lengths of 6 to 90 m. Spacing for these transects ranged from 15 cm to 2 m. Additionally, three basin-scale surveys were undertaken, with transect lengths ranging from 800 to 2000 m and spacing (which was less regular for the basin-scale surveys) of up to 400 m.

For the slope-scale features, the snow surface topography was surveyed using a folding ruler and an inclinometer. The distance along the snow surface was measured to the nearest cm using the folding ruler and the slope angle between the measurement points was measured to the nearest degree using the inclinometer (a Suunto compass

clinometer). In some cases, the protective lid for the depth measuring platform was used as a flat surface to aid measuring the angle between the measurement points. Horizontal and vertical distances were calculated relative to the start of the transect using simple trigonometry.

The biggest source of error for the position surveying was in measuring the angle of inclination between the measurement points. To reduce error, the same operator measured all slope angles during the survey. Accuracy was estimated to be $\pm 2^{\circ}$, which gives a vertical measurement error of approximately 3.5 cm per 1 m surface distance. For slope angles of 30°, this source of error results in discrepancies of up to 1.8 cm. When other error sources are taken into account, including errors associated with measuring the surface measurements and the fact that the hole where the penetrometer was inserted was sometimes obscured or enlarged, reasonable estimates for slope-scale surveying errors are about 5 cm per 1 m surface distance, or 5% for both horizontal and vertical measurements. Errors associated with the penetrometer measurements have been previously discussed in detail in Chapter 2.

For the basin-scale surveys, position and elevation were measured using a GPS (Garmin eTrex Vista), with a stated accuracy of ± 15 m. From experience in mountain environments, where satellite signal quality is often suboptimal, a more realistic accuracy assessment is ± 30 m.

The snow depth, or height of snow (HS) was measured at each point for most of the surveys. To prevent possible damage to the penetrometer tip, a regular avalanche probe was used rather than the penetrometer. HS was measured as close as possible to the penetrometer measurement point, and care was taken to keep the probe vertical during measurement. Measurements of HS become less accurate on steeper terrain, since the error is a function of the cosine of the angle of the push relative to the slope angle. For a slope angle of 15°, a 5° deviation from vertical in the down-slope direction results in HS

error of 2.5 cm over a 1 m push (10 cm for a typical Roger's Pass HS of around 4 m). It should be noted that this error also applies to the penetrometer measurements. Trees, especially mature evergreens, are consistently vertical and this fact was exploited to increase the accuracy of both probe and penetrometer pushes. The probe/penetrometer operator would use a tree for alignment in one direction (side-to-side) and the assistant would check the alignment in the orthogonal, front-to-back direction, for which it is hard for the operator to assess.

5.3.2 Geostatistical methods

Information about the spatial correlation of snowpack properties can be gleaned using a variogram (e.g. Davis, 1973, p.383). In a variogram[2], semivariance $\gamma(h)$ is plotted against the separation distance, h. $\gamma(h)$ is defined as (e.g. Gringarten and Deutsch, 2001):

$$\gamma(h) = \frac{1}{2}\mathrm{Var}[Z(x+h) - Z(x)] = \frac{1}{2n(h)}\sum_{i=1}^{n(h)}(Z(x_i+h) - Z(x_i))^2, \tag{5.1}$$

where Z is a stationary, random function, x is a location, and $n(h)$ is the number of data at the separation distance h. The prefix *semi* refers to the $\frac{1}{2}$ term in Equation 5.1, which has its origin in the fact that the observations are paired, and the relevant quantity is the variance per point (Bachmaier and Backes, 2008).

In order to satisfy the conditions of stationarity, the trend was usually removed from the data set for which a variogram was produced. The nature of the trend varied from transect to transect; however, since no deterministic models were used in establishing the trends, trend fitting was kept as simple as possible. The trends are presumed to represent a regional (across the scale of the survey) causal effect, and contain interesting information to that effect. The nature of each trend and how it may relate to causal processes

[2]There is some inconsistency in the literature over the use of the terms variance, semivariance, variogram and semivariogram (see Bachmaier and Backes, 2008). In this study, I follow Gringarten and Deutsch (2001) — a practical guide — and adopt the term semivariance for the term $\gamma(h)$ and use the term variogram to describe the plot of $\gamma(h)$ with h.

is discussed in the individual transect sections. Since the variograms are produced from trend-removed data, they therefore contain information regarding the intrinsic variability of the system, as well as information about variability not explained from the trend analysis. A hypothetical variogram is shown in Figure 5.1. The range is the separation distance beyond which no further increase in semivariance is observed. This is the limit of spatial correlation over the extent of the survey. The sill is the semivariance value at which the variogram levels off. The nugget represents variability that is smaller than the measurement scale, including measurement errors. If the nugget dominates the semivariance, then the measurement scheme has not done a good job of characterising the spatial correlations of the system, or there is no autocorrelation for the variable being assessed. The nugget is sometimes referred to as the intrinsic variability.

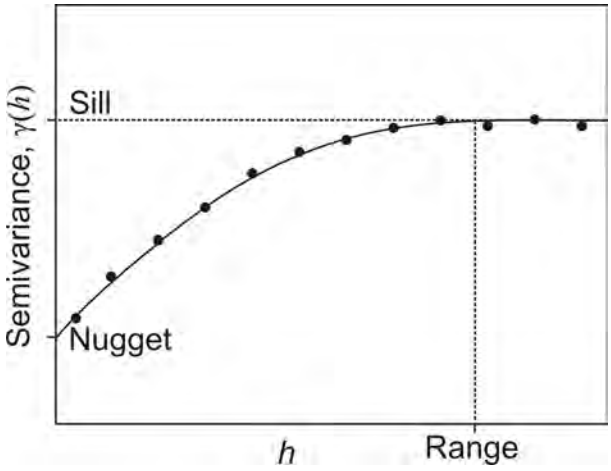

Figure 5.1: Hypothetical variogram indicating the range, sill and nugget.

Since each transect was performed over a different slope feature, and the aim of the study was not to build a predictive model, detailed variogram models were not fitted to the sample variograms (although for some variograms, visually estimated variogram models are shown). Instead, the variograms were used as a descriptive tool to help characterise the spatial correlations of snow properties over certain terrain features.

5.3.3 Scale and climatic issues

As a result of the different scales, care is needed when comparing the variability between the different transects. In general, the variability across the features is only applicable at the scale measured; however, the features were chosen to be representative of those commonly found in alpine terrain. As such, they may be indicative for variability across similar features in other areas with a similar transitional snow climate. It is reiterated that no information is available at distances less than half the sample spacing.

The constraint of the similar snow climate should be expanded upon a little, since this is also an important point. For very thin snowpacks with high temperature gradients (a continental snow climate), variations in hardness will be affected strongly by thermodynamic metamorphic processes in the snowpack in addition to variations due to uneven deposition, transportation and ablation. For snowpacks with particularly high moisture content and relatively warm temperatures (a maritime snow climate), settling rates may be much higher, resulting in different layer structures (depth and thickness) as well as different hardness gradients within the snowpack. Short of undertaking further surveys in areas with maritime and continental snow climates (for which, sadly, there was no time during this study), the transitional snow climate where these surveys were undertaken offers a good compromise. Persistent weak layers, such as surface hoar, form in the transitional snow climate (although depth hoar is rare), as do crusts and runnels from rain events.

5.4 Results and analysis

5.4.1 Avalanche flank transect

The unreleased snow adjacent to a skier-triggered avalanche at the Bostock-Schuss site was surveyed with a transect approximately perpendicular to the flank of the avalanche

(Figure 5.2). This avalanche occurred on 17-Feb-2007 and was a size 2.5 avalanche, triggered by a skier from 100 m away. The failure layer of the avalanche was the 04-Feb-2007 surface hoar layer, which was recorded as 1 cm thick in a nearby manual snow profile. At the survey point, the slope angle was 32° and faced east. The elevation was 1225 m. A manual profile was done approximately 100 m from the survey location on a similar aspect (Appendix E, Figure E.1). The transect was collected approximately 2 hours after the avalanche occurred. This transect is presented first, since it actually represents a relatively uniform slope with low spatial variability. In this way it provides (as far as scale considerations permit) a control for other slope-scale transects over features that were more spatially variable. The area also contained an interesting tensile fracture that extended into the unreleased snow.

The tensile slab fracture that extended into the unreleased snow defined the top of a "block" of the slab that was displaced downslope just slightly. The block did not slide but instead remained attached at its lower and right hand margins. The fracture extended about 5 m beyond the flank into the unreleased snow (Figure 5.2a is foreshortened, so the scale is deceptive). The width of the fracture varied from 20 mm at the flank to 5 mm about 2 m into the unreleased snow. At about 3 m, the fracture was visible, but there was no discernable opening. The fracture was not completely straight; instead there were multiple straight line segments, each join subtending an angle of approximately 110°. It was assumed that the presence of the tensile fracture indicated that the weak layer had fractured (in shear) between the tensile fracture and the avalanche flank but not on the side away from the avalanche flank.

During the transect survey, care was taken not to stress the weak layer, which may have resulted in whumpfing (or worse, avalanching) the slope, which would have fractured the snow in the weak layer beyond the tensile fracture. This was done by digging a trench below the level of the weak layer into the substratum; the operators walked along this

trench and therefore did not apply stress to the weak layer.

The transect of the penetrometer profiles from the avalanche flank in to the unreleased snow on the margins of the avalanche is shown in Figure 5.3. A visual inspection of this transect shows slight fluctuations in layer depths, with no particular periodicity. The fluctuations are on the order of 2 cm, which is within bounds of measurement error, so it is unlikely that these fluctuations represent true variability. The amplitude of the lower portion of the profiles on the right of the transect (further away from the flank) appears to be greater than on the left. Four layers were identified in the transect by manual inspection of the penetrometer profiles. These were: a thick top layer of low resistance snow, the layer above the weak layer, referred to as the slab, the 04-Feb-2007 weak layer and the substratum.

In order to test whether there was any hardness change across the fracture, the mean force-resistance was calculated from each profile for the weak layer, the slab and the substratum. The results are shown in Figure 5.4. The mean force-resistance of each layer shows a gently rising trend with distance into the unreleased snow. However, at the location of the fracture, the gradient of this line increases. This effect is most pronounced with the substratum, however, the force-resistance change associated with the weak layer is also quite pronounced.

The difference in mean force-resistance for each layer between the fractured and unfractured zone was tested using a t test. Additionally, differences in weak layer thickness and weak layer depth were also tested. The results are shown in Table 5.2 There was a significant force-resistance difference across the fracture for each layer, with the mean force-resistance for the weak layer changing from 0.85 to 1.14 N. This corresponds to a hand hardness change from 1F to 1F+. Interestingly, the weak layer was 1 mm thinner for the unfractured snow on average, this result was significant at α=0.05. There was no significant change in depth to the weak layer.

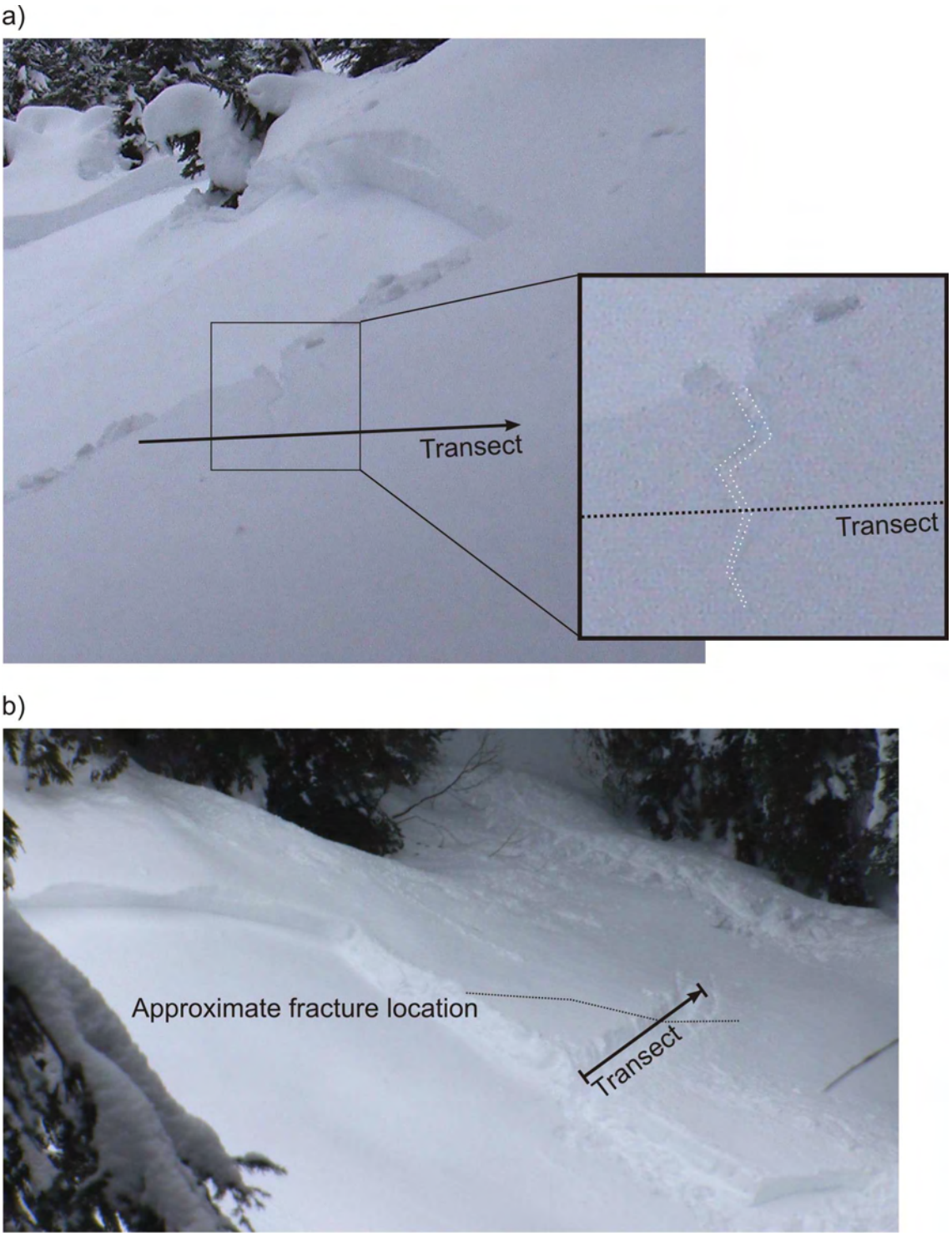

Figure 5.2: Photos of the Bostock-Schuss avalanche flank transect site. a) Before data collection. Transect (solid black line) marked with the direction given by the arrow. Detail shows the fracture extending into the unreleased snow. b) Different view after data collection. ASARC photos.

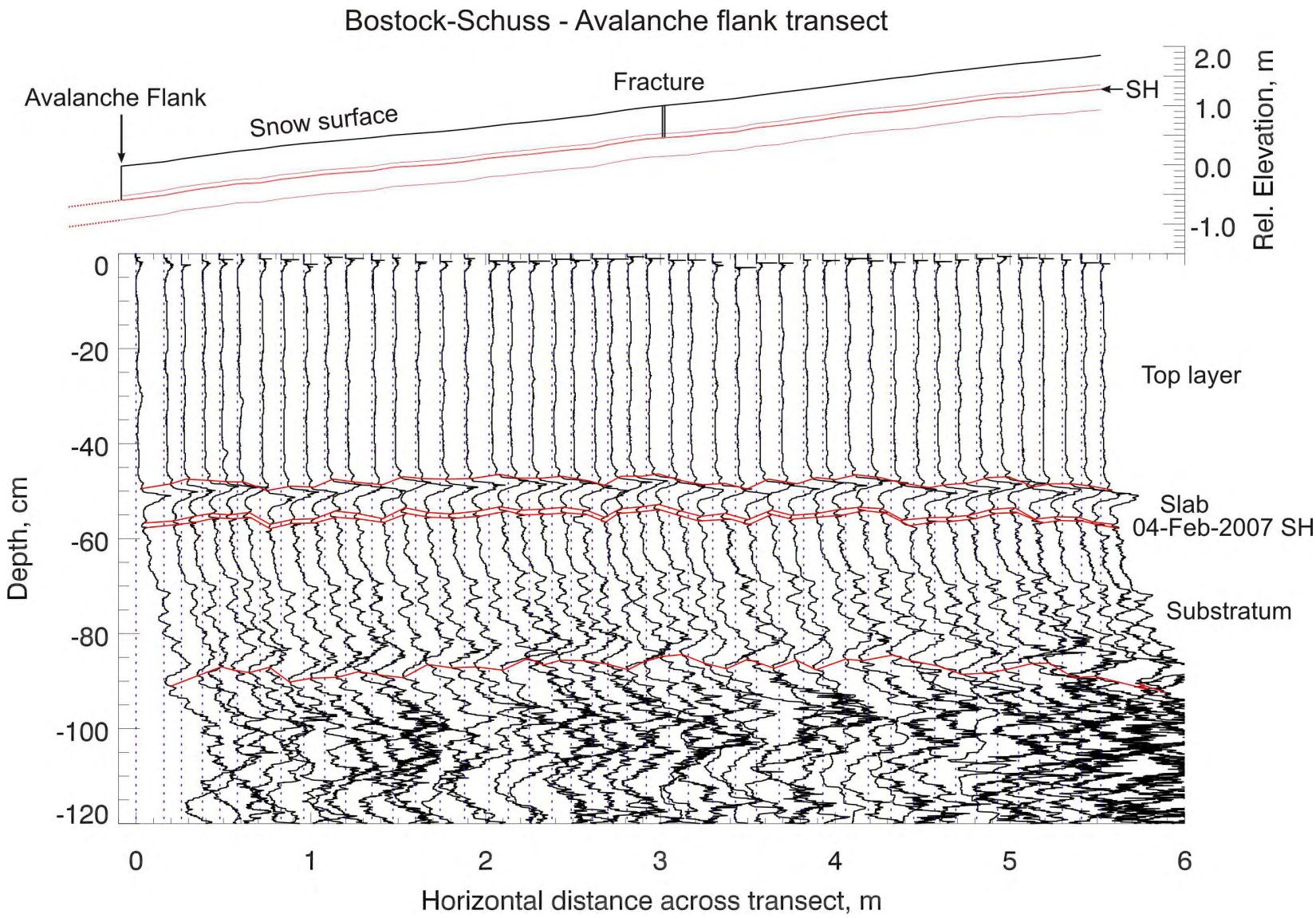

Figure 5.3: Avalanche flank transect, 17-Feb-2007 from the Bostock-Schuss site. Upper pane shows snow surface and ground topography. Lower pane shows top 120 cm of penetrometer profiles. Interpreted layer interfaces shown as solid red lines in both panes.

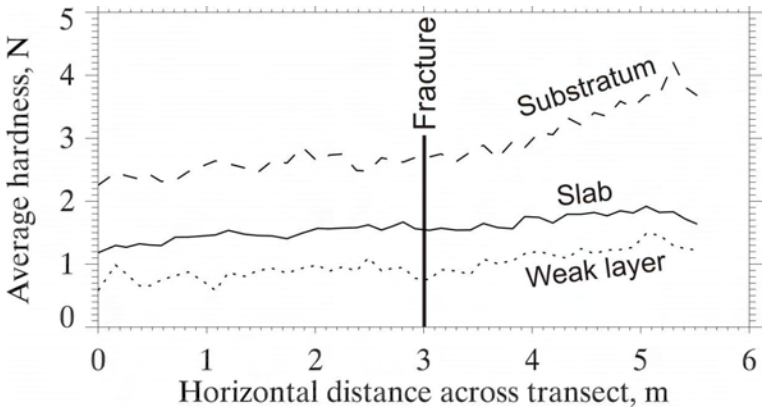

Figure 5.4: Plot of average layer hardness for the weak layer (dotted line), slab (solid line) and substratum (dashed line) for the Bostock-Schuss avalanche flank transect.

Table 5.2: Snow property variations across a fractured slab. n=46 for each case.

Property	Mean value, fractured snow	Mean value, unfractured snow	t	p
Slab force-resistance	1.46 N	1.71 N	6.80	<0.001
Weak layer force-resistance	0.85 N	1.14 N	6.34	<0.001
Substratum force-resistance	2.54 N	3.23 N	7.27	<0.001
Weak layer thickness	10.0 mm	9.0 mm	2.26	0.014
Weak layer depth	54.7 cm	55.0 cm	1.01	0.159

The variogram of force-resistance in the weak layer using original data, prior to removal of a trend (Figure 5.5), shows a discontinuity at a spacing of 2.7 m. There is a change in the spatial structure of the force-resistance at this point and it is almost certainly associated with the fracture. The increase in variance at spacings greater than the minimum distance from either side of the transect to the fracture is due to the higher force-resistance gradient on the right hand side of the transect. Note that this effect is particularly high since the fracture is almost in the centre of the transect.

The trend in the force-resistance data was removed by fitting different linear trends on either side of the fracture. Variograms for the trend removed data for the slab, weak layer and substratum are shown in Figures 5.5b)–d) respectively. The variograms for the weak layer and the substratum have been reduced to the nugget effect (where there is no

discernible increase in semivariance across the variogram from the level of the nugget), indicating that all the measurable spatial structure can be accounted for by the linear trends. The variogram for the slab, however, does show a residual trend. By visual inspection, the shape of the variogram resembles that of a Gaussian variogram model. This indicates that the residual variability represents a smoothly varying feature; the fact that the sill had not been reached indicates that the length scale associated with this feature is beyond the extent of the transect. One possible explanation is that this layer was subjected to spatially non-linear temperature variations due to the proximity to the trees at the edge of the glade.

An interesting question is whether it was the differences in the snow properties that caused the fracture to arrest (assuming that it did arrest at all, and that the whole slope up to the trees didn't whumpf and simply not slide), or whether the changes in snow properties resulted from the fracture. The hardness of the substratum increased across the fracture, and since the properties of the substratum were probably unaffected by the fracture, this indicates that there was probably a hardness gradient in the weak layer and the slab prior to the avalanche. A good explanation for the hardness change in the weak layer is that the proximity to the trees reduced the sky view, inhibiting surface hoar growth on the right of the transect, producing slightly smaller crystals. This gave a more resistant weak layer that resisted fracture propagation, resulting in a tensile fracture in the slab opening up at that point.

What about the weak layer thickness? The idea of smaller surface hoar crystals is consistent with a thinner slab; however, it was expected that the weak layer on the side that had fractured would be thinner. Kronholm (2004) (manually) measured a reduction in weak layer thickness of 5 mm across a similar fracture. There are three possible reasons to explain why this was not observed. First, it is possible that the weak layer didn't fracture at all, and a tensile crack simply opened up, displacing the block

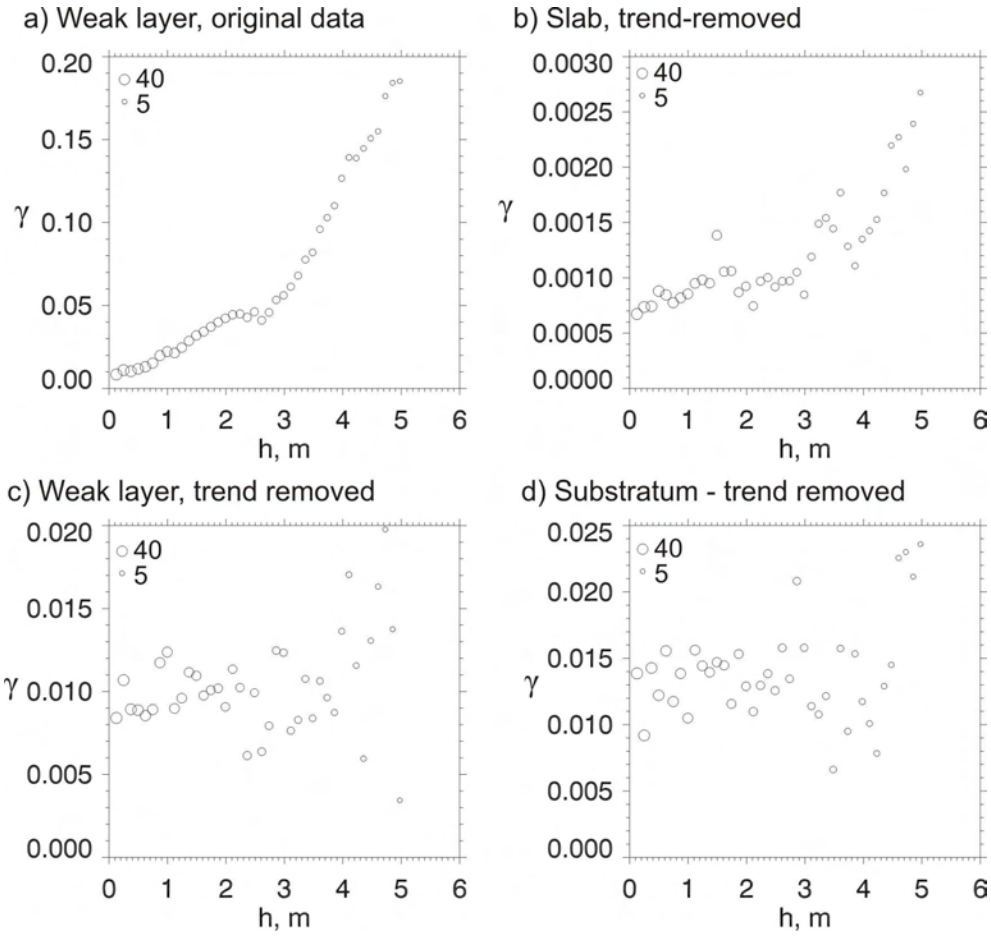

Figure 5.5: Variograms of force-resistance for the avalanche flank transect for a) the weak layer using original data; b) the slab using trend removed data; c) the weak layer using trend removed data; and d) the substratum using trend removed data. Number of sample pairs, $n(h)$, indicated by the circle size and scaled between the values shown.

down-slope slightly without fracturing the weak layer. This is unlikely, since the weak layer would have had to accommodate considerable strains associated with a down-slope displacement of 20 mm (in the order of 200%) without fracturing. Second, the weak layer on both sides of the tensile fracture in the slab may have fractured, as suggested above. This is more likely than there being no fracture at all in the weak layer; presumably the fracture in the weak layer arrested somewhere, but this could have been beyond the end of the transect.

The third possibility is that the weak layer was fractured on one side of the tensile

fracture and not the other, but the penetrometer was not able to distinguish the collapse, either through inaccuracies in measurement, or because the amount of collapse was not particularly great (Dave Gauthier, 2007, personal communication). Propagation saw tests (Gauthier and Jamieson, 2008) in a nearby area that was assumed to have whumpfed due to the remotely triggered avalanche indicated high propagation propensity. It is possible that the weak layer could fracture, even in a fairly thick weak layer such as the 04-Feb-2007 surface hoar without fully collapsing. If this is the case, then there may be a possibility for "refracturing", meaning that a second fracture could propagate through the same weak layer. This reloading of an already failed weak layer is claimed to have been observed in the field but is thought to be rare (Bruce Jamieson, 2007, personal communication).

5.4.2 Wind affected slopes

Two transects were performed across wind affected slopes.

Poetry Slopes – wind transect

The Poetry Slopes site with the transect line marked is shown in Figure 5.6. The survey covered two large wind ridges, each with a topographic amplitude in the order of 1 m. The second ridge (further in the distance in Figure 5.6) was a little more pronounced than the first. The total length of the transect was 26 m and the intended spacing was 50 cm. When the transect topography was surveyed, it was found that the actual average spacing was 54 cm, and spacing ranged from 49 cm to 56 cm. For variogram analysis on this transect, spacing was assumed to be regular at 54 cm.

The Poetry Slopes site was at an elevation of 1885 m and faced east. Average slope angle was approximately 18°. The site was located just below a bench that allowed winds to be channeled around a north-east trending ridge line at this point. It was frequently windy at this site. The winds blew across the bench and through the trees visible at the

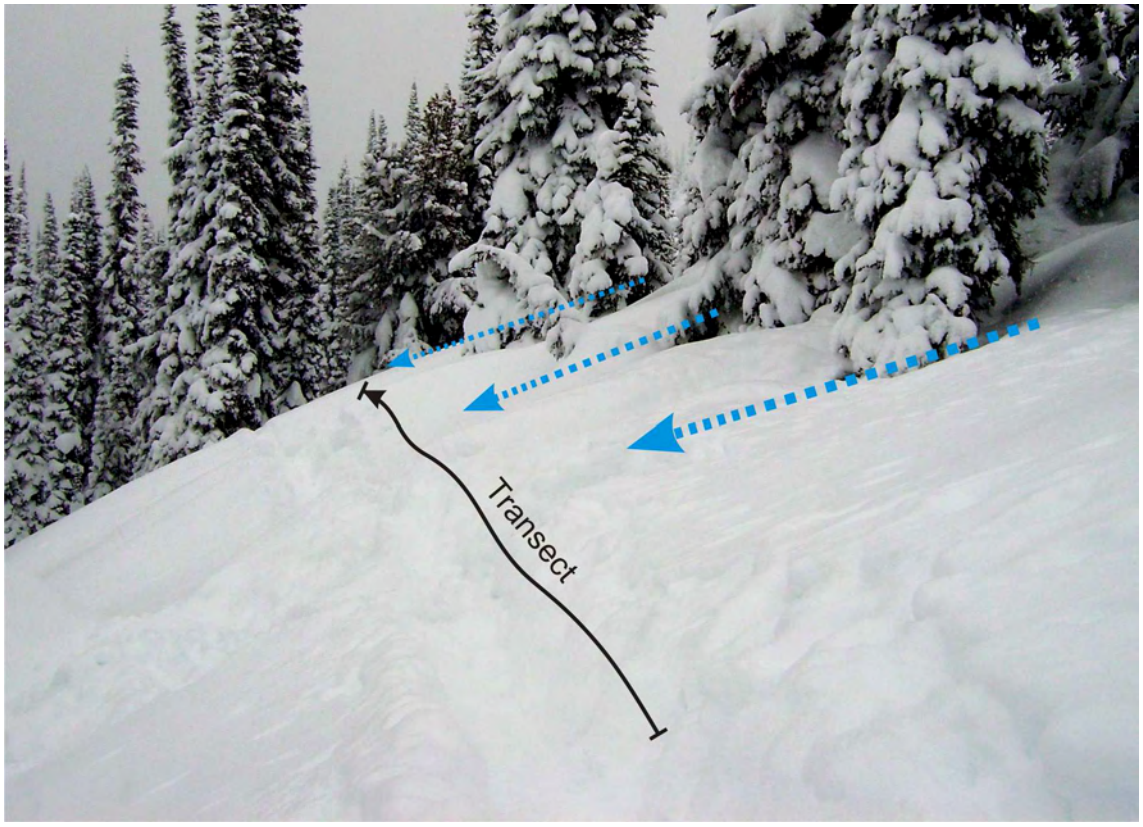

Figure 5.6: Photo of the Poetry Slopes site, surveyed on 07-Jan-2007. Approximate transect line shown (solid black line) with direction indicated with the arrow. Dashed blue lines indicate patterns of increased wind through gaps in the trees. ASARC photo.

top right of Figure 5.6; prevailing wind patterns are indicated with blue dashed arrows. A manual profile was collected at this site (Appendix E, Figure E.2).

The transect of penetrometer profiles is shown in Figure 5.7. Two layer interfaces were traced across this transect with the assistance of the layer tracing algorithm described in Section 4.3. The upper layer interface was a spike associated with an abrupt hardness change at approximately 80 cm. The layer tracing algorithm gives the depth to the top of the wavelet rather than the actual peak. The lower layer interface was also associated with a hardness change, this time at a depth of 100 cm. Although no performance statistics were recorded, the layer tracing algorithm performed quite well tracing these layers (manual corrections were made when the correct layer was not identified), although

the tracing program proved to be quite cumbersome for practical use. The fact that the output gave the location of the top of the wavelet was also limiting, since in reality, the highest peak (for a crust) or the lowest trough (for a weak layer) is more likely to be of interest. This modification would be relatively easy to implement and is recommended for the future. The layer tracing algorithm was only used for this transect; layer interfaces on other transects were picked manually.

The lower pane of Figure 5.7 shows the position of the layers relative to the snow surface. It appears as though there are smaller scale features in the layers with amplitudes of approximately 10 to 20 cm and wavelengths of approximately 2 to 4 m. The "peaks" associated with these features actually represent areas where recent erosion has occurred, since they are closer to the snow surface.

The snow surface and layer interfaces follow the general trend of the ground terrain, that is a gentle downwards slope to the right of the transect. However, the smaller features of the snow surface do not appear to be consistent with the ground terrain. The middle layer between the two identified layer interfaces appears to get thinner in the middle of the transect. This is possibly an area that was subjected to scouring during a wind event, removing material from this layer.

Simple linear trends were removed from the snow surface topography, the layer interface depths and the mean force-resistance for layers 1 and 2 are shown on Figure 5.7. Variograms were constructed for these properties, using the trend removed data (Figure 5.8). The variogram of the snow surface topography (Figure 5.8a) shows a peak at a separation distance of approximately 8 m; this corresponds to the larger wind ridges (or wind pillows) that can be seen in Figure 5.6. The fact that the variogram reduces in amplitude beyond this peak suggests that there is some periodicity to these broad wind features.

The variogram for the topography of the interface between layer 1 and layer 2 is

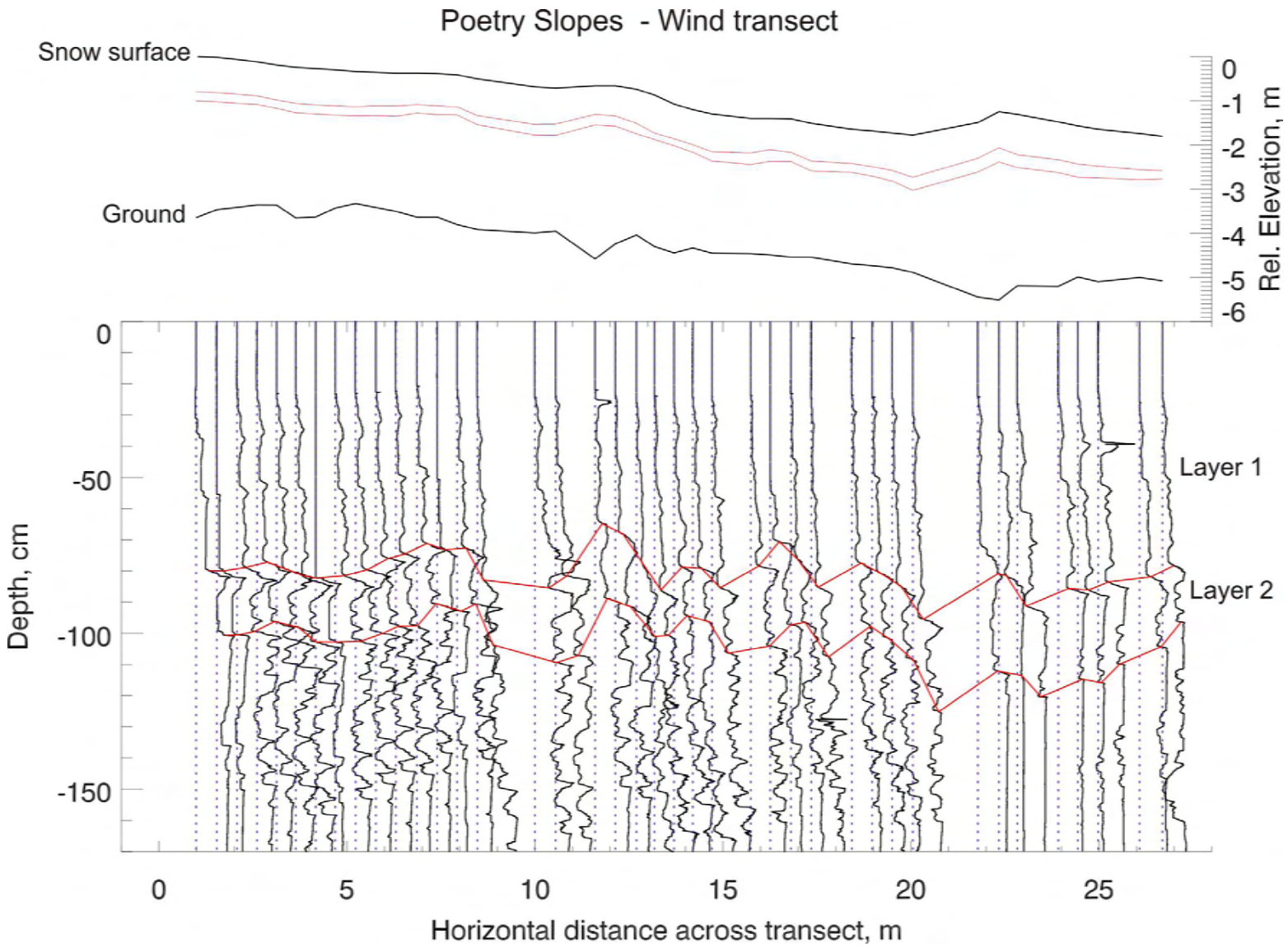

Figure 5.7: Wind affected slope transect, 07-Jan-2007 at the Poetry Slopes site. Upper pane shows snow surface and ground topography. Lower pane shows top 160 cm of penetrometer profiles. Interpreted layer interfaces shown as solid red lines in both panes.

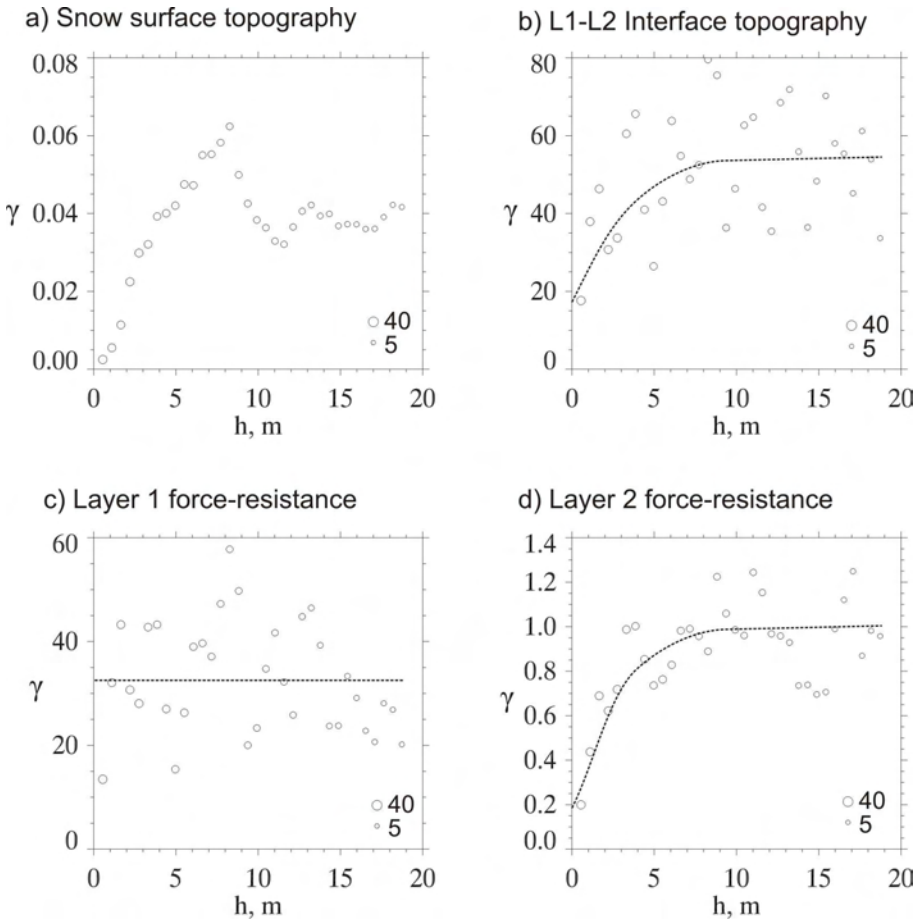

Figure 5.8: Variograms for trend-removed snow properties from the Poetry Slopes wind transect: a) Snow surface topography; b) layer 1 – layer 2 interface topography; c) layer 1 force-resistance; d) layer 2 force-resistance. Indicated variogram models were fitted by visual inspection. Number of sample pairs, $n(h)$, indicated by the circle size and scaled between the values shown.

shown in Figure 5.8b. The semivariance is much higher for the interface topography compared with the snow surface topography. Some of this increased variance is likely due to measurement errors associated with the penetrometer depth measurements; however, it also appears as though this layer interface is more variable than the snow surface. It appears as though the sill has been detected at this measurement scale; the associated range is approximately 8 m, which is consistent with the major variations in the snow surface.

The variogram for the mean force-resistance is quite different for layer 1 (Figure 5.8c)

compared with layer 2 (Figure 5.8d). Layer 1 shows very little spatial correlation; the nugget effect dominates in this case. The most likely reason for this is the fact that the upper layer is very thick and also encompasses the upper region of soft snow, which the penetrometer does not characterise well. For this reason, this layer is not well suited for further analysis. Layer 2, however, shows a relatively strong spatial correlation, again up to a separation distance of approximately 8 m.

Since the spatial correlation scales are consistent between the layer interface topography and the mean force-resistance for layer 2, it suggests that these factors may be related. This makes physical sense, since wind blowing over the topography at the time of deposition will scour some regions of the snow surface and deposit snow in others. It is hypothesised that since the wind blown snow comprises of small, mechanically broken fragments, the areas where the snow is deposited (the high points) should have a higher force-resistance than the troughs associated with erosion.

In order to test this hypothesis, the mean force-resistance across the transect for layer 2 was compared to the depth of the interface between layer 1 and layer 2 (Figure 5.9). The trend removed data were used in both cases and the plots were normalised to the maximum absolute value for each property. By visual inspection, the broad scale variations of approximately 8 m in wavelength appear to correlate quite well. This is confirmed by a significant Pearson correlation coefficient of 0.40 (p=0.010). However, the smaller scale variations in topography appear to be out of phase with the hardness; for these smaller scale features (on the order of 4 m wavelength) the troughs appear to be harder than the peaks. This likely explains the relatively low value for the correlation coefficient.

Birkeland and others (1995) found that wind ridges were positively correlated with snow hardness. This study suggests that the broader scale wind features exhibit this tendency, but that smaller scale features may be superimposed where the scoured area

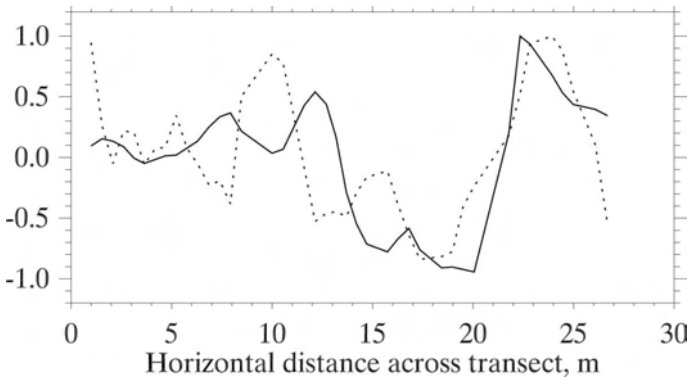

Figure 5.9: Normalised plots of layer 1 – layer 2 interface depth (solid line) and mean force-resistance (dotted line) for layer 2 identified in the Poetry Slopes wind transect.

is harder than the peak.

Roundhill – wind transect

The site of the Roundhill wind transect is shown in Figure 5.10. The Roundhill site was a southeast-facing slope, with an approximate slope angle of 8°. The site was about 100 m from a broad, wind-exposed ridge, on the lee side (off the right hand side of Figure 5.10). A line of trees provided a wind baffle, although wind was able to pass through gaps in the trees, producing the wind ridges visible in Figure 5.10. The transect was 14 m long and mean profile spacing was 31 cm (±4 cm). A manual snow profile done at this site is shown in Appendix E, Figure E.3.

The main wind features are of similar dimensions to those of the Poetry Slopes site, and these are clearly seen in the transect of penetrometer profiles (Figure 5.11). The structure of the wind ridges is, however, quite different. Once again, it should be noted that the internal structure in the lower pane is relative to the snow surface, so the apparent peaks actually represent scoured areas with less snow cover than the apparent troughs. It may be more intuitive to refer to the upper pane of Figure 5.11 to view the internal layer patterns; in this pane the vertical axis is height. In the Poetry Slopes transect, the two layer interfaces followed the general shape of the snow surface topography quite

Figure 5.10: Photo of the Roundhill site, surveyed on 15-Mar-2007. Approximate transect line shown (white line) with direction indicated with the arrow. Dashed blue lines indicate prevailing wind to the left and slightly towards the viewer. ASARC photo.

well, although smaller scale features were superimposed onto the broad features. In the Roundhill transect, the internal layers show an evolution of the wind ridges over time, with the topography of the lower interfaces being quite different in magnitude (actually flatter, from the argument above, although it appears to be more undulating) to the snow surface topography. Regular, smaller scale features are not apparent on the Roundhill transect.

Layers in the Roundhill wind transect appear to alternate between periods of ridge development, where the amplitude of the wind ridges increased and periods of relative quiescence, where little or no increase in wind ridge amplitude occurred. Variograms of layer thickness and force-resistance were produced for two layers, one representative of a

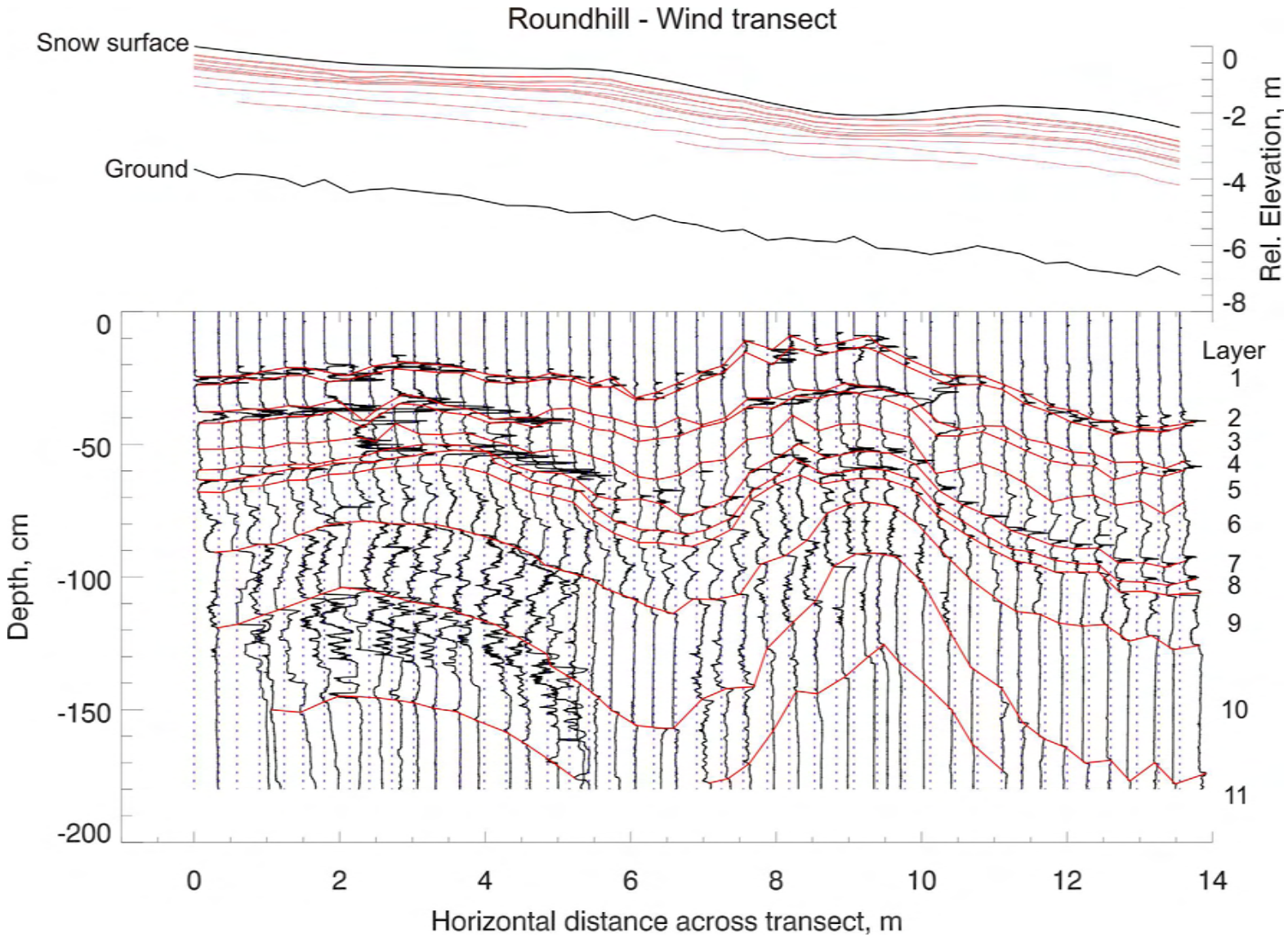

Figure 5.11: Wind affected slope transect, 15-Mar-2007 at the Roundhill site. Upper pane shows snow surface and ground topography. Lower pane shows penetrometer profiles. Interpreted layer interfaces shown as solid red lines in both panes.

period of assumed quiescence (layer 3) and one representative of a period of assumed wind ridge growth (layer 10). A linear trend was removed from the layer thickness and force-resistance data prior to constructing the variograms, which are shown in Figure 5.12. The variogram for layer 3 thickness (Figure 5.12a) shows very little spatial structure, indicating that variations in layer thickness for this layer are not spatially correlated. A similar lack of spatial correlation in this layer is also seen with force-resistance (Figure 5.12c). Layer 10, however, shows a definite spatial trends for both layer thickness and force-resistance. The variogram for layer thickness (Figure 5.12b) is dominated by a large peak at a spacing of approximately 4 m, suggesting a periodicity at approximately that wavelength. Interestingly, this periodicity is not as evident for force-resistance (although there is a small peak at a spacing of 6 m) despite the force-resistance appearing to be more variable over the wind ridges. The fact that the sill appears not to have been reached indicates that additional spatial variations are associated with the force-resistance of this layer, of a scale greater than the extent of the survey.

A plot of the coefficient of variability of layer thickness plotted against mean layer depth for the first ten layers identified in the Roundhill wind transect is shown in Figure 5.13. Layers showing a high coefficient of variability of layer thickness are associated with high energy deposition environments (high winds). The plot shows four layers that show particulary high coefficient of variability: layers 1, 6, 9 and 10. It is likely that these layers were deposited during storms associated with high wind speeds.

5.4.3 Rain runnel transect

Small scale rain runnels were surveyed at the Fidelity Study Slope site using the SABRE penetrometer. This site was at 1885 m and faced east. A general view of the site and the specific transect are shown in Figure 5.14. The transect width was 1.3 m and the spacing was 5 cm; because of the small spacing, great care was necessary to ensure that

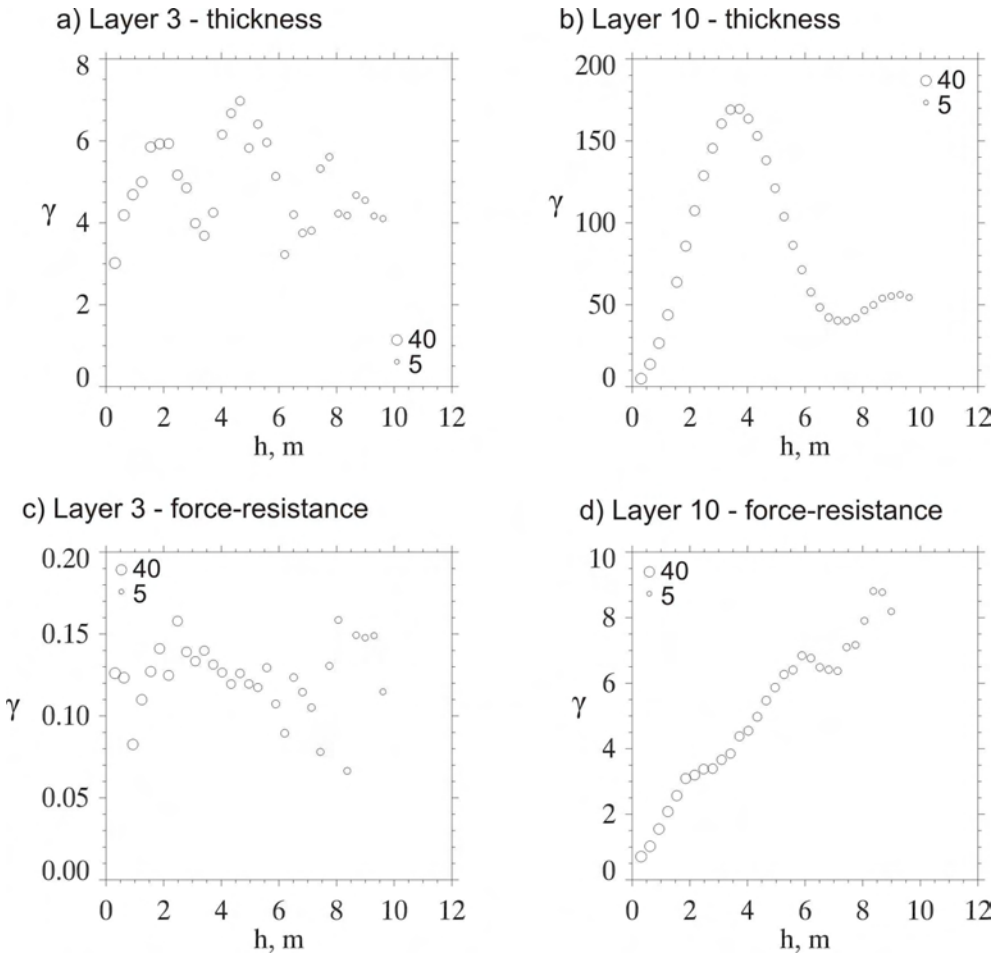

Figure 5.12: Variograms for trend-removed snow properties from the Roundhill wind transect: a) Layer 3 thickness; b) layer 10 thickness; c) layer 3 force-resistance; and d) layer 10 force-resistance.

the penetrometer pushes were vertical and that the surrounding snow was not disturbed during the survey.

Hourly meteorological data from a nearby automatic weather station showed that starting at 1300 hrs on 11-Mar-2007, approximately 23 mm of rain fell over a 15 hour period. During this time, temperatures reached 2°C. On the next day (12-Mar-2007), temperatures dropped rapidly to -10° and a further 20 cm of snow fell with light winds. The survey was undertaken on 13-Mar-2007, under broken skies, with an air temperature of -4.9°C. In the location used for the survey, the snow surface was flat. The runnels

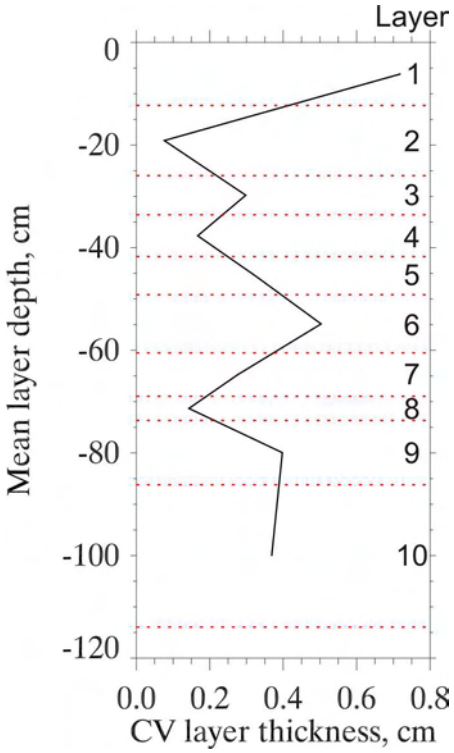

Figure 5.13: Plot of coefficient of variability (CV) of layer thickness against mean layer depth for layers identified in the Roundhill wind transect.

that were caused by the rain event had been filled in with the 10 cm of fresh snow at this location. The manual snow profile that was done immediately in front of the runnel transect is shown in Appendix E, Figure E.4.

The transect is shown in Figure 5.15. Since the surface topography relative to the transect line was flat, the interpreted layer interfaces in the lower pane represent the actual shape of the subsurface features. The upper layer interface represents the snow surface at the end of the rain event, which can be characterised as a stiff, undulating crust that froze during the cold temperatures following the rain event. Two percolation zones are evident (labeled PZ in Figure 5.15); these have eroded (melted) a second crust visible below the rain crust, which would have been in existence prior to the rain event. At the time of the transect, the moisture in these percolation zones had not yet refrozen. The temperature profile from a nearby manual snow pit indicates that snow

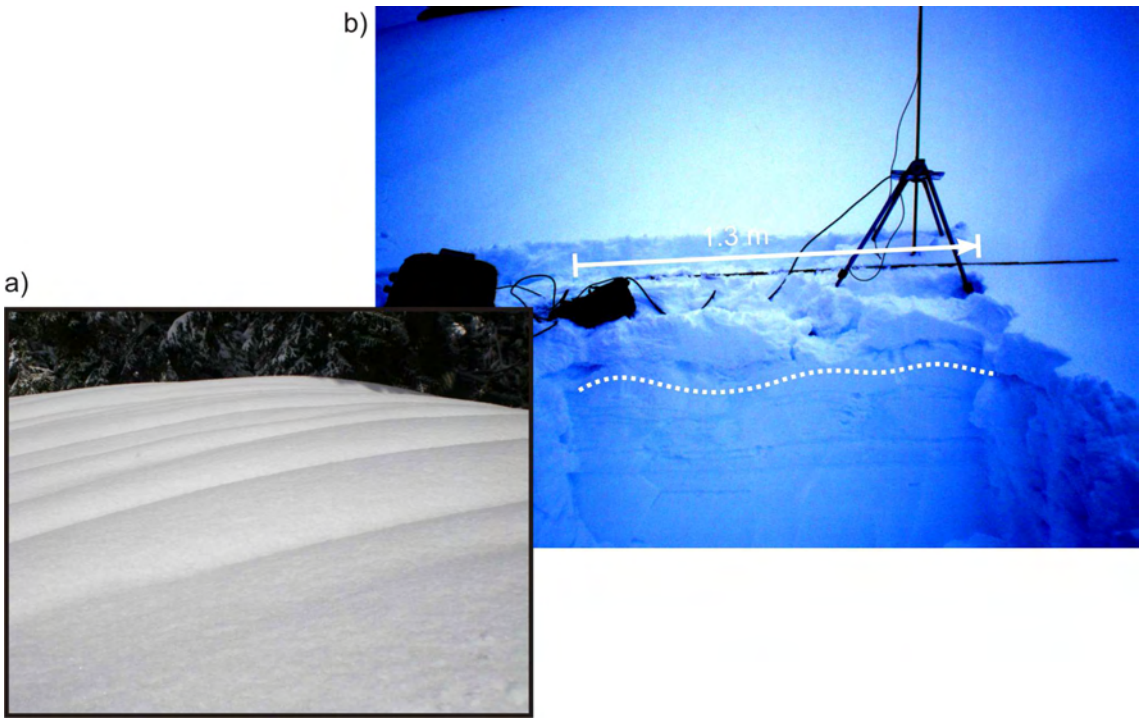

Figure 5.14: Photos of the runnel feature at the Fidelity Study Slope site: a) general view of slope runnel features just prior to survey; b) section showing the actual runnel features surveyed, the transect location and the penetrometer apparatus (contrast enhanced to show layers). Note the smooth snow surface at the survey location. ASARC photos.)

temperatures were very close to 0°C at a depth of 30 to 50 cm. For the runnel on the right, percolation continued below another stiff layer at 60 cm. The water below this layer refroze, evident by the discontinuous crust visible at a depth of 65 cm. Since 20 cm of snow fell between the rain event and the time of the survey, this means that the total depth of rain penetration was 50 cm. The proportion of the cross-sectional area of the transect affected by infiltration is approximately 30%.

These observations are consistent with results from Conway and Benedict (1994), who found that ice crusts in the snow formed barriers to the vertical infiltration of water. Once ice crusts are broached, vertical infiltration proceeds rapidly until a new crust or stiff layer is reached, at which point water moves in a slope-parallel direction. Conway and Benedict reported total infiltration depths of approximately 40 cm for a storm when

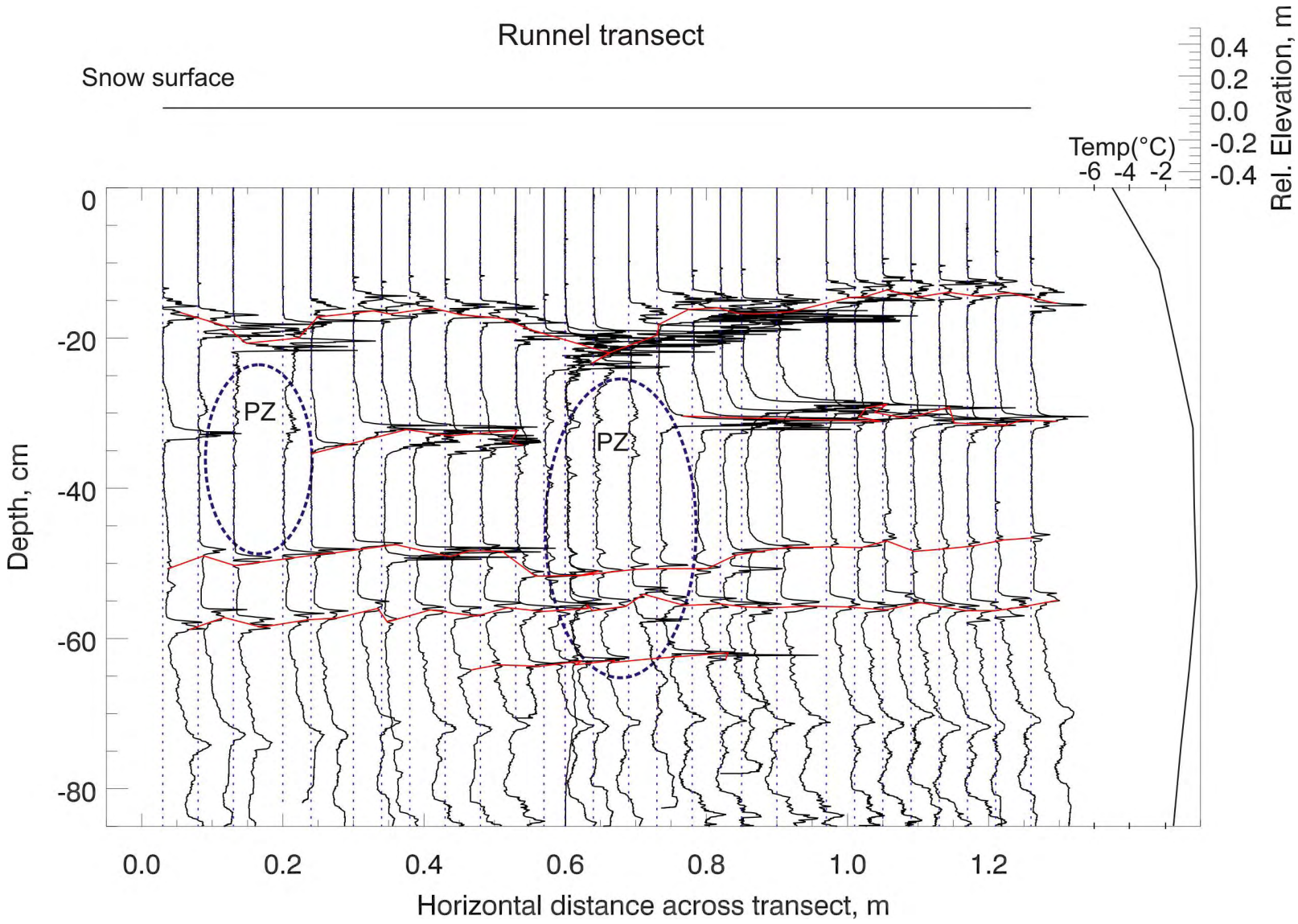

Figure 5.15: Runnel transect, 13-Mar-2007 from the Fidelity Study Slope site. Upper pane shows snow surface (flat). Lower pane shows penetrometer profiles as well as a temperature profile from a nearby manual snow pit. Interpreted layer interfaces shown as solid red lines. Interpreted location of percolation zones (PZ) shown with blue dashed ellipses.

19 mm of rain fell over a 10 hour period and suggested that water channels often occupied less than 50% of the total volume of the snowpack.

It is likely that if there is a weak layer present in the snowpack, the initial effect of a rain event of this type results in a significant short-term reduction in snow stability. This is due to rapid loading of the snowpack, resulting in dramatically increased applied shear stress and strain rates at the weak layer. Once the water begins to freeze, however, the snow gains significantly in strength, and the vertical columnar structures are effective at supporting the snowpack, increasing snow stability.

5.4.4 Gully transect

Figure 5.16 shows the Above Fidelity Station site, where the gully transect was surveyed. The gully was approximately 17 m wide, with a vertical drop of 3 m from the top of the gully sides to its base. The two sides of the gully faced east and south respectively. Maximum slope angle was 34° on the east-facing slope and 30° on the south-facing slope. The Above Fidelity Station site was at an elevation of 1910 m and the terrain surrounding the gully had a slope angle of 8°. During the survey, the weather was clear, with an initial air temperature of 0.2°C. Two manual profiles were collected at this site: one near the top of the east-facing slope and one near the base of the south-facing slope. These manual profiles are shown in Appendix E, Figures E.5 and E.6 respectively.

The transect across this terrain feature is shown in Figure 5.17. There are a few things that can be noted from this transect. There are two prominent crusts visible on the south-facing slope, which are not visible on the east aspect. The upper surface hoar layer (buried on 13-Mar-2006) is visible across the whole transect. A prominent density change is visible at depths of 65 to 75 cm on the east-facing slope; on the south-facing slope, the depth to this layer is approximately 55 cm. Other layers in the transect show a similar reduction in depth. Below this density change there is another surface hoar layer

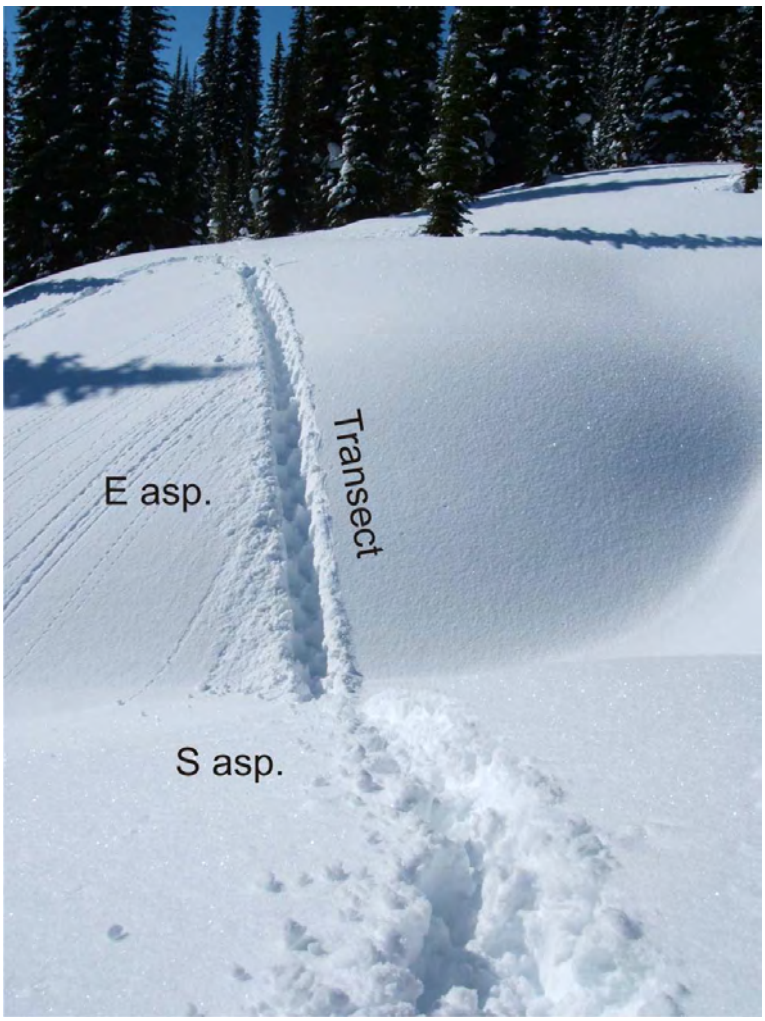

Figure 5.16: Photo of the Above Fidelity Station gully transect site, surveyed on 20-Mar-2006. Slope aspects indicated. Transect was surveyed toward the foreground of the photo. ASARC photo.

in the snowpack (buried on 10-Feb-2006), which is not continuous across the transect, but fades out towards the base of the gully.

The presence of the crusts on the south-facing slope, as well as the reduction in layer depth on this aspect, indicates that increased daytime solar warming has caused melt-freeze cycles on the south-facing side of the gully, causing the crusts and resulting in increased rates of settlement. The discontinuous lower surface hoar layer is partly evident on the south facing slope, a little way up from the base of the gully. This indicates that

the reason why the surface hoar is not evident at the base of the gully may not be due to aspect. Instead, it is more likely that extra loading on this layer due to the presence of melt water in the centre of the gully caused compaction resulting in the destruction of the surface hoar at this point. This is supported by evidence from the manual snow profile done near the base of the south-facing slope, which shows wet layers in the snowpack at depths between 30 to 40 cm (Figure E.6).

About half way up each side of the gully, the depth of the layers is at a minimum (just barely, possibly within the range of measurement error). This location corresponds with the location of well developed surface hoar layers on both aspects. These points are likely the most unstable locations on the feature, although no signs of instability were observed during testing.

5.4.5 Boulder field transect

A transect was collected over a boulder field on 26-Jan-2007 (Figure 5.18). As can be seen in the photo, there was considerable ground roughness associated with this site. The elevation was 1315m and the site faced east. Average slope angle was 29°. A manual profile was taken at the left hand side of the transect on the day after the transect was collected. This is shown in Appendix E, Figure E.7.

The transect (Figure 5.19) shows a couple of interesting features. First, the lowest layer that can be readily distinguished in the profiles and traced continuously across the transect lies at a depth of between 110 and 120 cm below the snow surface. Above this level, layer thickness is quite consistent, except for the top layer, and the layers show gently undulating characteristics consistent with the broad shape of the topography. The top layer is considerably thicker above the troughs in the underlying layers, indicating that recently, snow has filled in some of the undulations. Below the interface at 110 to 120 cm, layer thickness varies dramatically, consistent with regions that were rapidly

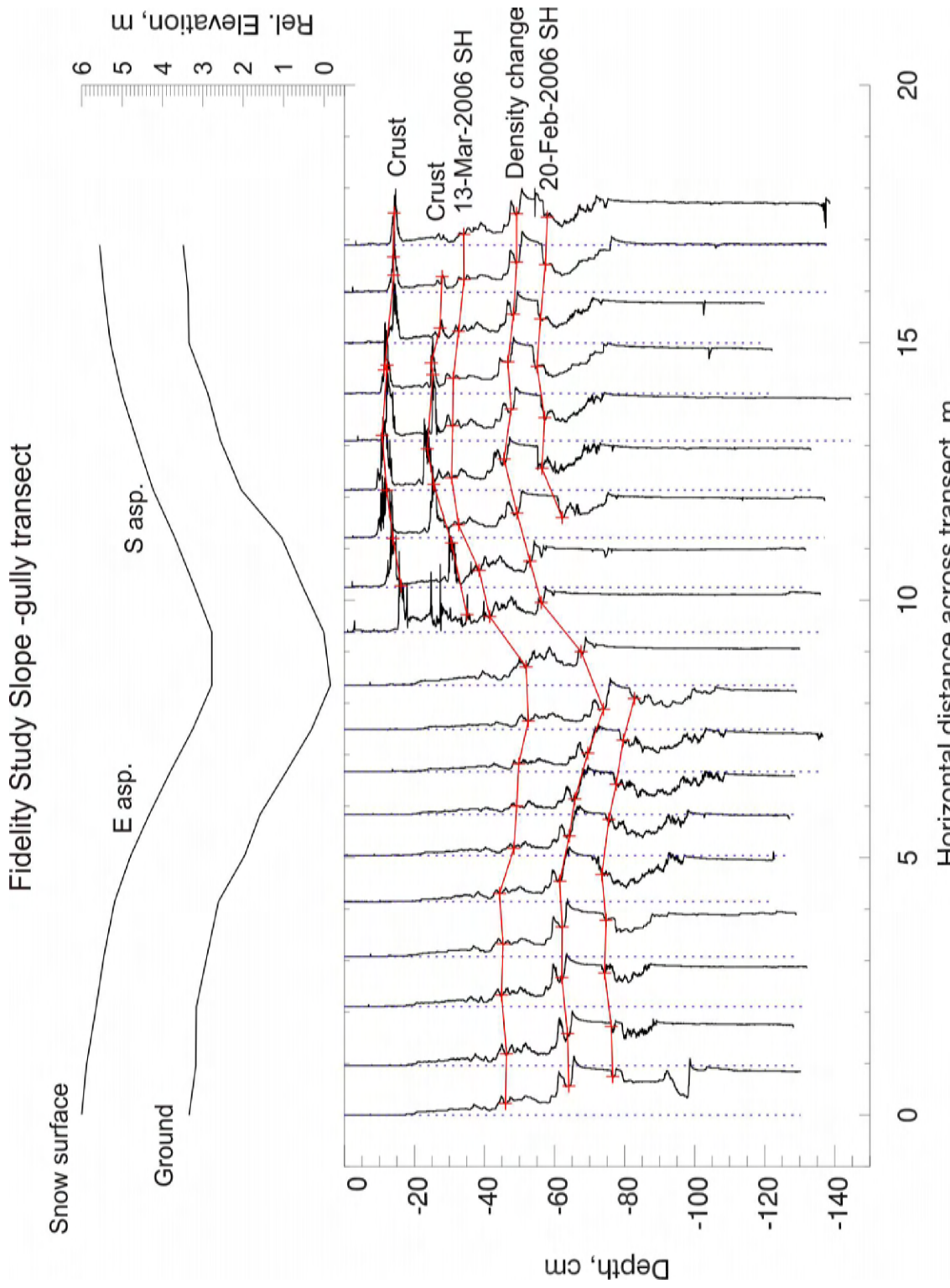

Figure 5.17: Gully transect, 20-Mar-2006 from the Above Fidelity Station Site. Upper pane shows snow surface and ground topography. Lower pane shows penetrometer profiles. Interpreted layer interfaces shown as solid red lines in both panes.

Figure 5.18: Photo of the Loop-Ross boulder field site, surveyed on 26-Jan-2007. Approximate location of the transect shown by the solid white line, with direction of the transect indicated with the arrow. ASARC photo.

filled in when the snowpack depth was lower.

Second, there is a characteristic signal at the base of several of the profiles. The signal at these points is characterised by a widely fluctuating force-resistance; the thickness of this layer, where it exists, is approximately 10 to 15 cm. Note that some of the penetrometer pushes did not penetrate to the base of the snowpack and therefore were not able to measure this layer (indicated by dotted lines that extend below the penetrometer signal on Figure 5.19). On the manual profile (Figure E.7), this layer was marked as a crust, probably formed during an early season rain event in November 2006. At the base of this layer, there are some areas which show very low sections of force-resistance, e.g. at 2.2 and 3.3 m from the start of the transect. These are possibly locations where depth hoar has grown, reducing the strength of the crust. These areas are commonly in the troughs between the boulders, although some are found on the top of the boulders. Since

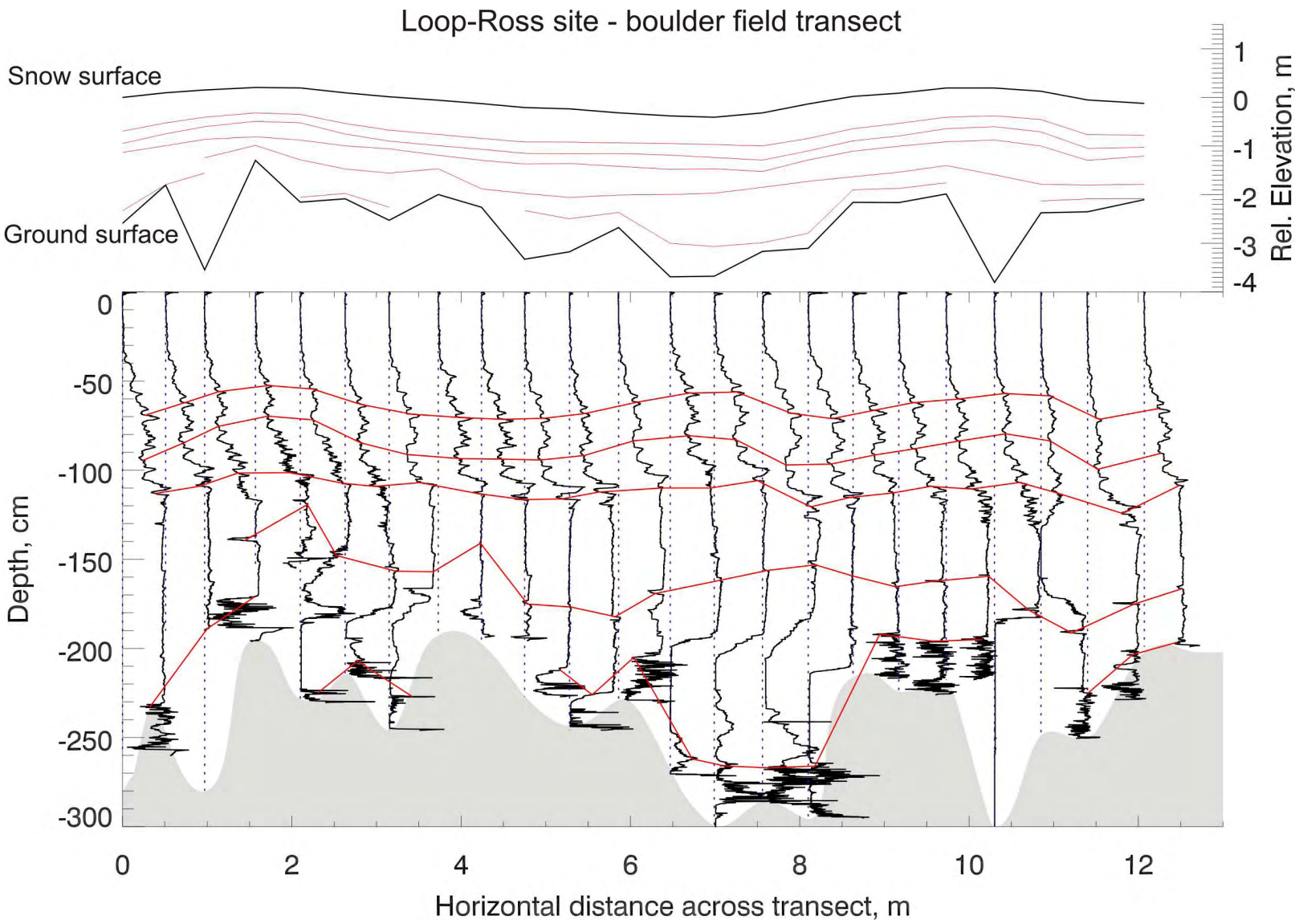

Figure 5.19: Boulder field transect, 26-Jan-2007 from the Loop-Ross Site. Upper pane shows snow surface and ground topography. Lower pane shows penetrometer profiles and ground terrain relative to snow surface (grey region). Interpreted layer interfaces shown as solid red lines in both panes.

overall, the distribution is not consistent with the location of the tops of the boulders, and since cavities were noticed in both the manual profile and some of the penetrometer pushes, it is possible that depth hoar at this site developed close to the cavities, where cold air was able to infiltrate, producing high temperature gradients. In a high snow area such as this, this cavity mechanism may be important for depth hoar development since without the cavities, temperature gradients may not reach the level required for depth hoar development.

5.4.6 Aspect change

A transect was performed around all aspects of a knoll at a site known as Gopher Butte (Figure 5.20), at an elevation of 1940 m. There was sparse tree cover on the more westerly aspects of the knoll (Figure 5.20a); on the easterly aspects, there were only isolated trees (Figure 5.20b). Over the knoll, slope angles varied from flat at the top to approximately 30° on the sides. The transect was surveyed around the top of the knoll, with the aim of maintaining a constant elevation. Some small elevation changes occurred, but the total elevation variation was only 3 m. Along the line of the transect, slope angle varied from 11 to 20° with a median of 15°. Due to technical problems with the penetrometer, the transect was surveyed over two days, with the first 18 pushes obtained on 21-Feb-2007 and the remainder, a further 28 pushes, obtained on 22-Feb-2007. Two manual snow profiles were done, one on the first day close to the third push on a northwest aspect (Appendix E, Figure E.8) and one close to push 26 on a southeast aspect (Appendix E, Figure E.9).

The aspect transect is shown in Figure 5.21. Four layer interfaces were identified, marking the lower boundaries of layers 1 to 4 on Figure 5.21. Not all the layer boundaries could be identified over all aspects. The interface between layer 1 and layer 2 was not visible on west and southwest aspects and the lower layer boundary of the lower layer was

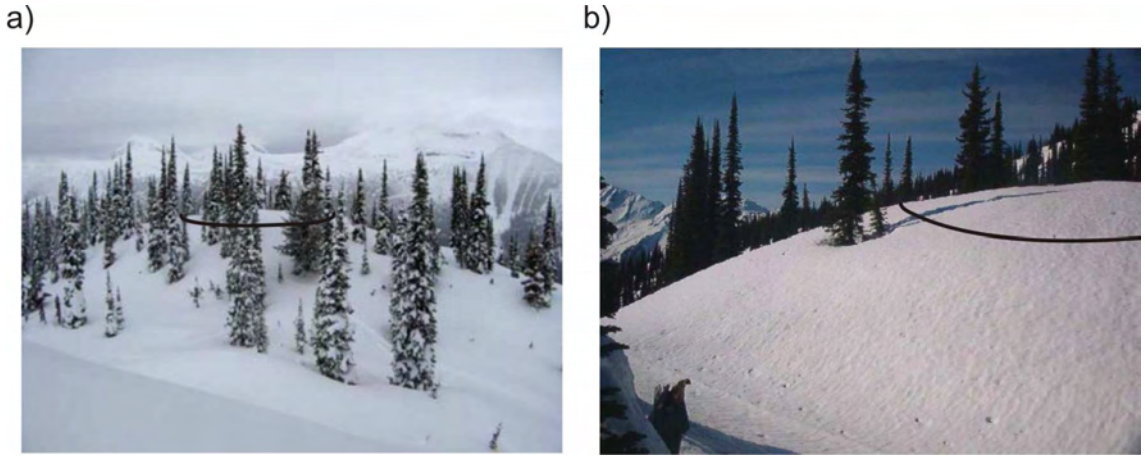

Figure 5.20: Photos of the Gopher Butte aspect transect site: a) west-facing slopes; b) east-facing slopes. Approximate location of transect shown. ASARC photos.

not visible on east, north and northwest slopes. The depth of the layer interfaces varies considerably with aspect, as does the height of snow. By visual inspection (since the layers were not all continuous), layer thickness on north aspect slopes is approximately 1.5 times the layer thickness on south aspect slopes.

The shape of the layer interface depth variations suggest a relationship between the cosine of the aspect, θ, and interface depth. A plot of $cos(\theta)$ against the lower interface depth for layer 2 is shown in Figure 5.22a). A linear regression line was fitted ($p<0.001$) with $R^2=0.76$. The amount of incoming solar radiation also follows a relationship with the cosine of the solar zenith angle (Bakermans, 2006, p.162). Therefore it is likely that variations in incoming solar radiation account for some of the variations in layer interface depth seen in Figure 5.21.

An alternative interpretation is that the prevailing wind direction has an effect on wind transport. A plot of the number of degrees from southwest against the interface depth for layer 2 is shown in Figure 5.22b). There appears to be a reasonable relationship between these two variables, $R^2=0.65$ in this case ($p<0.001$), suggesting that direction to the prevailing wind also has an effect on variability. It is quite reasonable that at a site like Gophur Butte, both solar radiation and wind transport would have significant

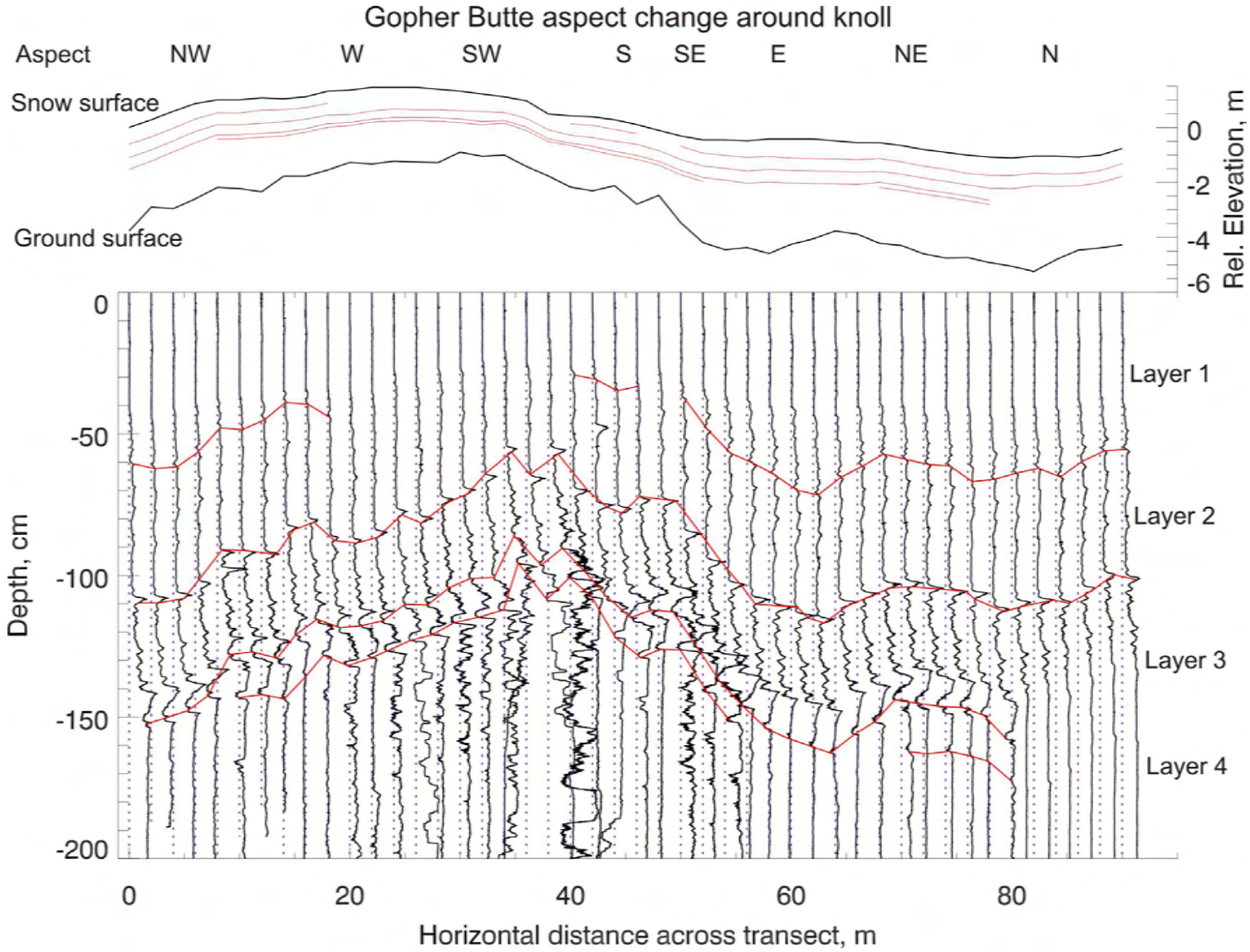

Figure 5.21: Aspect transect, 21 to 22-Feb-2007 around Gopher Butte Knoll. Upper pane shows snow surface and ground topography. Lower pane shows penetrometer profiles. Interpreted layer interfaces shown as solid red lines in both panes.

impacts on controlling layer depth.

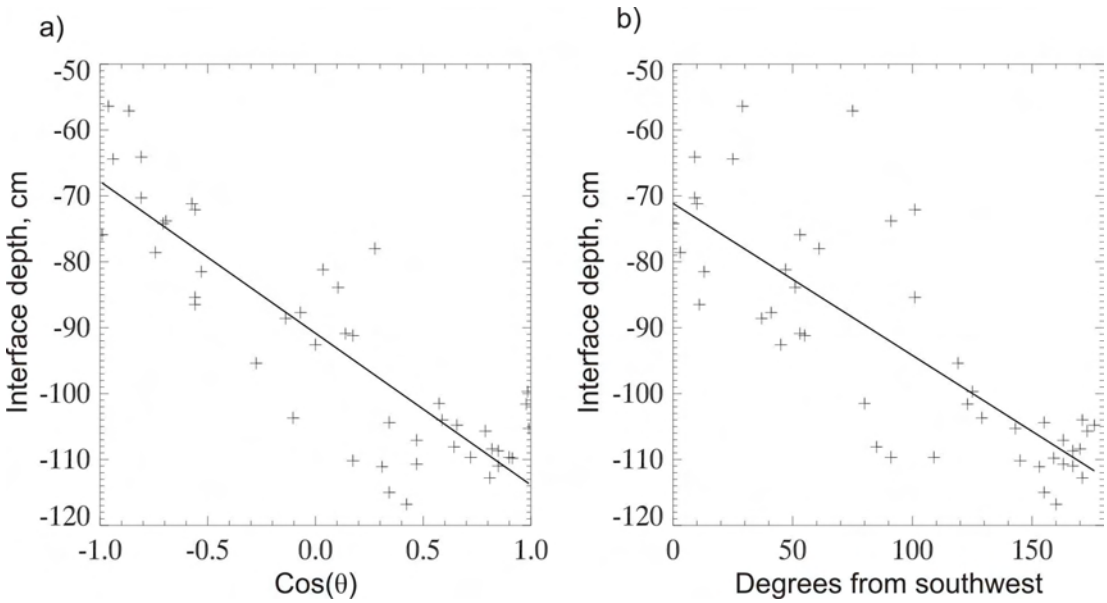

Figure 5.22: Plots of a) cosine of the slope angle with interface depth (R^2=0.76) and b) degrees from southwest with interface depth (R^2=0.65), for the lower interface of layer 2 for the Gopher Butte aspect transect.

5.4.7 Elevation change

A basin-scale elevation transect was done on Mount Fidelity on 13-Mar-2007. The transect was surveyed at different points along the road leading up to the Fidelity observation station. The site locations used for the survey were not exactly in a straight line, since the road has many switchbacks, and suitable sites (approximately uniform slopes away from trees) were not available at all points along the road. However, the broad nature of the flank of the mountain meant that aspect changes were not too severe. Seven profiles were collected at sites with aspects ranging from 45° to 110°. All the sites were in sheltered locations. A manual snow profile was collected at the highest site along the transect, at an elevation of 1850 m (Appendix E, Figure E.10).

The transect is shown in Figure 5.23. Despite the large changes in elevation between the sites, certain layer interfaces could be traced across the transect. The features that

were possible to trace across the whole transect were prominent crusts. It appears as though these features can be quite spatially consistent at the basin scale (especially towards the end of the winter, when temperatures across a wider elevation band are likely to be warmer). Some crust layers, particularly those towards the base of the profiles, were only visible at lower elevations. The profiles show a general trend of increasing height of snow with elevation. The depth to the layer interfaces mirrors this trend and the variations with elevation appear to be quite linear. On average, the upper three layer interfaces were 3.5 times thicker at 1850 m than at 1120 m.

Coefficients of determination from simple linear regression of the layer depth with elevation produced R^2 values of between 0.96 to 0.99 for the four upper layer interfaces. R^2 for the relationship between the the height of snow and elevation was 0.86. The ratio of layer interface depth to snow depth is approximately consistent for each layer. The trend of increasing snowpack depth with elevation is expected. Snowfall amounts are generally much higher at high elevation weather stations compared with those lower in the valleys. Additionally, ablation rates are lower, due to lower temperatures. The degree of linearity is perhaps surprising, however, since snowfall amounts vary due to complex interactions between temperature, humidity and orographic influences. The transect was surveyed in mid March. It is likely that differences between accumulation and ablation are more pronounced at different elevations at that time of year compared to earlier in the winter, when less ablation takes place.

5.5 Summary and conclusions

An effective method for measuring and visualising the spatial variability of snow properties over alpine terrain features has been presented. Snowpack property variability associated with these features has been related to physical processes. Transects such as

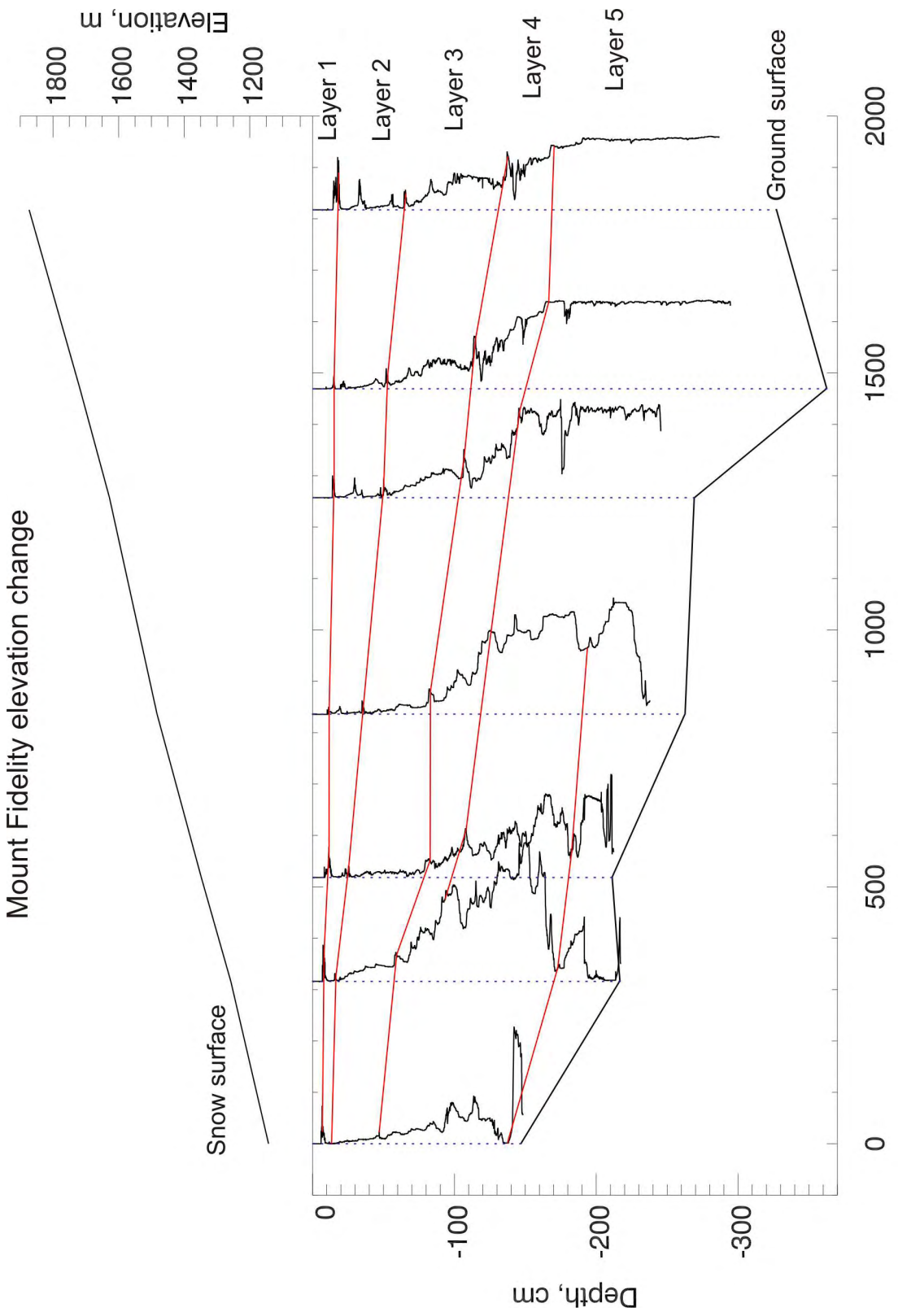

Figure 5.23: Elevation transect, 13-Mar-2007 from 1120 to 1850 m elevation on Mount Fidelity. Upper pane shows elevation change. Lower pane shows penetrometer profiles. Interpreted layer interfaces shown as red lines.

the ones presented in this study can be used as case histories, which may help avalanche practitioners to develop mental images of snowpack variability, enabling them to make better field assessments of slope stability.

Layer interfaces were traced across most transects with a high degree of spatial continuity. However, layer depth, thickness and penetration resistance were found to vary considerably over most of the features surveyed. Features that were particularly associated with high spatial variability were: wind ridges, aspect changes, elevation changes, snow surrounding boulders and runnels caused by rain events.

Snow properties were measured over a tensile fracture associated with an avalanche, where the weak layer on one side of transect was presumed to have fractured but not on the other, and were found to vary across the fracture. The mean force-resistance was significantly greater (a difference of 1F to 1F+) in the weak layer for the unfractured snow compared to the fractured snow. Force-resistance values also increased across the fracture for the substratum but not for the slab. The weak layer was found to be thinner on the unfractured snow, allowing conjecture that the surface hoar crystals were smaller at this point, giving a possible reason for fracture arrest.

Runnels caused by a rain event were surveyed and the maximum depth of water infiltration was found to be 50 cm. Infiltration was found to be largely confined to vertical percolation channels, except for a surface layer, which formed a strong crust on refreezing. Between the rain surface and the maximum infiltration depth across the transect surveyed, 30% of the cross-sectional area was affected by water infiltration.

Across one wind affected slope, the hardness of wind-deposited areas was found in general to be greater than that of wind-scoured areas, although smaller features were superimposed onto this general trend that showed the opposite effect. On a second wind affected slope, wind ridges were shown to have been built up during discrete storm periods, interspersed with periods of relative quiescence. The layers associated with

storms were strongly spatially correlated, whereas layers deposited in conditions assumed to be calmer were not spatially correlated within the measurement scale.

Over a transect done at constant elevation around all aspects of a knoll, weak layer depths were found to vary according to the cosine of the aspect. Layer thickness on north aspect slopes was approximately 1.5 times that of layer thickness on the south aspect slopes. This was related to the combined effects of changes in the degree of incoming solar radiation and to the direction of the prevailing wind.

Elevation changes over a basin-scale transect produced linear changes in the height of snow as well as to layer interface depths in the upper snowpack.

For the transects analyzed using geostatistics, splitting the transects into layers was found to be important, since variability and spatial correlations were layer dependent. However, it may be beneficial to find a way to analyze the transects without having to manually identify layer interfaces. This would remove the subjectivity associated with determining the layer depths, especially for layers that are not well defined. One possible approach for this could be to pixelize the transect; the pixels would have a horizontal dimension equal to the profile spacing, a vertical dimension slightly greater than the vertical error (say, 5 cm) and a value equal to the mean force-resistance over that interval.

Chapter 6

Conclusions

6.1 Penetrometer validation

The SABRE penetrometer used in this study was effective for reliably characterising variations of force-resistance with depth in the snowpack. Subsequent to modifications of the depth measurement system, depths to layer interfaces could be determined with an accuracy of ± 1 cm and a precision of 1 mm. Weak layers of a thickness of 5 mm or greater could be reliably detected in the penetrometer signal. In snow with a hardness of 4 finger or greater, the high resolution nature of this instrument gives a far more detailed hardness profile compared with manual hardness measurements. However, due to the relatively heavy tip, the penetrometer was not able to measure snow with a hand hardness less than 4 finger.

The inability of the SABRE penetrometer to reliably detect weak layers less than 5 mm thick may be a detriment for operational use of this instrument for avalanche forecasting, since weak layers less than 5 mm thick are frequently identified by forecasters as potential avalanche failure planes. This is especially true for facet-crust combinations, where the layer of facets, either above or below the crust, is often quite thin. With prior knowledge of the existence of such a weak layer, it would be possible, using the SABRE penetrometer, to detect the crust and infer the presence of the weak layer from that. However, this approach would not provide any quantitative information about the hardness of the weak layer.

During a typical field day, up to 80 penetrometer profiles could be collected at a site; this number could easily be increased if surveying of the topography was not required

(or done by another operator). The ability to collect a large number of profiles quickly is important when studying the spatial variability of snowpack properties, since these properties also vary over time.

6.2 Rate effects and snow deformation analysis

Rate effects were not found to have a significant impact on force-resistance measurements for velocity ranges of 0.5 to 100 cm s^{-1} for the dry snow layers tested and 5 to 100 cm s^{-1} for the moist snow layer tested (Section 3.4.1). From these results, the recommended operational push velocity for the SABRE penetrometer is given as 30 to 100 cm s^{-1}; the increased lower end of this velocity range is in view of the sufficient momentum required to maintain steady velocity for transitions into more resistant snow. The penetrometer should not stop during the course of a push.

Patterns of snow deformation ahead of the penetrometer tip were assessed using particle image velocimetry (Section 3.4.2). Two distinct zones associated with snow particle deflection around the SABRE penetrometer's 12 mm rounded tip were found: a compacted zone, characterised as a plug of densified snow that is pushed ahead of the penetrometer tip; and a deformation zone, a broader zone beyond the compacted zone, formed by radial outward pressure from the snow in the compacted zone. The compacted zone was found to extend approximately 1 cm beyond the end of the tip for high density dry snow and approximately 2 cm beyond the end of the tip for low density moist snow.

Deformation below the penetrometer tip was found to be in compression and in shear. At the lateral margin between the compacted zone and the deformation zone, rates of shear were particularly high. Low-confidence estimates for typical strain rates below the penetrometer tip were made and found to be in the order of 0.1 to 1 s^{-1} for both compressive and shear strain rates (Section 3.5.2).

In the initial stages of penetrometer movement, prominent spikes in the force signal were seen for more resistant snow. These spikes were associated with the development the compacted zone ahead of the penetrometer tip. At some point, shear forces exceed the strength of the snow being compacted, and a plug of densified snow is pushed ahead of the rounded penetrometer tip. The spikes were contained within the first 6 cm of data from the penetrometer signals. It was suggested that this effect may also be seen for rapid transitions between low resistance and high resistance snow, although this was not tested.

6.3 Layer detection and identification

In order to help trace weak layers, crusts and other layers of interest across transects of penetrometer profiles, a layer tracing algorithm was developed (Section 4.3). The algorithm used a deconvolution technique to highlight the position of a wavelet (a small portion of the signal representing the weak layer/interface), on a profile onto which the layer was being traced. This method was successful in tracing layers across transects in 13 out of 15 cases tested. The layer tracing algorithm performed well for crusts and prominent weak layers; however, it did not perform as well tracing indistinct layers and weak layers that were next to a crust. For weak layer–crust combinations, it may often be possible to trace the crust and infer the position of the weak layer from the crust.

A framework for extending the layer tracing method to the case of detecting weak layers with no prior knowledge of weak layer existence was presented (Section 4.4). In this framework, the profile being analyzed would be tested against a database of weak layer wavelets identified by expert interpretation from previous penetrometer profiles, with the wavelets in the database corresponding to unstable layers associated with avalanche activity. If an element in the signal being tested was found to be similar in shape to

one of the unstable weak layer wavelets, this layer would be flagged as a potential failure interface and appropriate further investigation could be undertaken.

A method for predicting the fracture character of failure interfaces associated with compression tests was presented that was able to discriminate between *sudden* and *other* fracture character groups for 80% of cases (Section 4.5). Weak layer thickness, maximum hardness gradient 5 mm below the weak layer and the average hardness gradient 20 mm above the weak layer contributed the most to discriminating between the two groups. For this model, it was assumed that the depth of the potential failure plane is known; it is expected that model performance would drop considerably when the depth to the interface is not specified.

It would be possible to devise an operational model to combine layer detection, using the framework outlined in Section 4.4 with the predictive fracture character model described in Section 4.5. In that way, critical weak layers could automatically be detected from the pentrometer signal and assessed to see whether they were likely to be associated with sudden fractures. This could potentially allow rapid screening of penetrometer profiles, for example, by a ski hill operation checking ski runs to ensure there was no continuous facet or surface hoar layer present in the snowpack.

6.4 Case studies of spatial variability

When penetrometer profiles collected in a transect across an alpine terrain feature are appropriately displayed, variations in the layered structure of snow over the feature can be readily visualised. This has an application for training avalanche practitioners by providing case studies of snowpack variability. Such case studies can help practitioners develop mental images of how the snowpack varies over certain terrain features, allowing better assessments of stability to be made.

Patterns of variability were assessed over wind affected slopes, a gully, a slope with rain runnels, a boulder field, elevation and aspect changes, and the unreleased snow adjacent to the flank of an avalanche. The continuity of layers across features was generally high, even when considerable changes in layer depth, thickness and force-resistances were observed. Using geostatistics, some layers were found to have a strong spatial correlation structure and others were found to have little spatial correlation. For conclusions regarding observations about these individual terrain features, please refer to Section 5.5.

6.5 Recommendations for further work

6.5.1 Penetrometer design

The following recommendations are presented regarding improving force-resistance penetrometer design. Since the recommendations encompass many aspects of the penetrometer design, if these changes were implemented it may be advantageous to design an instrument from scratch to accommodate them. Alternatively, the SnowMicroPen (SMP) could be considered for future studies, which already includes many of the design points listed below.

- The size of the penetrometer tip should be significantly reduced and its shape made sharper. This will reduce the size of the compacted zone of snow ahead of the tip.

- A blade design should be considered for the penetrometer tip. This would require redesigning the lower penetrometer shaft in a way that will prevent rotational and torsional forces from affecting force transmission to the load cell.

- The recording frequency should be substantially increased to help detect thin weak layers and to eliminate the interpolation errors associated with the depth measurements. This would require changes to the load cell, electronic circuits, analogue to

digital conversion and the data recording device.

- The size and complexity of the depth measuring platform should be decreased. Ideally having no measuring platform is preferred, and further investigations into the source of the error in the accelerometer signal might help determine whether this approach can be revived with sufficient accuracy. If not, then redesigning the existing depth platform to be smaller and easier to use is an option, or else optical or electromagnetic technology might be employed to measure the penetrometer depth.

6.5.2 Remote penetrometer installation

Considerable value (from an operational point of view) could be added to penetrometer measurements if they could be collected remotely, without the need for a human operator. This could be accomplished by means of a remote penetrometer installation; such an installation could be located in an area that may otherwise be inaccessible for human operators due to slope stability concerns or because of the time taken to reach a far away site. An appropriate design would incorporate a mechanism for selecting push locations in previously unsurveyed snow; this could be an articulated arm, or a track along which the penetrometer could slide. Additionally the penetrometer would need to be automatically driven into and retracted from the snowpack, and the information relayed to the control centre. Significant engineering challenges would have to be overcome to design such an installation to be reliable and able to operate under extreme weather conditions.

6.5.3 Anisotropic nature of weak layers

The snowpack property measured by force-resistance penetrometers such as the SABRE penetrometer is the vertical (or slope normal in the case of the SMP) compressive strength. While this property is very useful for defining stratigraphic layers within the

snowpack, it may not be the best property for determining snow stability. The strength of weak layers, and in particular, persistent weak layers, is anisotropic. They are able to resist a considerable amount of vertical load; however, their resistance to slope parallel forces is far lower. This can result in very low slope-parallel shear strength; measurement of this property may give a better indication of the propensity for layer failure compared with vertical compressive strength.

Measuring a continuous log (to borrow terminology from borehole geophysics) of shear strength though the snowpack is a challenging problem. If perfected, however, it could offer significant benefits for avalanche forecasting by enabling rapid identification weak layers that are critical for avalanche formation. Two ideas are presented here that may help direct future research into this problem.

1. Inclined measurements (see Figure 6.1a). Shallow angle penetrometer pushes may allow the slope-parallel compressive strength to be measured. While this is not shear strength per se, it may be that slope-parallel compressive strength is more closely related to shear strength than vertical compressive strength. Simultaneous vertical and inclined pushes may better help determine the slope-parallel compressive strength by allowing the vertical component to be removed from the inclined signal (which would be a combination of vertical and slope-parallel components). Careful consideration of depth measurements would be required in order to match the depth signals, and also because the shallow push angle would amplify inaccuracies in the depth signal. A guide frame may be necessary to achieve the required depth accuracy and allow consistent push angles to be attained.

2. Rotating blade mechanism (see Figure 6.1b). It may be possible to design a penetrometer with a rotating blade that drives itself through the snowpack like a corkscrew. If the orientation of the penetrometer was slope normal and the blade

set so that it was almost slope parallel, but with the leading edge of the blade angled slightly downwards, the instrument would drive itself into the snow if the blade was turned. The resistance of the blade to turning could be measured continuously with depth.

Again, it is not immediately clear whether such an instrument would measure the true shear strength; more probably it would measure slope-parallel compressive strength. Therefore, significant modeling and testing would be required to determine the exact nature of the measurements and how they relate to shear strength. Additionally, careful consideration would need to be given to ensure that the deformation caused by one pass of the blade did not impact the snow strength for subsequent passes; this could be adjusted for by tuning the pitch of the blade. Penetration through resistant crusts may be problematic with this design.

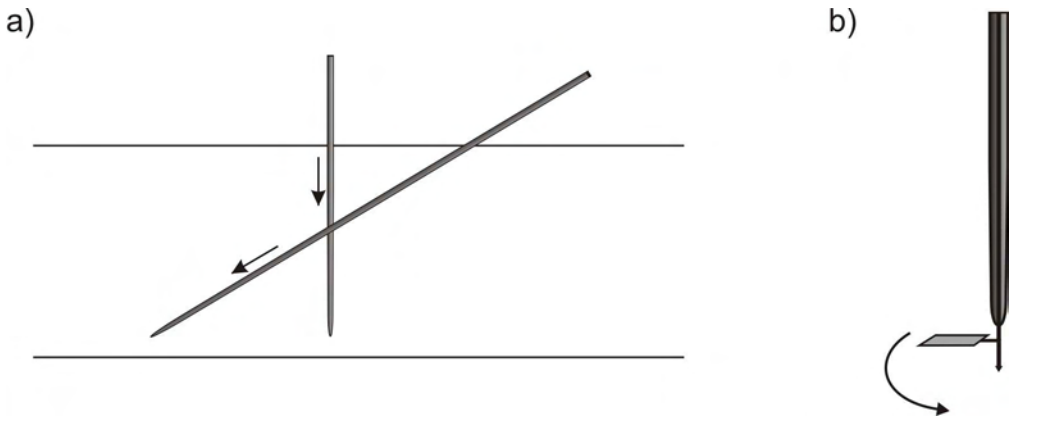

Figure 6.1: Ideas for penetrometer design for assessing the shear strength of snow. a) Simultaneous vertical and inclined penetrometer pushes. b) Penetrometer design with a rotating, slope parallel blade.

6.5.4 Snow deformation analysis

The snowbox experiments to investigate snow deformation patterns should be repeated using a split-axis penetrometer. This would allow the effect of the initial build up of the

compacted zone to be investigated further. It would also allow reliable calculations of strain rates below the penetrometer tip to be made.

Further investigations should also be undertaken on the effect of layer transitions on snow deformation. Of particular interest is what happens when the penetrometer tip breaks through a crust. If there is a thin weak layer beneath the crust, does the ejection of crustal fragments prevent the weak layer from being detected?

It may be possible, with systematic analysis of deformation patterns across interfaces with different snow properties, to develop filters to enhance the accuracy of the penetrometer signal at layer transitions. This may lead to better detection of thin weak layers.

6.5.5 Weak layer identification from penetrometer signals

A weak layer detection model could be implemented using the framework described in Section 4.4 (see in particular Figure 4.3). This would require further data collection to build a database of penetrometer profiles containing weak layers associated with unstable slopes. Additionally, further work on refining the algorithm would likely be required. In particular, the relationship between spike strength and wavelet length needs to be investigated.

For effective weak layer detection, it is recommended that microstructural information, such as the length scale associated with grain bond ruptures (Jamieson, 1999), that has been detected by the SMP, be included in any weak layer detection model. By combining the deconvolution technique, which detects signal shape, and a model based on identifying characteristic microstructural parameters, a reliable method for detecting weak layers associated with avalanche activity is quite within the realm of possibility.

Improvements to the fracture character prediction model will also enhance the ability to assess critical weak layers from penetrometer signals. The model would benefit from

a larger data set, which would allow better model definition, better model validation, and allow discrimination between sudden planar and sudden collapse fracture character categories.

6.5.6 Spatial variability

Further transects, or in the future, grids of penetrometer profiles across alpine terrain features will be useful for helping assess the spatial variability of snowpack properties over different types of terrain feature. Improvements in visualisation techniques could allow interactive 3-D models of snowpack structure to be built. Such models could be a valuable tool for training people to avoid potentially unstable avalanche terrain.

Assessing the spatial variability of snow across transects could prove to be very useful for operations considering expanding into new terrain, such as a ski hill developing a new mechanical lift, or a heli-skiing operation considering a new run. Careful analysis of such transects could indicate potential problem areas, such as areas with unusually thin snow cover, areas prone to windslab formation, or areas of unusual variability over uneven terrain or due to wind drifting.

The spatial continuity of critical weak layers is of particular importance for determining the avalanche danger level. In order for rapid assessment of slope stability to be made by field technicians, survey data needs to be processed in real time in the field. For this to be achieved, further development of processing and visualisation techniques suitable for rugged, hand-held computers is required. Techniques for highlighting critical weak layers and assessing their spatial continuity are vital for helping realise the true potential of spatial penetrometer data.

Bibliography

Abe, O., 1999. A new generation rammsonde having multiple sensors, *Bosai Kagaku Gijutsu Kenkyujo Kenkyu Hokoku (Report of the National Research Institute for Earth Science and Disaster Prevention)*, (59), 11–18.

Abe, O., R. Decker, B. Sensoy, T. Ikarashi, D. Ream and B. Tremper, 1999. Snow profile observations for avalanche forecasts using the new generation rammsonde, *Seppyo no kenkyu (Researches on snow and ice)*, **61**(5), 369–375.

Armstrong, R. L. and B. R. Armstrong, 1987. Snow and avalanche climates of the western United States: A comparison of maritime, intermountain and continental conditions, Avalanche Formation, Movement andEffects (Proceedings of the Davos Symposium, September 1986)., no. IAHS Publ. no. 162.

Atwater, M. M., 1954. Snow avalanches, *Scientific American*, **190**(1), 26–31.

Bachmaier, M. and M. Backes, 2008. Variogram or semivariogram? Understanding the variances in a variogram, *Precision Agriculture*, –.

Bader, H., 1939. Mineralogical and structural characterization of snow and its metamorphism, Der Schnee und seine Metamorphose (Translation: SIPRE - Snow, Ice and Permafrost Research Establishment, 1954. Snow and its metamorphism, Corps of Engineers, US Army, Translation No. 14.), Beitrage zur Geologie der Schweiz, Geotechnische Serie, Hydrologie, Lieferung 3, Bern, 2–55.

Bader, H.P. and B. Salm, 1990. On the mechanics of snow slab release, *Cold Regions Science & Technology*, **17**(3), 287–300.

Bak, P., 1996. How Nature Works: the Science of Self-Organized Criticality, Copernicus.

Bakermans, L.A., 2006. Near-Surface Snow Temperature Changes over Terrain, (Master's thesis), Dept. Civil Engineering, University of Calgary, Calgary, AB, Canada.

Bažant, Z. P., G. Zi and D. M. McClung, 2003. Size effect law and fracture mechanics of the triggering of dry snow slab avalanches, *Journal of Geophysical Research*, **108**(B2), 2119–2129.

Birkeland, K. W., 2004. Comments on Using Shear Quality and Fracture Character to Improve Stability Test Interpretation, *The Avalanche Review*, **23**(2).

Birkeland, K. W., K. J. Hansen and R. L. Brown, 1995. The spatial variability of snow resistance on potential avalanche slopes, *Journal of Glaciology*, **41**(137), 183–190.

Birkeland, K. W. and R. F. Johnson, 1999. The stuffblock snow stability test: comparability with the rutschblock, usefulness in different snow climates, and repeatability between observers, *Cold Regions Science and Technology*, **30**, 115–123.

Birkeland, K. W., K. Kronholm, M. Schneebeli and C. Pielmeier, 2004. Changes in the shear strength and micro-penetration hardness of a buried surface-hoar layer, *Annals of Glaciology*, **38**, 223–228.

Blöschl, G., 1999. Scaling issues in snow hydrology, *Hydrological Process*, **13**, 2149–2175.

Blöschl, G. and M. Sivapalan, 1995. Scale issues in hydrological modelling: a review, *Hydrological Processes*, **9**(3-4), 251–290.

Bradley, C. C., 1966. The snow resistograph and slab avalanche investigations, Proceedings of the International Symposium on Scientific Aspects of Snow and Ice Avalanches, Davos, April 5-10, 1965, International Association of Hydrological Sciences, Publication 69, 251–260.

Brown, R. L. and K. W. Birkeland, 1990. A comparison of the Digital Restograph with the Ram Penetrometer, Proceedings of the International Snow Science Workshop (1990: Bigfork, Montanna, USA), 19–30.

Campbell, C., 2004. Spatial Variability of Slab Stability and Fracture Properties in Avalanche Start Zones, (Master's thesis), Dept. of Civil Engineering, University of Calgary, Calgary, Alberta, Canada.

Campbell, C., L. Bakermans, J. B. Jamieson and C. Stethem, 2007. Current and future snow avalanche threats and mitigation measures in Canada, *Tech. rep.*, Canadian Avalanche Centre for Public Safety and Emergency Preparedness Canada, Revelstoke, BC, 103 pp.

Campbell, C. and J. B. Jamieson, 2005. Spatial variability of rutschblock results in avalanche start zones, Proceedings of the International Snow Science Workshop (2004: Jackson Hole, Wyoming), 288–297.

Campbell, C. and J. B. Jamieson, 2007a. Spatial clusters of slab stability and snowpack properties within avalanche start zones, Proceedings of the International Snow Science Workshop (2006: Telluride, Colorado), 44–53.

Campbell, C. and J. B. Jamieson, 2007b. Spatial variability of slab stability and fracture characteristics within avalanche start zones, *Cold Regions Science and Technology*, **47**(1-2), 134–147.

Canadian Avalanche Association, 2002. Observation guidelines and recording standards for weather, snowpack and avalanches, *Tech. rep.*, A revision of: NRCC Technical Memorandum No. 132, 78 pages.

Canadian Avalanche Association, 2007. Observation guidelines and recording standards

for weather, snowpack and avalanches, *Tech. rep.*, A revision of: NRCC Technical Memorandum No. 132, 78 pages.

Chernouss, P. A., 1995. Spatial and time variability of avalanche predictors and accuracy of their estimatons., Sivardière, F., ed., Les apports de la recherche scientifique à la sécurite neige, glace et avalanche. Actes de Colloque, Chamonix, France, 30 mai–3 juin 1995., ANENA, Chamonix, France, 123–127.

Colbeck, S., E. Akitaya, R. Armstrong, H. Gubler, Lafeuille J., K. Lied, D. M. McClung and E. Morris, 1990. International classification for seasonal snow on the ground, *CR-REL Report MP 2794*, International Association of Scientific Hydrology.

Colbeck, S. C., 1991. The layered character of snow covers, *Reviews of Geophysics*, **29**(1), 81–96.

Conger, S., 2006. Field report on the validation of a Capacitec snow profile probe in an avalanche forecasting application., Proceedings of the International Snow Science Workshop (2006: Telluride, Colorado).

Conger, S., 2007. Validation of a Capacitance Snow Density Probe in an Avalanche Forecasting Setting, (Master's thesis), Dept. Geography, University of British Columbia, Vancouver, Canada.

Conway, H. and J. Abrahamson, 1984. Snow stability index, *Journal of Glaciology*, **30**(106), 321–327.

Conway, H. and J. Abrahamson, 1988. Snow-slope stability – a probabilistic approach, *Journal of Glaciology*, **34**(117), 170–177.

Conway, H. and R. Benedict, 1994. Infiltration of water into snow, *Water Resources Research*, **30**(3), 641–649.

Crocker, J. C. and D. G. Grier, 1996. Methods of digital video microscopy for colloidal studies, *Journal of Colloid and Interface Science*, **179**(1), 298–310.

Davis, J. C., 1973. Statistics and Data Analysis in Geology, John Wiley & Sons, Inc.

Dowd, T. and R. L. Brown, 1986. A new instrument for determining strength profiles in snow cover, *Journal of Glaciology*, **32**, 299–301.

Ellerbruch, D. A. and H. S. Boyne, 1980. Snow stratigraphy and water equivalence measured with an active microwave system, *Journal of Glaciology*, **26**(94), 225–233.

Federolf, P. A., 2005. Finite Element Simulation of a Carving Ski, (Ph.D. thesis), Swiss Federal Institute of Technology, Zurich.

Floyer, J. A., 2003. Statistical Avalanche Forecasting using Meteorological Data from Bear Pass, British Columbia, Canada, (Master's thesis), Dept. Geography, University of British Columbia, BC, Canada, 98 pages.

Floyer, J. A. and J. B. Jamieson, 2006. Empirical analysis of snow deformation below penetrometer tips, Proceedings of the International Snow Science Workshop (2006: Telluride, Colorado), 555–561.

Föhn, P. M. B., 1988. Snowcover stability tests and the areal variability of snow strength, Proceedings of the International Snow Science Workshop (1988: Whistler, British Columbia), 262–273.

Foster, R., M. Louge, K. Clifford and R. Decker, 2002. Rapid measurements of snow stratigraphy using a portable penetration field instrument, *EGS XXVII General Assembly, Nice, 21-26 April 2002, abstract #617*, **27**.

Fritton, D. D., 1990. A standard for interpreting soil penetrometer measurements, *Soil Science*, **150**(2), 542–550.

Fujino, K. and G. Wakahama, 1985. Snow stratigraphy measured by an active microwave system, *Annals of Glaciology*, **6**, 207–210.

Fukue, M., 1979. Mechanical Performance of Snow Under Loading, (Ph.D. thesis), Tokai University.

Fukue, M. and R. Yong, 1987. Mechanical and physical properties of snow, Snow property measurement workshop, April 1-3, 1985, Chateau Lake Louise, Alberta, Canada, NRCC Associate Committee on Geotechnical Research, no. Technical memorandum 140.

Fukuzawa, T. and H. Narita, 1993. An experimental study on the mechanical behaviour of a depth hoar layer under shear stress: preliminary report, Proceedings of the International Snow Science Workshop (1992: Breckenridge, Colorado), 171–175.

Fyffe, B. and M. Zaiser, 2004. The effects of snow variability on slab avalanche release, *Cold Regions Science and Technology*, **40**(3), 229–242.

Gauthier, D. M., 2007. A Practical Field Test for Fracture Propagation and Arrest in Weak Snowpack Layers in Relation to Slab Avalanche Release., (Ph.D. thesis), Dept. of Civil Engineering, University of Calgary, Calgary, Canada.

Gauthier, D. M. and J. B. Jamieson, 2008. Evaluation of a prototype field test for fracture and failure propagation propensity in weak snowpack layers, *Cold Regions Science and Technology*, **51**(2-3), 87–97.

Gill, W. R., 1968. Influence of compaction hardening of soil on penetration resistance, Transactions of the American Society of Agricultural Engineers, vol. 11, 741–745.

Gleason, J. A., 2005. Particle image velocimetry; a new technique to measure strain in

loaded snow, Proceedings of the International Snow Science Workshop (2004: Jackson Hole, Wyoming).

Greene, E., K. W. Birkeland, K. Elder, G. Johnson, C. Landry, I. McCammon, M. Moore, D. Sharaf, C. Sterbenz, B. Tremper and K. Williams, 2004. Snow, Weather and Avalanches: Observational Guidelines for Avalanche Programs in the United States, American Avalanche Association and USDA Forest Service National Avalanche Center.

Grenander, U. and H. Cramér, 1959. Probability and Statistics: The Harald Cramér Volume, Wiley.

Gringarten, E. and C. V. Deutsch, 2001. Teacher's aide variogram interpretation and modeling, *Mathematical Geology*, **33**(4), 507–534.

Gubler, H., 1975. On the rammsonde hardness equation, Snow Mechanics Symposium; Proceedings of the Grindelwald Symposium, Grindelwald, Bernese Oberland (Switzerland) April 1974: International Association of Hydrological Sciences Publication No. 114, 110–121.

Gubler, H. and M. Hiller, 1984. The use of microwave FMCW radar in snow and avalanche research, *Cold Regions Science and Technology*, **9**(2), 109–119.

Habermann, M., J. Schweizer and B. J. Jamieson, in press. Influence of snowpack layering on human-triggered snow slab avalanche release, *Cold Regions Science and Technology*.

Haefeli, R., 1939. Snow mechanics with references to soil mechanics, Der Schnee und seine Metamorphose (Translation: SIPRE - Snow, Ice and Permafrost Research Establishment, 1954. Snow and its metamorphism, Corps of Engineers, US Army, Translation No. 14.), Beitrage zur Geologie der Schweiz, Geotechnische Serie, Hydrologie, Lieferung 3, Bern, 58–218.

Haegeli, P., 2005. Winter backcountry use trend estimates for western Canada, *Tech. rep.*, Canadian Avalanche Association, Revelstoke, BC, 22 pp.

Haegeli, P. and D. M. McClung, 2003. Avalanche characteristics of a transitional snow climate–Columbia Mountains, British Columbia, Canada, *Cold Regions Science and Technology*, **37**(3), 255–276.

Hakstian, A. R., J. C. Roed and J. C. Lind, 1979. Two-sample T-2 procedure and the assumption of homogeneous covariance matrices, *Psychological Bulletin*, **86**, 1255–1263.

Hassan, T. and S. Kyriakides, 1992. Ratcheting in cyclic plasticity, part I: uniaxial behavior, *International Journal of Plasticity*, **8**(1), 91–116.

Heierli, J., 2005. Solitary fracture waves in metastable snow stratifications, *Journal of Geophysical Research*, **110**, F02008.

Heierli, J. and M. Zaiser, 2006. An analytical model for fracture nucleation in collapsible stratifications, *Geophysical Research Letters*, **33**, L06501.

Heierli, J. and M. Zaiser, 2008. Failure initiation in snow stratifications containing weak layers: nucleation of whumpfs and slab avalanches, *Cold Regions Science and Technology*, **52**(3), 385–400.

Hentz, S, F. V. Donze and L. Daudeville, 2004. Discrete element modelling of concrete submitted to dynamic loading at high strain rates, *Computers & Structures*, **82**(29-30), 2509–2524.

van Herwijnen, A. and B. Jamieson, 2005. Fracture character in compression tests, Proceedings of the International Snow Science Workshop (2004: Jackson Hole, Wyoming), 182–191.

van Herwijnen, A. and B. Jamieson, 2007a. Fracture character in compression tests, *Cold Regions Science and Technology*, **47**(1-2), 60–68.

van Herwijnen, A. and J. B. Jamieson, 2007b. Snowpack properties associated with fracture initiation and propagation resulting in skier-triggered dry snow slab avalanches, *Cold Regions Science and Technology*, **50**(1-3), 13–22.

Himachal Safety Systems, 2004. Jillett SABRE snow penetrometer for avalanche analysis. User's manual version 3.1., Himachal Safety Systems, 52 pp.

Holmgren, J., M. Sturm, N. E. Yankielun and G. Koh, 1998. Extensive measurements of snow depth using FM-CW radar, *Cold Regions Science and Technology*, **27**(1), 17–30.

Huggel, C., S. Zgraggen-Oswald, W. Haeberli, A. Kääb, A. Polkvoj, I. Galushkin and Evans S. G., 2005. The 2002 rock/ice avalanche at Kolka/Karmadon, Russian Caucasus: assessment of extraordinary avalanche formation and mobility, and application of QuickBird satellite imagery, *Natural Hazards and Earth System Sciences*, **5**, 173187.

Hummel, P. M., 1946. The accuracy of linear interpolation, *The American Mathematical Monthly*, **53**(7), 364–366.

Hummel, P. M., 1947. A Note on Interpolation, *The American Mathematical Monthly*, **54**(4), 218–219.

Ifeachor, E. C. and B. W. Jervis, 1993. Digital Signal Processing, Addison-Wesley.

Jamieson, J. B., 1987. A review of methods and instruments for measuring snow hardness, unpublished.

Jamieson, J. B., 1995. Avalanche Prediction for Persistent Snow Slabs, (Ph.D. thesis), University of Calgary.

Jamieson, J. B., 1999. The compression test – after 25 years, *The Avalanche Review*, **18(1)**, 10–12.

Jamieson, J. B., L. Bakermans and P. Haegeli, 2008. Field observations for localizing snow avalanche danger, Proceedings of the 4th Canadian Conference on Geohazards, Quebec City, QC, May 19-24 2008., 543–550.

Jamieson, J. B. and T. Geldsetzer, 1996. Avalanche Accidents in Canada, Vol. 4, 19841996, Canadian Avalanche Association.

Jamieson, J. B., T. Geldsetzer and C. Stethem, 2001. Forecasting for deep slab avalanches, *Cold Regions Science and Technology*, **33**(2-3), 275–290.

Jamieson, J. B. and C. D. Johnston, 1993. Rutschblock precision, technique variations and limitations, *Journal of Glaciology*, **39**(133), 666–674.

Jamieson, J. B. and C. D. Johnston, 2001. Evaluation of the shear frame test for weak snowpack layers, *Annals of Glaciology*, **32**(2-3), 207–221.

Jamieson, J. B. and J. Schweizer, 2000. Texture and strength changes of buried surface-hoar layers with implications for dry snow-slab avalanche release, *Journal of Glaciology*, **46**(152), 151–160.

Jamieson, J. B., J. Schweizer, P. Haegeli and C. Campbell, 2007. Can stability tests help recreationalists assess the local avalanche danger?, Proceedings of the International Snow Science Workshop (2006: Telluride, Colorado), 468–477.

Johnson, J. B., 2003. A statistical micromechanical theory of cone penetration in granular materials, *Technical report 03-3*, CRREL, 43 pp.

Johnson, J. B. and M. A. Hopkins, 2005. Identifying microstructural deformation mechanisms in snow using discrete-element modeling, *Journal of Glaciology*, **51**(174), 432–442.

Johnson, J. B. and M. Schneebeli, 1998. Snow strength penetrometer, United States Patent no. 5,831,161.

Johnson, J. B. and M. Schneebeli, 1999. Characterizing the microstructural and micromechanical properties of snow, *Cold Regions Science and Technology*, **30(1-3)**, 91–100.

Johnson, R. F. and K. W. Birkeland, 2002. Integrating shear quality into stability test results, Proceedings of the International Snow Science Workshop (2002: Penticton, BC), 508–513.

Klein, G. J., 1946. Method of measuring the significant characteristics of a snow-cover, *Technical memorandum 5*, National Research Council of Canada associate committee on soil and snow mechanics, Ottawa.

Klein, G. J., 1950. Canadian survey of physical characteristics of snow-covers, *Technical memorandum 15*, National Research Council of Canada associate committee on soil and snow mechanics, Ottawa.

Koh, G., N. E. Yankielun and A. I. Baptista, 1996. Snow cover characterization using multiband FMCW radars, *Hydrological Processes*, **10**(12), 1609–1617.

Kronholm, K., 2004. Spatial Variability of Snow Mechanical Properties with Regard to Avalanche Formation, (Ph.D. thesis), University of Zrich.

Kronholm, K. and K. W. Birkeland, 2005. Integrating spatial patterns into a snow avalanche cellular automata model, *Geophysical Research Letters*, **32**, L19504.

Kronholm, K., M. Schneebeli and J. Schweizer, 2004. Spatial variability of micropenetration resistance in snow layers on a small slope, *Annals of Glaciology*, **38**, 202–208.

Kronholm, K. and J. Schweizer, 2003. Snow stability variation on small slopes, *Cold Regions Science and Technology*, **37**(3), 453–465.

Kronholm, K., J. Schweizer, C. Pielmeier and M. Schneebeli, 2003. Spatial variability of snowpack stability on small slopes studied with the stuffblock test, 2nd International Conference on Avalanches and related Subjects, Kirovsk, Russia, 3-7 September 2001, in press.

Kronholm, K., J. Schweizer and M. Schneebeli, 2002. Spatial variability of snow stability on small slopes, Proceedings of the International Snow Science Workshop (2002: Penticton, BC), 549–557.

LaChapelle, E.R. and R.I. Perla, 1967. Alta Avalanche Study, Project B, Report No. 2, *Tech. rep.*, US Department of Agriculture Forest Service, 10 pages.

LaChapelle, E. R., 1966. Avalanche forecasting a modern synthesis, Proceedings of the International Symposium on Scientific Aspects of Snow and Ice Avalanches, Davos, April 5-10, 1965, International Association of Hydrological Sciences, Publication 69, 350–356.

LaChapelle, E. R., 1980. The fundamental processes in conventional avalanche forecasting, *Journal of Glaciology*, **26**(94), 75–84.

LaChapelle, E. R. and R. L. Armstrong, 1976. Nature and causes of avalanches in the San Juan Mountains, Armstrong, R. L. and J. D. Ives, eds., Avalanche Release and Snow Characteristics – San Juan Mountains, Colorado, Institute of Arctic and Alpine Research, University of Colorado, Boulder, CO,, no. 19, 23–40.

Landry, C. C., 2002. Spatial Variations in Snow Stability on Uniform Slopes: Implications for Extrapolation to Surrounding Terrain, (Master's thesis), Dept. Earth Sciences, Montana State University, MT, USA, 194 pages.

Landry, C. C., K.W. Birkeland, K. Hansen, J. Borkowski, R. Brown and R. Aspinall, 2004. Variations in snow strength and stability on uniform slopes, *Cold Regions Science and Technology*, **39**(2-3), 205–218.

Landry, C. C., J. J. Borkowski and R. L. Brown, 2001. Quantified loaded column stability test: mechanics, procedure, sample-size selection, and trials, *Cold Regions Science and Technology*, **33**(2-3), 103–121.

Leinbach, J., 1995. Wiener spiking deconvolution and minimum-phase wavelets: a tutorial, *The Leading Edge*, **14**(3), 189–192.

Logan, N., 1993. Snow temperature patterns and artificial release, Proceedings of the International Snow Science Workshop (1992: Breckenridge, Colorado), 37–46.

Louchet, F., 2001. Creep instability of the weak layer and natural slab avalanche triggerings, *Cold Regions Science and Technology*, **33**, 141–146.

Louge, M. Y., R. L. Foster, N. Jensen and R. Patterson, 1998. A portable capacitance snow sounding instrument, *Cold Regions Science and Technology*, **28**, 73–81.

Louge, M. Y., R. Steiner, S. C. Keast, R. Decker, J. Dent and M. Schneebeli, 1997. Application of capacitance instrumentation to the measurement of density and velocity of flowing snow, *Cold Regions Science and Technology*, **25**, 47–63.

Lutz, E., K. W. Birkeland, K. Kronholm, K. Hansen and R. Aspinall, 2007. Surface hoar characteristics derived from a snow micropenetrometer using moving window statistical operations, *Cold Regions Science and Technology*, **47**(1-2), 118–133.

Mackenzie, R. and W. Payten, 2002. A portable, variable-speed, penetrometer for snow pit evaluation, Proceedings of the International Snow Science Workshop (2002: Penticton, BC), 294–300.

Male, D. H. and D.H. Gray, 1981. Handbook of Snow :Principles, Processes, Management and Use, Pergamon.

Manly, B. F. J., 1994. Multivariate Statistical Methods – A Primer, Chapman and Hall/CRC, 2 ed.

Marshall, H. P., G. Koh and R. R. Forster, 2004. Ground-based frequency-modulated continuous wave radar measurements in wet and dry snowpacks, Colorado, USA: an analysis and summary of the 2002-03 NASA CLPX data, *Hydrological Processes*, **18**(18), 3609–3622.

Marshall, H. P., M. Schneebeli and G. Koh, 2007. Snow stratigraphy measurements with high-frequency FMCW radar: Comparison with snow micro-penetrometer, *Cold Regions Science and Technology*, **47**(1-2), 108–117.

McCammon, I. and J. Schweizer, 2002. A field method for identifying structural weaknesses in the snowpack, Proceedings of the International Snow Science Workshop (2002: Penticton, BC), 477–481.

McCammon, I. and D. Sharaf, 2005. Integrating strength, energy and structure into stability decisions, *The Avalanche Review*, **23**, 18–19.

McClave, J. T. and T. Sincich, 2006. Statistics, Pearson Prentice Hall, 10th edition ed.

McClung, D. M., 1977. Direct simple shear tests on snow and their relation to slab avalanche formation, *Journal of Glaciology*, **19**(81), 101–109.

McClung, D. M., 1979. Shear fracture precipitated by strain softening as a mechanism of dry slab avalanche release, *Journal of Geophysical Research*, **84**(B7), 3519–3526.

McClung, D. M., 1981. Fracture mechanical models of dry slab avalanche release, *Journal of Geophysical Research*, **86**(B11), 10783–10790.

McClung, D. M., 1995. Use of knowledge in avalanche forecasting, *Defence Science Journal*, **45**(2), 117–123.

McClung, D. M. and P. Schaerer, 1993. The Avalanche Handbook, The Mountaineers, second edition ed., 271 pp.

McClung, D. M. and P. Schaerer, 2006. The Avalanche Handbook, The Mountaineers, third edition ed., 342 pages.

McClung, D. M. and J. Schweizer, 2006. Fracture toughness of dry snow slab avalanches from field measurements, *Journal of Geophysical Research*, **111**, F04008.

McClung, D. M. and J. Tweedy, 1993. Characteristics of avalanching: Kootenay Pass, British Columbia, Canada, *Journal of Glaciology*, **39**(132), 316–322.

McClung, D. M. and J. Tweedy, 1994. Numerical avalanche prediction: Kootenay Pass, British Columbia, Canada, *Journal of Glaciology*, **40**(135), 350–358.

Mellor, M., 1964. Properties of snow, *Tech. Rep. III-A1*, CRREL, Hanover, NH.

Mellor, M., 1965. Explosions and snow, *Tech. Rep. Part III, Section A3a*, CRREL, Hanover, NH.

Mellor, M. and J. H. Smith, 1966. Strength studies of snow, *research report 168*, CRREL, 28 pp.

Mock, C. J., 1995. Avalanche climatology of the continental zone of the southern rocky mountains, U.S.A., *Physical Geography*, **16**, 165–187.

Mock, C. J. and K. W. Birkeland, 2000. Snow avalanche climatology of the Western United States mountain ranges, *Bulletin of the American Meteorological Society*, **81**(10), 2367–2392.

Mock, C. J. and P. A. Kay, 1992. Avalanche climatology of the western United States, with an emphasis on Alta, Utah, *The Professional Geographer*, **44**(3), 307–318.

de Montmollin, V., 1982. Shear tests on snow explained by fast metamorphism, *Journal of Glaciology*, **28**(98), 187–198.

Mulqueen, J., J. V. Stafford and D. W. Tanner, 1977. Evaluation of penetrometers for measuring soil strength, *Journal of Terramechanics*, **14**(3), 137–151.

Narita, H., T. Fukuzawa, N. Maeno and W. Ma, 1992. Sample shear deformation of snow containing a weak layer, presented at the Symposium on Snow and Snow-Related Problems in Nagaoka, Japan, 14-18 September, 1992.

NRCC, 1981. Guidelines for weather, snowpack, and avalanche observations, *Technical memorandum 132*, Avalanche Research Centre, National Research Council of Canada, Ottawa.

Palmer, A. C. and J. R. Rice, 1973. The GGrowth of slip surfaces in the progressive failure of over-consolidated clay, *Proceedings of the Royal Society of London. Series A, Mathematical and Physical Sciences*, **332**(1591), 527–548.

Park, S. K. and R. A. Schowengerdt, 1983. Image reconstruction by parametric cubic convolution, *Computer Vision, Graphics, and Image Processing*, **23**(3), 258–272.

Pearce, D. C. and L. W. Gold, 1951. The Canadian snow survey 1947–1950, *Technical memorandum 21*, National Research Council of Canada associate committee on soil and snow mechanics, Ottawa.

Pielmeier, C. and M. Schneebeli, 2000. Measuring snow profiles with high resolution: interpretation of the force-distance signal from a snow penetrometer, Proceedings of the International Snow Science Workshop (2000: Big Sky, Montana), 215–222.

Pielmeier, C. and M. Schneebeli, 2003a. Developments in the stratigraphy of snow, *Surveys in Geophysics*, **24**, 389–416.

Pielmeier, C. and M. Schneebeli, 2003b. Stratigraphy and changes in hardness of snow measured by hand, ramsonde and snow micro penetrometer: a comparison with planar sections, *Cold Regions Science and Technology*, **37**(3), 393–405.

Pielmeier, C. and J. Schweizer, 2007. Snowpack stability information derived from the SnowMicroPen signal, *Cold Regions Science and Technology*, **47**(1-2), 102–107.

de Quervain, M., 1950. Die Festigkeitseigenschaften der Schneedecke und ihre Messung, *Pure and Applied Geophysics*, **18**(1), 179–191.

Reisberg, D. and D. Chambers, 1991. Neither pictures nor propositions: what can we learn from a mental image?, *Canadian Journal of Psychology*, **45**(3), 336–352.

Robinson, E. A. and S. Treitel, 1980. Geophysical Signal Analysis, Prentice-Hall, Inc.

Roch, A., 1949. Report on snow avalanche conditions in the U.S.A. western ski resorts from the 26th of January to the 24th of April, 1949, *Internal report 174*, Swiss Federal Institute for Snow and Avalanche Research, Davos, Switzerland.

Savage, S., 2007. Deep slab avalanche hazard forecasting and mitigation: the South Face

at Big Sky ski area, Proceedings of the International Snow Science Workshop (2006: Telluride, Colorado), 483–490.

Schaap, L. H. J. and P. M. B. Föhn, 1987. Cone penetration testing in snow, *Canadian Geotechnical Journal*, **24**(3), 335–341.

Schneebeli, M. and J. B. Johnson, 1998. A constant-speed penetrometer for high-resolution snow stratigraphy, *Annals of Glaciology*, **26**, 107–111.

Schneebeli, M., C. Pielmeier and J. B. Johnson, 1999. Measuring snow microstructure and hardness using a high-resolution penetrometer, *Cold Regions Science and Technology*, **30**, 101–114.

Schweizer, J., 1998. Laboratory experiments on shear failure of snow, *Annals of Glaciology*, **26**, 97–102.

Schweizer, J., 2002. The rutschblock test procedure and application in Switzerland, *The Avalanche Review*, **20**(5), 14–15.

Schweizer, J. and C. Camponovo, 2001. The skier's zone of influence in triggering slab avalanches, *Annals of Glaciology*, **32**, 314–320.

Schweizer, J. and J. B. Jamieson, 2003. Snowpack properties for snow profile analysis, *Cold Regions Science and Technology*, **37**(3), 233–241.

Schweizer, J. and J. B. Jamieson, 2007. A threshold sum approach to stability evaluation of manual snow profiles, *Cold Regions Science and Technology*, **47**(1-2), 50–59.

Schweizer, J., J. B. Jamieson and M. Schneebeli, 2003. Snow avalanche formation, *Reviews of Geophysics*, **41**(4).

Schweizer, J., K. Kronholm, J. B. Jamieson and K. W. Birkeland, 2007. Spatial variability – so what?, Proceedings of the International Snow Science Workshop (2006: Telluride, Colorado), 365–376.

Schweizer, J. and T. Wiesinger, 2001. Snow profile interpretation for stability evaluation, *Cold Regions Science and Technology*, **33**(2-3), 179–188.

Seligram, G., 1936. Snow Structure and Ski Fields, Macmillan and Co. Ltd., London.

Shapiro, S. S. and M. B. Wilk, 1965. An analysis of variance test for normality (complete samples), *Biometrika*, **52**, 591–611.

Sihvola, A. and M. Tiuri, 1986. Snow Fork for field determination of density and wetness profiles of a snow pack, *Transactions on Geoscience and Remote Sensing*, **GE-24**, 717–721.

SIPRE, 1954. Instructions for making and recording snow observations, *Instruction manual 1*, Snow, Ice and Permafrost Research Establishment, Corps of Engineers, U.S. Army.

Smith, K. A. and C. E. Mullins, 2001. Soil and Environmental Analysis, CRC press, 2 ed.

Sommerfield, R. A., 1980. Statistical models of snow strength, *Journal of Glaciology*, **26**(94), 217–223.

StatSoft, Inc., 2007. Electronic Statistics Textbook, Tulsa, OK: StatSoft.

Stethem, C., J. B. Jamieson, P. Schaerer, D. Liverman, D. Germain and S. Walker, 2003. Snow avalanche hazard in canada - a review, *Natural Hazards*, **28**(2), 487–515.

Stewart, K. W., 2002. Spatial Variability of Slab Stability within Avalanche Start Zones, (Master's thesis), University of Calgary, 103 pages.

Stewart, K. W. and J. B. Jamieson, 2002. Spatial variability of slab stability within avalanche start zones, Proceedings of the International Snow Science Workshop (2002: Penticton, BC), 544–548.

Tabachnick, B. G. and L. S. Fidell, 2007. Using Multivariate Statistics, Pearson/Allyn & Bacon, 5 ed.

Taylor, F. J., 1994. Principles of Signals and Systems, McGraw-Hill.

Taylor, J. R., 1982. An Introduction to Error Analysis : the Study of Uncertainties in Physical Measurements, University Science Books.

UNESCO, 1970. Seasonal snow cover, *Tech. rep.*, UNESCO, IASH, WMO, Technical papers in hydrology 2.

White, D. J. and M. D. Bolton, 2004. Displacement and strain paths during plane-strain model pile installation in sand, *Géotechnique*, **54**(6), 375–397.

White, D. J., W. A. Take and M. D. Bolton, 2003. Soil deformation measurement using particle image velocimetry (PIV) and photogrammetry, *Géotechnique*, **53**(7), 619–631.

White, D. J., W. A. Take, S. E. Bolton and S. E. Munachen, 2001. A deformation measurement system for geotechnical testing based on digital imaging, close-range photogrammetry, and PIV image analysis, 15th International Conference on Soil Mechanics and Geotechnical Engineering, Istanbul, Turkey., Balkema, Rotterdam, 539–542.

Wilkinson, L., 1990. SYSTAT: The System for Statistics, Evanston, IL:SYSTAT, Inc.

Yan, H. B., S. M Hu and R. Martin, 2004. Morphing based on strain field interpolation, *Computer Animation and Virtual Worlds*, **15**(3-4), 443–452.

Yosida, Z., 1956. Physical studies on deposited snow part II: mechanical properties, *Contributions from Institute of Low Temperature Science, Hokkaido University, Sapporo, Japan*, (No. 9), 1–81.

Zaiser, M., 2004. Slab avalanche release viewed as interface fracture in a random medium, *Annals of Glaciology, vol. 38, p.9-14*, **38**, 9–14.

Appendix A

SABRE specifications

The SABRE penetrometer is shown in Figure 1.4. In addition to the components shown, a small external battery pack containing a 9 V battery was also required; this component also performed analogue-to-digital signal conversions to permit the signals to be recorded onto a Pocket PC. The SABRE penetrometer was supplied with software designed to facilitate the capture, processing and visualisation of penetrometer profile data.

The specifications of the sensors are shown in Table A.1. Values are taken from the supplied manual (Himachal Safety Systems, 2004) and a calibration sheet supplied with the instrument. In its unmodified state, data from all four sensors was recorded at 500 Hz onto a Pocket PC.

For the modified penetrometer, data from the force transducer (Table A.1) and a rotary depth encoder wheel (Table A.2) were recorded onto a Campbell Scientific Datalogger (see Appendix B for datalogger specifications). Data from the force transducer were recorded at 1000 Hz and data from the rotary encoder wheel were recorded at 100 Hz.

Table A.1: Specifications of the SABRE penetrometer sensors.

Force transducer	
Type	Piezo-electric
Range	0 to 100 N
Resolution	±0.01 N
Sensitivity	16.87 mV per N after signal conditioning
Temp range	-40 to 50°C
Temperature sensor 1	
Type	Thermopile
Range	-40 to 85°C
Resolution	±1°C
Sensitivity	not specified (non-linear)
Temperature sensor 2	
Type	Thermister
Range	not specified
Resolution	not specified
Sensitivity	not specified
Accelerometer	
Type	MEMS
Range	up to 1000 g (where g is acceleration due to gravity)
Sensitivity	80 mV per g
Temp Range	-40 to 85°C

Table A.2: Specifications of the TR1-TruTrac^{TM} rotary encoder wheel.

TR1-TruTrac^{TM}	
Type	Rotary, optical encoder wheel
Manufacturer	Encoder Products Company
Wheel diameter	200 mm
No. divisions	1024
Output	5 V square wave
Wheel material	Aluminum with urethane face
Temp range	-40 to 85°C

Appendix B

Datalogger specifications

Table B.1: Specifications of the Campbell Scientific CR1000 datalogger as configured for operation with the SABRE penetrometer and custom depth encoder.

Program execution	
Program execution rate	100 Hz
Program measurements	10 analogue (force) and 1 pulse (depth)
Analogue inputs	
Accuracy:	
0 to 40°C	4.002 mV + 0.06% of reading
-25 to 0°C*	4.002 mV + 0.12% of reading
-40 to -25°C	4.002 mV + 0.18% of reading
Measurement range	±5000 mV
Resolution	1.333 mV
Pulse input	
Maximum counts per scan	16.7×10^6
Voltage threshold for count	Transition from 0.9 to 2.2 V
General specifications	
Temp range	-55 to 85°C
Power supply	9 to 16 V
Weight	1.0 kg
Typical current drain:	
Sleep mode	∼0.6 mA
Program running, keypad not backlit	∼35 mA
Program running, keypad backlit	∼128 mA

Appendix C

Correlation between hand hardness and density

The information here pertains to the information used to create Figure 2.21.

These data come from an extensive snow profile database (n=5371) of hand hardness measurements for individual snow layers which were recorded together with density measurements made using a 100 cm^3 snow density kit. A hardness value was assigned to each hand hardness value according to Table C.1. These values were based on strength values given by Colbeck and others (1990), with the mean values used for each hand hardness category, reduced by a factor of 4 to take into account that the North American hand hardness scale applies a pressure of 10 to 15 N (mean of 12.5) whereas the International hand hardness scale applies a pressure of 50 N. For + qualifiers, one third of the difference to the next category is added, for *(*-) qualifiers, one third of the difference to the previous category is subtracted. The exponential regression line was found to be highly significant at α=0.05 with p<0.001.

Table C.1: Numerical hardness (strength) values assigned to each hand hardness category

Hand hardness category	Numerical hardness value (Pa)
F-	80
F	120
F+	440
4F-	760
4F	1,080
4F+	4,320
1F-	7,560
1F	10,800
1F+	43,200
P-	75,600
P	108,000
P+	272,000
K	600,000

Appendix D

Estimate of lateral spreading in the snowbox experiments

The following calculation gives an estimate for the lateral spreading in the snowbox deformation experiments in Chapter 3. Only lateral spreading is considered here, which affects the horizontal extent of the deformation zone. Additional material may also be deflected vertically downwards, adding to the vertical extent of the deformation zone; extra vertical deformation is not considered here.

The geometry for extra lateral spreading around the shaft is shown in plan view in Figure D.1. Without the constraint of the snowbox wall, some of the snow from the region occupied by the penetrometer shaft would normally be redistributed within the region A_{out}. Instead, the presence of the snowbox wall causes this snow to be deposited in a densified form in the region A_e (dark shaded region in Figure D.1). It is assumed that the extra snow is densified to the same snow density as the snow in the compacted zone. The extra volume of snow per unit shaft length that must be accommodated is given by:

$$A_e = \frac{A'_c(\rho_c - \rho_0) + A'_d(\bar{\rho}_{d_out} - \rho_0)}{\rho_c} \tag{D.1}$$

where A'_c is the sub-region of A_{out} associated with the compacted zone and A'_d is the sub-region of A_{out} associated with the deformation zone. ρ_0 is the density of undeformed snow, ρ_c is the density of snow in the compacted zone and $\bar{\rho}_{d_out}$ is the mean density of snow that with no constraint would have been deposited in the region A_{out}. A'_c and A'_d are given by:

$$A'_c = r_c^2 \cos^{-1}\left(\frac{r_s}{r_c}\right) - r_s\sqrt{r_c^2 - r_s^2} \tag{D.2}$$

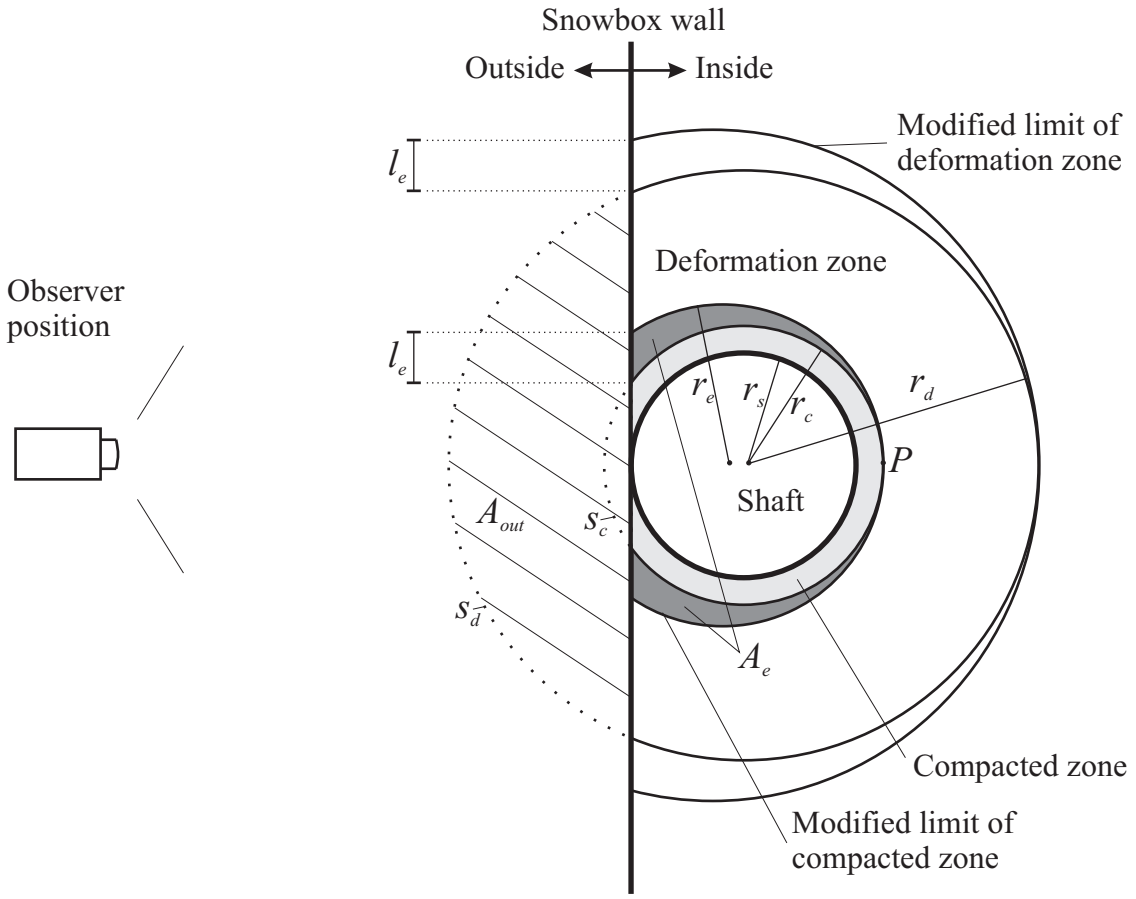

Figure D.1: Plan view of geometry used to assess the effect of lateral spreading on the snow deformation experiments. The extra lateral spreading due to the edge effect is denoted by l_e. The hashed region A_{out} represents the hypothetical region outside the snowbox where snow would have been deformed in the absence of the snowbox wall.

$$A'_d = \left(r_d^2 \cos^{-1}\left(\frac{r_s}{r_d}\right) - r_s\sqrt{r_d^2 - r_s^2} \right) - A'_c \tag{D.3}$$

where r_s is the radius of the penetrometer shaft, r_c is the radius of the compacted zone and r_d is the radius of the deformation zone.

The density of the snow in the deformation zone, ρ_d, is assumed to vary as a linear function with radial distance with $\rho_d = \rho_c$ at r_c and $\rho_d = \rho_0$ at r_d. $\bar{\rho}_{d_out}$ is approximated by:

$$\bar{\rho}_{d_out} \approx \frac{(s_c\rho_c + s_d\rho_0)}{(s_c + s_d)} \tag{D.4}$$

where s_c and s_d are the segment lengths of the extensions to the compacted zone and

deformation zone respectively outside the snowbox.

l_e represents the extra lateral spreading (which we assume to be equal in both the compacted zone and deformation zone) due to the edge effects that would be observed when looking on at the experiments from the side. It is assumed that the extra snow material expands the compacted zone to a cylindrical form (cut off by the edge of the snowbox) with the condition that the unconstrained compacted zone and the modified compacted zone touch at point P in Figure D.1. l_e is given by:

$$l_e = \frac{(2\sqrt{r_c^2 - r_s^2}) - (2\sqrt{r_e^2 - r_s^2})}{2} \tag{D.5}$$

where r_e is the radius of the modified compaction zone. The two terms in the numerator of the RHS of Equation D.5 represent the lengths of the two chords (in plan view) formed by the intersection of the original compacted zone and the modified compacted zone respectively with the snowbox wall. A_e is related to r_e by:

$$A_e = \left(\pi r_e^2 - (r_e^2 \cos^{-1}\frac{d_e}{r_e} - d_e\sqrt{r_e^2 - d_e^2})\right) - (A_c - A_c') \tag{D.6}$$

where $d_e = r_c - (r_e - r_s)$ (the distance between the centre of the modified compacted zone and the snowbox wall) and $A_c = 2\pi r_c^2$ (the volume per unit area of the original compacted zone).

Values of l_e were calculated by first by equating Equations D.1 and D.6 and iteratively solving for r_e using the parameter values shown in Table D.1. l_e was then be found using Equation D.5. The calculations are sensitive to $r_d - r_s$, the radial extent of the deformation zone. Floyer and Jamieson (2006) report mean values for the radial deformation extent of 7 mm for snow densities around 100 kg m^{-3} and 12 mm for snow densities around 330 kg m^{-3}. Figure D.2 shows how l_e varies for different values of ρ_c/ρ_0 and $r_c - r_s$ using these two values for the deformation extent, that correspond approximately to the snow properties of layer 1 and layer 2 respectively from the snow deformation

experiments. The extent of the compaction zone and the ratio of undisturbed to compacted snow are very hard to assess and were not measured directly in the deformation experiments. However, some reasonable approximations are used, based on observations from the deformation experiments. For layer 1, the compacted zone extent appears to be relatively small, approximately 1 mm; the low density of this layer gives relatively little mass of snow to redistribute. The compacted zone density is assumed to be 240 kg m^{-3} (ρ_c/ρ_0 =3), which from Figure D.2a gives l_e ≈1 mm. For layer 2 the compacted zone extent appears to be approximately 3 mm, and a compacted snow density of 430 kg m^{-3} (ρ_c/ρ_0 =1.3) is assumed, giving l_e ≈2 mm.

These values are presented as a best estimate for the lateral spreading effect in the deformation experiments. Confidence for these values is not high, especially in view of the complicated deformation patterns associated with the rounded tip shape.

Table D.1: Values used in the lateral spreading effect calculations.

Parameter	Description	Value/range
$r_c - r_s$	radial extent of compaction zone	0 to 5 mm
$r_d - r_s$	radial extent of deformation zone	7, 12 mm
ρ_c/ρ_0	relative snow compaction	1 to 5
$2r_s$	penetrometer shaft diameter	12 mm

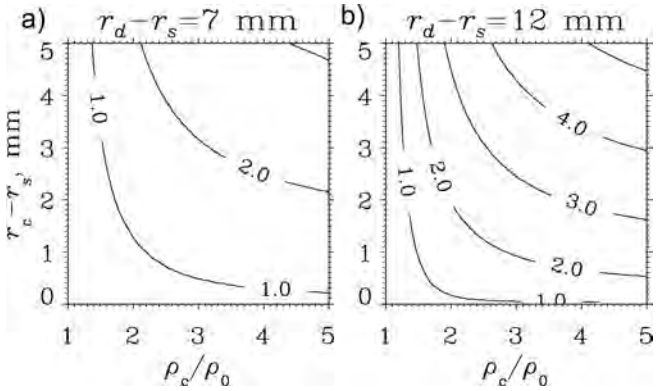

Figure D.2: Contour plots of lateral spreading l_e, for a range of values for the radial extent of the compaction zone ($r_c - r_s$) and the ratio of compacted to uncompacted snow (ρ_c/ρ_0). a) radial extent of the deformation zone, $r_d - r_s = 7$ mm; b) $r_d - r_s = 12$ mm

Appendix E

Manual snow profiles for the spatial variability case studies

The following pages show the manual snow profiles that were conducted at the transect sites. All manual profiles were collected on the same date as the penetrometer transect was performed, except for the Loop-Ross site boulder field transect, which was collected the day after the transect.

The reader is referred to Canadian Avalanche Association (2002) for explanations for the symbols on the manual snow profiles. For grain type symbols, see Table 2.1.

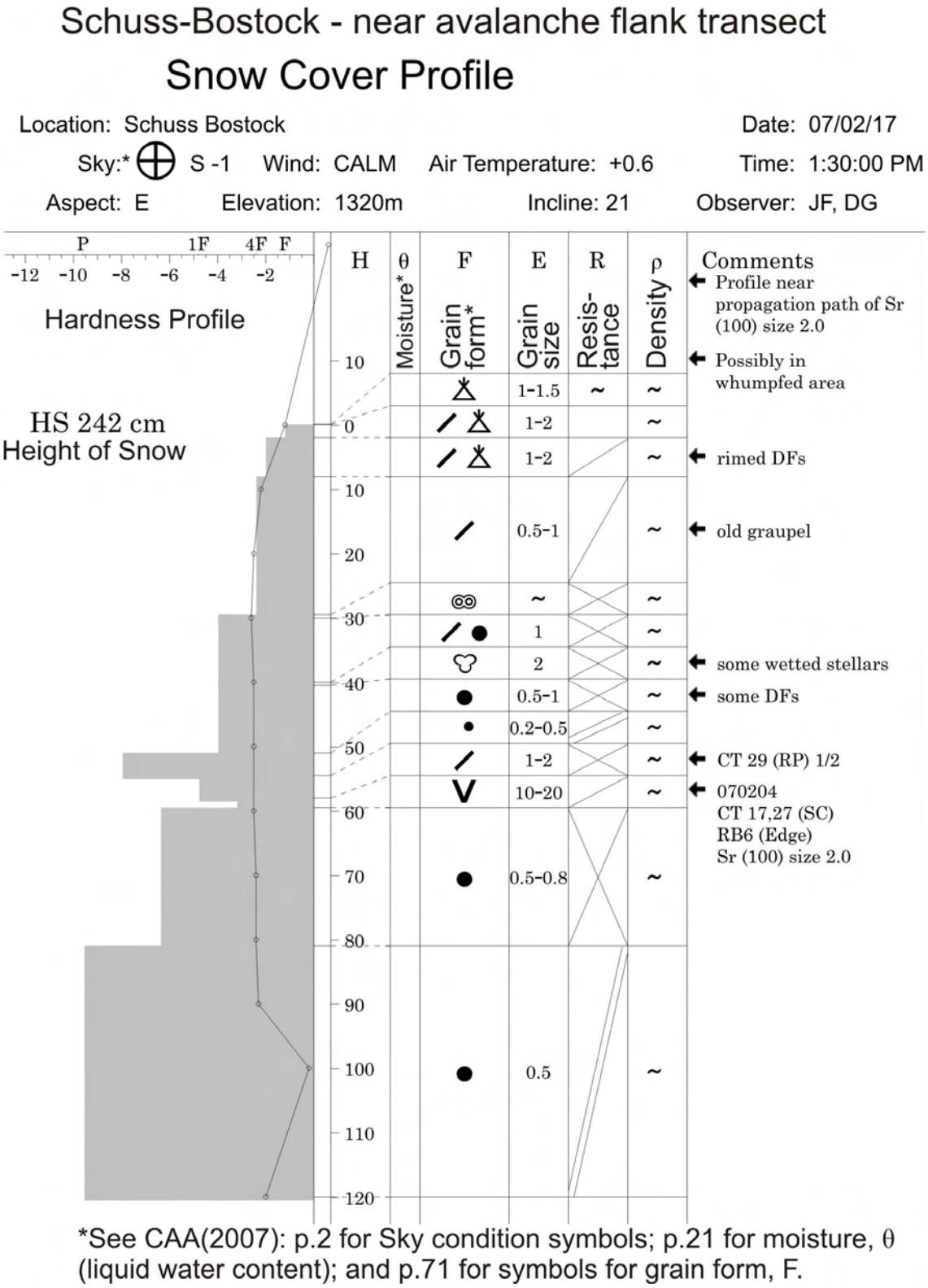

Figure E.1: Manual snow profile for the Bostock-Schuss avalanche flank transect.

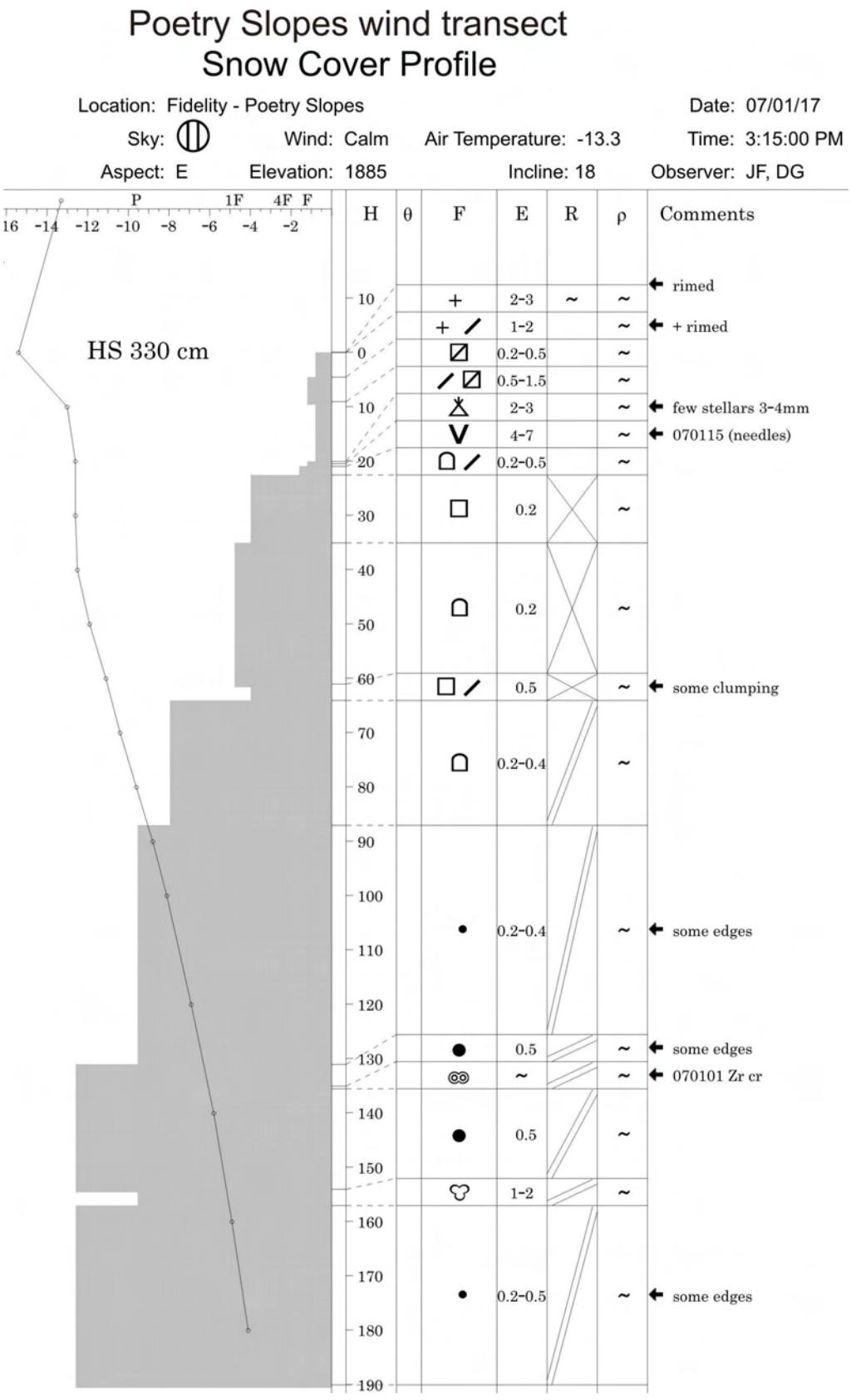

Figure E.2: Manual snow profile for the Poetry Slopes wind transect.

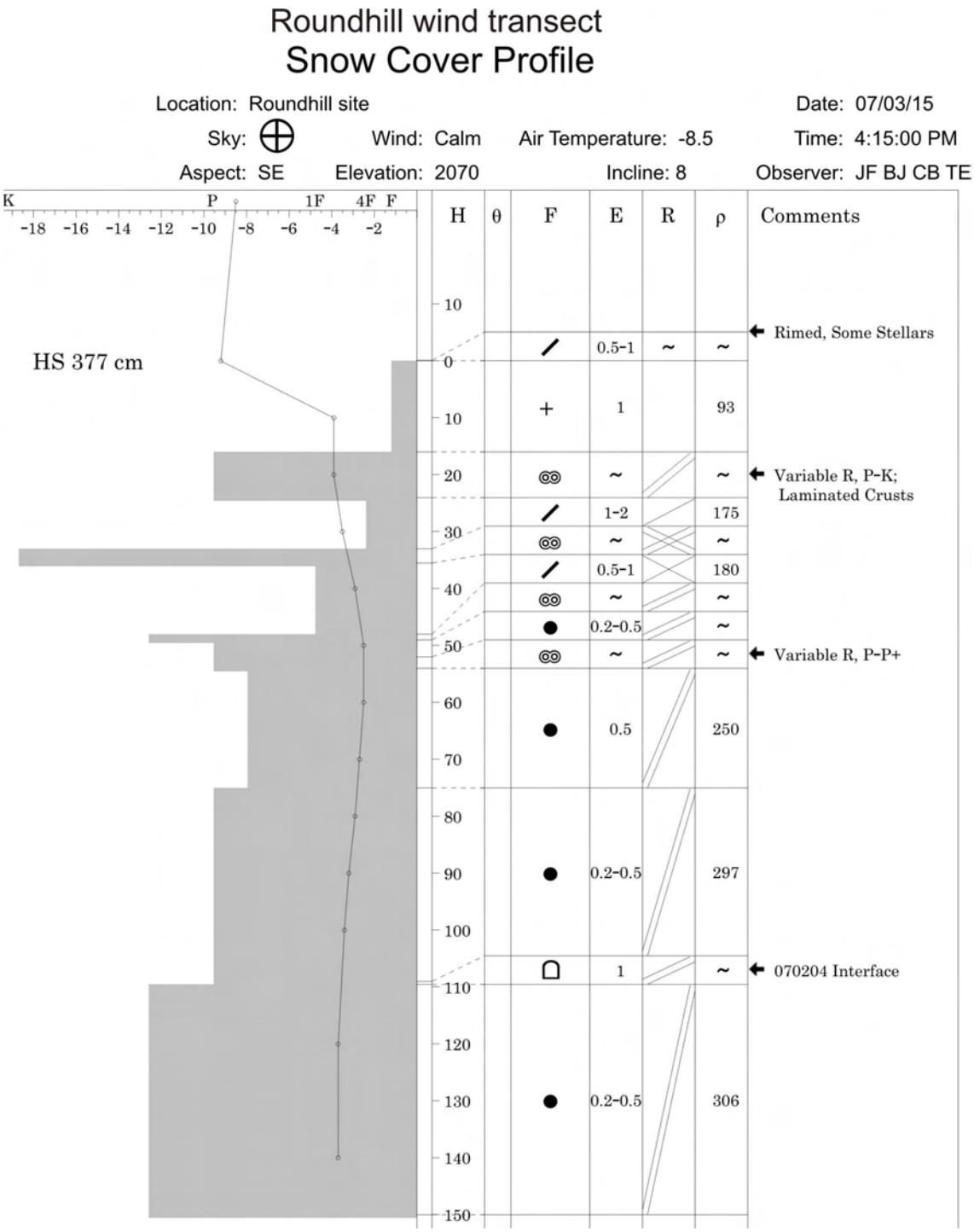

Figure E.3: Manual snow profile for the Roundhill wind transect.

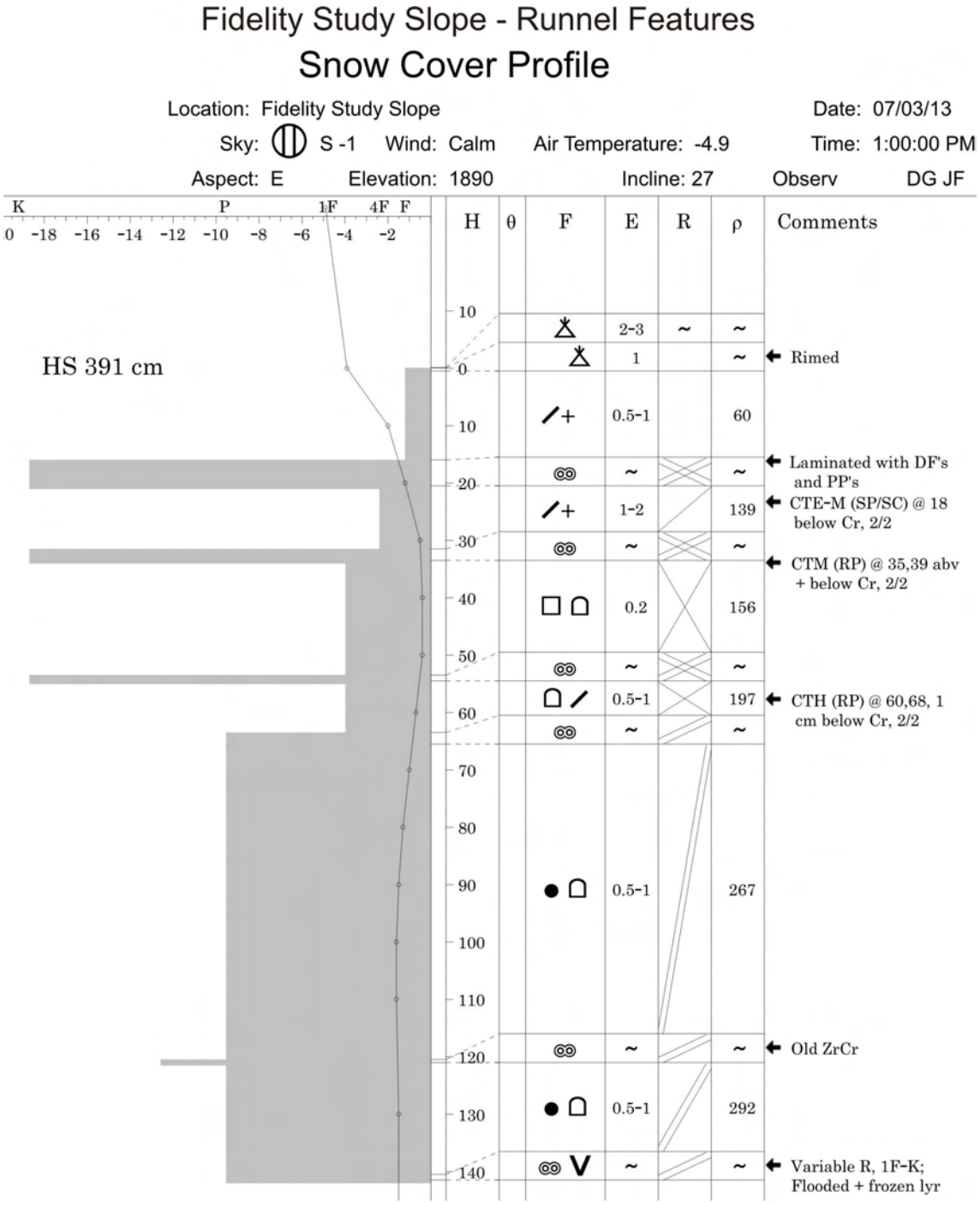

Figure E.4: Manual snow profile for the Fidelity Study Slope runnel transect.

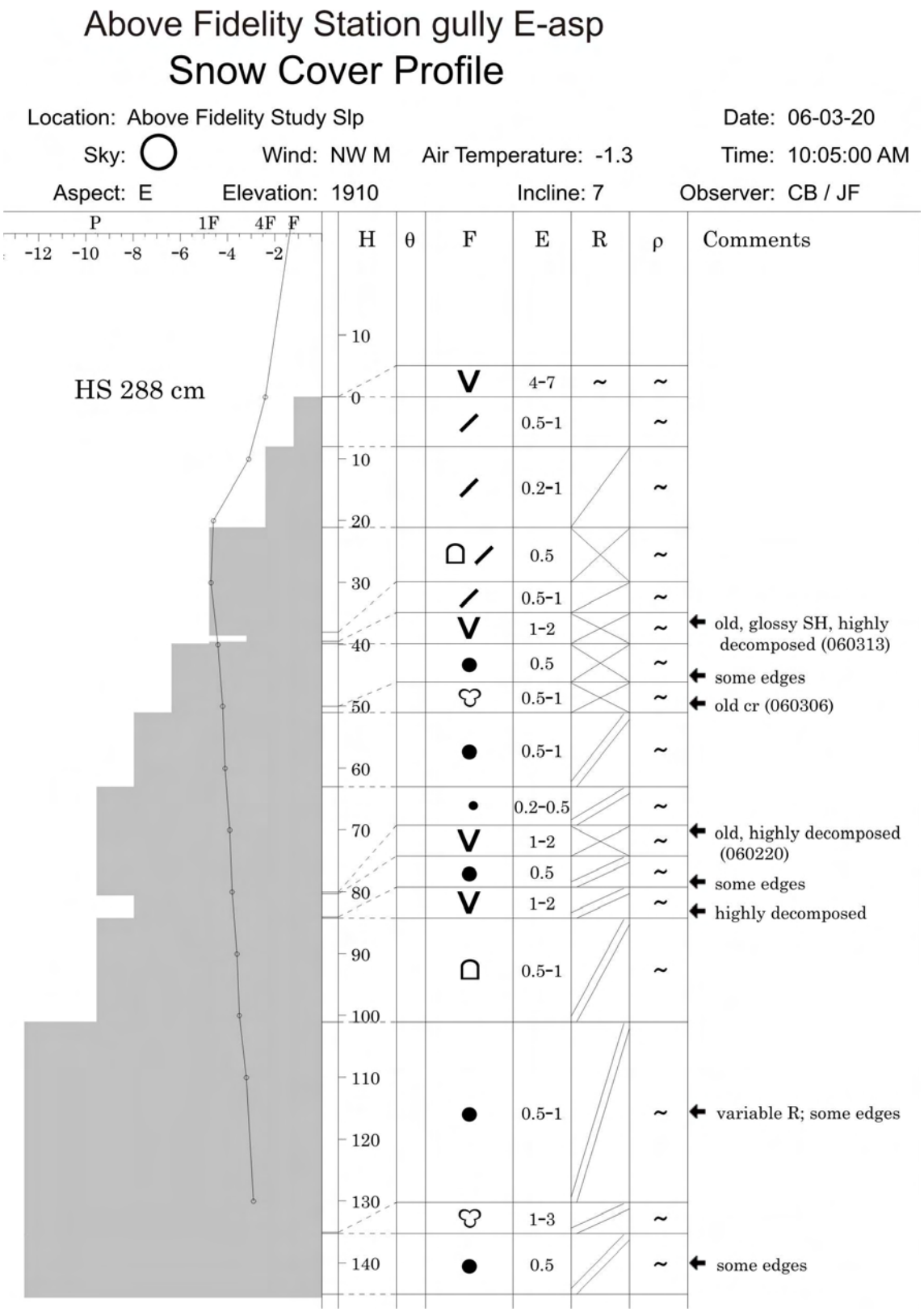

Figure E.5: Manual snow profile for the Above Fidelity Station gully transect, east aspect.

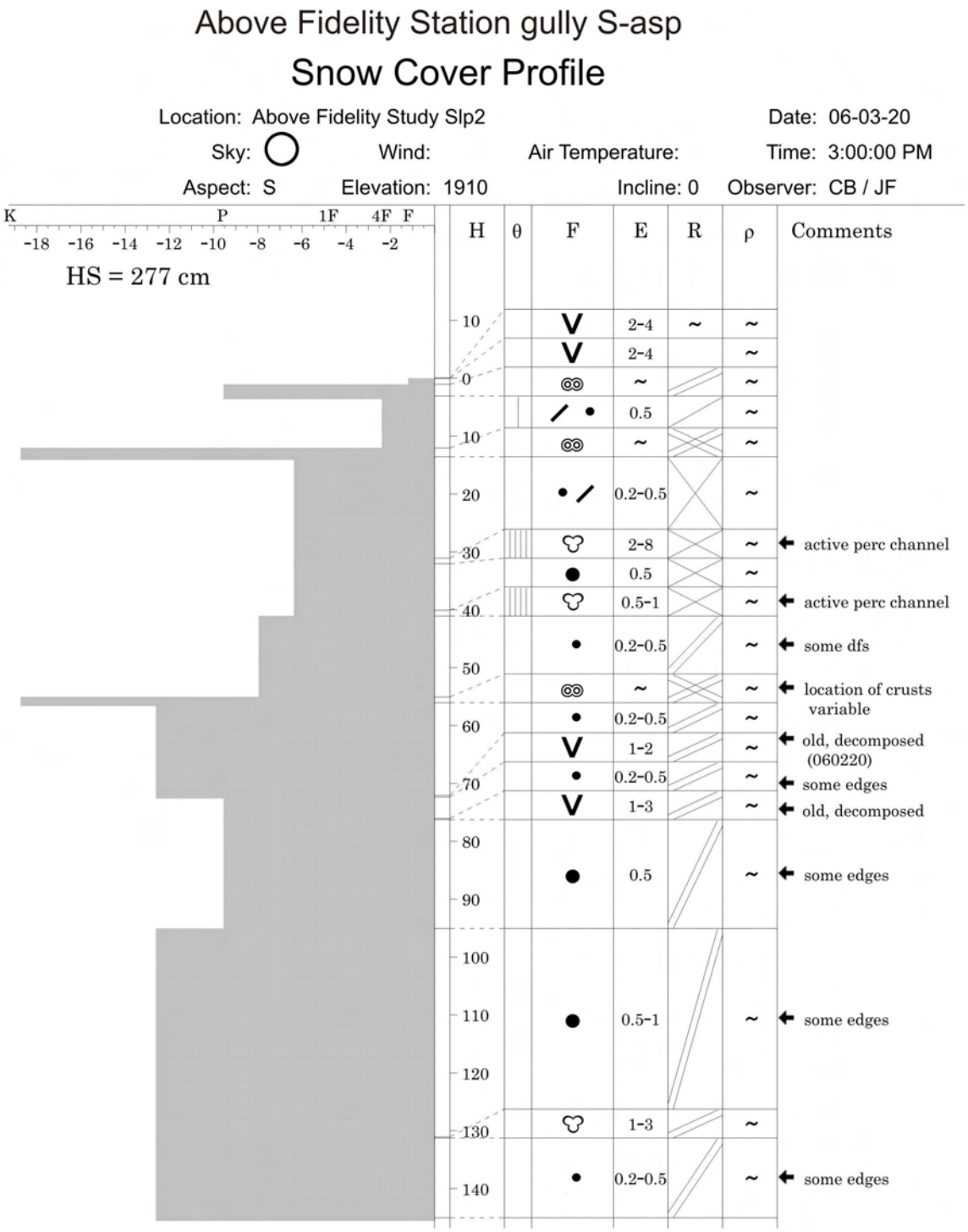

Figure E.6: Manual snow profile for the Above Fidelity Station gully transect, south aspect.

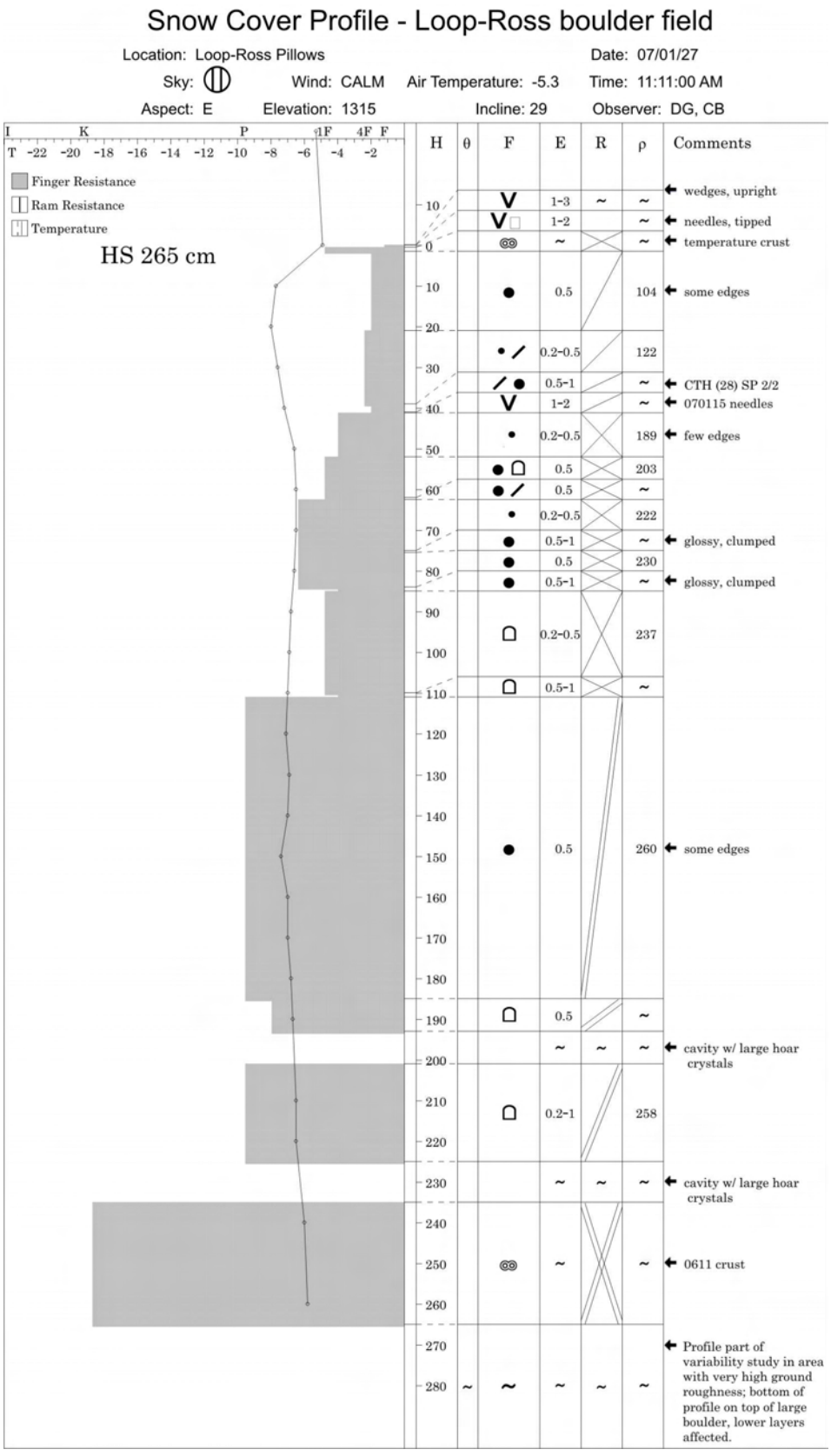

Figure E.7: Manual snow profile for the Loop-Ross boulder field transect.

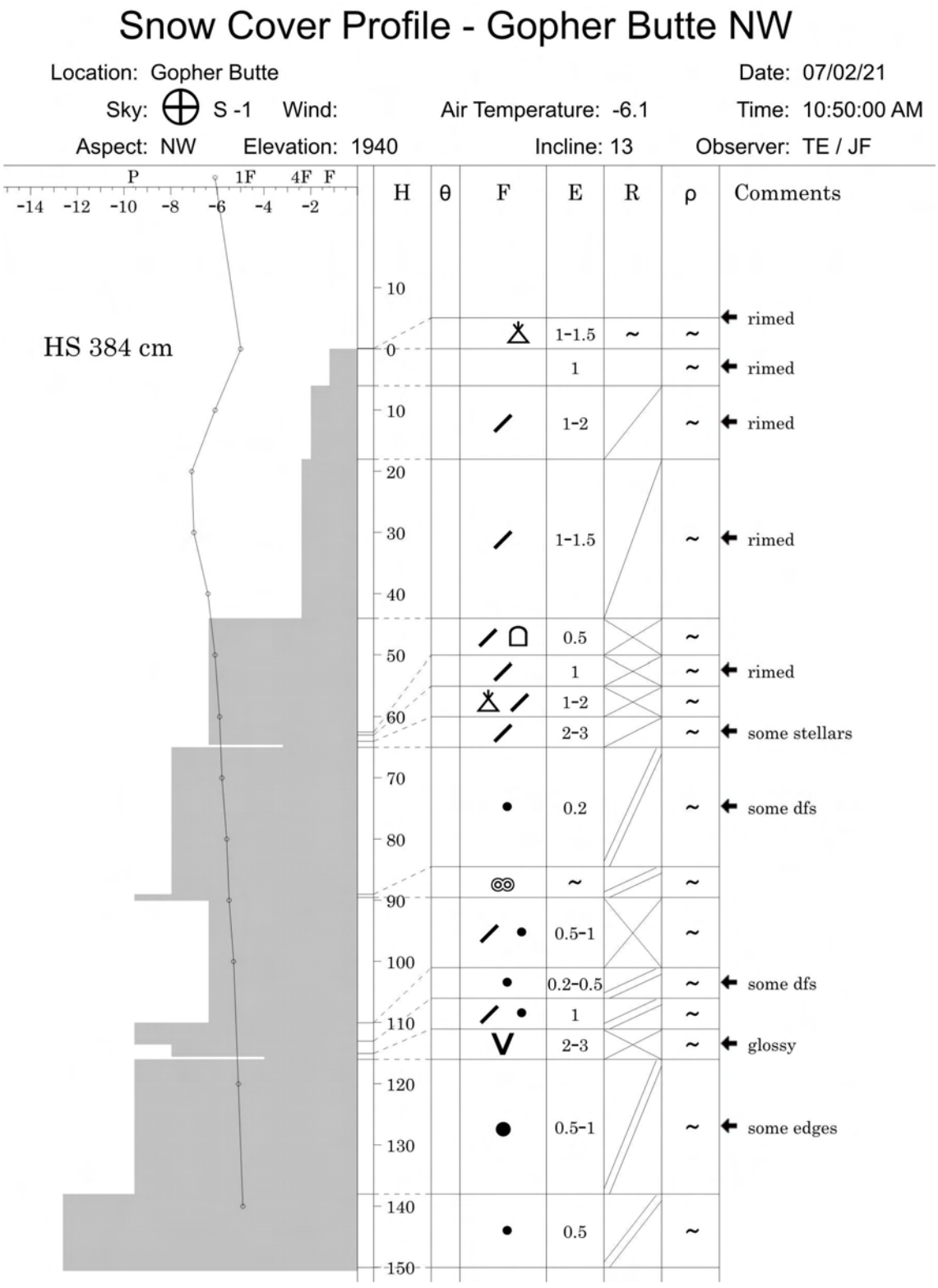

Figure E.8: Manual snow profile for the Gopher Butte aspect transect – northwest-facing slopes.

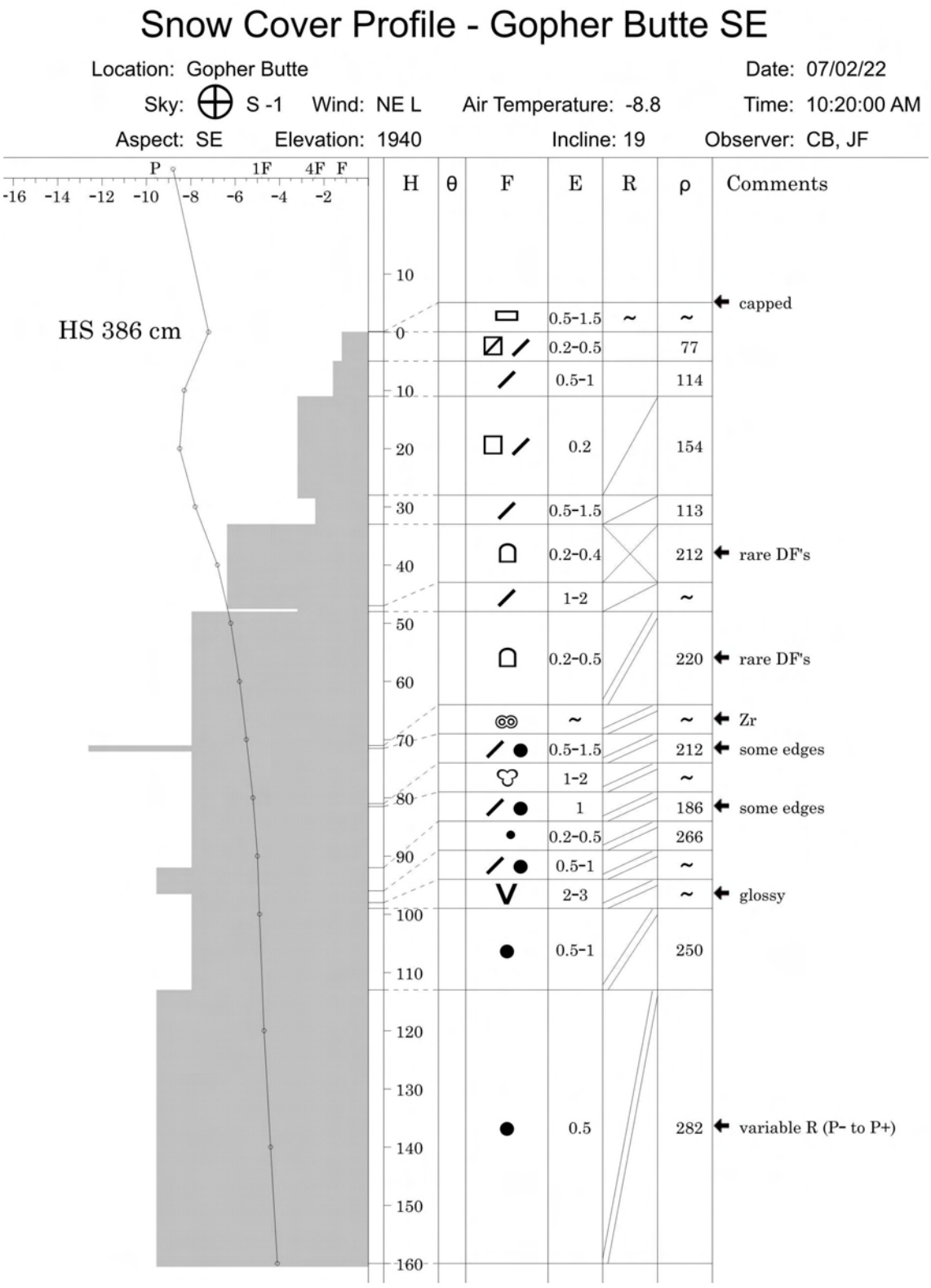

Figure E.9: Manual snow profile for the Gopher Butte aspect transect – southeast-facing slopes.

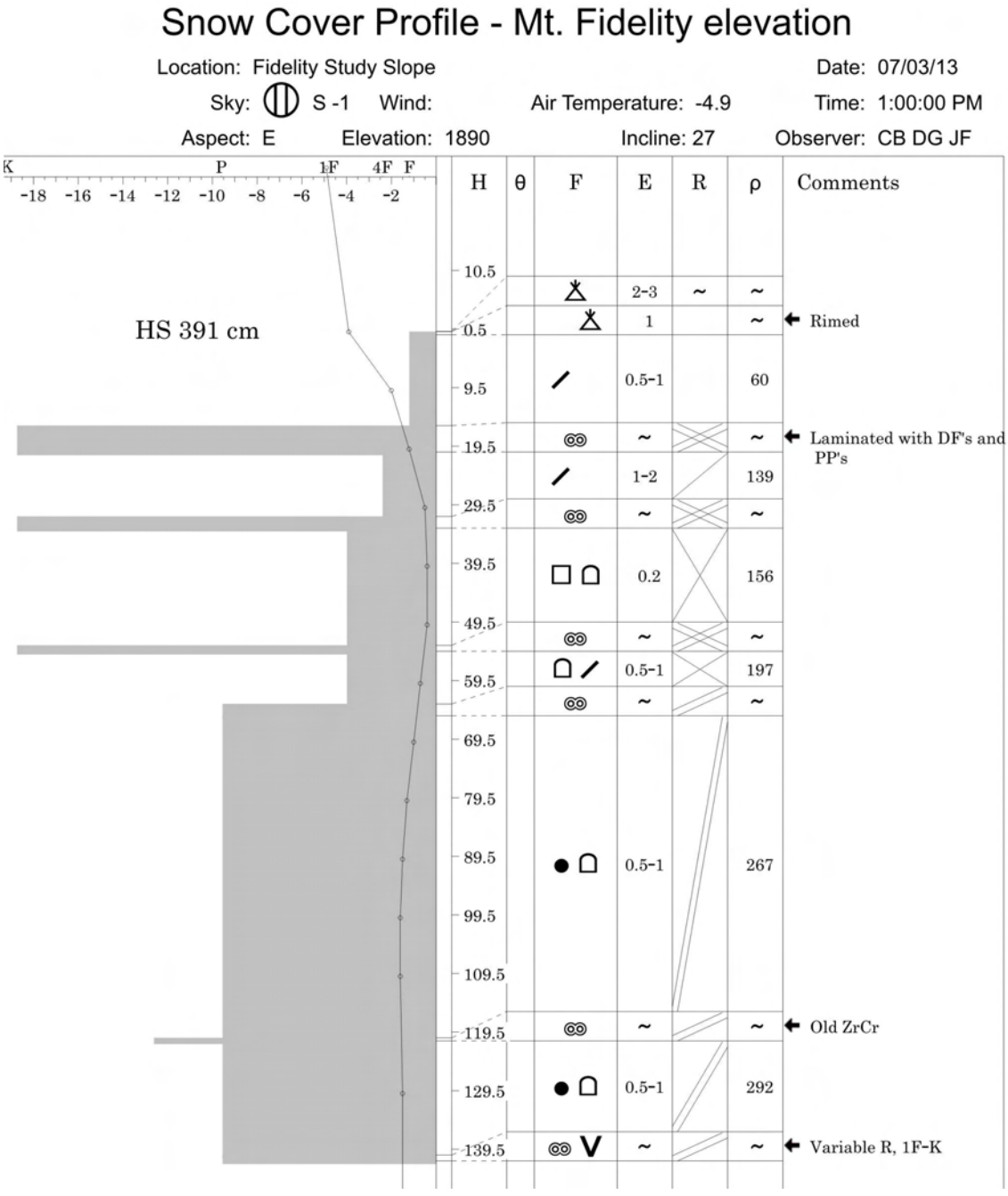

Figure E.10: Manual snow profile for the highest elevation site on the Mount Fidelity elevation transect.